Gust Load Alleviation by Fluidic Actuators on a Blended-Wing-Body Configuration

Yonghong Li

Department of Mechanical Engineering
University of Sheffield

A thesis submitted in partial fulfilment of the requirements for the degree of
Doctor of Philosophy

Supervised by Professor Ning Qin

July 2020

I would like to dedicate this thesis to my wife, son and daughter.

Abstract

Gusts are of critical importance to aircraft designs, as gust loads often define the maximum critical loads that the aircraft structures will experience in flight. In practice, a large amount of structure mass penalty has to be made to withstand the critical load. Therefore, accurate gust load prediction and efficient gust load alleviation approaches will contribute to the future aircraft designs pursuing ‘Green Aviation’, through providing a potentially alternative way for drag reduction by decreasing the aircraft structure weight.

This research focuses on gust response simulations and gust load alleviation using URANS solutions. A numerical tool coupling three-dimensional URANS, structural dynamic equations of motion and Field Velocity Method is set up, validated and used for this project.

Instead of the traditional approaches for gust load alleviation using control surfaces, such as ailerons, elevators or spoilers, this study aims to explore the feasibility and effects of two different fluidic actuators for load control and gust load alleviation for subsonic and transonic flow conditions. One is circulation control (CC) via jet blowing tangential through the trailing-edge Coanda surfaces. The other is normal microjet blowing perpendicular to the aerofoil or wing surfaces.

Detailed comparisons of load control mechanisms and capabilities under constant and dynamic blowing momentum coefficients between CC and normal microjet blowing are firstly conducted for subsonic and transonic incoming flows. The feasibility and effects of gust load alleviation by these two approaches are firstly tested on a 2-D NACA0012 aerofoil and a simple 3-D wing.

A blended-wing-body (BWB) configuration as well as its structural model are generated by reference to the Boeing 2nd-generation BWB model. The influence of spanwise load distributions on the BWB performance is evaluated, followed by the studies of gust load alleviation by these two methods under reference gust conditions defined by the certification specifications of large commercial aircraft covered by the European Union Aviation Safety Agency (EASA) CS-25.

The results from the case studies demonstrate that both CC and normal microjet blowing have the capability for load control and gust load alleviation for subsonic and transonic incoming flows. However, CC exhibits stronger load control capability under subsonic speed, while normal microjet blowing performs better at transonic range. Due to the fast-frequency response characteristic, these methods are capable for adaptive gust load controls. On the BWB model, the reference gust load defined by EASA CS-25 can be well suppressed by either CC or normal microjet blowing.

This research provides further insights into the feasibility and effects of load control and gust load attenuation by means of circulation control and normal microjet blowing. This improved understanding of these two load control means can contribute to the design of future more efficient transport aircraft for reduced drag and emission.

Acknowledgements

I would like to give my sincerely gratitude to my supervisor, Professor Ning Qin, for all the advices and help throughout my Ph.D. study. I have learned and benefited a lot from his thorough and valuable knowledge. The most impressive part is his rigorous scientific altitude which I believe that will benefit me for my following academic life. I would also like to thank my second supervisor, Dr. Jose Curiel Sosa for his insightful advices and comments.

I would like to thank all my friends, especially in Room RD14 for their support and friendship. I have to say that I had a really great time together with them during my stay in the University of Sheffield. In particular, I am grateful to Feng Xie, Alistair John, Thomas PR Pratt, Jose Daniel Perez Munoz, Razvan M Apetrei and Jed Hollom in the Aerodynamics group for the inspiring and insightful discussions about my research. I would like to thank Matthew J. Forster for generously providing the configuration of the 6% thick elliptical circulation control aerofoil.

I would also like to acknowledge High Speed Aerodynamics Institute, China Aerodynamics Research and Development Center for the financial support of my Ph.D. study. I would like to give my sincere gratitude to the unit directors and colleagues there for so many helps they provided for me in pursuing the doctoral degree. There are far too many people to be enlisted in this acknowledgment. Here, I would like to particularly pick Binbin Lv, Pengxuan Lei, Hongtao Guo, Yong Huang, Xin Peng, and Xiaobing Wang for the advices and help in aeroelasticity and BWB model design.

Last, but not least, my gratitude and respect always go to my beloved parents, wife, son and daughter in China. I would like to say sorry to my wife for leaving her alone to take care of our beloved son and daughter in this hardest time. I would also like to thank my parents-in-law for helping taking care of the family during my absence. Without the

support from my beloved family, I would not have managed to carry out my Ph.D. study.

Contents

List of figures

List of tables

Nomenclature

x, y, z	Cartesian variables in streamwise, spanwise and vertical directions
ξ, η, ζ	Generalized coordinate
$\hat{\boldsymbol{Q}}$	Conservative variables
$\hat{\boldsymbol{F}}, \hat{\boldsymbol{G}}, \hat{\boldsymbol{H}}$	Inviscid flux terms
$\hat{\boldsymbol{F}}_v, \hat{\boldsymbol{G}}_v, \hat{\boldsymbol{H}}_v$	Viscid flux terms
Pr	Prandtl number
γ	Specific heat ratio
$\tau_{x_i x_j}$	Shear stresses
u,v,w	Velocity component in x, y, z direction, respectively
$\dot{q}_{x_i}$	Heat flux terms
a	Sound velocity
Re	Reynolds number
$\boldsymbol{q}$	Generalized coordinate
M_∞	Free-stream flow Mach number
U_∞	Free-stream flow velocity in x direction
w_g	Gust velocity
w_{g0}	Magnitude of the peak, or design gust velocity

L_g	Gust wavelength
H_g	Gust gradient
ω	Gust frequency
$\boldsymbol{M}$	Generalized mass matrix
$\boldsymbol{C}$	Generalized damping matrix
$\boldsymbol{K}$	Generalized stiffness matrix
$\boldsymbol{Q}$	Generalized force
Φ	Generalized mode value
c	Chord length for aerofoil
$\bar{c}$	Mean aerodynamic chord length
b	Semi-chord length for aerofoil
l	Span length
S	Reference area
m	Wing mass
s	Non-dimensional time
t	Physical time
λ_m	Dimensionless mass parameter
$\emptyset$	Wagner function
Ψ	Küssner function
$\ddot{z}$	Acceleration rate in z direction
C_L	Lift coefficient
C_D	Drag coefficient
C_{mx}	Wing root bending moment coefficient
Cm	Pitching moment coefficient
$\frac{\partial C_L}{\partial \alpha}$	Lift coefficient slope

C_μ	Momentum coefficient
$C_{\mu 0}$	Peak momentum coefficient with ‘one-minus-cosine’ profile
C_p	Pressure coefficient
α	Angle of attack
t/c	Average wing thickness ratio
λ	Span taper ratio
$\Lambda_{\frac{1}{4}}$	Wing sweep angle
W_{to}	Designed take-off weight
W_{zf}	Designed zero fuel weight

Abbreviations

CC	Circulation control
NPR	Nozzle pressure ration
rmbr	Root bending moment relief factor
EASA CS-25	European Union Aviation Safety Agency Certification Specifications
BWB	Blended wing body
CFD	Computational fluid dynamics
URANS	Unsteady Reynold-Averaged Navier-Stokes equations
FVM	Field Velocity Method
BAH wing	A jet transport wing named by Bisplinghoff, Ashley, and Halfman

Chapter 1

Introduction

1.1 Background and motivations

Load control is an important topic in aerodynamics, as it can potentially provide an alternative way for drag reduction through decreasing the aircraft structure weight. It is well known that the structure mass is not determined by the cruise condition but is dictated by the critical load cases such as gust and manoeuvring loads. Guo *et al*. [1] indicated that the gust loads can be larger than the manoeuvring loads, and generate the most critical load cases that some aircraft will experience in flight. Figure 1.1 demonstrates the sketch of spanwise load distributions on a typical civil transport aircraft under the cruise and gust encountering conditions. Compared to the cruise condition, the spanwise loading especially on the wing will experience a significant increase when encountering gusts. This increase will affect the riding comfort of the passengers, and sometimes can be detrimental for the aircraft structure safety if the gust load is violent enough. For the safety of large commercial aircraft, airworthiness authorities have specified typical gust models as a requirement for the certification specifications of large commercial aircraft covered by European Union Aviation Safety Agency Certification Specifications (EASA CS-25) [2]. To cope with these critical load cases, aircraft structures need to be well built to withstand the forces and stress caused by gusts with a large amount of mass penalty, since it is challenging to build the structure that is both light and robust. However, from another point of view, if the load can be effectively alleviated, lighter structures may be built and thus resulting in the reduction in drag and fuel consumption.

Currently, for gust load alleviation, it is to deflect control flaps to create forces and moments to attenuate gust loads. In this process, sensors are used to provide the information for the calculation of gust loads and then provide the signals to the controllers. Ailerons, elevators or spoilers are normally used as the control surfaces for gust load alleviation. However, a common problem in using control surfaces for gust load alleviation is their slow response time. Being unsteady aerodynamic disturbances, gusts can have high frequencies. As pointed out by Al-Battal *et al*. [3, 4], control surfaces exhibit low-frequency response, which is ineffective at high gust frequency, due to their large inertia.

Up to now, little attention has been put on exploring more effective gust load alleviation methods with fast response. Most research activities have been focused on gust load attenuation system designs especially on the design of control laws [5, 6], such as linear quadratic Gaussian method [7, 8], and optimal control algorithms [9].

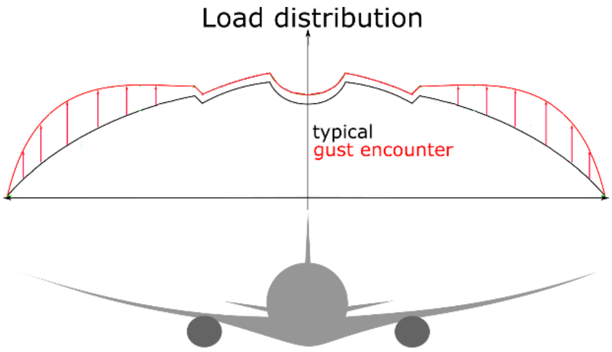

Figure 1.1 The sketch of the spanwise load distributions under cruise and gust encountering conditions

Fluidic actuators, such as blowing or suction, synthetic jets, and oscillating jets, have been studied for many decades in the field of active aerodynamic flow control. Most of the studies focused on changing the momentum balance in the boundary layer to achieve aerodynamic improvement, such as lift augmentation, drag reduction, stall delay, etc. Recently, fluidic actuators have seen renewed interest for their potential application for modern aircraft flight control. Being able to fly and control aircraft without conventional control surfaces (namely flapless control) is one of the targets for future aircraft design with benefits including fewer moving parts, possibly less weight [10], less maintenance and enhanced stealth characteristics [11]. One of the promising methods to replace these traditional flaps is to employ fluidic actuators.

A few studies have been carried out to evaluate the capability of fluidic actuators as flight control effectors. These studies include a joint project [11-13] carried out by BAE Systems, University of Manchester and Cranfield University to demonstrate technologies of circulation control (CC) for flapless control; control effects by means of CC on a diamond wing tailless UAV conducted experimentally by Cook *et al*. [14]; numerical study of CC as a roll effector on the generic SACCON UCAV configuration carried out by Hoholis *et al*. [15] and the effects for providing manoeuvrability by CC on a tailless vehicle evaluated by Wilde *et al*. [16].

Some initial investigations have also been launched on mainly 2-D aerofoils to determine the capability in reducing and managing lift by surface jet blowing, to find alternative ways for load control. For example, de Vries *et al*. [17] performed numerical studies at steady conditions on the NACA0018 aerofoil at the incoming Mach number 0.176 with a normal jet placed on the upper surface trailing edge, and significant lift reduction was obtained. Al-Battal *et al*. [3] compared the capability between normal blowing and upstream blowing for lift reduction experimentally.

As can be seen, initial researches have been carried out to test the capability of fluidic actuators including CC and surface jet blowing for load control, but these studies were conducted under low speed and steady incoming flow conditions on mainly 2-D aerofoils. Little attention has been given for evaluating the capabilities by these methods for gust load alleviation.

The motivation of this project is to study the feasibility and effect for gust load attenuation by means of fluidic actuators through CFD simulations. Two fluidic actuators including CC and normal microjet blowing, will be studied and compared for their capabilities in gust load alleviation for subsonic and transonic incoming flow conditions.

1.2 Aim and objectives

This study aims to increase the understanding on the capabilities of fluidic actuators including CC and normal microjet blowing for load control and gust load alleviation for subsonic and transonic flow conditions.

Key objectives are summarized as the followings:

1) Setup a numerical tool for the simulation of gust response and active flow controls - As it is the first study to carry out gust load alleviation by CC and normal microjet blowing, a numerical tool which are capable for the simulation of gust responses and flow controls by fluidic actuators needs to be set up and validated.

2) The comparisons of flow control mechanisms and load control capabilities between CC and normal microjet blowing for subsonic and transonic speeds - The differences of flow control mechanisms between these two fluidic actuators need to be better understood to get insight into their capabilities for load control and gust load alleviation under different incoming flow conditions.

3) The investigation of unsteady actuation of these two fluidic actuators - Since gusts are unsteady flow perturbations, the control of gust disturbances by fluidic actuators involves dynamic adjusting the momentum coefficients. Therefore, it is crucial to investigate the dynamic actuation characteristics of these approaches.

4) The investigation of gust load alleviation effects by these two fluidic actuators - The demonstration of the feasibility and effects of gust load alleviation by means of CC and normal microjet blowing is the final objective of this project. The understanding of the effects for gust load alleviation will be progressively obtained on a 2-D aerofoil, a simple 3-D wing and finally a BWB model under the reference discrete gusts defined by EASA CS-25.

5) The understanding of the correlation between wing structural weight reduction and root bending moment relief - The correlation between wing structural weight and root bending moment relief is used for the understanding of the influence of spanwise load distribution on the BWB performance and how gust load control benefits the structural weight reduction.

1.3 Thesis outline

This thesis is organised by eight chapters including the current introduction. Other chapters are formed as follows:

- Chapter 2 - Literature reviews: state-of-art progress in load control, methods for gust response simulations and gust load alleviation is reviewed and discussed in this chapter.

- Chapter 3 - Numerical methods and validation: in this chapter, the numerical methods are briefly described. A numerical tool is set up and validated for simulations of gust responses, CC and normal microjet blowing.

- Chapter 4 - Comparison of load control capability between CC and normal microjet blowing: this chapter compares the flow control mechanisms and load control effects between CC and normal microjet blowing with constant and dynamic blowing momentum coefficients under steady incoming flow conditions.

- Chapter 5 - Aerofoil and BAH wing gust load alleviation: the feasibility and effects of CC and normal microjet blowing for gust load alleviation is first demonstrated on the 2-D aerofoil and the simple 3-D BAH wing.

- Chapter 6 - Blended-wing-body model setup and influence of spanwise load distribution on the performance: a BWB geometry including its aerodynamic and structural models are generated in this chapter; the correlation between wing structural weight and root bending moment relief is built up; based on this, the influence of spanwise load distribution on the BWB performance under transonic speed is investigated.

- Chapter 7 - Blended-wing-body gust load alleviation: the effects of CC and normal microjet blowing are applied and tested on the BWB model for load control and gust load alleviation.

- Chapter 8 - Conclusions: finally, this chapter gives a summary of conclusions and findings, together with the recommendations for future work.

Chapter 2

Literature reviews

Given the objective of this thesis is to understand the feasibility and effects of load control and gust load alleviation using fluidic actuators, the involved topics include load control, gust load prediction, gust load alleviation, and fluidic actuators. The available studies relative to these topics will be reviewed in this chapter to get an insight into the research status on these topics.

2.1 Benefits of load control

It is undeniable that air travel makes the intercity transport convenient and brings significant economic growth in different countries. However, in the meantime, the negative impacts on the environment and climate [18] have become more pronounced and have attracted much attention from aviation industries. For economic and ecological considerations, calling for reduction in fuel consumption and exhaust emissions is urgent for future aircraft. For this purpose, aviation industries have set a series of goals to pursue ‘Green Aviation’. For example, the primary goal of Europe’s Fight-path 2050 is to reduce CO_2 emissions of aircraft by 75% relative to 2005 levels [19]; the so-called N+3 goal of NASA is to reduce Nitrogen oxides (NOx) emission up to 80% in the landing-takeoff process and reduce fuel burn by 60% for an airliner entering service in 2030-35 [20]. To achieve these objectives, a number of technologies, such as shock control [21-24], laminar flow control [25-31], turbulent drag reduction [32-35], etc., as well as novel aircraft concepts (see Figure 2.1), such as BWB or hybrid wing body (HWB) [36], ‘double-bubble’ concept [37], truss-braced wing (TBW) concept [38], box-wing concept [39], etc., are under development to explore a better aerodynamic performance. However, the lack of application of these technologies mentioned above on current aircraft indicates that there are still great challenges in science, especially in terms of practical application. Meanwhile, with the increasing development and maturity in computational fluid dynamics (CFD) and aerodynamic design optimisation, the aerodynamic efficiency of modern swept supercritical wings has almost been reached to its extreme. Further achievement in aerodynamic improvement through the design optimisation on modern swept supercritical wings will be limited.

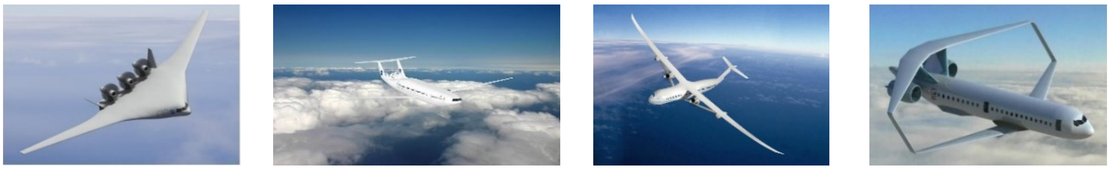

BWB [40] ‘Double-Bubble’ [37] TBW [38] Box wing [39]

Figure 2.1 Novel aircraft concepts

Recently, more focuses have been given to the study on load control, since it provides an alternative way for drag reduction that is to reduce the aircraft structure weight. One of the associated debates on whether the wing should be designed to an ‘elliptic’ spanwise loading for the smallest induced drag or to a triangular-like spanwise loading for the saving of structure weight at subsonic speeds has been ongoing for decades. Jones [41] investigated the influence of the distribution of span loading on induced drags of the wing with fixed lift and bending moment in subsonic speed. It was demonstrated that 15% decrease in induced drag was achieved by 15% increase in span length, but with a smooth triangular-like loading for the relief of root bending moments. The effects of root bending moments relief on a B777-class aircraft was examined by Iglesias and Mason [42]. It was found that the decrease of wing structure weight is roughly linear following the decrease in wing root bending moments, which means that 15% wing weight reduction will be achieved if the bending moment is reduced roughly by 15%. In Iglesias and Mason’s study, the increase of the additional induced drag due to the wing root bending moment reduction relative to the model with elliptic spanwise load distribution appeared in a parabolic correlation. Consequently, during the low range of the root bending moment decrease (from zero to 6%), the total weight is reduced. However, there will be no benefit for the net weight saving due to the increase in fuel consumption because of higher induced drag increase when the root bending moment relief becomes higher referring to a more triangular spanwise loading configuration. Jansen *et al.* [43] using a coupled aero-structural procedure, studied the trade-off between induced drag and wing weight of novel wing configurations including box-wing and C-wing configurations reference to a B737-900 class airframe. These studies all concluded that a reduced bending moment shifting from the elliptic design would benefit the overall performance.

Takahashi [44] made an opposite conclusion after the investigation on a large civil transport aircraft and a medium business jet: tailoring the spanwise loading to reduce the wing root bending moment will save some wing structure weight, but results in the cost of more fuel consumption due to the higher drag. He argued that for the large civil transport, only 50% of the wing structure weight seemed to be linearly corresponding to root bending moment relief, while Iglesias *et al.* [42] described a 100% correlation between these two factors.

Compared to the traditional aircraft layout, the integrated BWB layout performs substantial aerodynamic improvements and is considered being one of the promising layouts for future aircraft [45]. A series of studies including airframe design [36, 46], structure analysis [47, 48], aerodynamic analysis and optimization [49, 50], acoustic investigation [51, 52], *etc.* have been carried out. Qin *et al.* [53] first conducted the investigation on the influence of spanwise lift distribution on aerodynamic efficiencies for a BWB configuration. It was found that, for high transonic condition when the shock wave was strong, the elliptic load distribution did not produce the highest aerodynamic efficiency because of the impact of wave drag apart from the induced drag.

The above studies show a debatable view about which spanwise load distribution was better, but one certain thing is that the reduction of the load is beneficial for structure weight saving. As is well known that, the mass of the structure is determined by the critical load cases, not the cruise load. If the critical load the aircraft experience in flight can be controlled and alleviated timely, then a lighter structure might be designed without compromising the safety, resulting in turn the improved aircraft performance.

As pointed out in Ref. [1, 54], gust loads often define the critical loads. Therefore, if effective methods can be used for timely gust load alleviation, then less mass compensation associating to the critical gust load is needed in the aircraft structure design. For this end, two main issues should be addressed:

- One is to predict the gust loads accurately, which is an important driver and a fundamental input for structural design.

- Another one is to design effective methods for load control and gust load alleviation, which is the assurance and reason for the reduction of aircraft structure weight.

2.2 Gust load prediction methods

For the gust load prediction, it is to assess the responding forces and moments due to gust perturbations [55]. To predict these unsteady aerodynamic effects, there are three main methods including wind tunnel experiments, analytical and CFD methods. The investigation status of these methods will be described briefly below.

2.2.1 Wind tunnel experiments

Most of the published experiments were conducted in low-speed range. Generally, continuous sinusoidal gust is used with oscillating vanes or wings with thin aerofoil profiles mounted upstream of wind tunnel test sections for gust generations.

A research group comprised of NASA Langley Research Centre, Boeing and Air Force Research Laboratory (AFRL), carried out a series of experiments [56-59] on two Sensor-Craft concepts including a joined wing and a flying wing concepts. The system response and active control characteristics were investigated since 2005 in NASA Langley Transonic Dynamics Tunnel. Initial experiments were conducted with rigid models [56]. The plunging and pitching modes were set free in the following studies [58]. Different control laws, as well as control strategies with various combinations of control surfaces, were tested and evaluated in these experiments. The performance of using leading-edge stagnation point sensors as feedback signals of gust perturbation for gust load alleviation was examined in NASA's Transonic Dynamics Tunnel (TDT) by Mangalam [60]. It was demonstrated to be a practical way to provide the information of the aerodynamic turbulence, especially to provide valuable lead-time control input compared to systems using only inertial sensors. The effects of several control laws for flutter suppression and gust load alleviation were assessed on the supersonic transport aircraft (S4T) also in NASA TDT [61]. Similarly, fuzzy logic control using ailerons on the inner and outer sections of a wing with a high aspect ratio was tested in the China

Academy of Aerospace Aerodynamics low-speed wind tunnel and was proven to reduce the gust response by 20 to 27 percent at freestream velocity of 30 m/s under both random and sinusoidal gusts [62]. Gust load alleviation using piezoelectric actuators was tested on a flexible wing by Bi *et al*. in 2017 [63].

In 2010, the aerodynamic responses of an elastic wing under gust turbulence was conducted experimentally [64] in the transonic wind tunnel (DNW-TWG) (see the assembly of the testing models in Figure 2.2). The wing mounted upstream is the gust generator. Different gust disturbances can be generated by exciting the wing with prescribed motions. This wing has a symmetric NACA0010 profile with a small thickness which is essential in transonic wind tunnels as the chocking effect will become apparent if the wing has a high thickness section. During the experiment, the dynamic response under generic gusts was investigated.

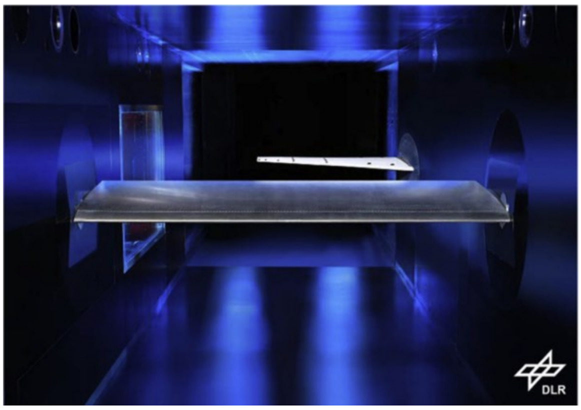

Figure 2.2 Assembly of the testing models, (picture from Ref. [65])

In general, the literature in the field of wind tunnel tests of gust responses is quite rare and even less when it is confined to the transonic range. It is because it makes this an expensive task if experimental data are used in each aircraft design stage as various gust load conditions need to be considered. Another disadvantage of experimental data is that they always come too late when design options have already been narrowed [66]. One of the motivations of developing CFD methods for gust simulations is to reduce the reliance on experimental data. As pointed out in the Summary Report [66] of the project ‘AeroGust’, in the aircraft design process, the gust load would be used earlier if gust load calculations can be made using CFD in place of experiments. It is the trend that wind tunnel tests will be reduced and CFD calculations will play a more important role in predicting gust load for aircraft designs.

2.2.2 Analytical methods

Any component of gust velocity perpendicular to the flight path will change the effective angles of attack. Under the assumptions of incompressible and irrotational flow conditions, for a 2-D flat plate, the Wagner function [67] provides the indicial response of the circulatory part of the lift with the consideration of the effect of the shed wake due to step changes in angles of attack. Küssner function [67] describes an analytical formulation for lift responses due to sharp-edged gusts based on potential flow theory. These methods are used to generate aerodynamic responses as a function of time to instantaneous changes in aircraft motions. These analytical methods were proven to be accurate in low subsonic speeds and were used as comparable data in literature [68-71] for CFD validations for gust response.

Assuming a 2-D flat plate with a chord length c moving with velocity U_∞ initially at a small angle of attack α, it is then subjected to an instantaneous change in the angle of attack of Δα. The corresponding change in the lift response can be expressed as

$$\Delta L(s) = \frac{1}{2}\rho U_\infty^2 c \frac{\partial C_L}{\partial \alpha} \Delta\alpha \emptyset(s) \tag{2-1}$$

where, $\frac{\partial CL}{\partial \alpha}$ is the slope of the lift coefficient, $s = \frac{U_\infty \Delta t}{c}$ is the non-dimensional time (what needs to be mentioned here is that, in some of the references, s is calculated by the semi-chord length as $s = \frac{U_\infty \Delta t}{b}$. In this thesis, s is all defined by the chord length c for 2-D aerofoil and the mean aerodynamic chord length $\bar{c}$ for 3-D wing) and $\emptyset(s)$ is the Wagner function [55, 67] which can be defined approximately for the incompressible flows as

$$\begin{cases} \emptyset(s) = 0 & (s \leq 0) \\ \emptyset(s) = \dfrac{s+1}{s+2} & (s > 0) \end{cases} \tag{2-2}$$

The Wagner function often appears in exponential forms which are easier to manipulate in terms of Laplace transforms. R.T. Jones [72] was the first to give these exponential forms based on his previous work [73] about a correction method of the unsteady lift for finite wings from two-dimensional theory. Here, only the analogous expression with an exponential form for infinite-aspect-ratio wings from Ref. [72] is listed below as

$$\emptyset(s) \cong 1 - 0.33e^{-0.091s} - 0.67e^{-0.6s} \tag{2-3}$$

The Küssner function provides how the lift build up when experiencing vertical sharp-edged gusts. Assuming w_g is the gust velocity, and the effective change of angles of attack is

$$\tan(\Delta\alpha) \approx \Delta\alpha = \frac{w_g}{U_\infty} \tag{2-4}$$

Therefore, the change in lift in response to the penetration of the sharp-edged gust is expressed as

$$\Delta L(s) = \frac{1}{2}\rho U_\infty^2 c \frac{\partial C_L}{\partial \alpha} \Delta\alpha \Psi(s) = \frac{1}{2}\rho U_\infty^2 c \frac{\partial C_L}{\partial \alpha} \frac{w_g}{U_\infty} \Psi(s) \tag{2-5}$$

where, $\Psi(s)$ is the Küssner function which can be defined in the form of non-dimensional time s approximately as [55]

$$\Psi(s) = \frac{2s^2 + s}{2s^2 + 2.82s + 0.40} \tag{2-6}$$

in the exponential form,

$$\Psi(s) \cong 1 - 0.5e^{-0.26s} - 0.5e^{-2s} \tag{2-7}$$

The above Eq. (2-3) and Eq. (2-7) describe the theory of lift build-up to step changes of angles of attack and sharp-edged gusts under incompressible flows. For subsonic compressible flows, numerous work [74-78] have been done for developing appropriate analytical expressions for dynamic responses as an extension of Wagner and Küssner functions.

In linearized compressible flow, Lomax [78] formulated the exact closed-form expressions for small-time durations. For a step change in an angle of attack $\Delta\alpha$, the lift response is expressed as

$$\Delta C_L(s) = \frac{4}{M_\infty}\left(1 - \frac{1 - M_\infty}{M_\infty}s\right)\Delta\alpha,\ \ 0 \le s \le \frac{M_\infty}{1 + M_\infty} \tag{2-8}$$

For a sharp-edged gust, the expression of the lift coefficient is given by

$$\Delta C_L(s) = \frac{4s}{\sqrt{M_\infty}} \cdot \frac{w_g}{U_\infty},\ \ 0 \le s \le \frac{M_\infty}{1 + M_\infty} \tag{2-9}$$

2.2.3 CFD methods

For simulating the gust response through CFD methods, the most straightforward way is to introduce the gust velocity through the far-field boundary conditions. However, this method has a problem to control the dissipating of the gust disturbances through the computational domain. Because it needs not only the high-fidelity CFD codes, but also a fine mesh along the whole domain. This inevitably leads to a very high computational cost which deteriorates the feasibility since the simulation cost in gust response calculation is already high [55]. Another way is to use the 6-DOF motions [79] of the entire domain to simulate the aircraft instantaneous movement for the alternative gust perturbation, but these methods cannot simulate the traveling gust. A widely used method is to prescribe the instantaneous gust velocity at every mesh point in the domain, which is called Grid Velocity or Field Velocity Method.

2.2.3.1 Field Velocity Method

Using CFD as the tool to calculate aerodynamic responses to step change of angles of attack and gusts was first attempted by Parameswaran *et al.* [69, 70]. The so-called approach of Field Velocity Method (FVM) or Grid Velocity Method was incorporated into a Euler/Navier-Stokes solver for lift-response calculations due to the encountering of step changes in angles of attack and sharp-edged gusts on an aerofoil. The grid velocity is the velocity of each grid point in the computational domain. During the dynamic motion of the aerofoil or aircraft, any change of the motion can be thought of the change in the grid velocity. This method decouples the input parameters naturally. For example, if an aerodynamic surface encounters a step change of angles of attack, it will introduce the pitch rate by rotating the aerofoil to the target angle of attack. However, FVM just introduces a vertical velocity component into the flow field. It is identical to a pure step change in angles of attack. As a result, the time histories of the pitch rate and angles of attack are decoupled consequently [70]. This approach also has the advantage to overcome numerical dissipation problems of the gust disturbances [80].

FVM is a significant advance in gust response research field, which has been used to model a range of gust encountering responses [71, 81-83] and also has been implemented into different CFD codes. For example, NASA has implemented various gust profiles by FVM into its in-house CFD code FUN3D [84]. The EZNSS [85] CFD code was enhanced with the capability of gust response simulations and had been used for gust response analysis of complex models with elasticity effects [81]. Gust models defined as field velocity with a specific form and amplitude were also introduced to *elsA* using URANS solutions [86]. DLR-TAU was equipped with the FVM to simulate gust responses [87]. Though in this method, the gust is assumed to be frozen, that is to say, the effects of the aircraft responses on the gust are not considered, it has been shown that this influence is neglected for gusts with practical lengths [87]. Wales [88] further demonstrated that there is almost no influence if the gust lengths are larger than the aerofoil length (or average chord length of the aircraft). A collaborative research project called AeroGust [66] (Aeroelastic Gust Modelling) has been carried out between industry and academia funded by the European Union’s Horizon 2020 Research and Innovation Programme. This project is to investigate and develop improved simulation methods for gusts. One of the project conclusions is that FVM is an effective way for gust load predictions.

2.2.3.2 Gust response considering aeroelasticity

Undeniably, flexibility is more significant and aeroelasticity is playing a more and more important part in future aircraft designs. For example, it will be unsuitable and may bring fatal errors to consider a highly flexible wing to be rigid when conducting gust load calculations. As pointed out by Sucipto *et al.* [89], structural dynamics and aerodynamics will be coupled strongly during the gust encountering for the flexible aircraft. This formulates a complex fluid-structure interaction (FSI) problem which requires powerful multi-physics tools to cope with.

As it is already time-consuming to simulate gust responses using high-fidelity CFD method especially when small time step is needed, it can be imagined that it will be more costly if aeroelasticity is coupled in the simulation. Therefore, it is easy to understand that low-fidelity approaches are widely used for gust load calculations considering aeroelasticity. For example, Kűssner and Wagner functions are coupled into the unsteady strip theory to predict gust loads [90]. Doublet Lattice Method (DLM) [91] and Unsteady Vortex Lattice Method (UVLM) based on potential flow theory are also typically used in industry. However, for either complex aerodynamic geometries or complex flows involve shock waves or separations, these methods are not capable to produce accurate results.

Based on flexible 2-D aerofoils, high-fidelity FSI solutions (Navier–Stokes equations coupling with linear and nonlinear structural mechanics equations) and low-fidelity solutions were compared for the gust responses by Sucipto *et al.* [89]. It was demonstrated that the low-fidelity solutions followed the high-fidelity results well if the gust was weak and no separation appeared in the flow. Otherwise, for separated flow (the gust was strong), the low-fidelity methods cannot predict the large oscillations in gust responses as exhibited correctly by the high-fidelity methods. Through this comparison, the authors also pointed out that low-fidelity solutions were not suitable in advanced flexible wing designs due to high physical complexities involved in the highly nonlinear fluid-structure interactions.

It is true that a higher-fidelity, to some extent referring to a higher-order CFD for the calculation of gust response is becoming more and more significant for modern aircraft designs which tend to be more flexible and with a transonic cruise Mach number.

Yang and Obayashi [92] were supposed to be the first to use a direct coupling between URANS and structural dynamic equations of motion to analyse gust responses for a supersonic transport model. The aeroelastic equations of motion are based on Lagrange's energy equations using generalized coordinates, which is

$$\ddot{q}_i + 2\omega_i\zeta_i\dot{q}_i + \omega_i^2 q_i = \frac{F_i}{M_i}, \qquad i = 1,2,\cdots,n \tag{2-10}$$

where, q_i is the generalized displacement, ω_i is the natural frequency, ζ_i is the generalized damping ratio of each mode, F_i and M_i are the generalized mass and force of each mode respectively. This method is the same as the aeroelastic equations of motion incorporated in the CFL3D code used in this study which will be described in Chapter 3.

Following this, similar methods were used in other studies of gust simulations. For example, gust load analysis were carried out by Chen *et al.*[93], where URANS and structural dynamic equations of motion were coupled for fluid-structure interactions and the FVM was used for the gust input. Zhou *et al.* [80, 93, 94] carried out the studies on transonic aeroelastic moving gust responses and aeroservo-elastic analysis.

Coupling the CFD code (DLR-TAU) and the computational structural mechanics software (PyCSM), fluid-structure simulations with gust perturbation were carried out to compare with the experimental data for a flexible wing [65]. The governing differential equations of motion were solved in modal coordinates. The structural mode shapes, as well as the natural frequencies, were calculated by MSC MSC.NASTRAN beforehand.

In general, investigations of gust responses by numerical methods coupling with structural dynamic equations are still rare up to now due to the complexity as well as the high cost of time. Even so, it is believed that these methods will have an important role to play in gust load predictions for future aircraft designs.

2.3 Load control and gust load alleviation approaches

As mentioned previously, ailerons, elevators or spoilers are normally used by current civil aircraft as the control surfaces for gust load alleviation [95, 96]. The first commercial airplane to incorporate a Gust Load Alleviation (GLA) system using ailerons is the Tristar L-1011 from the 1980s [97] after the successful implementation of GLA technology on the military aircraft C-5A [98]. The effectiveness of GLA system consisting ailerons and spoilers was tested on the Airbus A300 [99] and firstly implemented on the Airbus A320 [100]. During the following decades, very little attention has been put on exploring new gust load alleviation methods but on the technology for detection of atmospheric disturbances and on the GLA system designs, especially on the design of control laws [62].

Even if very few, several researchers have initiated the investigation of novel approaches, such as passive control devices for gust load alleviations and fluidic actuators for load controls.

2.3.1 Passive control devices

Guo *et al.* investigated the effects of a passive twist wingtip as a gust-load alleviation device on a flying-wing configuration [101] and a 200-seater airliner [1] respectively. This concept shown in Figure 2.3 is to use a separate wing-tip section connected to the main wing by a spring. As the shaft is located ahead of the aerodynamic centre, this device will have a nose-down twist under the gust-induced aerodynamic force resulting in gust load alleviation. The results showed significant reduction of gust-induced wing-tip displacement and root bending moment. Compared to the current active control methods, this passive control concept is attracting as it is independent of extra energy.

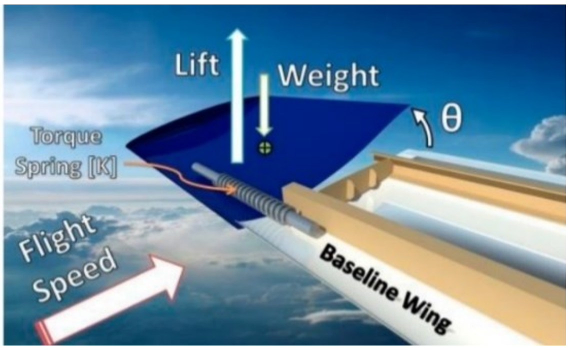

Figure 2.3 The concept of passive twist wingtip from Ref. [1]

Similar to the ideas pointed out by Guo *et al.*, Castrichini [102-104] investigated the effects for the alleviation on wing root bending moments at gust conditions by a flexible wing-fold device. The key idea was to introduce a hinge with the line which was not parallel to the incoming flow direction (see Figure 2.4 (c)) but was rotated outboard with a hinge orientation Λ to allow the wing tip to rotate (see Figure 2.4 (d)). Therefore, folding the wingtip with the angle of θ will reduce the local angle of attack, which can be calculated as $\Delta\alpha = -tan^{-1}(tan\theta sin\Lambda)$. The results indicated that suitable designs of the control device are capable for gust load alleviation. It was also observed that the load alleviation capabilities are highly sensitive to the stiffness of the hinge spring and the wing-tip mass. It will be a problem in application as it is impracticable to change the mass or the hinge spring stiffness according to different incoming flows.

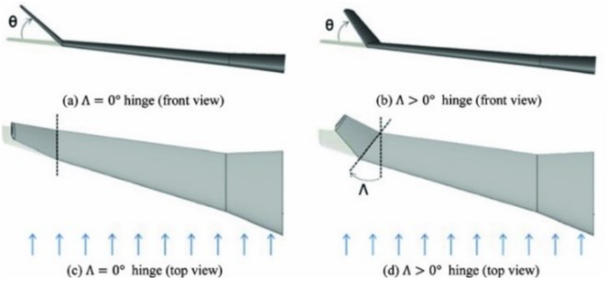

Figure 2.4 Hinge orientations from Ref. [103]

2.3.2 Active fluidic actuators

Fluidic actuators have seen resurgent interest these years for their potential application for modern aircraft flight control, as to replace the conventional control surfaces for flapless control.

2.3.2.1 Surface jet blowing or suction

Fluidic actuators, such as blowing or suction, synthetic jets, and oscillating jets, have been widely studied as means of active flow control methods for decades. Most of these researches focused on modifying the momentum balance in the boundary layer to achieve aerodynamic improvement. For example, on top of transition delay and drag reduction, these methods have been proven to be practical ways to prevent flow separations or to augment lift. Due to plenty of studies on the subjects of flow mechanism [105-107], comparison of different actuators' effectiveness [108-112], parameter studies including geometry parameters [113, 114], injection or suction parameters [115, 116], excitation parameters [117-119], influence of locations and layouts [120], etc., meaningful achievements have been obtained using fluidic actuators for improving aerodynamic performance.

Changing the way of thinking from lift augmentation, if fluidic actuators can be used in reducing and managing lift, then alternative ways relative to current technologies could be applied in gust load alleviations. Compared to current techniques comprising of ailerons or spoilers, fluidic actuators are easy to deploy. Most importantly, fluidic actuators belong to the region of high frequency in terms of response compared to current technologies [4].

A few researchers have realized this potential application of fluidic actuators. Preliminary investigations numerically and experimentally have been carried out to evaluate their capabilities for load control, but mainly on 2-D aerofoils.

Synthetic jet actuators have been investigated experimentally as load control on the NACA0015 aerofoil for reshaping aeroelastic responses including limit cycle oscillation and flutter by Rao *et al*. [121]. The results showed an improvement of more than 15% of the flutter speed by the synthetic jet actuators using a PID controlled loop [122]. Load alleviation study in Ref. [123] using synthetic jets on the NACA0012 aerofoil achieved 21% of gust load alleviation under a sharp-edged gust. Microjets being small pneumatic jets using high-speed flow blowing normal to the aerofoil or wing surface have been studied as approaches for load control, but mainly on wind turbine blades at low-speed regions. For example, de Vries *et al.* [17] conducted numerical studies of a non-rotating NACA0018 aerofoil with microjets located near the trailing edge under freestream Mach number of 0.176. Significant changes in lift were observed for the angle of attack ranging from -10° to 10°. Moreover, the results also showed that approximately 50% of the total change in the lift could be obtained within the non-dimensional time $s = \frac{U_\infty \Delta t}{c} = 1$, indicating its rapid load control response characteristic. Blaylock *et al.* [124, 125] compared the load control effects of microjets and microtabs deployed on the NACA0012 aerofoil trailing edge. The results showed that both concepts had a similar load control mechanism by affecting the trailing-edge flow, and therefore produced very similar aerodynamic load control effects. However, Heathcote *et al.* [126] conducted wind tunnel tests for comparing the effects of blowing (microjets) and microtabs, and pointed out that blowing and microtabs were viable methods for load control but with very different behaviours: the blowing deflected the wake upwards thereby reducing lift, conversely the microtabs promoted separation over the upper surface resulting in lift reduction. He also noted the nearly constant lift change across all angles of attack by microjet blowing located at the trailing edge, which was constant with the result drawn by de Vries *et al.* [17]. However, for microtabs, optimal location varied according to the angle of attack. At small ones, it is preferable to place the microtabs near the trailing edge, while locations near the leading edge were better when the angle of attack is high. de Vries *et al.* [17] performed numerical studies at the steady condition on the NACA0018 aerofoil at M_∞= 0.176 with a normal jet placed on the upper surface trailing edge and a significant lift reduction was obtained. Al-Battal *et al.* [4] assessed the capability of blowing for lift reduction experimentally. Two different blowing directions, normal and upstream (see Figure 2.5), from the upper surface of the NACA0012 aerofoil under the steady incoming flow velocity of 20 m/s and a range of angles of attack from 0° to 20° were compared. The results indicated that the chordwise location of normal blowing had a dramatic influence on the load control effects in terms of lift reduction. Normal blowing at x/c=0.95 induced a lift coefficient decrease of 0.15 under the maximum blowing momentum coefficient. However, moving the microjet further forward, the lift change was negligible and even no lift decrease was induced when normal blowing was placed near the leading edge. A further experiment of the upstream blowing on the same model shown in Figure 2.5 was conducted by Al-Battal *et al* [127] to investigate the unsteady actuation property under steady incoming flows. The time lag in lift responses corresponding to blowing actuation frequency has been observed due to the change in the circulation and the vorticity shedding. The time delay became more significant with increasing angles of attack because of more separated flow. The effects of the slot blowing on unsteady aerodynamic load control with a freestream velocity from 6.7 m/s to 22.2 m/s on NACA0018 aerofoil was experimentally evaluated by Mueller-Vahl *et al*. [128]. The results showed that the lift oscillation due to the unsteady incoming flow can be effectively counteracted by dynamically adapting the slot blowing velocity.

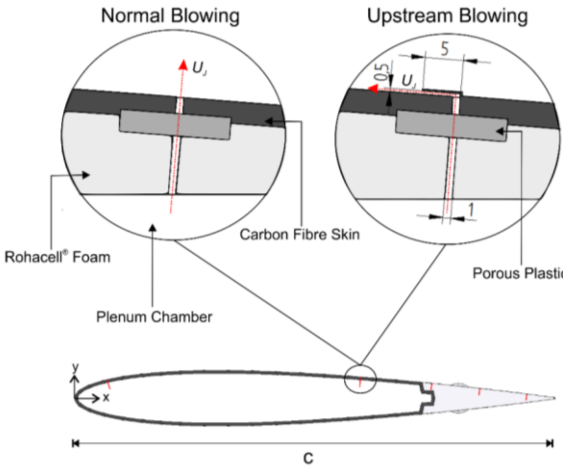

Figure 2.5 Two different blowing directions investigated in Ref. [4]

2.3.2.2 Circulation control by jet blowing through the trailing-edge Coanda device

Unlike the normal jet blowing which works on the direction perpendicular to the aerofoil or wing surface, circulation control (CC) using Coanda effect uses tangential surface jets to change the aerodynamic properties of the aerofoil or wing. The Coanda effect describes the tendency of a high-speed jet flow staying attached to a convex surface (see Figure 2.6) due to the balance between centrifugal forces and low static pressures created by the high-speed jet [129]. The high-speed jet flow entrains the external flow to follow it as to ‘bend down’ over the curved surface which generates the circulation increase, and thus results in lift augmentation. Similarly, lift reduction can be obtained through placing the jet slots on the lower surface. Conventionally, a CC device system consists of an air plenum, a rounded trailing edge and an orifice which is the slot exit of the CC jet.

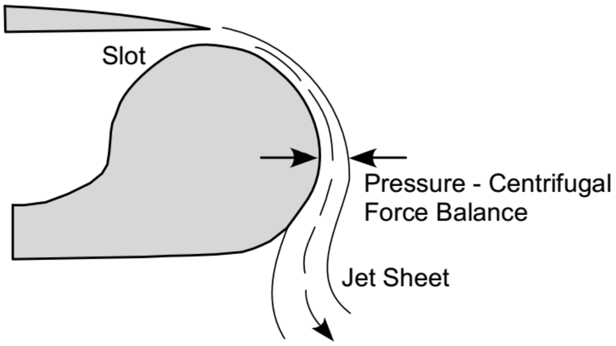

Figure 2.6 Trailing edge CC [129]

The initial intention for the development of the CC system was for short landing and take-off capability, especially by the US Navy, looking for ways to improve aircraft operation from carriers [130]. Many tests including a full-scale flight test and design works have been done on the A-6 Intruder [131]. The effectiveness and efficiency of CC for manoeuvrability control of fixed and rotary-wing aircraft have also been researched through various experiments and numerical studies. After the wind tunnel test on a diamond wing tailless aircraft, Cook *et al*. [14] pointed out that the CC device exhibited good aerodynamic performance similar to a traditional flap with an equivalent size on a fixed wing under modest blowing momentum coefficients, and the response characteristic was essentially linear. Experimental and computational work seeking for a design using trailing-edge blowing to eliminate the trailing-edge flaps, or use leading-edge blowing to eliminate the need for leading-edge slats have been done on a Boeing 737 aircraft [130, 132]. A joint project [11-13] has been carried out by University of Manchester, Cranfield University and BAE Systems to demonstrate new technologies for flapless control, and a drone has been designed named MAGMA which finished its first flight trial in 2017. Instead of traditional control surfaces, this project assessed the manoeuvrability of two novel technologies. One is to deploy CC on the wing sections and another one is to use the fluidic thrust vectoring placed on the centre body [14]. Hoholis [15] extended a numerical study of CC as a roll effector on the generic SACCON UCAV configuration. This work was done with a freestream Mach number 0.145 and was concluded that CC can produce similar rolling moments to flaps at low angles of attack. The effects for providing manoeuvrability by CC on a tailless vehicle was evaluated by Wilde *et al*. [16]. The results show that CC units could provide similar three-axis control effects relative to the split flap elevons.

Numerous computational studies have been done for CC aerofoils, but most of the work was confined to low-speed range with low blowing momentum coefficients since most of the experimental data are only available in these conditions. Byung-Young [133] compared the spatial accuracy and the influence of turbulence models on simulations to predict aerodynamic properties of a CC aerofoil under M_∞= 0.116. The results indicated that spatial accuracy had a negligible influence, but two-equation turbulence models performed better compared to the one-equation models. Christopher [134] compared URANS and LES approaches on a CC aerofoil under the incoming flow velocity of 34 m/s. He concluded that turbulence models incorporated curvature effects could produce better agreement of jet separation locations with LES. The calculation with freestream M_∞= 0.12 conducted by Swanson [135] also indicated that turbulence model including curvature effects had agreed the best against the experimental data, such as the surface pressures and streamlines.

Explicit algebraic Reynolds stress (EARSM), Menter k-ω SST and Wilcox k-ω turbulence models were compared in the numerical studies of CC placed on the aerofoil upper surface conducted by Forster [136] in transonic range. These three models generated similar pressure distributions on the main aerofoil section and agreed well with the experimental data in Ref. [129]. For the shock position, it was consistent between numerical and experimental results that the shock position moved afterward with the increasing blowing rates. For the Coanda jet detachment, both the SST and EARSM models predicted with reasonable accuracy. Among the few studies on CC devices at transonic speed, Forster [136] also conducted numerical studies on different Coanda devices on the supercritical McDonnell Douglas DLBA032 aerofoil to evaluate the influence of Coanda surfaces with a step, different radius-to-slot height ratios and nozzle shapes.

In general, the above reviewed literatures demonstrate that the RANS-based CFD methods can predict the CC jet flow with a reasonable accuracy.

2.4 Gust models

Gust being a complicated phenomenon is also referred to atmospheric turbulence. The following two idealized categories of gusts are generally considered in industry for aircraft design, namely [55]:

- Discrete gusts: the instantaneous gust velocity profile is usually defined by a deterministic form, such as ‘one-minus-cosine’ and ‘sharp-edged’ shapes.

- Continuous turbulence: the gust velocity varies randomly.

‘One-minus-cosine’ gust is the typical discrete gust defined by the certification specifications of large commercial aircraft covered by the EASA CS-25 [2]. The gust profile is shown in Figure 2.7 and according to EASA CS-25, the gust shape can be expressed as

$$w_g(x_g) = \frac{w_{g0}}{2}\left(1 - \cos\left(\frac{2\pi x_g}{L_g}\right)\right), \qquad 0 \le x_g \le L_g \tag{2-11}$$

where, w_{g0} is the magnitude of the peak gust velocity; L_g is the gust wavelength or twice the ‘gust gradient’ H_g. According to EASA CS-25, the gust wavelength is in the range from 9 to 107 m. In practice, the typical value is $12.5\bar{c}$ ($\bar{c}$ is the mean aerodynamic chord length). The design gust velocity w_{g0} changes with gust wavelength and altitude which is expressed in relations of the gust gradient H_g (in m), the reference gust velocity w_{ref} and the flight profile alleviation factor F_g, as

$$w_{g0} = w_{ref} F_g \left(\frac{H_g}{106.17}\right)^{\frac{1}{6}} \tag{2-12}$$

where, w_{ref} decreases linearly from 17.07 m/s equivalent airspeed (EAS) at sea level to 13.41 m/s EAS at 4572 m and then again to 6.36 m/s EAS at 18,288 m. The flight profile alleviation factor F_g is related to the aircraft weight and the maximum operating altitude [55].

$$F_g = \frac{1}{2}\left[F_{gz} + F_{gm}\right] = \frac{1}{2}\left[\left(1 - \frac{Z_{m0}}{76200}\right) + \sqrt{R_2 \tan\left(\frac{\pi R_1}{4}\right)}\right] \tag{2-13}$$

$$R_1 = \frac{W_{MLW}}{W_{MTOW}}, \qquad R_2 == \frac{W_{MZFW}}{W_{MTOW}} \tag{2-14}$$

where, Z_{m0} is the maximum operating altitude, W_{MLW} is the maximum landing weight, $W_{MZFW}$is the maximum zero-fuel weight and W_{MTOW} is the maximum take-off weight.

Assuming an aircraft cruising with the speed U_∞ and encountering a one-minus-cosine gust, the gust penetrating distance is $x_g = U_\infty t$, and Eq. (2-11) can be rewritten as

$$w_g(x_g) = \frac{w_{g0}}{2}\left(1 - \cos\left(\frac{2\pi U_\infty t}{L_g}\right)\right) = \frac{w_{g0}}{2}(1 - \cos(\omega t)) \tag{2-15}$$

An equivalent gust frequency can be obtained as $\omega = \frac{2\pi U_\infty}{L_g}$ in radians or $\omega = \frac{U_\infty}{L_g}$ in Hz.

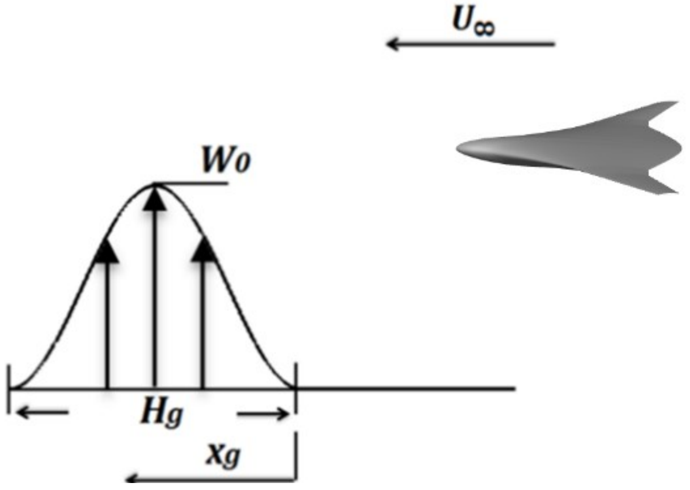

Figure 2.7 Velocity profile of ‘one-minus-cosine’ gust

2.5 Summary

Various kinds of technologies, as well as new aircraft configurations, are under investigation for future aircraft drag reduction, which is the urgent requirement for reducing fuel consumption and exhaust emissions. Gust loads which in most cases determine the critical extreme loads, play a significant part through much of the aircraft design process and have significant influence on structure design, weight, and aerodynamic performance. Therefore, it is of vital importance to predict gust loads accurately and to find effective gust load alleviation methods.

FVM has been demonstrated to be a practical way to introduce the arbitrary gust profiles to the flow field in the gust response simulations. Since the future aircraft structure might become more flexible, structural dynamics and aerodynamics would couple in an increasingly stronger way in load analysis, as well as gust response. For an accurate prediction of gust load for flexible models, aeroelasticity should be considered. The structural dynamic equations of motion coupling with three-dimensional URANS provide a solution for the calculation of fluid-structure interactions.

Investigations on fluidic actuators including the normal jet blowing and upstream blowing as means of load control have been carried out, but the available researches were limited in the low speed on steady 2-D aerofoils. Preliminary researches have been carried out to test CC as manoeuvre effectors compared to traditional control surfaces. No investigations have been carried out to test the feasibility and effects of gust load alleviation using normal microjet blowing or CC covering subsonic and transonic speed ranges of practical importance for civil aviation.

Chapter 3

Numerical methods and validation

3.1 Numerical methods

The numerical solver set up for this study is based on the open-source CFD code of the Computational Fluids Laboratory 3-Dimensional (CFL3D) [137] from NASA Langley Research Centre. CFL3D is a structured-grid based CFD code which has the capability to solve the generalized full and thin-layer Navier-Stokes equations [138]. It has been validated for various applications from simple flat plates to complete complex configurations in subsonic to hypersonic flows [138-143]. In addition, this code is also capable to carry out static and dynamic aeroelastic analyses.

This code solves the RANS equations in the time-dependent conservation law form. Pressure and convective terms are discretized by third-order upwind-biased spatial differencing. Second-order differencing is used to discretize viscous terms. An implicit method is applied for the time advancement for the steady and unsteady flows. The inviscid flux is discretized using Roe's approximate Riemann solver and the viscous flux uses the second-order central-difference scheme. MUSCL approach of van Leer is used to determine state-variable interpolations at the cell interfaces. Min-Mod limiter is used in the simulation. Convergence acceleration approaches including multigrid and local time-step scaling are available. The solver has a number of turbulence models from 0-equation to 2-equation models [137, 138].

The main methodologies from Ref. [137] are present below briefly.

3.1.1 Governing equations

In the form of generalized coordinates, the 3-D time-dependent compressible Navier-Stokes equations can be expressed as follows [137]

$$\frac{\partial \hat{\boldsymbol{Q}}}{\partial t}+\frac{\partial\left(\hat{\boldsymbol{F}}-\hat{\boldsymbol{F}}_v\right)}{\partial \xi}+\frac{\partial\left(\hat{\boldsymbol{G}}-\hat{\boldsymbol{G}}_v\right)}{\partial \eta}+\frac{\partial\left(\hat{\boldsymbol{H}}-\hat{\boldsymbol{H}}_v\right)}{\partial \zeta}=0 \tag{3-1}$$

where, $\hat{\boldsymbol{Q}}$ is the conserved variables, $\hat{\boldsymbol{F}}$, $\hat{\boldsymbol{G}}$, $\hat{\boldsymbol{H}}$ are the vectors of inviscid fluxes, and $\hat{\boldsymbol{F}}_v$, $\hat{\boldsymbol{G}}_v$, $\hat{\boldsymbol{H}}_v$ are the vectors of viscous fluxes.

$$J=\frac{\partial(\xi,\eta,\ \zeta,t)}{\partial(x,y,z,t)}=\begin{vmatrix}\xi_x & \xi_y & \xi_z & \xi_t\\ \eta_x & \eta_y & \eta_z & \eta_t\\ \zeta_x & \zeta_y & \zeta_z & \zeta_t\\ 0 & 0 & 0 & 1\end{vmatrix}$$

$$\hat{Q}=\frac{Q}{J}=\frac{1}{J}\begin{bmatrix}\rho\\ \rho u\\ \rho v\\ \rho w\\ e\end{bmatrix},\quad \hat{F}=\frac{1}{J}\begin{bmatrix}\rho U\\ \rho U u+\xi_x p\\ \rho U v+\xi_y p\\ \rho U w+\xi_z p\\ (e+p)U-\xi_t p\end{bmatrix},\quad \hat{G}=\frac{1}{J}\begin{bmatrix}\rho V\\ \rho V u+\eta_x p\\ \rho V v+\eta_y p\\ \rho V w+\eta_z p\\ (e+p)V-\eta_t p\end{bmatrix}$$

$$\hat{H}=\frac{1}{J}\begin{bmatrix}\rho U\\ \rho W u+\zeta_x p\\ \rho W v+\zeta_y p\\ \rho W w+\zeta_z p\\ (e+p)W-\zeta_t p\end{bmatrix},\quad \hat{F}_v=\frac{1}{J}\begin{bmatrix}0\\ \xi_x\tau_{xx}+\xi_y\tau_{xy}+\xi_z\tau_{xz}\\ \xi_x\tau_{xy}+\xi_y\tau_{yy}+\xi_z\tau_{yz}\\ \xi_x\tau_{xz}+\xi_y\tau_{yz}+\xi_z\tau_{zz}\\ \xi_x b_x+\xi_y b_y+\xi_z b_z\end{bmatrix}$$

$$\hat{G}_v=\frac{1}{J}\begin{bmatrix}0\\ \eta_x\tau_{xx}+\eta_y\tau_{xy}+\eta_z\tau_{xz}\\ \eta_x\tau_{xy}+\eta_y\tau_{yy}+\eta_z\tau_{yz}\\ \eta_x\tau_{xz}+\eta_y\tau_{yz}+\eta_z\tau_{zz}\\ \eta b_x+\eta_y b_y+\eta_z b_z\end{bmatrix},\quad \hat{H}_v=\frac{1}{J}\begin{bmatrix}0\\ \zeta_x\tau_{xx}+\zeta_y\tau_{xy}+\zeta_z\tau_{xz}\\ \zeta_x\tau_{xy}+\zeta_y\tau_{yy}+\zeta_z\tau_{yz}\\ \zeta_x\tau_{xz}+\zeta_y\tau_{yz}+\zeta_z\tau_{zz}\\ \zeta_x b_x+\zeta_y b_y+\zeta_z b_z\end{bmatrix}$$

ρ is desity, $(u,\ v,\ w)$ are Cartesian velocities, contravariant velocities (U, V, W) are:

$$\begin{cases} U = \xi_x u + \xi_y v + \xi_z w + \xi_t \\ V = \eta_x u + \eta_y v + \eta_z w + \eta_t \\ W = \zeta_x u + \zeta_y v + \zeta_z w + \zeta_t \end{cases} \tag{3-2}$$

e is the total energy per unit volume, p is pressure, $\tau_{x_i x_j}$ is shear strssess, and $\dot{q}_{x_i}$is the heat flux:

$$p = (\gamma - 1)\left[e - \frac{\rho}{2}(u^2 + v^2 + w^2)\right] \tag{3-3}$$

$$\begin{aligned} b_{x_i} &= u_j \tau_{x_i x_j} - \dot{q}_{x_i} \\ \tau_{x_i x_j} &= \mu\left(\frac{\partial u_i}{\partial x_j} + \frac{\partial u_j}{\partial x_i}\right) - \frac{2}{3}\mu\frac{\partial u_k}{\partial x_k}\delta_{ij} \\ \dot{q}_{x_i} &= -\left[\frac{M_\infty \mu}{Re_{L_R}\Pr(\gamma - 1)}\right]\frac{\partial a^2}{\partial x_i} \end{aligned} \tag{3-4}$$

In general, the equations computed are:

$$\frac{1}{J}\frac{\partial Q}{\partial t} = R(Q) \tag{3-5}$$

$$R(Q) = -\left[\frac{\partial\left(\hat{\boldsymbol{F}} - \hat{\boldsymbol{F}}_v\right)}{\partial \xi} + \frac{\partial\left(\hat{\boldsymbol{G}} - \hat{\boldsymbol{G}}_v\right)}{\partial \eta} + \frac{\partial\left(\hat{H} - \hat{\boldsymbol{H}}_v\right)}{\partial \zeta}\right] \tag{3-6}$$

An additional term to satisfy the Geometric Conservation Law (*GCL*) is required for unsteady deforming mesh computations

$$\begin{aligned} R(Q) &= -\left[\frac{\partial\left(\hat{\boldsymbol{F}} - \hat{\boldsymbol{F}}_v\right)}{\partial \xi} + \frac{\partial\left(\hat{\boldsymbol{G}} - \hat{\boldsymbol{G}}_v\right)}{\partial \eta} + \frac{\partial\left(\hat{H} - \hat{\boldsymbol{H}}_v\right)}{\partial \zeta}\right] \\ GCL: &\quad \boxed{+\ Q\left[\frac{\partial}{\partial t}\left(\frac{1}{J}\right) + \frac{\partial}{\partial \xi}\left(\frac{\xi_t}{J}\right) + \frac{\partial}{\partial \eta}\left(\frac{\eta_t}{J}\right) + \frac{\partial}{\partial \zeta}\left(\frac{\zeta_t}{J}\right)\right]} \end{aligned} \tag{3-7}$$

For gust response simulation using FVM, the prescribed gust velocity is added to the mesh deformation velocity on every grid point depending on the space and time as:

$$v_{grid}[(x,y,z),t] \rightarrow v_{grid}[(x,y,z),t] - v_{gust}[(x,y,z),t] \tag{3-8}$$

Based on the dynamic mesh module in CFL3D, the functions based on the FVM is added with the capability to simulate arbitrary gust shapes.

3.1.2 The structural dynamic equations of motion

The structural dynamic equations of motion and time-marching method will be described below briefly and more details can be found in [144, 145].

Based on Lagrange's energy equations, the equations can be expressed as:

$$\boldsymbol{M\ddot{q}} + \boldsymbol{C\dot{q}} + \boldsymbol{Kq} = \boldsymbol{Q}, \qquad q^T = [q_1, q_2 \cdots] \tag{3-9}$$

where $\boldsymbol{q}$ is generalized displacement vector; $\boldsymbol{K}$ is generalized stiffness matrix; $\boldsymbol{C}$ is generalized damping matrix; $\boldsymbol{M}$ is generalized mass matrix, and $\boldsymbol{Q}$ is the generalized force.

The generalized force for mode *i* is:

$$\boldsymbol{Q_i} = q_\infty \left\{ \iint c_p \boldsymbol{\Phi_i} \cdot \boldsymbol{ds} \right\} \tag{3-10}$$

where, $\boldsymbol{\Phi}$ are the mode shapes.

3.1.2.1 Time-marching method [146]

Equation (3-9) can be rewritten in the form of two first-order differential equations [55] with states defined as $x_1 = q$ and $x_2 = \dot{q}$ then $\dot{x_1} = x_2$

$$\dot{x_2} + 2\omega_n \zeta_n x_2 + \omega_n^2 x_1 = \frac{Q_n}{m_n} \tag{3-11}$$

where, $\omega_1, \cdots, \omega_N$ are the natural frequencies of each mode, $m_1, \cdots, m_N$ are the generalised masses, $\zeta_1, \cdots, \zeta_N$ are the generalized damping ratio of each mode.

Each normal mode equation can be represented in first-order state-space form as:

$$\dot{x}_i = Ax_i + B\frac{Q_i}{m_i}, x_i = [\dot{q}_i \; q_i]^T \tag{3-12}$$

$$A = \begin{bmatrix} 0 & 1 \\ -\omega_n^2 & -2\omega_n\zeta_n \end{bmatrix}, B = \begin{bmatrix} 0 \\ 1 \end{bmatrix} \tag{3-13}$$

Eq. (3-11) is a finite-dimensional linear differential equation which can be solved as:

$$x(t) = \Phi(t)x(t_0) + \int_0^t \exp[A(t-\tau)]\, Bu(\tau)\, d\tau \tag{3-14}$$

$\Phi(t) = \exp[A(t)]$ is the state transition matrix and $u(\tau) = \frac{Q(\tau)}{m}$.

Assuming the time step size is *T*, the evolution of Eq. (3-14) for time step (n+1) can be obtained by the following expression.

$$\begin{aligned} x[(n+1)T] &= \Phi(T)x(nT) \\ &+ \int_{nT}^{(n+1)T} \exp\big[A\big((n+1)T - \tau\big)\big]\, Bu(\tau)\, d\tau \end{aligned} \tag{3-15}$$

Since, between the time interval $nT < t < (n+1)T$, the generalized force $u(t)$ is unknown, the integral part of Eq. (3-15) must be approximated. To cope with the approximation, a predictor step and a corrector step were used as follows:

Predictor step:

$$\tilde{x}^{n+1} = \Phi x^n + \frac{1}{2}\theta B(3u^n - u^{n-1}) \tag{3-16}$$

where, $\theta = \int_0^T \exp[A(T-\tau)]\, d\tau$.

The computing mesh will be updated using the predicted modal solution $\tilde{x}^{n+1}$ after the predictor step, and then the flow will be converged to generate the force u^{n+1} for the time $n+1$ to carry out the corrector step as follows:

Corrector step:

$$x^{n+1} = \Phi x^n + \frac{1}{2}\theta B(u^{n+1} + u^n) \tag{3-17}$$

Second order backward differencing is applied to couple fluid-structure interaction in the code. Since the fluid dynamics solver is also second order, therefore, the overall scheme is second order accurate [137].

The following sections demonstrate the validation problems in gust responses, simulations of circulation control and normal microjet blowing.

3.2 Validation of gust response simulation

This validation work contains the following two parts as:

- For the first part, the lift responses of a rigid 2-D aerofoil (NACA0012) encountering a step change of angles of attack, sharp-edged gusts and 'one-minus-cosine' gusts are simulated and compared with analytical results and other numerical reference data. Through this work, the added FVM in the code is validated, and grid sensitivity, as well as time step influence are studied.
- The second part includes two test cases. The first one investigates a 3-D straight wing with a uniform NACA0012 aerofoil shape along the spanwise direction which has the freedom to move vertically when encountering a sharp-edged gust. The second one considers a 3-D elastic wing with plunging and elastic motions encountering a square-wave gust. Through these case studies, the solver set up here coupling three-dimensional URANS, structural dynamic equations of motion and FVM is validated.

3.2.1 Gust responses of a fixed 2-D NACA0012 aerofoil

At the very beginning, grid sensitivity is studied to compare indicial responses of lift coefficients under a step change in angles of attack with three different C-type grid resolutions, namely a coarse 121×41 mesh, a medium 221×81 mesh, and a fine 421×121 mesh. For these three grid resolutions, the first grid distance from the aerofoil surface is kept constant to make a constant $y^+ \sim O(1)$. Figure 3.1 shows the medium grid.

The step change of angle of attack is set to approximately 4.6° for $M_\infty = 0.5$. The input in the numerical code is the vertical velocity of the CFD grids as

$$w_g = w_0 U_{step}(s) \quad \begin{cases} U_{step}(s) = 0, s < 0 \\ U_{step}(s) = 1, s \geq 0 \end{cases} \tag{3-18}$$

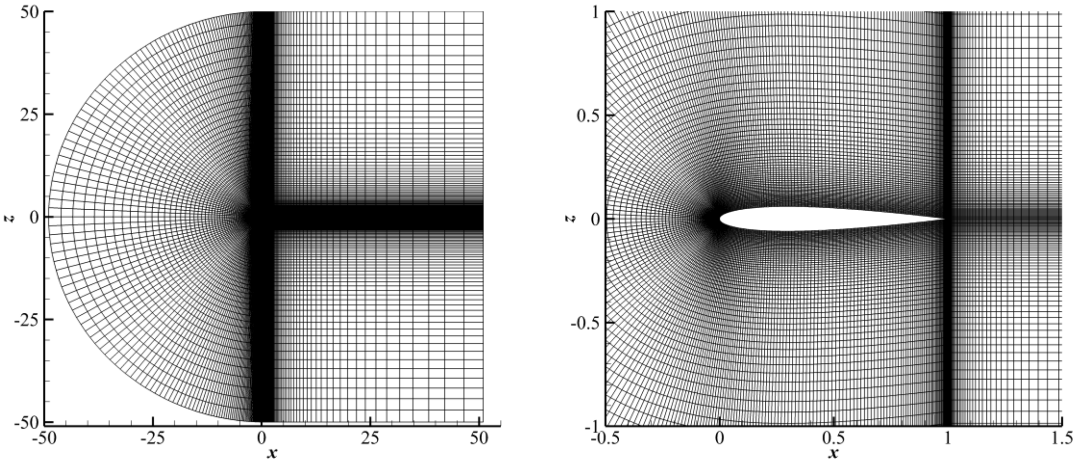

Figure 3.1 Medium grid of the 2-D NACA0012 aerofoil

Here, s is the non-dimensional time; $U_{step}(s)$ is the step function; $w_0 = 0.08U_\infty$, U_∞ is the freestream velocity. The spatial convergence results are shown in Figure 3.2(a), which indicate that the influence of these three grid resolutions is negligible. The medium grid was chosen for the following studies.

For the unsteady flow simulations, appropriate time step should be found to obtain the accurate numerical solutions and to minimize the CPU time for iterations [147]. Three time-step solutions ($\Delta s = 0.00625, 0.0125, 0.0625$) were used to perform a time step convergence study (see the results in Figure 3.2(b)). When choosing time steps, it should be made sure that the time step is acceptable to satisfy the CFL stability condition while is not extremely small [71]. From the results, it is clear that the lift response of $\Delta s = 0.0125$ is similar with that of $\Delta s = 0.00625$. However, when the time step increases to 0.0625, the lift response deviates from the other two time-step solutions. Here, $\Delta s = 0.0125$ was chosen.

For validation of simulating the gust responses using the present solver, three cases are tested on the 2-D NACA0012 aerofoil including responses to the step change in angles of attack, sharp-edged gusts and 'one-minus-cosine' gusts.

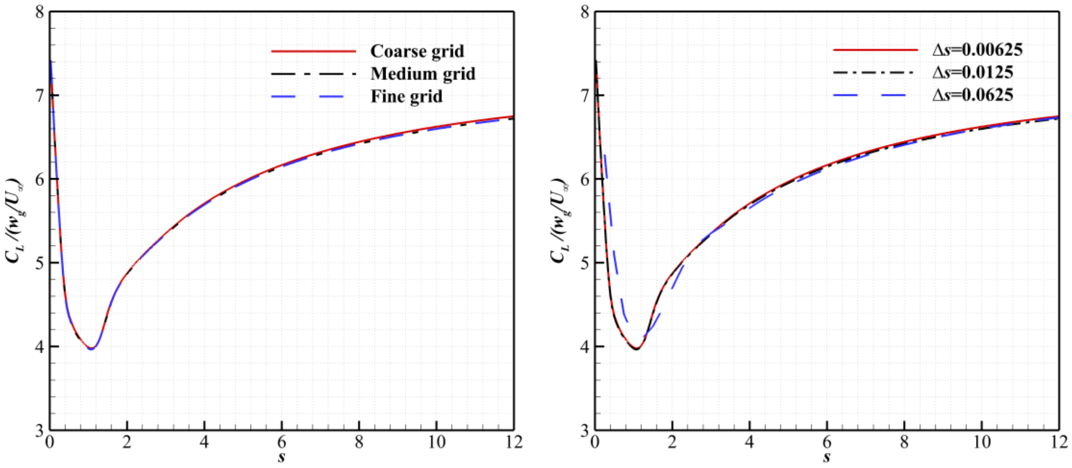

(a) Spatial convergence study (b) Time-step convergence study

Figure 3.2 Lift coefficient response due to a step change of the angle of attack (M_∞= 0.5)

3.2.1.1 The step change in the angle of attack

Lift-coefficient responses to a step change in the angle of attack $\Delta\alpha = 4.6°$, under three Mach numbers 0.3, 0.5, 0.8 are studied. The lift responses are compared with the exact closed-form expressions obtained by Lomax [78] at small time durations, see Figure 3.3(a). At low Mach numbers, the closed-form resolution and the present results follow each other closely. They deviate from each other with increase in Mach numbers. It is because closed-form resolution was derived based on linearized potential equations for a flat plate at low speeds, and thus does not provide accurate results for finite-thickness aerofoils at higher Mach numbers as proposed by Raveh *et al.* [71]. This indicates that the closed-form resolution is not valid at transonic speed, while URANS solutions apply throughout this flow range. The lift responses for non-dimensional time up to 7.5 under these three Mach numbers are compared to the results in Ref. [69] and the Wagner function as shown in Figure 3.3(b). The present results and the numerical reference data which are also based on URANS solutions have a good agreement. The Wagner function is closer to the numerical results for M_∞= 0.3 where compressibility is relatively weak. Large discrepancy appears between the URANS responses and the Wanger function at M_∞= 0.5 and 0.8, indicating its limitations to cope with compressibility. Another limitation is that it cannot predict the initial response. Based on Theodorsen's theory [148], the initial unsteady lift is the non-circulatory load because of the flow's impulsive motion which causes the sudden changes of the pressures on the aerofoil surface. Alternatively, considering the flow is stationary and the aerofoil moves impulsively, the lift is created by compression wave acting on the aerofoil lower surface and expansion wave acting on the upper side. The non-circulatory lift decays rapidly from its initial value. Unlike the non-circulatory lift, the circulatory lift originates from the vorticity shedding into the wake to compensate for the circulation changes around the aerofoil according to the conservation of circulation from Kelvin's theory [70]. The results show that the Wagner function cannot predict the non-circulatory lift. Compared to the closed-form function and Wagner function, the current numerical methods can accurately predict the indicial lift responses due to the step change in angles of attack for subsonic and transonic speeds.

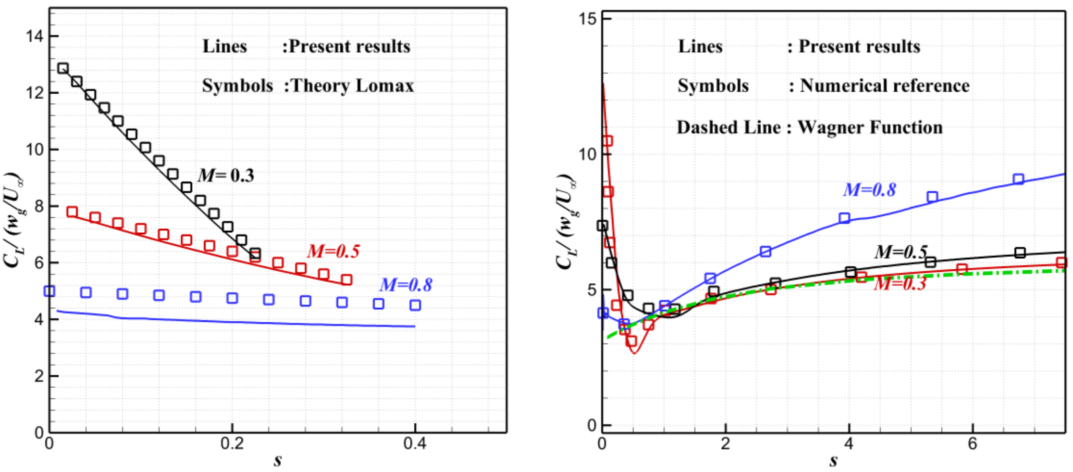

(b) Small-time durations

(b) Large-time durations, numerical reference data from Ref. [69]

Figure 3.3 Indicial lift responses to a step change of the angle of attack under different Mach numbers

3.2.1.2 Sharp-edged gusts

This case tests the response of the NACA0012 aerofoil to a sharp-edged gust. The gust front is located at the leading edge of the aerofoil at the initial time ($s = 0$) (see the sharp-edged gust profile in Figure 3.4). After the initial time step, the gust travels toward the aerofoil. In the numerical code, the gust velocity is assigned to all the grid points in the domain where the gust passed. Test cases with gust velocity w_g/U_∞= 0.08 under the freestream Mach number M_∞= 0.2 and 0.8 are considered.

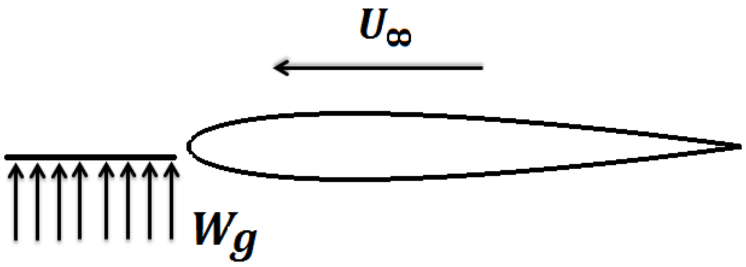

Figure 3.4 Sharp-edged gust profile

The Küssner function was used to compare with the present URANS results as shown in Figure 3.5 (a). The CFD results are normalized by the asymptotic value of the lift coefficient. Overall, a good match between the two results has been obtained at $M_\infty = 0.2$. As was the case of Wagner function for the step change in angle of attack, the Küssner function also show deviations for high Mach numbers from the URANS solutions.

Then Mach numbers 0.3, 0.5 and 0.8 are chosen to compare with the closed-form expression in Eq. (2-9) in small-time durations as shown in Figure 3.5(b). The gust velocities are all set to $w_g/U_\infty = 0.08$ for the three Mach numbers. It can be seen from Figure 3.5(b) that results are virtually identical at lower Mach numbers, while differences become apparent with the increase in Mach numbers. This is similar with the previous study in the indicial responses to the step change in the angle of attack.

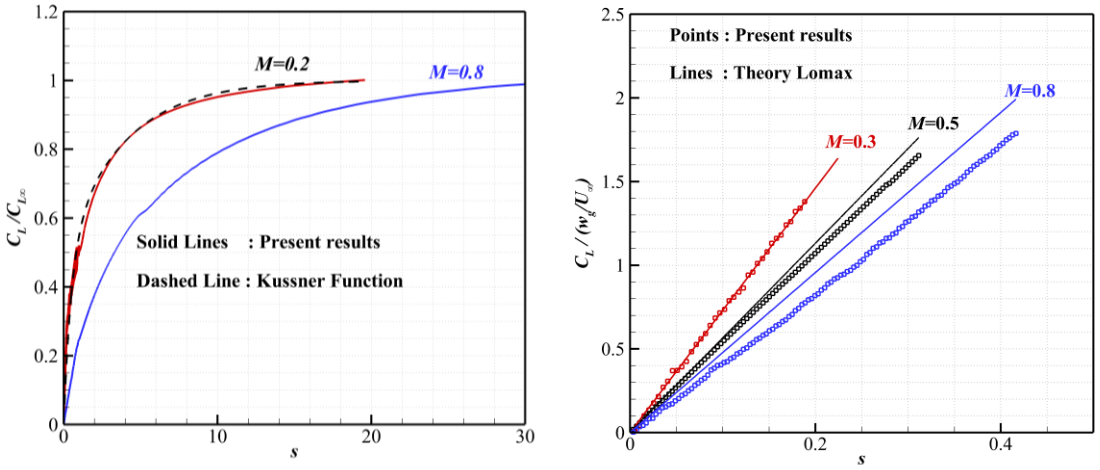

(a) Large-time durations ($M_\infty = 0.2$) (b) Small-time durations ($M_\infty = 0.3, 0.5, 0.8$)

Figure 3.5 Lift responses to sharp-edged gusts

3.2.1.3 One-minus-cosine gusts

The last 2-D validation test case is for one-minus-cosine gusts. Here, four cases are simulated and compared with numerical reference data from Ref. [71]. The first two cases have a freestream Mach number 0.2 with two different gust wavelengths $H_g = 5$ and 25 respectively and a constant gust velocity of $w_0/U_\infty = 0.014$. The second two cases have a freestream Mach number 0.7 with a constant wavelength $H_g = 5$ and two different gust velocity magnitudes $w_0/U_\infty = 0.040$ and 0.122 respectively. The comparisons are shown in Figure 3.6, where the present results and the reference data follow each other closely indicating a good agreement.

The above studies demonstrate that the URANS computational tool, via the introduced FVM shows good accuracy for gust responses without the limitation of the analytical functions mentioned above.

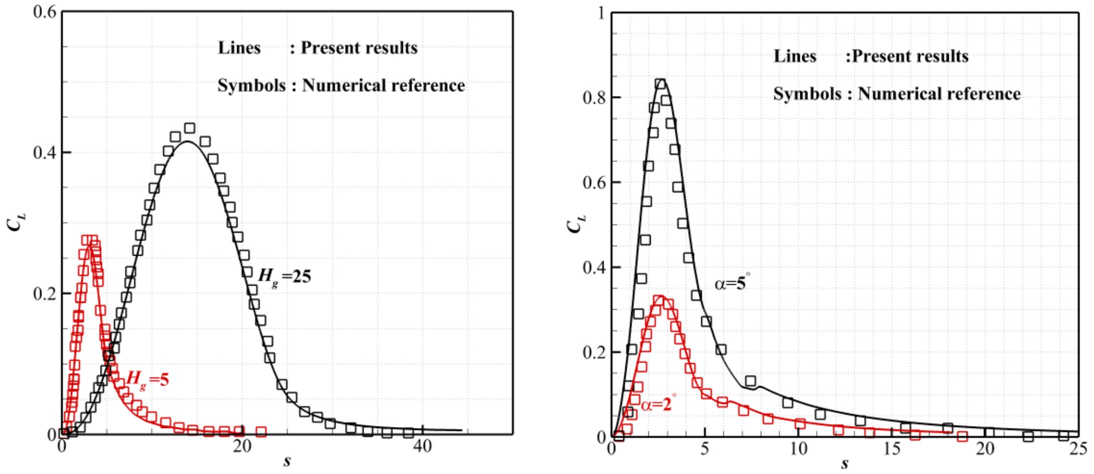

(a) M_∞= 0.2 (b) M_∞= 0.7

Figure 3.6 Lift responses to one-minus-cosine gusts

3.2.2 3-D straight wing with plunging

So far, in all the previous test cases the models are fixed without motions when encountering gusts. In the following test case, a 3-D straight wing with a uniform shape of the NACA0012 aerofoil along the spanwise direction is free to move up and down, which means the plunging mode is included when encountering gusts.

3.2.2.1 Analytical foundations

Here, the chord length, span length, and area of the straight wing are set to be *c*, *l,* and *S* respectively. Assuming the wing is flying at the freestream speed *U* into a sharp-edged gust with a magnitude velocity w_0, as the wing is free to move vertically, the governing differential equation of the disturbed motion is [149]

$$m\ddot{z} = -L_G - L_M = -\int_0^l L_G dy - \int_0^l L_M dy \tag{3-19}$$

where, m is the wing mass and z is the vertical displacement. L_G and L_M are aerodynamic forces due to the motion and the gust, respectively.

As mentioned before, the Küssner function is used to define the unsteady lift responses to sharp-edged gusts, so here the gust load L_G can be described as

$$L_G(s) = \frac{1}{2}\rho U^2 S \frac{dC_L}{d\alpha}\left[\frac{w_g(0)}{U}\Psi(s) + \int_0^s \frac{dw_g(\sigma)}{d\sigma}\Psi(s-\sigma)d\sigma\right] \tag{3-20}$$

where, $\frac{dC_L}{d\alpha}$ is the lift-curve slope which can be replaced by 2π for simplification in incompressible flow with thin aerofoil assumption.

The aerodynamic force caused by the wing motion during penetration into the sharp-edged gust is described by the sudden change in the angle of attack governed by Wagner function, therefore,

$$L_w(s) = \left[\frac{1}{2}\rho U^2 S \frac{dC_L}{d\alpha}\int_0^s \emptyset(s-\sigma)\frac{d}{ds}\left(\frac{\dot{z}}{U}\right)d\sigma + \frac{\pi}{4}\rho c S\ddot{z}\right] \tag{3-21}$$

Combining the above two equations into Eq. (3-19) and transforming to the variable s in all terms, we get

$$\begin{aligned} \frac{U^2}{\left(\frac{c}{2}\right)^2}\ddot{z}(s) = -\frac{1}{2}\rho U^2 S \frac{dC_L}{d\alpha}\Bigg[\int_0^s \frac{w_g(\sigma)}{U}\Psi'(s-\sigma)d\sigma \\ + \frac{2}{c}\int_0^s \ddot{z}\emptyset(s-\sigma)d\sigma + \frac{1}{c}\ddot{z}\Bigg] \end{aligned} \tag{3-22}$$

Applying the Laplace transformation, the acceleration can be solved as [67]

$$\ddot{z} = -\frac{0.5648}{\lambda_m + 0.25}\frac{Uw_0}{c}(A_1 e^{-0.13s} + A_2 e^{-s} + B_1 e^{\gamma_1 s} + B_2 e^{\gamma_2 s} + B_3 e^{\gamma_3 s}) \tag{3-23}$$

Assuming the aerodynamic force due to wing motion is neglected, the acceleration due to a sharp-edged gust can be obtained from steady-state aerodynamic theory, which is

$$\ddot{z}_{steady-state} = \frac{Uw_0}{\lambda_m c} \tag{3-24}$$

where, $\lambda_m = \frac{m/\pi\rho s\left(\frac{c}{2}\right)dC_L}{d\alpha}$ is the non-dimensional mass parameter of the wing.

Defining a dimensionless acceleration ratio as

$$\begin{aligned}\text{Acceleration ratio} &= \frac{\ddot{z}}{\ddot{z}_{steady-state}} \\ &= -\frac{0.5648\lambda_M}{\lambda_m + 0.25}(A_1 e^{-0.13s} + A_2 e^{-s} + B_1 e^{\gamma_1 s} + B_2 e^{\gamma_2 s} \\ &\quad + B_3 e^{\gamma_3 s})\end{aligned} \tag{3-25}$$

To deal with the compressibility in high subsonic speed, Bisplinghoff [149] introduced the Prandtl-Glauert correction to lift-curve slope which is

$$\left(\frac{dC_L}{d\alpha}\right)_M = \frac{1}{\sqrt{1-M^2}}\frac{dC_L}{d\alpha} \tag{3-26}$$

Then the dimensionless mass parameter λ_m becomes

$$\lambda_m = \frac{m\sqrt{1-M^2}}{\rho\left(\frac{c}{2}\right)S\frac{dC_L}{d\alpha}} \tag{3-27}$$

3.2.2.2 CFD results

To compare with the analytical data in Reference [149], the same four values of dimensionless mass parameter λ_m= 5.34, 13.33, 35.6 and 71.2 are used here under three incoming Mach numbers of 0.3, 0.5 and 0.8 and the gust velocity of $w_g/U_\infty = 0.08$.

Table 3.1 gives the calculation parameters of masses m and generalized mode value $\Phi = \frac{1}{\sqrt{m}}$ under different λ_m and Mach numbers. Here, the masses in Mach number 0.5 and 0.8 are calculated using Eq. (3-27) considering compressibility effects.

Table 3.1 Parameters in the simulations

λ_m	M	m	Φ	M	m	Φ	M	m	Φ
5.34	0.3	21.64	0.215	0.5	24.99	0.200	0.8	36.07	0.166
13.33		54.02	0.136		62.38	0.127		90.04	0.105
35.6		144.27	0.083		166.60	0.077		240.46	0.064
71.2		288.55	0.059		333.19	0.055		480.92	0.046

The CFD results of the non-dimensional acceleration ratios are compared with the analytical data in Ref. [149] shown in Figure 3.7. In different Mach numbers, the non-dimensional acceleration ratio is the same as long as λ_m is the same according to Eq. (3-25). From the comparison, good agreements exist at low Mach numbers, while large discrepancies appear when Mach number reaches to 0.8.

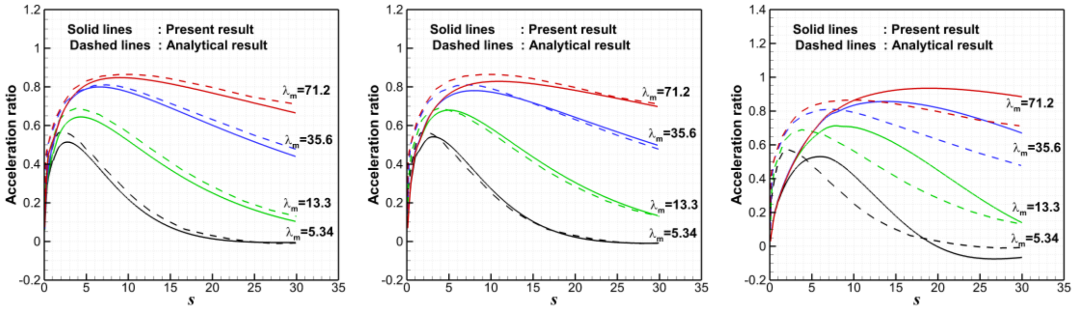

(a) $M_\infty = 0.3$ (b) $M_\infty = 0.5$ (c) $M_\infty = 0.8$

Figure 3.7 Comparisons of non-dimensional acceleration responses with data in Ref. [149]

As the wing has the freedom in the vertical direction when encountering the gust load, the acceleration will equal to zero and the model will move together with the gust in the same velocity at the final equilibrium state. From the previous results, it can also be noticed that, for a smaller value of λ_m, it takes less time to reach the maximum acceleration. Figure 3.8 (a) shows the velocity responses of different λ_m under M_∞= 0.3. Clearly, after a process of acceleration and a phase of deceleration, the model will reach a constant velocity of 8.15 (m/s) which is as same as the gust velocity $w_g = 0.08U_\infty = 0.08 * 0.3 * 340\ (\mathrm{m/s}) = 8.16\ (\mathrm{m/s})$. Figure 3.8 (b) compares the lift responses of these models with plunging motion to that of the same model without motion which is fixed when encountering gust loads. The result illustrates that the influences of unsteady aerodynamic forces due to motion are large for small values of the mass parameter. That is to say that it is more sensitive for the lighter model under the same gust loads. Due to the motion, the maximum gust load can be reduced significantly for the lighter models.

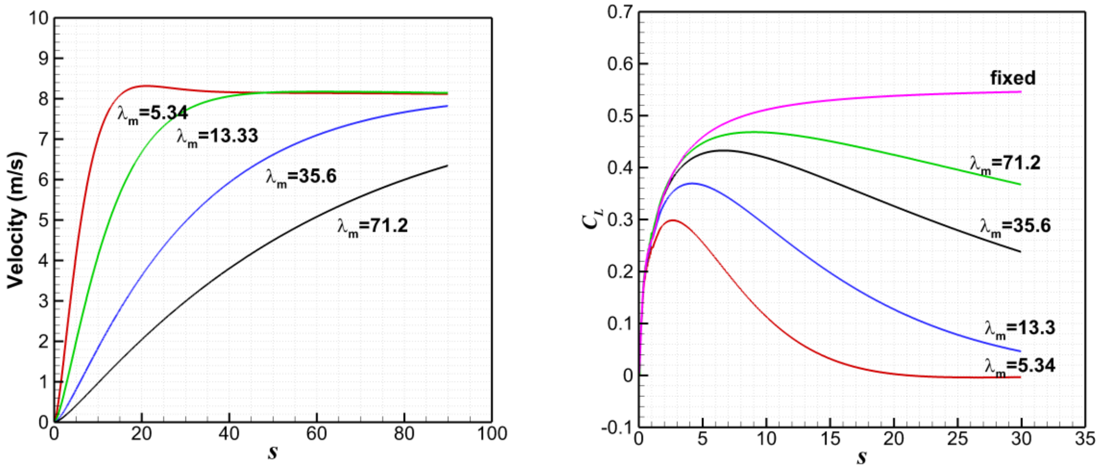

(a) Velocity history (b) Lift coefficient history

Figure 3.8 Velocity history and lift coefficient history (M_∞= 0.3)

3.2.3 Gust response of the BAH wing

A jet transport wing planform which commonly cited as BAH wing (Bisplinghoff, Ashley, and Halfman [67]) has been used in various researches as one of the standards in aeroelasticity field. The BAH wing is a half wing with a wingspan l= 12.7 m, a mean aerodynamic chord $\bar{c}$= 4.1275 m, and a wing area S= 52.42 m^2, (see the plan form in Figure 3.9). NACA65A004 aerofoil is used for the cross section.

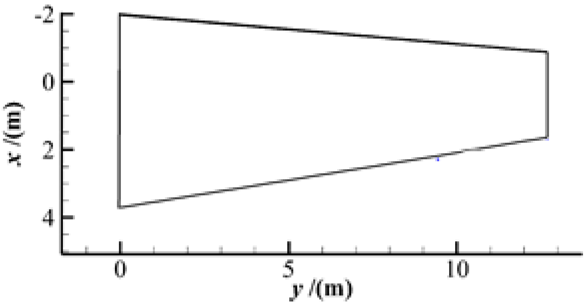

Figure 3.9 Planform of BAH wing

MSC.NASTRAN is a reliable software and enables high-fidelity structural analysis [150]. BAH wing has been adapted by Rodden *et al.* [151] as a MSC.NASTRAN demonstration problem for random gust response analysis [152]. For the validation of gust response simulation by the present numerical methods, the results of the example case of random gust response of the BAH wing in MSC.NASTRAN are replicated.

The structural information of the BAH wing is extracted from MSC.NASTRAN. In this study, two typical modes are included in the simulation. The first is the plunging mode and the second is the first bending elastic mode with a natural frequency of 2.44 Hz. The profile of these two modes is shown in Figure 3.10.

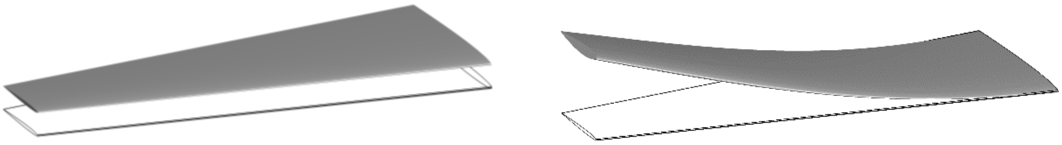

(a) Plunging mode (f= 0 Hz) (b) The first bending mode (f= 2.44 Hz)

Figure 3.10 The profile of the two modes used in this case study

In MSC.NASTRAN, the demonstration problem simulates the time history of the gust responses of the BAH wing due to a gust load. The gust is a square wave gust shown in Figure 3.11 with a duration of 2 seconds. The gust velocity (w_g) is taken as 0.01 times the incoming flow velocity of M_∞= 0.62, which is 2 m/s.

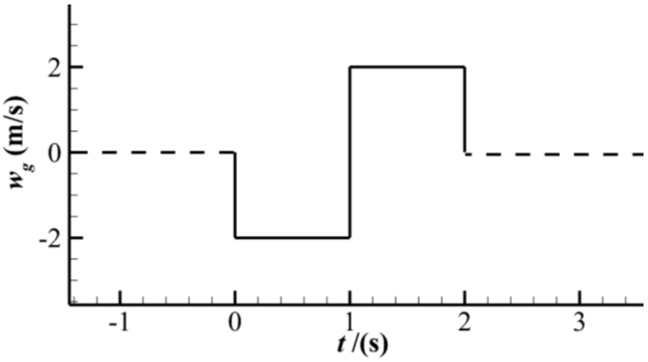

Figure 3.11 The profile of square wave gust

This problem is solved by the present numerical methods and the vertical displacement responses are compared with the MSC.NASTRAN [152] results as shown in Figure 3.12. As can be seen, the present results agree well with that calculated by MSC.NASTRAN. Also shown is that the displacement of the plunging mode is more significant than that of the first bending mode. The maximum displacement of the plunging mode is about -1.5 m which is about ten times of the first bending mode.

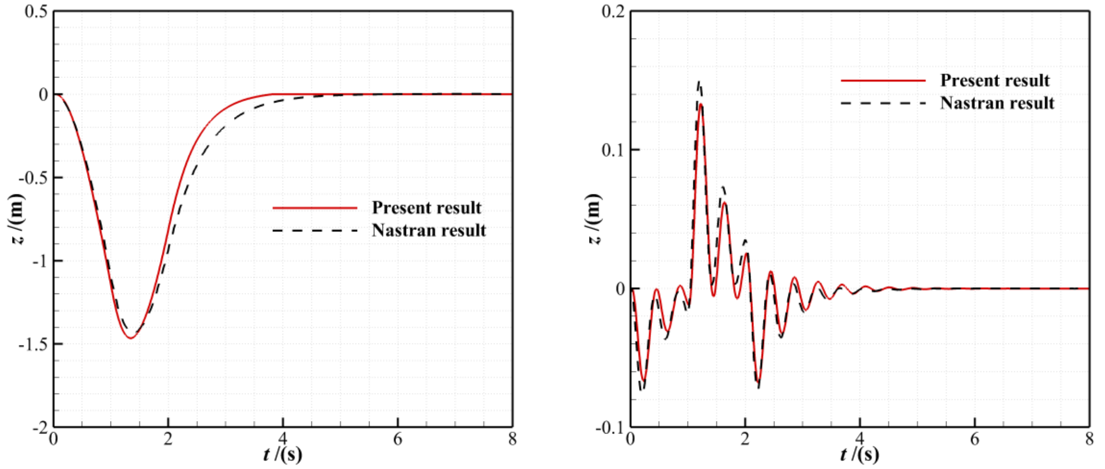

(a) wing-root displacement (b) wing-tip displacement relative to the wing root

Figure 3.12 Comparison of the real displacement responses

3.3 Validation of circulation control via jet blowing over trailing-edge Coanda surface

Alexander *et al.* [129] conducted a range of experiments to test the effects of CC on a straight wing with 0.75% cambered and 6% thick elliptic aerofoil. The experimental model had a span of twice chord lengths and had an end plate of one chord length in diameter to minimize the finite span effect. Figure 3.13 shows the geometry of the aerofoil as well as the 2.98:1 elliptical Coanda surface. The slot height is 0.12% of the chord length.

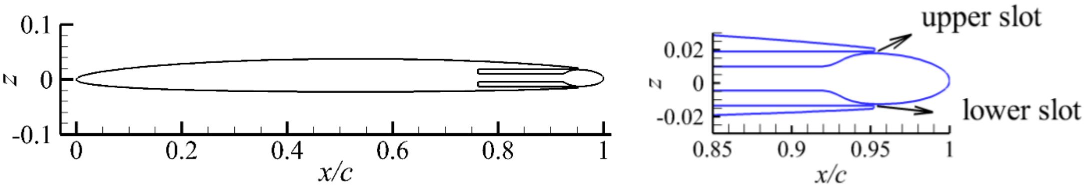

Figure 3.13 The elliptical aerofoil with Coanda surface

In order to wrap the wing model as well as the end plate using structured blocks, Forster *et al.* [153] used a slightly enlarging end plate having a diameter of 1.1 chord lengths in his CFD validation study. Both Cruz *et al.* [154] and Forster *et al.* [153] demonstrated that modelling of the viscous wall of the splitter plate included in the experiment provided closer solutions to the experimental data. Thus, an end plate with 1.1 chord lengths in diameter as well as a circular splitter plate with four chord lengths in diameter is included in the numerical simulation. Figure 3.14 shows the model and the mesh domain used for the simulation.

A grid refinement study is performed to investigate the effect of grid density on CC. The medium grid used in the previous 2-D aerofoil study is used here as the baseline aerofoil section grid that is 221 cells on the aerofoil. From this, 121 cells on the Coanda surface, 149 cells in the wall normal direction and 221 cells over the span of the aerofoil are used to create the 3-D mesh. The total grid size is about 11×10^6 and 12×10^6 for the model without and with blowing respectively. Based on this, a coarser mesh with half element of the baseline mesh and a finer mesh with twice of the elements are compared. During the refinement, the distance of the first grid point away from the wall was kept constant to keep the $y^+\sim O(1)$.

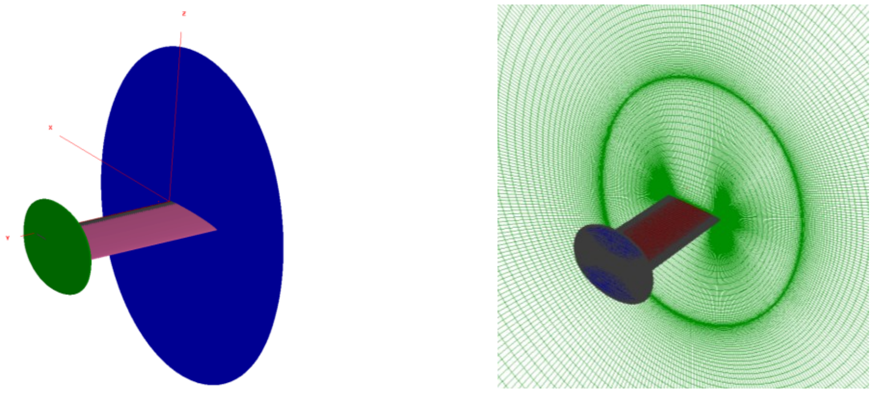

(a) The model with end plat and splitter plate (b) The mesh

Figure 3.14 The model and mesh generated based on the experimental model from Ref. [129]

The comparison of pressure coefficients on the midspan wing section between these three mesh resolutions and the experimental data at $M_\infty= 0.3$, $\alpha= 3^\circ$, $Re_c= 1.0\times10^6$ for the unblown case is shown in Figure 3.15. In order to show the 3-D effects on the pressure coefficients, the computational data of the 2-D aerofoil is also shown in the figure. The results show large discrepancies in the solutions between the 2-D aerofoil and the 3-D models. The 2-D aerofoil case overpredicted the pressure coefficients on both the upper and the lower surfaces, especially near the leading edge. The present results of the pressure coefficients for the 3-D model have a good agreement with the experimental data. The difference of the pressures from the medium mesh and the fine one is negligible. The magnitude of the pressure coefficient on the upper surface of the coarse mesh is slightly higher than the other two mesh resolutions, but the pressure coefficients on the lower surface of the three mesh resolutions are in good agreements.

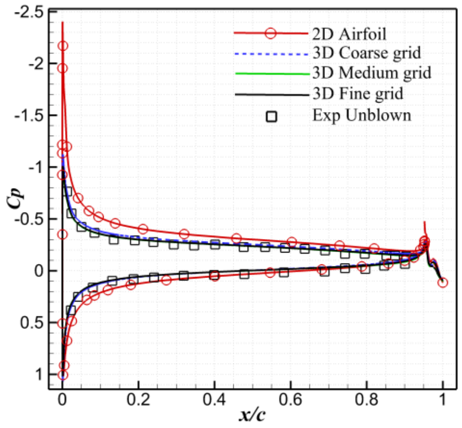

Figure 3.15 Comparison of the pressure distributions on the midspan wing section of the unblown case ($M_\infty= 0.3$, $\alpha= 3^\circ$)

The present results of the pressure coefficients of the models with the upper slot blowing momentum coefficient $C_\mu \approx 0.016$ and $C_\mu \approx 0.054$ at $M_\infty = 0.3$, $\alpha = 3^{\circ}$ are compared to the experimental data from Ref. [129] as shown in Figure 3.16(a). Figure 3.16(b) shows the comparison of the model with the lower slot blowing having a momentum coefficient $C_\mu \approx 0.006$ and $C_\mu \approx 0.028$. Figure 3.17 shows the comparisons at $M_\infty = 0.8$, $\alpha = 3^{\circ}$ for the upper slot blowing with $C_\mu \approx 0.008$ and the lower slot blowing with $C_\mu \approx 0.005$ and 0.011.

The jet blowing momentum coefficient (C_μ) is defined as

$$C_\mu = \frac{\dot{m} U_{jet}}{q_\infty A} \tag{3-28}$$

where, $\dot{m}$ is the mass flow rate, q_∞ is the freestream dynamic pressure, A is the surface area of the wing and U_{jet} is the jet velocity. Assuming the jet flow expands isentropically throughout the slot to the freestream static pressure, the jet velocity can be calculated by the following equation as

$$U_{jet} = \sqrt{\frac{2\gamma}{\gamma - 1} R T_0 \left[1 - \left(\frac{p_\infty}{p_{0,plenum}}\right)^{\frac{\gamma-1}{\gamma}}\right]} \tag{3-29}$$

where R is the gas constant, T_0 is the total temperature, γ is the ratio of specific heat, $p_{0,plenum}$ is the total pressure in the plenum and p_∞ is the freestream static pressure. The varying of the momentum coefficient (C_μ) is obtained by adjusting the nozzle pressure ration (NPR: $p_{0,plenum}/p_\infty$).

The computational pressure coefficients on the aerofoil surface and the Coanda surface match the experimental data reasonably well at $M_\infty = 0.3$. For the upper slot blowing, the results show that with the increase of momentum coefficient, the absolute values of the pressure coefficients on both the upper and lower surfaces increased, resulting in the increment in lift coefficients. The present results also captured the peak pressure near the aerofoil leading edge correctly. A near constant shift in the pressures on the first 60% of the chord with the increase in momentum coefficient was also captured well by the present results. For the lower slot blowing, with the increase of momentum coefficients, the absolute magnitudes of pressure coefficients on both the upper and lower surfaces decreased simultaneously, resulting in a decrease in lift coefficients.

For M_∞= 0.8, in general, the present numerical methods predicted the surface pressure well compared to the experimental data, but with a slightly overprediction of the pressure coefficients around the upper surface leading edge for both the unblown and blowing cases indicating a systemic deviation between the CFD and the experimental conditions.

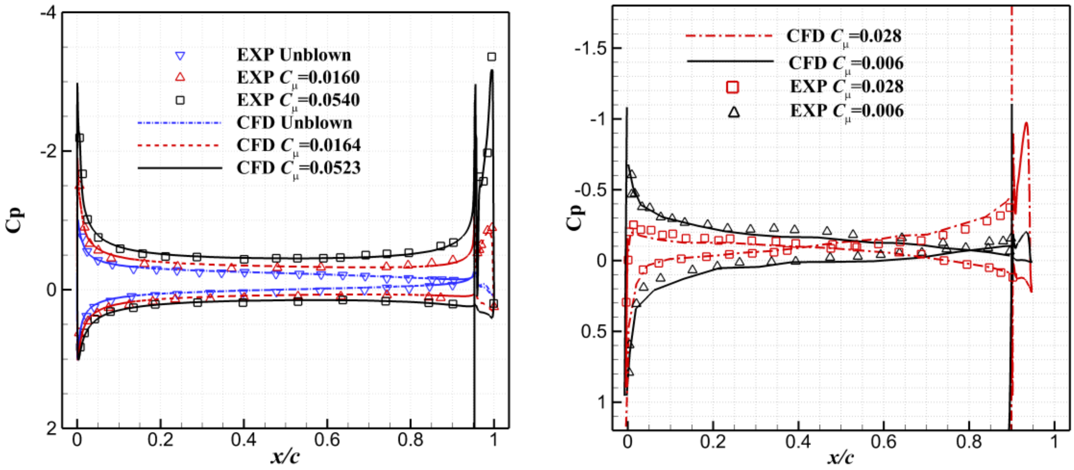

(a) Upper slot blowing (b) Lower slot blowing

Figure 3.16 Comparisons of pressure coefficients (M_∞= 0.3)

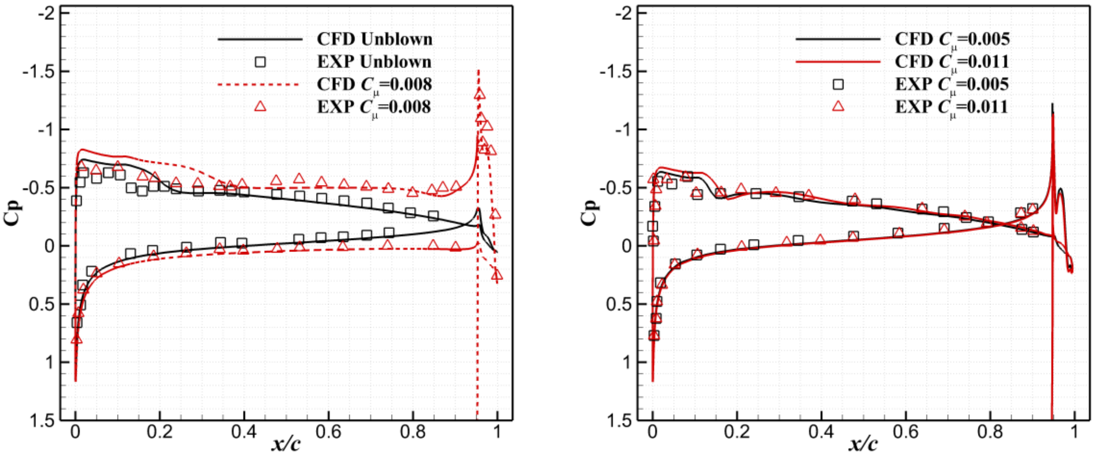

(a) Upper slot blowing (b) Lower slot blowing

Figure 3.17 Comparisons of pressure coefficients (M_∞= 0.8)

Figure 3.18 shows the comparisons of the changes in lift coefficients ($\Delta C_L = C_{L_{C_\mu \neq 0}} - C_{L_{C_\mu = 0}}$) due to the variation in blowing momentum coefficients between the experimental data and the present CFD results for both the upper slot blowing and lower slot blowing at M_∞= 0.3 and 0.8. According to the studies on CC [155, 156], the effectiveness of CC is not unlimited with the increase of momentum coefficient. The increment in lift as the blowing momentum coefficients increase to some extent will decrease due to the jet detachment. This phenomenon is called 'C_μ-stall'. For both Mach numbers, the present results captured the trends in lift augmentation with increased C_μ. However, in the large C_μ range, the CFD over predicted the value and the reason is unknown. Similar simulation work in Ref. [157] only compared the data of C_μ below 0.04, while it was compared up to C_μ=0.08 here. The maximum lift coefficient augmentation is up to about 0.6 for M_∞= 0.3. However, for M_∞= 0.8, the lift coefficient increment rolls off at a much smaller C_μ compared to that of M_∞= 0.3. The maximum lift coefficient augmentation for M_∞= 0.8 is only around 0.25 for the upper slot blowing, and -0.13 for the lower slot blowing, indicating the reduced load control capability of CC under transonic speed.

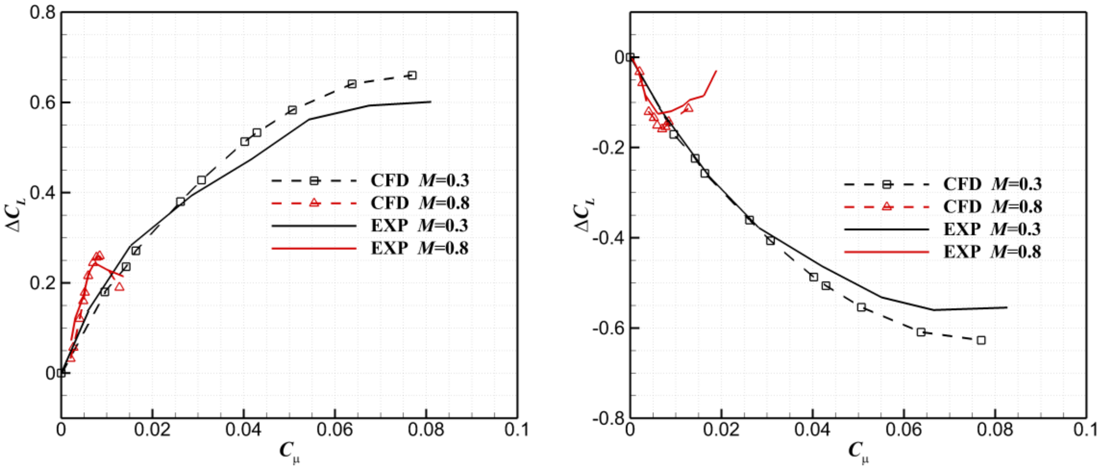

(a) Upper slot blowing (b) Lower slot blowing

Figure 3.18 Comparisons of changes in lift coefficients due to C_μ variation under M= 0.3 and 0.8, α= 3°

Figure 3.19 shows the Mach number contours along the mid-span wing section for the blowing cases with C_μ= 0.005 and 0.015. It is clear to see that when C_μ increased to 0.015, the CC jet detached from the Coanda surface reducing its capacity of entraining the external flow to follow the jet over the curved surface, resulting in a net reduction in the circulation of the aerofoil. In the meantime, during the calculation for C_μ= 0.015, the flow field could not converge to a steady state, but fluctuated periodically, resulting in the fluctuation in aerodynamic characteristics. Unsteadiness was also observed by Foster *et al.* [153] in the numerical study of transonic CC in the residual of the steady state solution.

From the comparisons of the surface pressure coefficients and the increment of the integral lift coefficients with the increase in blowing momentum coefficients, it can be seen that, in general, the present CFD tool was proven to be able to provide an accurate representation of the CC jet flow.

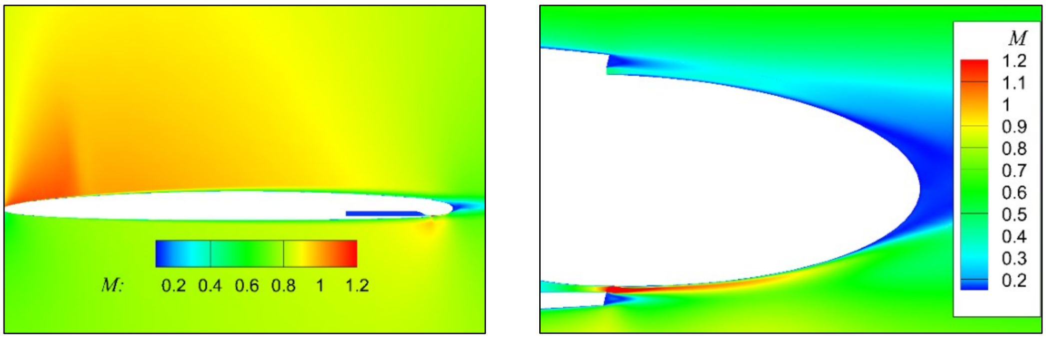

(a) C_μ= 0.011

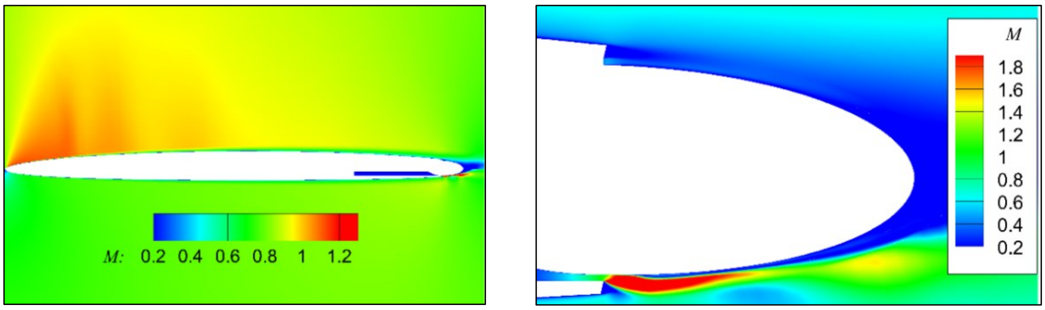

(b) C_μ= 0.015

Figure 3.19 Mach number contours for M_∞= 0.8, α= 3°

3.4 Validation of normal microjet blowing

Like tangential Coanda surface jets, normal microjets blowing perpendicular through the aerofoil or wing surfaces also have the capability of modifying the flow condition by pulling the fluid around a sharp trailing edge rather than a rounded Coanda device. Therefore, these two methods will have opposite lift changes when devices are placed on the same side of an aerofoil or a wing. For instance, Coanda jets blowing on the lower side of an aerofoil will decrease the lift, whereas the lift will be increased if a normal microjet is blowing on the lower side. As demonstrated previously, the aerofoil must be modified especially on the trailing edge to include the Coanda device, while the normal microjet has an advantage in maintaining the original aerofoil shapes, especially, the sharp trailing edges.

As has been demonstrated through the literature reviews in Chapter 2, the studies of the concept of surface microjet blowing have been lasting for decades. However, the researches were mainly focused on boundary layer control, such as keeping the flow attached or stall delaying. The investigations of microjets for load control are still rare and most of the available studies are at low freestream velocities as the research targets are mainly for wind turbine blades. Apart from CC, this study will also explore the feasibility and effect of gust load alleviation by means of normal microjet blowing for subsonic and transonic speeds with practical importance for civil aviation. Firstly, the validation of the simulation for normal microjet blowing is done, following by the investigation of the influence of microjet parameters including jet-slot location and width. This is to choose the appropriate microjet parameters for the following load control and gust load alleviation studies.

As has been demonstrated in the previous section that the present solver is capable to predict accurate results for CC-jet flows. To further validate the current methodology for normal microjet blowing, the numerical and experimental results conducted by de Vries *et al.* [17] are applied for the comparisons. The studies were conducted based on the 2-D NACA0018 aerofoil with microjet placing at $x/c = 0.9$.

To model the jet, Blaylock *et al.* [125] compared three different models: surface jets with constant velocities, surface jets with parabolic velocity profiles and jets created by plenums. The results showed close aerodynamic coefficients among these three models. This finding was consistent to the studies conducted by Rumsey [158] that the differences in aerodynamic coefficients between jets produced through plenums and jets generated from the surfaces were minimal. Therefore, jets originating from aerofoil or wing surfaces are used in this study.

The experimental model used by de Vries *et al.* [17] had the chord length of $c = 0.165$ m; jet width $h_{\text{jet}} = 0.001$ m placed at $x/c = 0.9$ on the NACA0018 aerofoil lower surface. The freestream velocity is $M_\infty = 0.176$, with the Reynolds number $Re_c = 6.6\times10^5$. The blowing velocity of the microjets is kept constant as $1.2U_\infty$. The pressure was only measured at four points on the aerofoil surface. In the reference, de Vries *et al.* also conducted numerical investigation using the commercial computational fluid dynamics software package ANSYA CFX 11.0. The total lift changes between the aerofoils with and without microjet blowing under the same incoming flow condition as the experiment were evaluated.

Figure 3.20 gives the comparisons of the calculated pressure distributions on models with and without microjet blowing to the experimental data from Ref. [17]. The comparison shows a good agreement, especially for pressures on the upper surface. Figure 3.21 presents the comparisons of the changes of lift coefficients between the present results and the reference data. In general, these results show a good match for both the models with and without microjet blowing. It is also clear that the lift coefficient augmentation $\Delta C_L \approx 0.4$ is obtained due to the microjet blowing with $U_{jet} = 1.2U_\infty$. In general, the present solver can capture the aerodynamic changes caused by microjet blowing, which can be used for the following load control and gust load alleviation studies using normal microjet blowing.

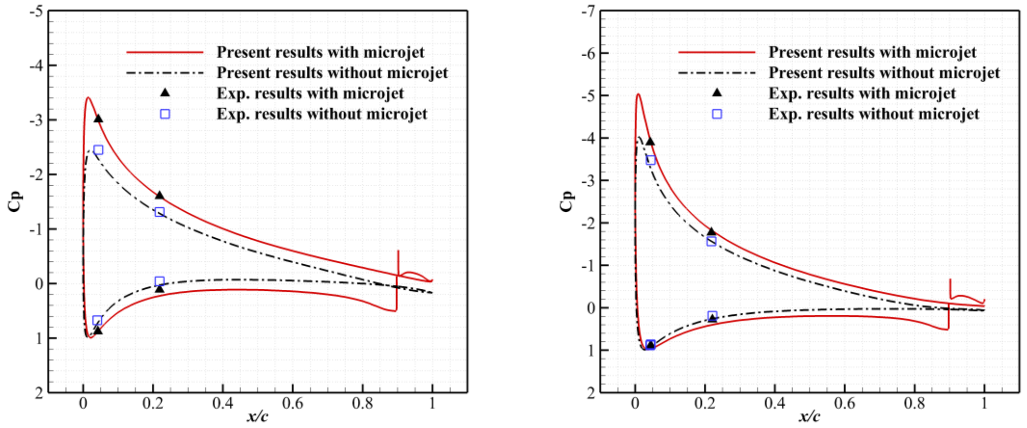

(a) α= 8° (b) α= 12°

Figure 3.20 Comparisons of present pressure distributions on the NACA0018 aerofoil to the experimental data in Ref. [17]

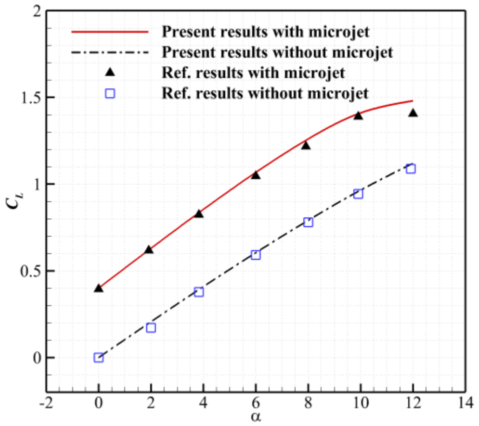

Figure 3.21 Present results of the lift coefficients compared to the reference numerical data from Ref. [17]

Al-Battal *et al*. [3] and Leopold [159] compared the efficiency of microjets placed on different chordwise locations on 2-D aerofoils. Similar conclusions were obtained from those two studies that microjets placed on the trailing edge are more effective. As those experiments were conducted under low incompressible flow, it is necessary to extend the study on the influence of microjet locations and jet-slot width to subsonic and transonic incoming flows. Figure 3.22 shows the sketch of the chordwise jet-slot width and the jet-slot location which is measured from the aerofoil leading edge to the middle of the jet slot.

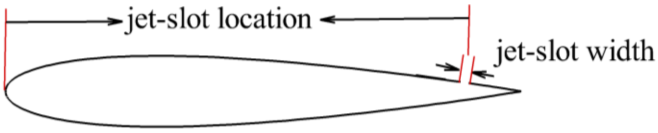

Figure 3.22 Sketch of the jet-slot width and location

To get a quantitative understanding of the influence of microjet location and jet-slot width on the changes of lift coefficients, the NACA0012 aerofoil is chosen to carry out this study. Firstly, to find an appropriate grid resolution for the simulation, three different C-type grid resolutions, namely a coarse 221×121 mesh, a medium 321×141 mesh (as shown in Figure 3.23, having 81 on the slot and the rest on the aerofoil section), and a fine 421×161 mesh are conducted on the aerofoil with slot-width of 0.5% at x/c= 0.95. For these three grid resolutions, the first grid distance from the aerofoil is kept constant to make a constant $y^+ \sim O(1)$.

Figure 3.23 shows the pressure coefficient distributions of the model with M_{jet}= 0.2 at M_∞= 0.3, α= 3° and the model with M_{jet}= 0.7 at M_∞= 0.7, α= 3° for these three grid resolutions. The results show a negligible influence from the grid. The medium grid resolution is used to construct the grids for other models with different jet-slot location.

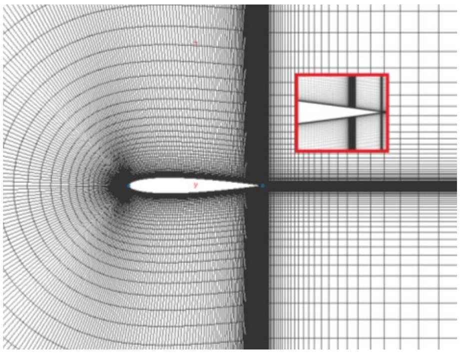

Figure 3.23 NACA0012 aerofoil with microjet at x/c= 0.95

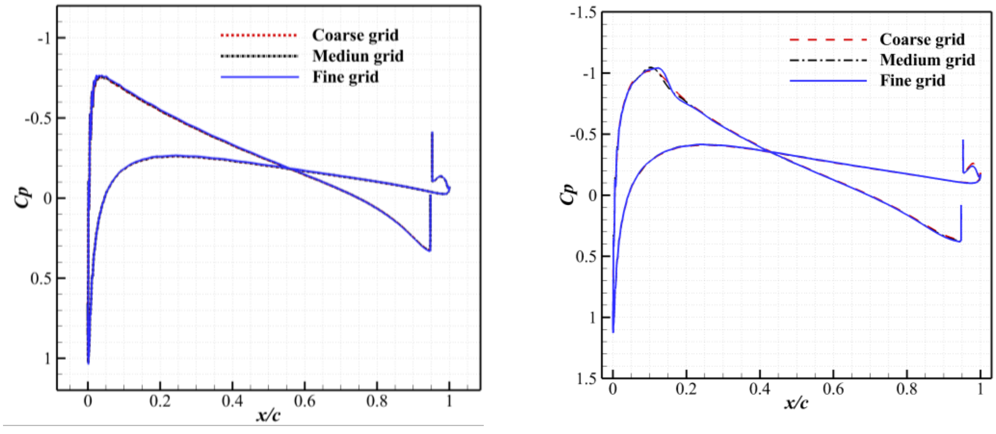

(a) M_∞= 0.3 (b) M_∞= 0.7

Figure 3.24 Influence of grid resolutions on surface pressure distribution

3.4.1 Influence of jet-slot location

The jet-slot locations ranging from x/c= 0.4 to 0.95 with the same jet-slot width of 0.5%c on the aerofoil upper surface are chosen to evaluate the influence of the jet-slot location. The jet velocity is chosen the same as the freestream velocity as U_{jet}= U_∞.

Figure 3.25 gives the results of lift coefficient reduction (ΔC_L= $C_{L,\ with\ jet}$ - $C_{L,\ without\ jet}$) against the jet-slot locations under M_{jet}= M_∞= 0.3 at α= 0° and 3°. It is clear that the magnitudes of the reduction in lift coefficient increase with microjets moving towards the trailing edge, and this trend is captured both at α= 0° and 3°. At α= 0°, the reduction in lift coefficient of ΔC_L= -0.09 is obtained due to the microjet blowing at x/c= 0.4, and this value reaches to ΔC_L= -0.33 when the microjet moves to x/c= 0.95. Noticeably, the magnitudes of lift coefficient reduction increase almost linearly with the microjet location moving from x/c= 0.7 to 0.95 for both α= 0° and 3°.

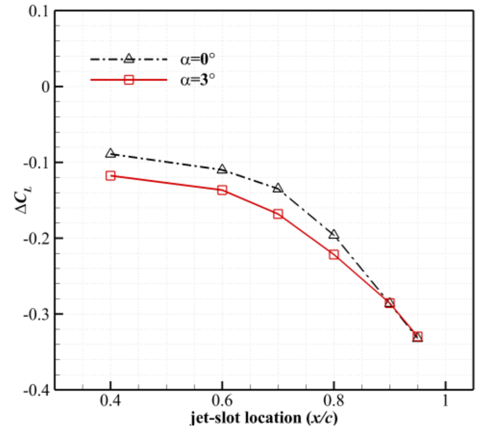

Figure 3.25 Influence of Microjet location on lift coefficient reduction with M_{jet}= M_∞= 0.3

Figure 3.26 presents the comparisons of the surface pressure coefficients between the baseline model and the models with microjet blowing. Figure 3.27 displays the velocity flow fields of the baseline model and models with microjets located at *x*/*c*= 0.4 and *x*/*c*= 0.9 at α= 0º. Also shown is the regions of interest around the microjets and the trailing edges. For the baseline model, it exhibits attached flow along both the aerofoil upper and lower surfaces. However, models with microjet blowing generate a separation region near the jet location, and the separation region is more apparent after the jet location than that before it. This separation region deflects the streamlines upwards near the jet location and blocks the flow over the upper surface. This increases the upper surface pressure coefficients ahead the blowing slot which can be noticed from Figure 3.26. However, behind the jet slot, the pressure recovers rapidly. From Figure 3.27 (c), it can be seen that this separation not only deflects the streamline above the upper surface, but also entrains the flow from the lower surface upwards. This entrainment accelerates the flow under the lower surface and results in a reduction in the pressure coefficients on the lower surface. Also shown is that the entrainment capability is stronger when the blowing is placed towards the trailing edge, as slight decreases of pressure coefficients are noticed with blowing slot moving towards the trailing edge as demonstrated in Figure 3.26 (b) The combined effects explain the reduction in lift coefficient with the normal microjet blowing relative to the baseline model.

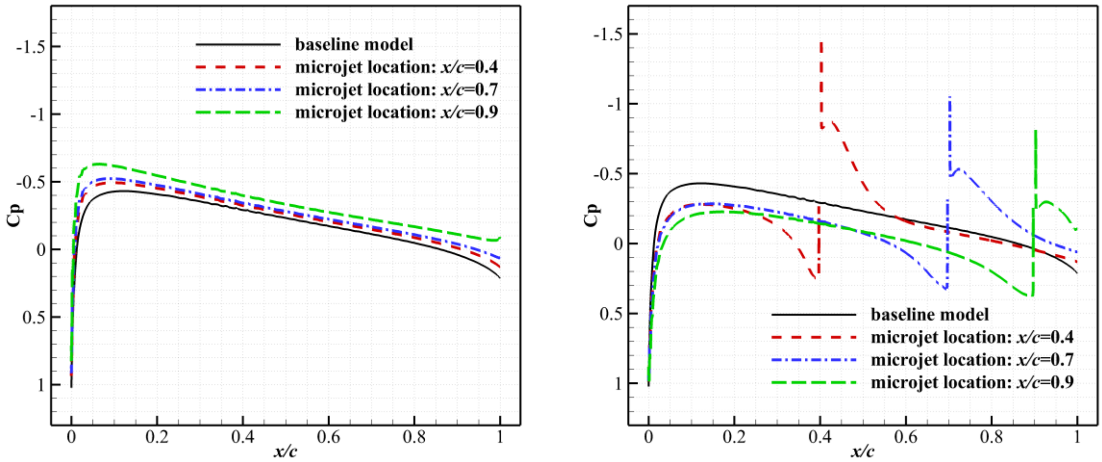

(a) Lower surface (b) Upper surface

Figure 3.26 Comparisons of pressure coefficients between the baseline model and microjet blowing models at M_{∞}= 0.3, α= 0º

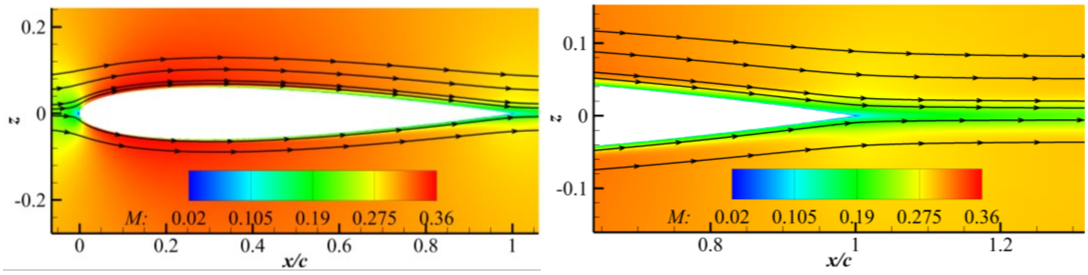

(a) baseline model

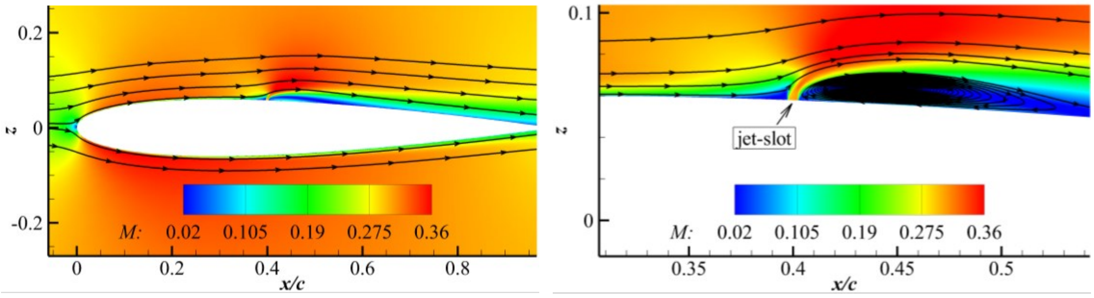

(b) microjet blowing, *x/c*= 0.4

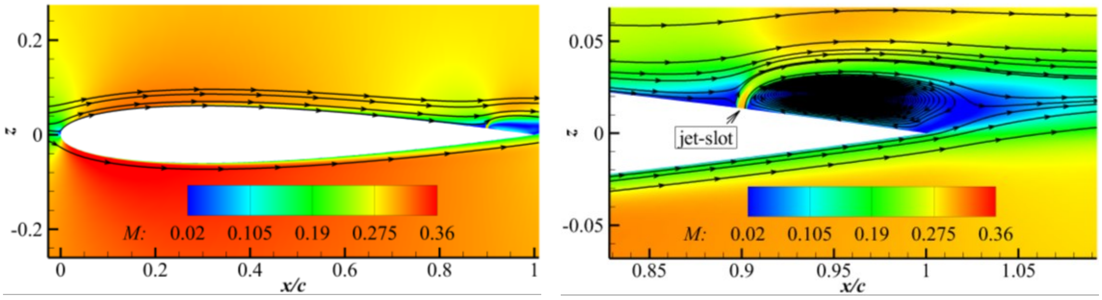

(c) microjet blowing, *x/c*= 0.9

Figure 3.27 Velocity flow fields and streamlines of the baseline model and models with microjet blowing for $M_{\text{jet}}= M_\infty= 0.3$, at $\alpha= 0^\circ$

For transonic range, a freestream Mach number of $M_\infty= 0.7$ is chosen to test the influence of jet-slot location. Because strong shock waves have already appeared at small angles of attack under $M_\infty= 0.7$ for NACA0012 aerofoil, which is adequate to represent the transonic flow characteristics. Figure 3.28 demonstrates the reductions of lift coefficients against microjet blowing locations with $M_{jet}= M_\infty = 0.7$. Like the results under $M_\infty =0.3$, blowing location near the trailing edge has a stronger load control effect, even though this effect becomes less apparent with the increase in angles of attack.

At α= 0º, the reduction in lift coefficient of ΔC_L= -0.45 is obtained due to the microjet blowing at x/c= 0.95, while it is only ΔC_L= -0.33 for M_{jet}= M_∞ = 0.3. This is much different to the load control capability of CC where the load control effects are much stronger under subsonic range than that in transonic speeds. The detailed comparisons of load control effects between CC and normal microjets blowing will be conducted in the next chapter.

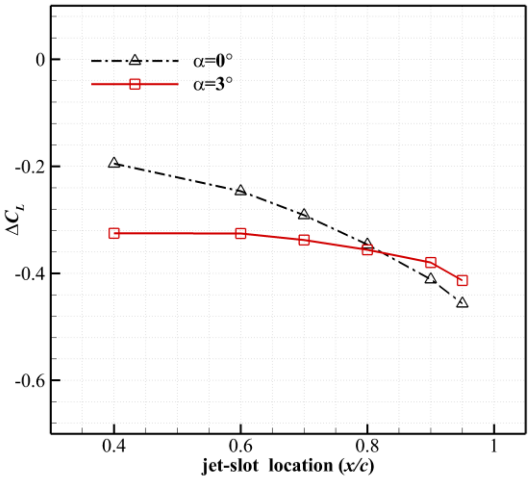

Figure 3.28 Influence of jet-slot location on lift coefficient reduction with M_{jet}= M_∞= 0.7

Comparisons of pressure coefficients between the baseline and blowing models at M_∞= 0.7 are shown in Figure 3.29 and Figure 3.30 for α= 0º and 3º, respectively. For the baseline model, shock wave at around x/c= 0.3 can be noticed in the pressure distribution and the velocity field shown in Figure 3.31 (a). When the microjets are actuated, the high-speed jet flow blocks and decelerates the external flow over the upper surface, resulting in the increase in upper surface pressure coefficients. The effects of the flow deceleration weaken and even eliminate the shock wave for the blowing cases. For the lower surface, it is similar to M_∞= 0.3 that, the separation near the trailing edge entrains external flow upwards, which accelerates the flow resulting in a reduction in the pressure coefficients. The reason why the lift reduction is less sensitive to the blowing locations with the increase in angles of attack is that the lower surface pressure coefficients are less sensitive to the blowing locations which can be noticed in Figure 3.29 (a) and Figure 3.30 (a).

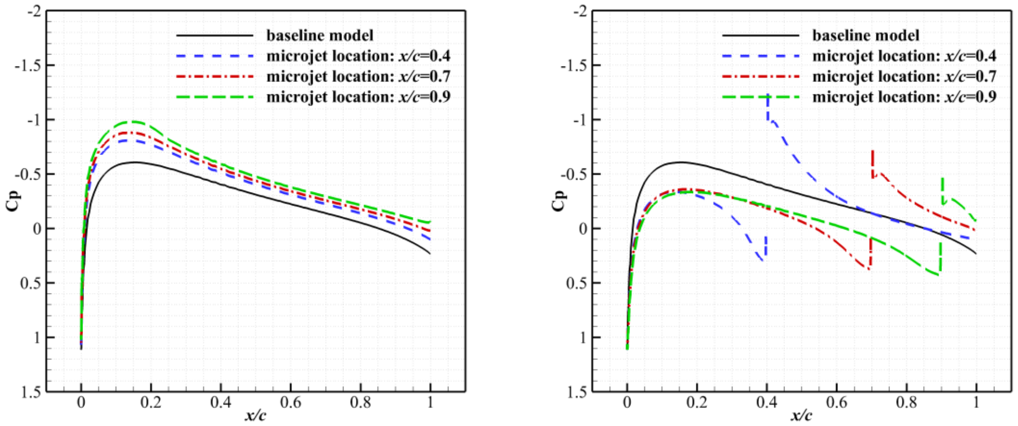

(a) Lower surface (b) Upper surface

Figure 3.29 Comparisons of the pressure coefficients at M_∞= 0.7, α= 0º

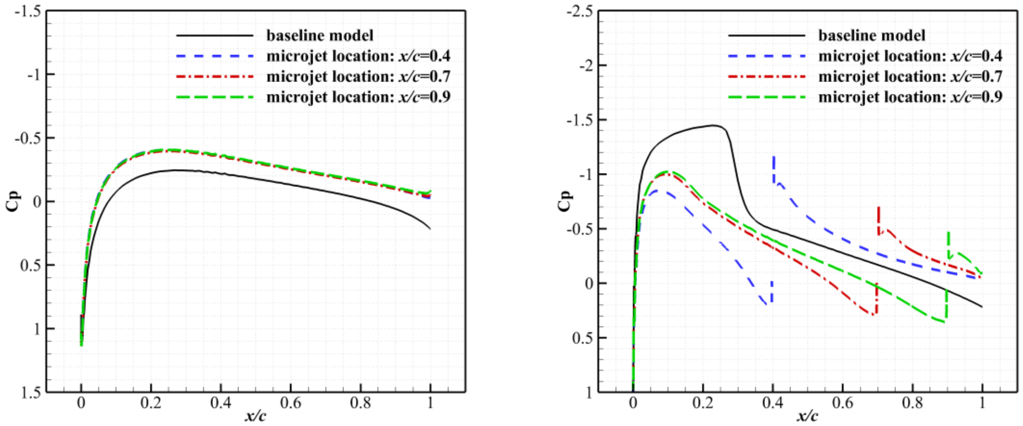

(a) Lower surface (b) Upper surface

Figure 3.30 Comparisons of the pressure coefficients at M_∞= 0.7, α= 3º

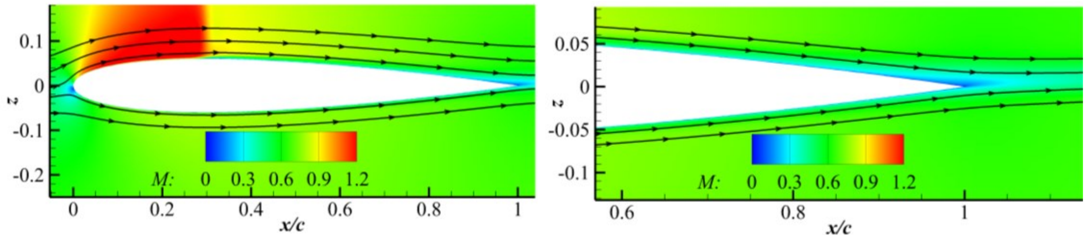

(a) Baseline model

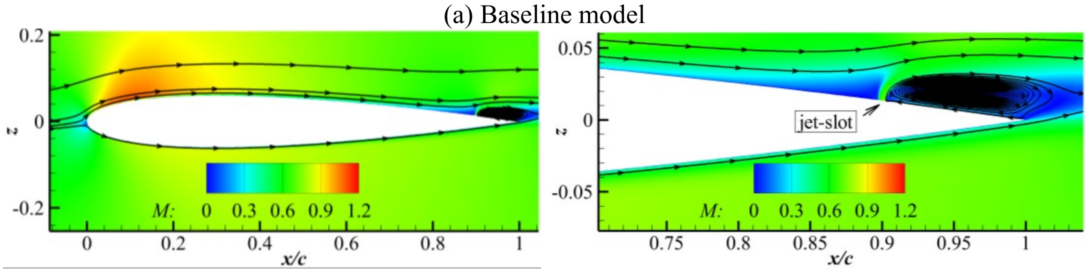

(b) Microjet blowing, *x/c*= 0.9

Figure 3.31 Velocity flow fields and streamlines for M_{jet}= M_∞= 0.7, at α= 3º

3.4.2 Influence of the jet-slot width

To evaluate the influence of chordwise width (h_{jet}) of the jet slot, jet-slot width ranging from 0.2%*c* to 1.0%*c* placed at x/c= 0.95 are compared under the same blowing momentum coefficient. Figure 3.32 gives the results of lift reduction for different jet-slot widths at M_∞= 0.3, α= 0º. Two blowing momentum coefficients of C_μ= 0.004 and 0.009 are used for the comparison. Noticeably, load control effects in terms of lift reduction increase with increasing in jet-slot width, especially when the width increases at small amount from 0.2%*c* to 0.5%*c*. However, this effect tends to be stable with the jet-slot width approaching to 1.0%*c* for both the test cases with C_μ= 0.004 and 0.009. The comparison of the pressure coefficients of models with different jet-slot widths under C_μ= 0.009 is shown in Figure 3.33 (a). It can be seen that the difference of pressure coefficients among models with jet-slot width above 0.5%c is small. The trend of the influence of jet-slot width on lift coefficient for M_∞= 0.7, α= 0º is similar to that of M_∞= 0.3 as shown in Figure 3.33 (b). Undeniably, smaller width of the jet-slot exit will have a smaller influence on the aircraft performance when these microjets are not in working conditions. Because the holes or slots introduced to the aircraft wing surfaces by these microjets will bring discontinuity to the wing surfaces. Table 3.2 presents the jet parameters used in some reference researches about surface jet blowing, where the average value of jet-slot width used in these studies is around 0.5%*c*. Therefore, in the following studies, 0.5*c*% is chosen for the width and x/c= 0.95 is chosen for the jet location.

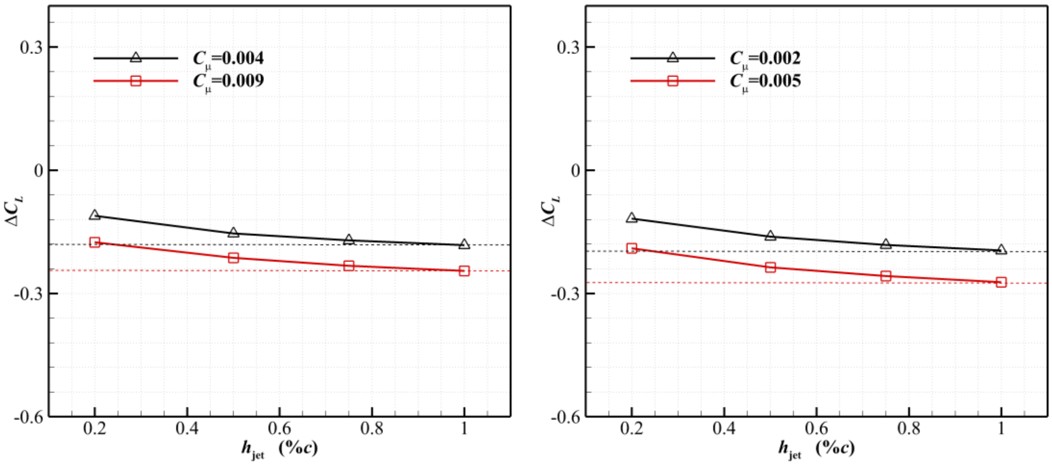

(a) $M_\infty = 0.3$ (b) $M_\infty = 0.7$

Figure 3.32 Influence of jet-slot width on lift coefficient at α= 0º

Table 3.2 Jet parameters in reference studies

Reference	Jet-slot width	Jet location (x/c)
Al-Battal *et al.* [4]	0.20%*c*	0.08-0.95
Eggert, *et al.* [160]	0.29% *c*	0.05
Blaylock, *et al.* [125]	0.50% *c*	0.95
de Vries, *et al.* [17]	0.61% *c*	0.9
Leopold *et al.* [159]	0.67%*c*	0.5

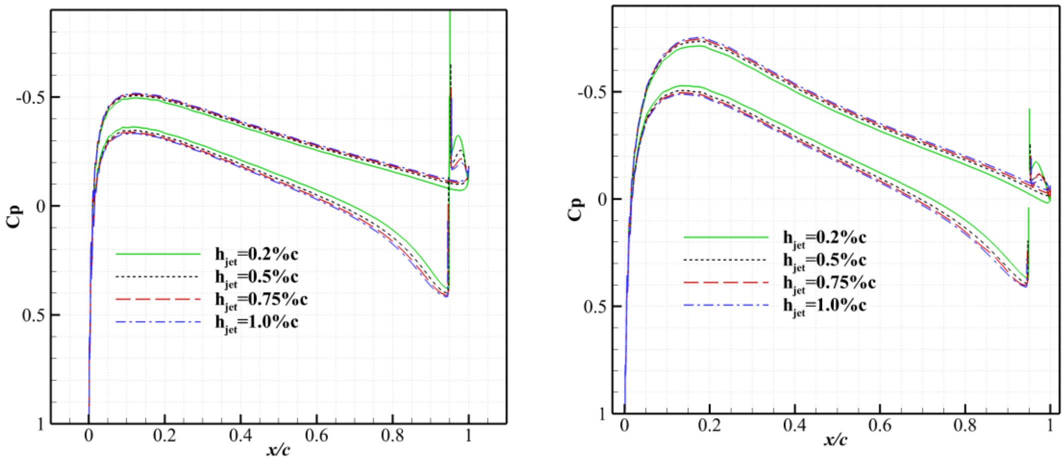

(a) $M_\infty = 0.3$ (C_μ= 0.009) (b) M_∞= 0.7 (C_μ= 0.005)

Figure 3.33 Comparison of pressure coefficients of models with different jet-slot width at α= 0º

3.5 Summary

This chapter contained the description of the numerical methods, the development and validation of the numerical tool for simulations of gust responses, CC and normal microjet blowing. The results can be summarised below:

- The present numerical tool is capable to simulate arbitrary gust load responses accurately and effectively for rigid models, models with motions and models considering aeroelasticity.

- For the CC validation, the RANS solutions have a good agreement with the experimental data in terms of surface pressures and the trends in lift augmentations due to the increase in CC jet blowing momentum coefficients. The load control effects start to decrease when the momentum coefficient reaches to some extent, namely the 'C_μ-stall' phenomenon is also well captured by the present numerical tool.

- The present numerical methods also show good accuracy for the simulation of normal microjet blowing. The results of the influence of microjet-slot location show that it is more effective to place the slot around the trailing edge due to the combined effects of the rapid pressure recovery and the entrainment capability of the separation flow behind the microjet slot. For the influence of jet-slot width ranging from 0.2%*c* to 1.0%*c*, the lift reduction firstly increases and then becomes stable with the increase in jet-slot width under the same blowing momentum coefficient.

Chapter 4

Comparisons of load control capability between circulation control and normal microjet blowing

In Chapter 3, the present solver had been validated for the simulation of CC and normal microjet blowing. To explore the feasibility and effects of gust load alleviation by means of these two methods, this chapter will evaluate and compare the load control mechanisms and capabilities of these two approaches for subsonic and transonic speeds. This is firstly conducted based on the 2-D NACA0012 aerofoil under steady incoming flow conditions (no gust perturbations). The 3-D BAH wing is then modified for further comparisons to evaluate the load control capabilities with spanwise effects.

Gusts are well-known to be disturbances with various frequencies. The performance of the dynamic responses of these fluidic actuators will have significant impacts on the gust load alleviations. To get an insight into load control effects under dynamic CC and normal microjet blowing, this chapter also evaluates the responses of the unsteady actuations of these two methods together with the study on the influence of the actuation frequencies.

4.1 Comparisons of load control capability between normal microjet blowing and circulation control on 2-D NACA0012 aerofoil under steady conditions

Firstly, the NACA0012 aerofoil is modified to include a Coanda surface and a plenum as the CC system. The aerofoil with normal microjet slot is the same as that used in Section 3.4 with a jet-slot width of 0.5*c*% placed at *x/c*= 0.95.

4.1.1 NACA0012 aerofoil with a trailing-edge Coanda surface

In order to include a Coanda surface at the aerofoil trailing edge, the aerofoil is truncated at *x*/*c_orig*= 0.943 (*c_orig* means the chord length of the aerofoil before being truncated) and a semi-circular trailing edge with a radius *r*/*c_orig*= 0.714% is added to the aerofoil. The trailing edge of the modified aerofoil is shown in Figure 4.1. According to Wetzel *et al*. [156], the parameters of Coanda surface especially the ratio of the slot-exit height to the Coanda surface radius have a substantial influence on the circulation control effect. As this study does not focus on the parameter study, the ratio of the slot-exit height to the radius being 1:20 is chosen for this study based on the results by Wetzel *et al*. [156].

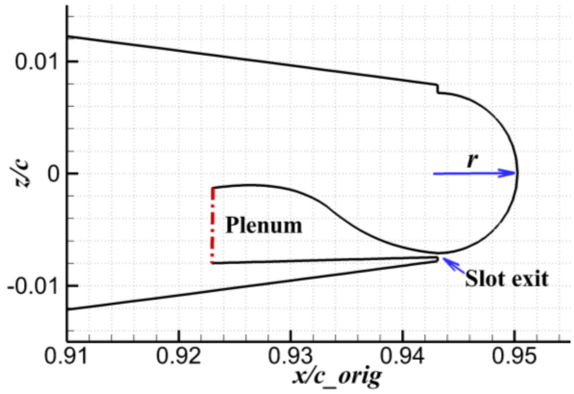

Figure 4.1 The trailing edge of the modified NACA0012 aerofoil

Based on the grid resolution study on the elliptic aerofoil in Section 3.3, a grid refinement study is performed on the NACA0012 aerofoil with CC. The medium grid used in the previous study is used here as the baseline aerofoil section grid that is 221 cells on the aerofoil, 121 cells on the Coanda surface and 149 cells in the wall normal direction as shown in Figure 4.2. Based on this, a coarse mesh with half of the elements and a fine mesh with twice of the elements are generated. During the refinement, the distance of the first grid point away from the wall was kept constant to keep the $y^+ \sim O(1)$. The comparisons of pressure coefficients on the aerofoil surface at M_∞= 0.3, α= 3°, Re_c= 1.0×10^6 and M_∞= 0.7, α= 3°, Re_c= 5.0×10^6 with the blowing momentum coefficients of C_μ= 4.93×10^{-3} and C_μ= 8.58×10^{-4} respectively, are shown in Figure 4.3. Like the grid convergence study in Section 3.2, the influence of these grid resolutions is negligible, and the medium grid resolution is chosen for the following studies.

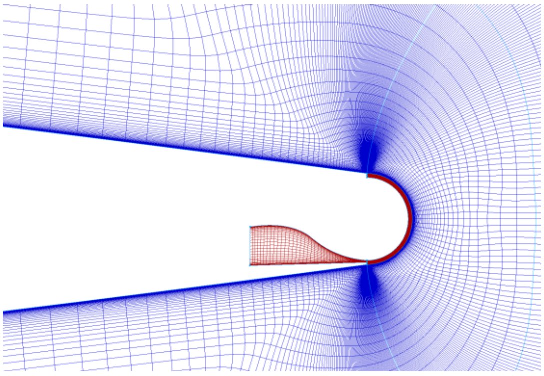

Figure 4.2 Medium mesh around the trailing edge for NACA0012 with Coanda surface

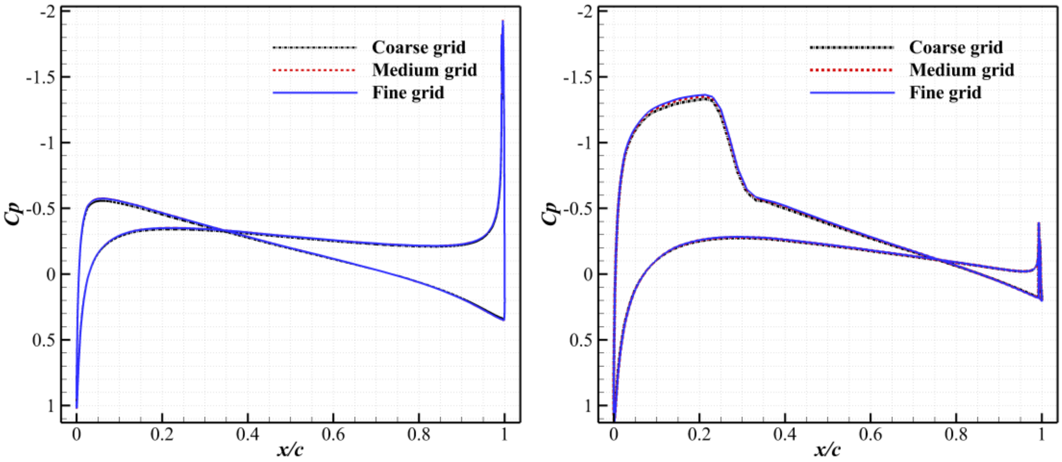

(a) M_∞= 0.3(C_μ=4.93×10^{-3}) (b) M_∞= 0.7(C_μ=8.58×10^{-3})

Figure 4.3 Influence of the grid resolution under M_∞= 0.3 and 0.7, α= 3°

4.1.2 Comparisons of load control capabilities

To get a quantitative understanding of the load control capabilities of CC and normal microjet blowing, the lift reduction effects by these two methods are compared under M_∞= 0.3 and M_∞= 0.7 at α= 3° with a range of blowing momentum coefficients. As the lift coefficient starts to oscillate when the blowing momentum coefficient increases to a certain value for both control methods, the standard deviation is also shown for the case with oscillation in the results. The phenomenon of lift oscillation was also observed by Foster *et al*. [153] in the numerical studies of CC on a supercritical aerofoil in the residual of the steady state solutions and Blaylock *et al*. [125] in the numerical study of normal microjet blowing on NACA0012 aerofoil.

For CC, the lift coefficient reductions due to different momentum coefficients are shown in Figure 4.4 (a). The load control effects are similar to the elliptic CC aerofoil in the previous validation study. CC has a much stronger load control capability under subsonic incoming flow than that of the transonic one. It is noticeable that the maximum reduction in lift coefficient reaches to -1.34 at M_∞= 0.3, whereas this value is only -0.27 at M_∞= 0.7. However, for normal microjet blowing, the load control capability at transonic range is stronger than that at subsonic speed as shown in Figure 4.4 (b).

For the comparison between CC and normal microjet blowing, results presented in Figure 4.5 clearly show that CC has a much stronger load control capability under subsonic range than that of normal microjet blowing. However, it is opposite under transonic range. Due to the early occurrence of 'C_μ-stall' for CC under transonic range, the load control capability of CC is limited. When the momentum coefficient is lower than the 'C_μ-stall' point, CC has a slightly better load control capability than normal microjet blowing. Because of the limitation of 'C_μ-stall', the load control capability declines with the increase in blowing momentum coefficient that is above 'C_μ-stall' point. Normal microjet blowing has better endurance in terms of the range of usable momentum coefficient, thus it can achieve a higher lift reduction at transonic incoming flow.

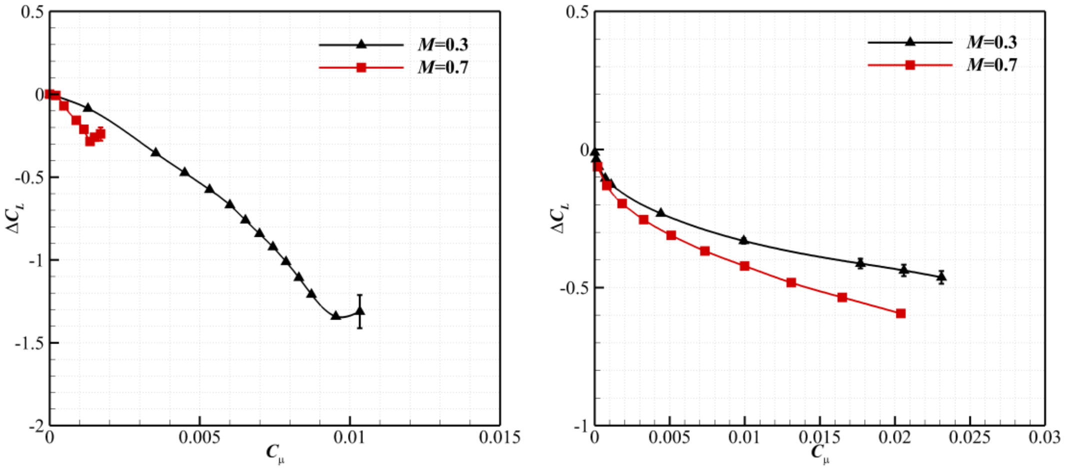

(a) CC (b) normal microjet

Figure 4.4 Load control capability of normal microjet and CC under different Mach numbers

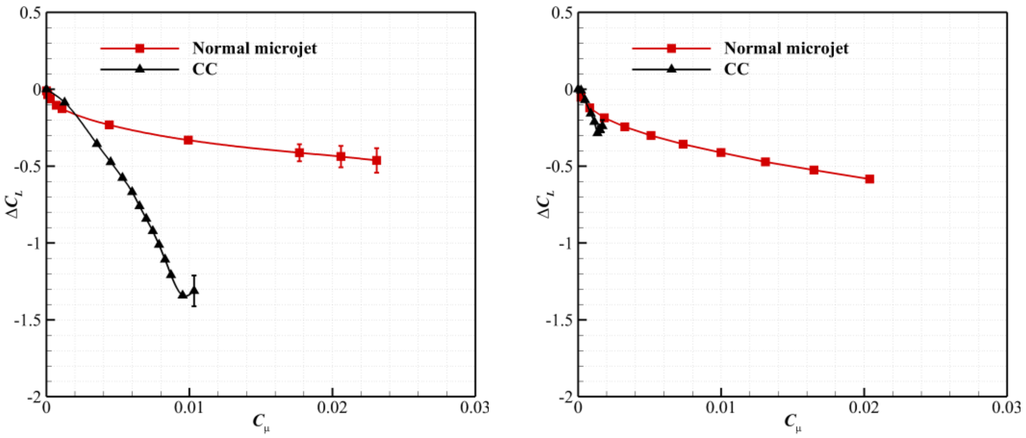

(a) $M_\infty = 0.3$ (b) $M_\infty = 0.7$

Figure 4.5 Comparison of load control capability between normal microjet and CC

It has been indicated in Section 3.3 that, the strong load control capability of CC under subsonic range is the combination results of the strong entrainment of the high-speed CC jet flow and the low-speed external flow around the main aerofoil section. To get an understanding of the influence of CC jets on the flow velocities around the aerofoil, the flow velocity measured 4%*c* above the upper aerofoil surface and 4%*c* beneath the lower aerofoil surface are shown in Figure 4.7. Because of the high-speed jet flow, streamlines from the lower aerofoil surface are entrained upwards obviously as shown in Figure 4.6 for the CC model with $C_\mu = 1.10\times10^{-2}$. It induces the acceleration of external flow near the lower surface as shown in Figure 4.7 (a). Meanwhile, this high-speed jet flow follows the curved Coanda surface up to the upper aerofoil trailing edge, resulting in the front streamlines being hindered and deflected upwards. As a result, it causes a reduction in flow velocity near the upper surface as shown in Figure 4.7 (b). This strong control of the velocity in the flow field around the aerofoil results in significant changes of surface pressures relative to the baseline aerofoil as given in Figure 4.9 (a).

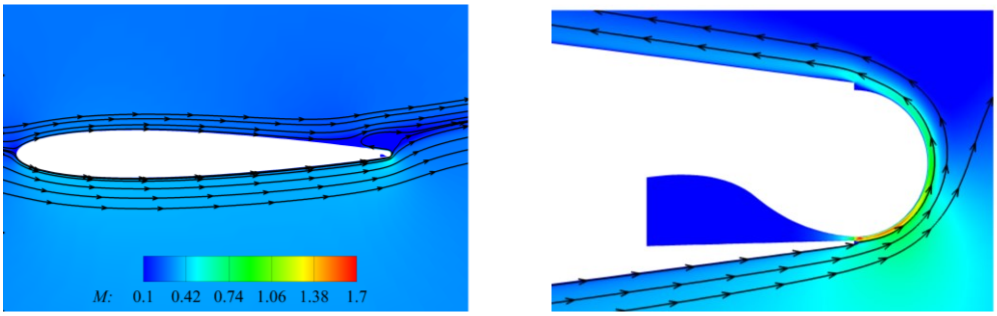

Figure 4.6 Streamlines of the model with $C_\mu = 1.10\times10^{-2}$ at $M_\infty = 0.3$, α= 3°

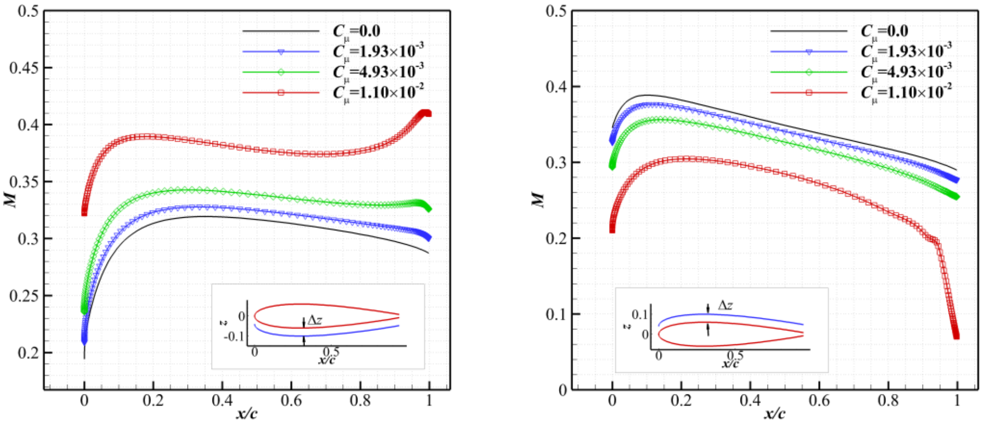

(a) Beneath lower surface (b) Above upper surface

Figure 4.7 Flow velocities along Δ*z*= 4%*c* under M_∞= 0.3, α= 3º among CC models

When the freestream velocity increases, the flow velocity around the aerofoil will increase. This will weaken the entrainment capability of CC jet. To see the changes of external flow velocity due to CC, the flow velocities for M_∞= 0.7 along the same slices as M_∞= 0.3 are shown in Figure 4.8. Compared to the baseline model without CC jet blowing (C_μ= 0.0), the changes of the flow velocity due to CC are small relative to the results of M_∞= 0.3. Also shown is that when the momentum coefficient increases from 0.0 to 2.01×10^{-3}, the flow velocity above the aerofoil decreases with the shock wave moving slightly forwards. This effect is also depicted by the surface pressure coefficient shown in Figure 4.9 (b). However, when the momentum coefficient further increases to 3.19×10^{-3}, the flow velocity does not decrease further but increase back to the value near that of the baseline model due to the detachment of the CC jet flow as shown in Figure 4.10.

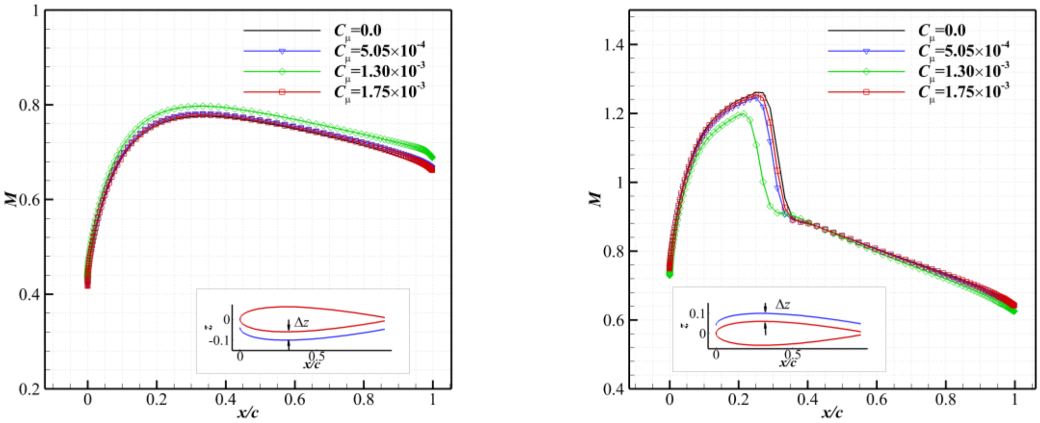

(a) Beneath lower surface (b) Above upper surface

Figure 4.8 Flow velocities along Δz= 4%c under M_∞= 0.7, *α*= 3º among CC models

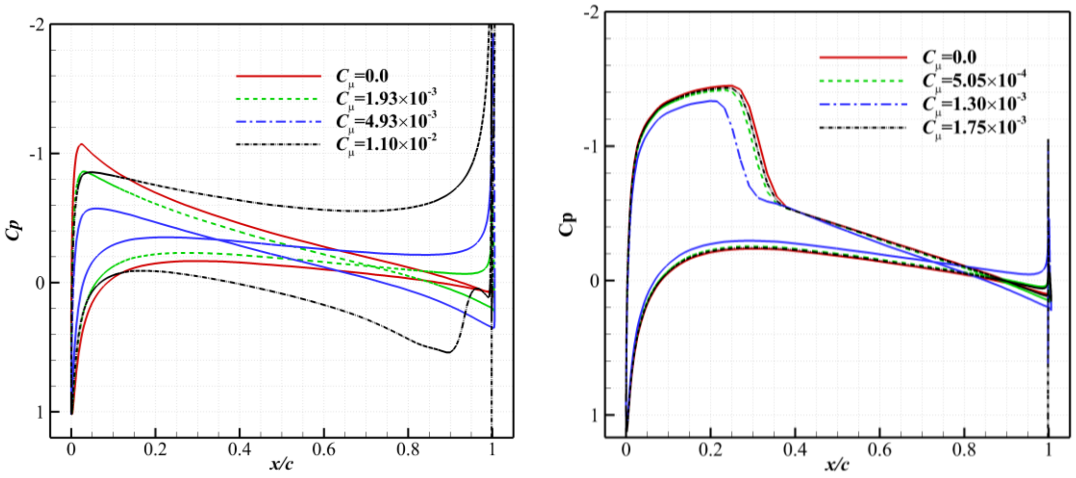

(a) M_∞= 0.3 (b) M_∞= 0.7

Figure 4.9 Pressure coefficient distributions on the CC aerofoil at α= 3º

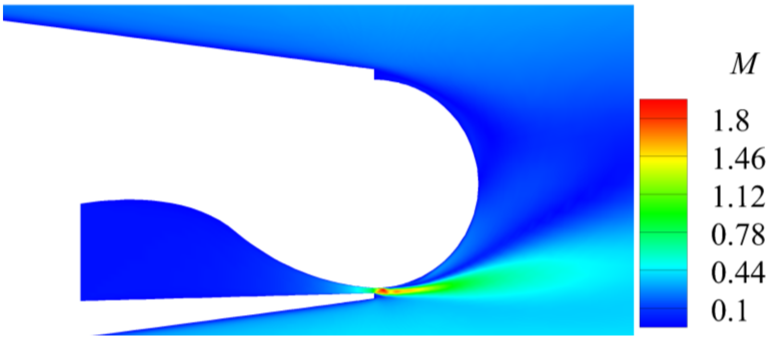

Figure 4.10 Mach number contour of the CC model with C_μ= 3.19×10^{-3} at M_∞= 0.7, α= 3º

The pressure coefficient distributions on the aerofoils with normal microjet blowing compared to the baseline model at M_∞= 0.7, α= 3º is given in Figure 4.11. A significant change in pressure coefficients among models with different blowing momentum coefficients has been observed. Like the effect of CC, normal microjet blowing also weakens the shock strength and pushes the shock wave forward with the increase in blowing momentum coefficient. Noticeably, normal microjet blowing shows a much stronger capability in controlling the pressure coefficients compared to CC under M_∞= 0.7. Because it is noticeable that when momentum coefficient reaches a certain value, the shock wave is eliminated as can be seen from the pressure coefficient distributions of the model with C_μ= 9.65×10^{-3}, due to the blocking effects of the microjet flow.

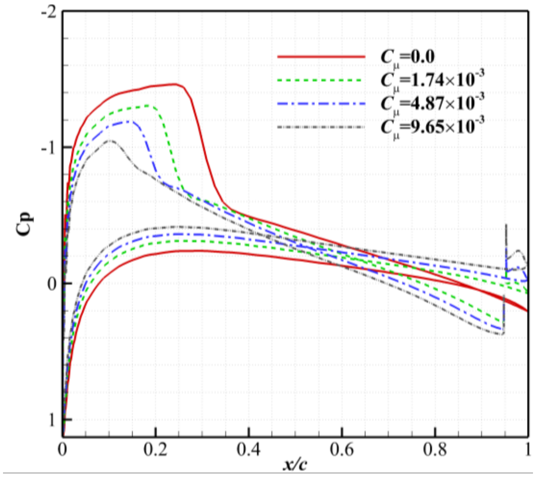

Figure 4.11 Pressure coefficient distributions for normal microjet blowing at M_∞= 0.7, α= 3°

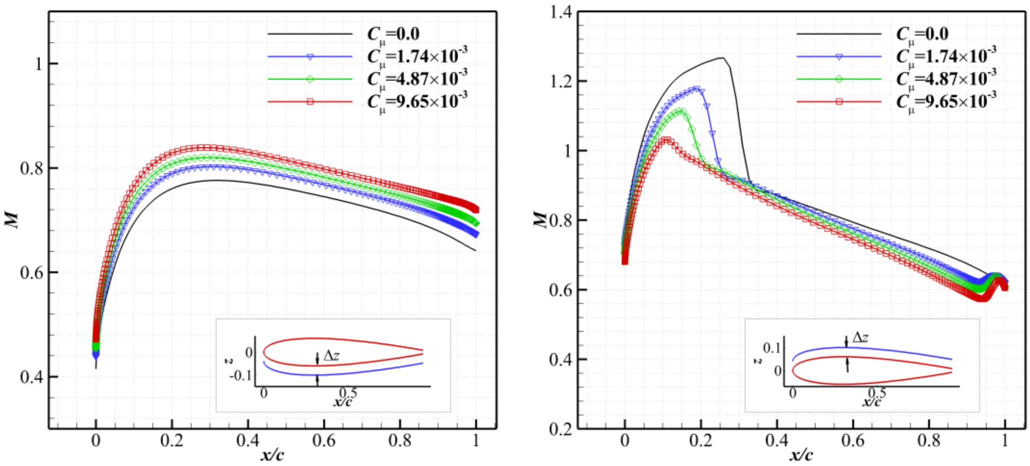

(a) Beneath lower surface (b) Above upper surface

Figure 4.12 Flow velocities along Δz=4%c for normal microjet blowing at M_∞= 0.7, α= 3°

This significant control effect can also be demonstrated by the flow velocities measured 4%*c* above and beneath the aerofoil surfaces given in Figure 4.12 and the Mach number contours and streamlines under different blowing momentum coefficients shown in Figure 4.13. The trend of the flow velocities against the blowing momentum coefficients is consistent to the results of the pressure changes shown in Figure 4.11. The shock wave is weakened and moved forward when the blowing momentum coefficient increases. Apart from showing the evolution of shock strength reduction with the increase in blowing momentum coefficients, the increase of the separation region behind the microjet slot can also be observed in Figure 4.13. Also shown is the flow above the aerofoil being deflected upwards more apparently with the increase in blowing momentum coefficients.

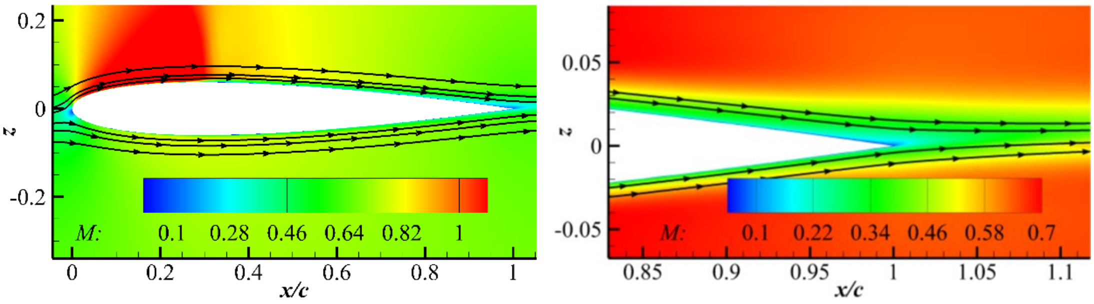

(a) baseline model

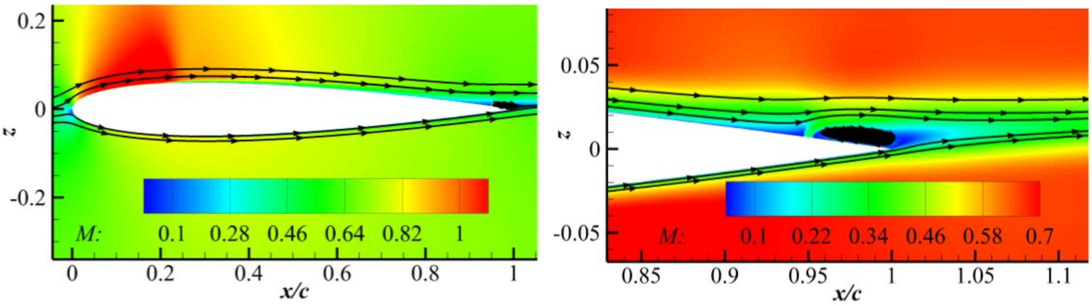

(b) $C_{\mu}= 1.74\times10^{-3}$

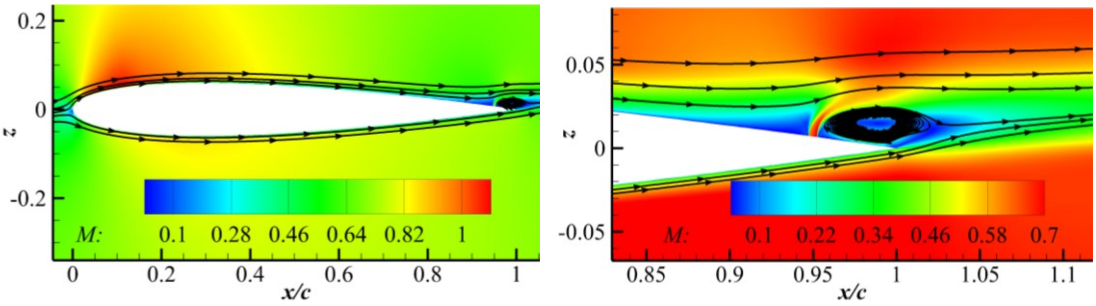

(c) $C_{\mu}= 9.65\times10^{-3}$

Figure 4.13 Evolution of the Mach number contours and streamlines with increase in the normal microjet blowing momentum coefficient at $M_{\infty}= 0.7$, $\alpha= 3^{\circ}$

4.2 Comparisons of load control capability between normal microjet blowing and circulation control on BAH wing under steady conditions

4.2.1 Numerical model setup of the BAH wing with circulation control

For the investigation of CC on the BAH wing, the original NACA65A004 aerofoil section is replaced by NACA0012 aerofoil to allow for CC device installation with reasonable thickness. As displayed in Ref. [67], the position of the aileron deployed on the BAH wing is from η= *y*/*b*= 0.74 (*b* stands for the semi-span length) to the wingtip. Based on this information, Coanda device with the same length in spanwise direction is included on the BAH wing as shown in Figure 4.14. The parameters of the Coanda device are the same as those used in the previous 2-D aerofoil study. The local aerofoil is truncated at *x*/*c_orig*= 0.943 (*c_orig* means the local chord length of the aerofoil before being truncated) and a semi-circular trailing edge with a radius *r*/*c_orig*= 0.714% is added to the trailing edge. The ratio of the slot-exit height to the radius is 1:20.

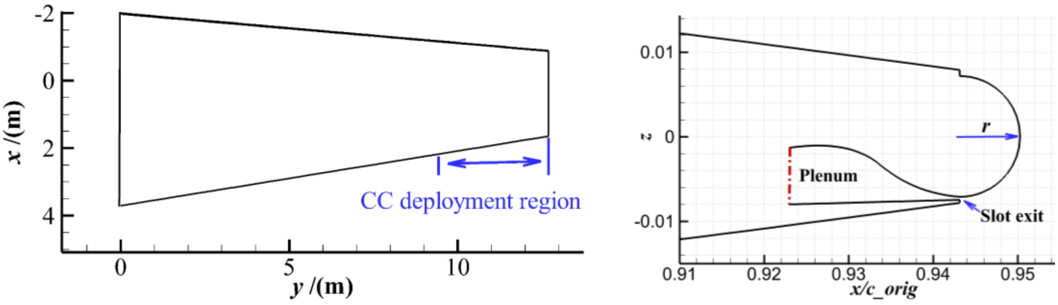

(a) CC location (b) CC device

Figure 4.14 The location of the CC on the BAH wing and the CC device

Based on the previous experience of grid resolutions for the simulations of CC, a baseline grid is generated for simulations of CC on the BAH wing as shown in Figure 4.15. The baseline grid has 221 cells on the wing aerofoil section, 121 cells on the Coanda surface, 149 cells in the wall normal direction and 121 cells over the span. The total grid size is about 6.1×10^6. From this, a coarser mesh and a finer mesh with a total number of cells of approximately 3.5×10^6 and 10.6×10^6, respectively are generated to conduct the grid refinement study. The mesh refinement ratio between the coarse and medium grids in each direction is about 1.2. During the refinement, the distance of the first grid point near the wall was kept constant to keep the $y^+ \sim O(1)$.

Table 4.1 gives the effects of grid resolutions on the aerodynamic coefficients at M_∞= 0.7, α= 3.0° under a blowing momentum coefficient C_μ= 1.57×10^{-4}. The estimation of aerodynamic coefficients with an 'infinite' grid is performed using the Richardson extrapolation by $C_{continuum} = C_{10.6\text{m}} + \frac{(C_{10.6\text{m}} - C_{6.1\text{m}})}{(r^2-1)}$, where r= 1.2. It is noticeable that for the lift and root bending moment coefficients (C_{mx}), the difference between the medium and the fine grids is less than 1.0%. The grid with 6.1×10^6 cells produced the lift coefficient that is within 2.1% of the continuum estimate, and it was less than 3.2% for the root bending moment coefficient. From these results, it was indicated that the medium grid gives reasonably accurate results while with computational cost efficiency.

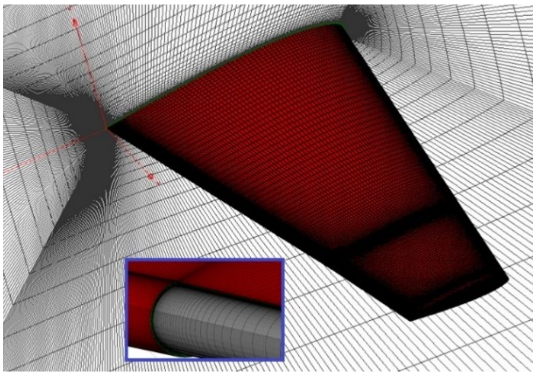

Figure 4.15 Grid topology on the BAH wing and around the Coanda surface

Table 4.1 Grid resolution effects on aerodynamic coefficients of BAH wing with CC (M_∞= 0.7, α= 3.0°, C_μ=1.57×10^{-4})

Grid size	3.5×10^6	6.1×10^6	10.6×10^6	Continuum
C_L	0.2819	0.2836	0.2856	0.2901
C_{mx}	0.1172	0.1190	0.1202	0.1229

4.2.2 Numerical model setup of the BAH wing with normal microjet slot

Being consistent to the spanwise location of CC on the BAH wing, a microjet slot with the same length in spanwise direction is included on the BAH upper wing surface as shown in Figure 4.16. The slot is located on 95% of the local chord length from the local leading edge with a slot width of 0.5% of the local chord length.

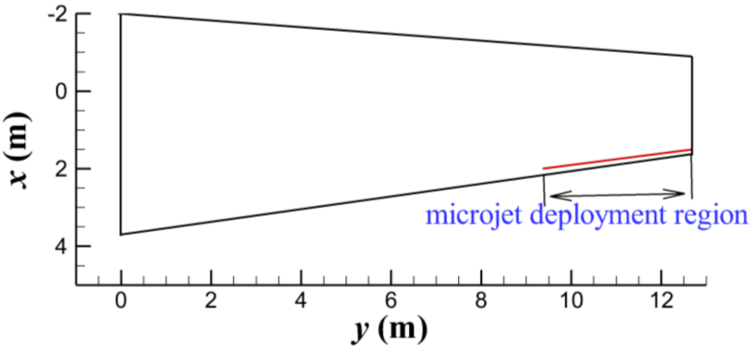

Figure 4.16 The location of the microjet slot on the BAH wing

Following the grid convergence study on the 2-D NACA0012 aerofoil with normal microjet slot in Section3.4, a baseline grid with 321 cells (including 81 on the slot) on the wing aerofoil section, 141 cells in the wall normal direction and 121 cells over the span is generated. Through the 2-D aerofoil grid influence study, it has been demonstrated that the number of cells on the aerofoil section (321 cells) and the wall normal direction (141 cells) is enough to provide reasonably accurate results. Keeping the number of cells on these two directions to be constant, the number of cells along the spanwise direction is evaluated. From the baseline one with 121 cells over the span, a coarser grid with 81 cells and a finer grid with 161 cells are generated.

Table 4.2 gives the effects of grid resolutions on the aerodynamic coefficients at M_∞= 0.7, α= 3.0° under a blowing momentum coefficient C_μ= 1.43×10^{-4}. It is noticeable that for the lift coefficient, the difference between the medium and the fine grids is less than 1.4%, and it is about 1.9% for the root bending moment coefficient. From these results, it was indicated that the medium grid is adequate to provide accurate results.

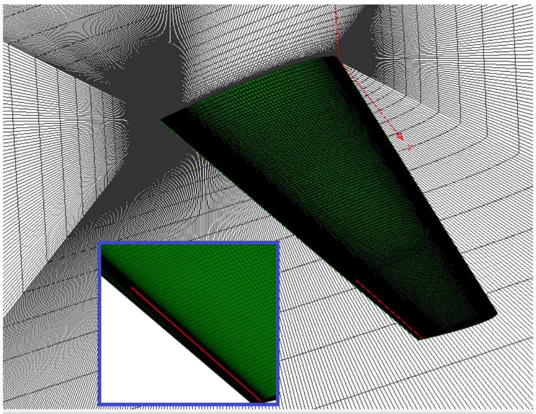

Figure 4.17 Grid topology on the BAH wing with microjet slot

Table 4.2 Grid resolution effects on aerodynamic coefficients of BAH wing with microjet slot (M_∞= 0.7, α= 3.0°, C_μ= 3.58×10^{-4})

Grid size	Coarse grid	Medium grid	Fine grid
C_L	0.2741	0.2755	0.2793
C_{mx}	0.1134	0.1140	0.1162

4.2.3 Load control capability comparisons under steady conditions

To get a quantitative understanding of the load control capability of CC and normal microjet blowing on the modified BAH wing, a series of computations with different momentum coefficients are conducted at M_∞= 0.3, α= 3°, $Re_{c_{ref}} = 4.13\times10^6$, and M_∞= 0.7, α= 3°, $Re_{c_{ref}} = 2.06\times10^7$.

The reductions of lift coefficients due to CC and normal microjet blowing are compared in Figure 4.18 and Figure 4.19. It is consistent with the comparisons on the 2-D aerofoil that CC performs much better under subsonic range, while normal microjet blowing under transonic speed.

Figure 4.20 shows the Mach number contours on the slices of η= 0.4 and 0.87, and the pressure coefficient distributions on the wing surface under C_μ= 8.1×10^{-4} for CC and C_μ=1.8×10^{-3} for normal microjet blowing. For the case with CC, compared to the streamlines shown at η= 0.4 where there is no CC deployment, the streamlines from the lower wing surface are entrained significantly upwards for the slice of η= 0.87 due to the high-speed CC jet flow. Due to the 'bend-up' of the streamlines, the flow near the upper trailing edge is hindered, resulting in the increase of the surface pressure around the upper trailing edge as shown around the wing-tip region coloured in red. For the case with normal microjet blowing, a significant increase in pressure coefficient in the region before the microjet slot can also be noticed because of the blockage of the high-speed microjet flow as mentioned previously.

From the comparison of the surface pressure distributions on the models with CC and normal microjet blowing, it can be seen that even though the physical mechanisms of CC and normal microjet blowing are different, the outcomes of their load control effects are similar. That is to increase pressures on the upper surface of the wing and reduce the pressure on the lower surface.

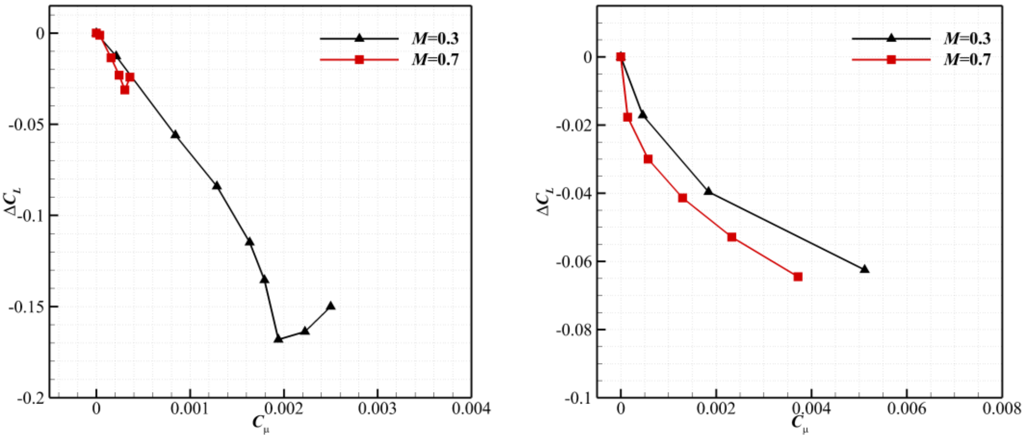

(a) CC (b) normal microjet

Figure 4.18 Load control capability of normal microjet and CC under different Mach numbers

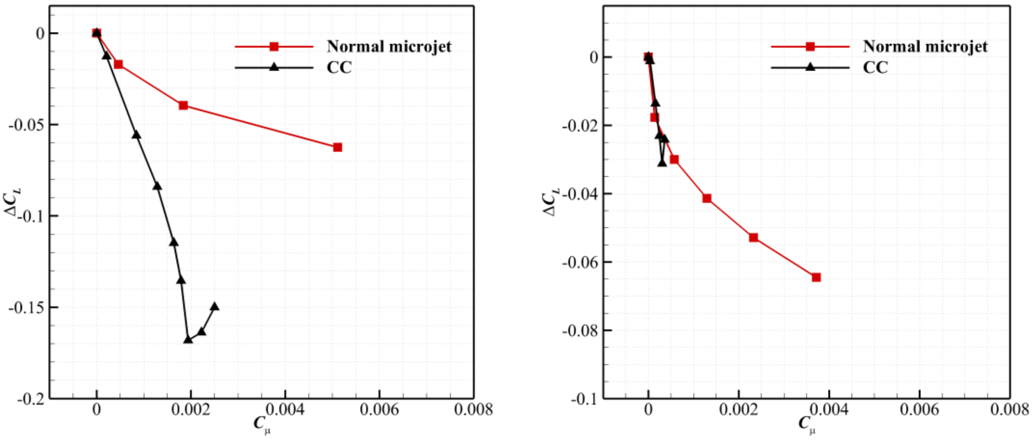

(a) M_∞ =0.3 (b) M_∞ =0.7

Figure 4.19 Comparison of load control capability between normal microjet and CC

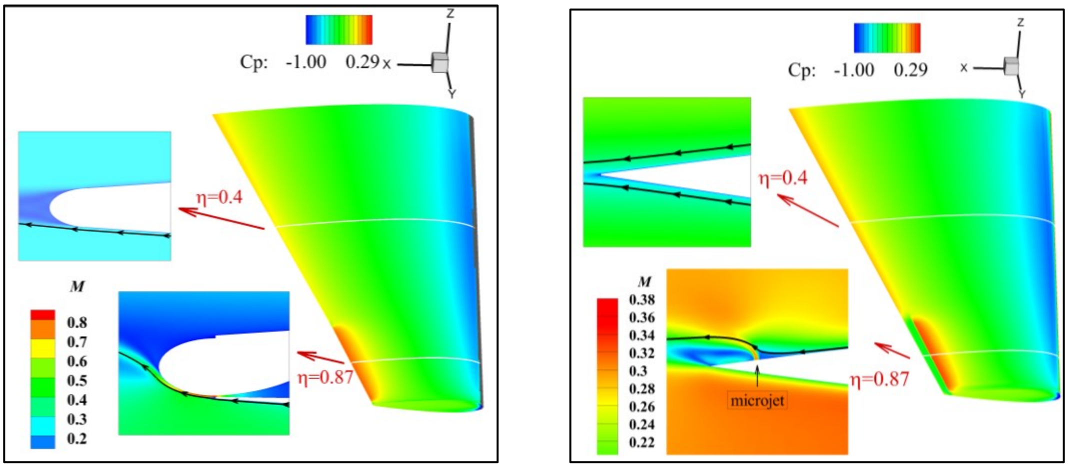

(a) CC (C_μ= 8.1×10^{-4}) (b) normal microjet blowing(C_μ=1.84×10^{-3})

Figure 4.20 Flow condition of typical sections and surface pressure distribution (M_∞= 0.3)

Since CC and normal microjet is only deployed on a part of the span around the wing tip, it is worth to evaluate the influence of CC and normal microjet blowing on the whole span load. To do this, the spanwise load distributions ($C_{L\ local}$ $*c/c_{ref}$) of the blowing cases are compared with the baseline model as shown in Figure 4.21 for M_∞= 0.3 and Figure 4.22 for M_∞= 0.7. For both cases with CC and normal microjet blowing, a more significant load control effect can be noticed around CC and normal microjet deployment region (η= 0.74 to 1.0). Also shown is that apart from this region, these two blowing methods also have control effects on the spanwise loads towards the wing root where there is no jet blowing placement, even though it is not so significant compared with the deployed region. It is noticeable that for the case of CC with C_μ= 1.83×10^{-3} at M_∞= 0.3, the maximum local load reduction is about -0.32 at η= 0.87, corresponding to the local lift coefficient reduction of about -0.46 as shown in Figure 4.23. This indicates the strong load control capability of CC under subsonic range.

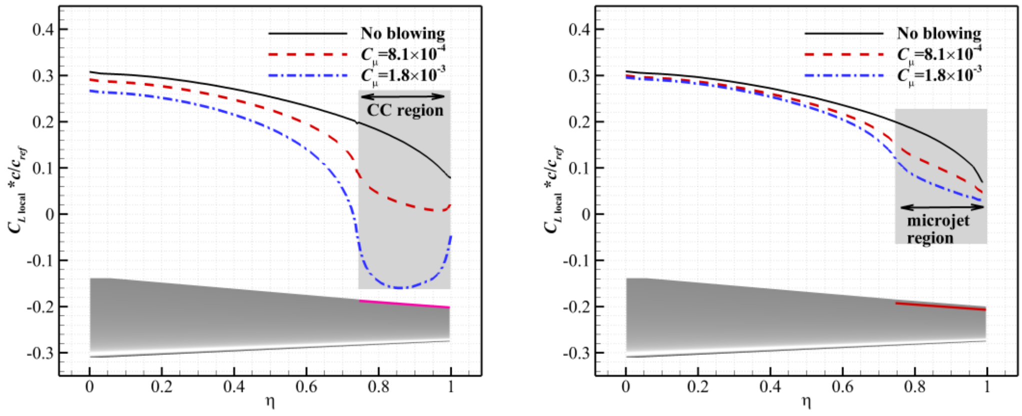

(a) CC (b) normal microjet blowing

Figure 4.21 Spanwise load distribution (M_∞= 0.3, α= 3º)

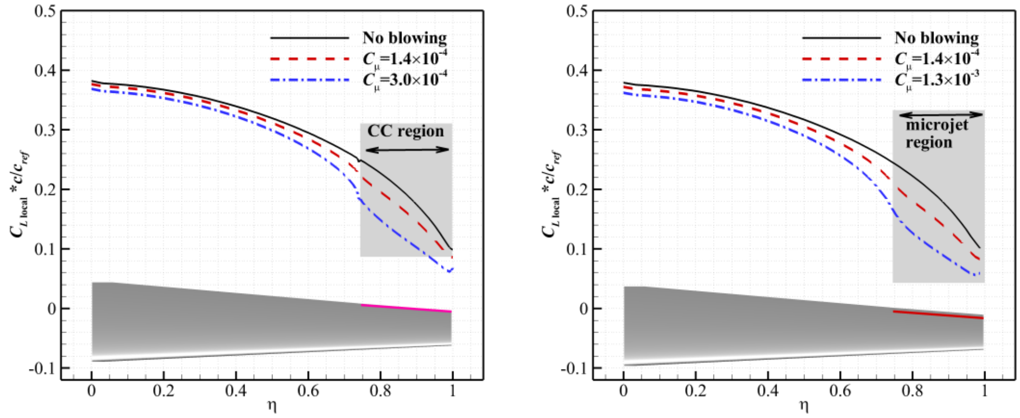

(a) CC (b) normal microjet blowing

Figure 4.22 Spanwise load (M_∞= 0.7, α= 3º)

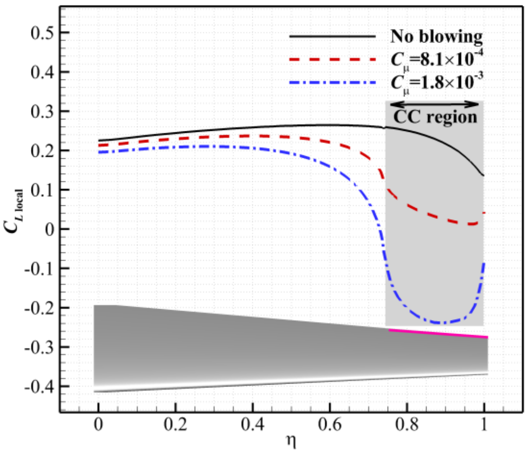

Figure 4.23 Spanwise local lift coefficient distribution due to CC (M_∞= 0.3, α= 3º)

4.3 Unsteady actuation of circulation control and normal microjet blowing

By far, the load control effects are all evaluated with constant blowing momentum coefficients. For an aircraft to successfully use a CC or normal microjet system, the performance of these methods under dynamic actuations is also an important requirement. It is especially crucial for high-frequency gust alleviations. This section evaluates the dynamic responses of CC and normal microjet blowing under transient and periodic actuations.

4.3.1 Transient actuation

To obtain an appropriate time step for the simulation of unsteady CC and normal microjet blowing, the response of the lift coefficient to transient actuation of these two methods is studied under M_∞= 0.3 and 0.7, α= 3° based on the BAH wing. Initially, the model is at a convergent steady flow and then the CC jet or the normal microjet is activated at s= 0 to a maximum coefficient of C_μ= 1.28×10^{-3} and C_μ= 2.9×10^{-4} under M_∞= 0.3 and 0.7 respectively. Non-dimensional time step Δs from 7×10^{-4} to 7×10^{-3} is evaluated as shown in Figure 4.24 and Figure 4.25.

The results demonstrate that the difference of the lift responses among these three different time steps is negligible, especially between Δs= 7×10^{-4} and 1.4×10^{-3}. Δs= 1.4×10^{-3} is chosen for the following studies. Under different time steps, the lift coefficients all reach to the same steady-state final value generally at around s= 7 for M_∞= 0.3 and s= 10 for M_∞= 0.7 after the activation of CC jet and normal microjet. Also shown in the results is that sharp decrease of the lift coefficient due to the blowing for both CC jet and normal microjet blowing happens at the first few non-dimensional time periods. This indicates that both CC jet and normal microjet blowing have a fast response characteristic. More than 50% of the total change in lift coefficient has been obtained within s= 1 as shown in the results. This is consistent with the findings by de Vries *et al.* [17] who conducted experiments and simulations using surface microjet blowing for active aerodynamic load controls on the NACA0018 aerofoil at M_∞= 0.176.

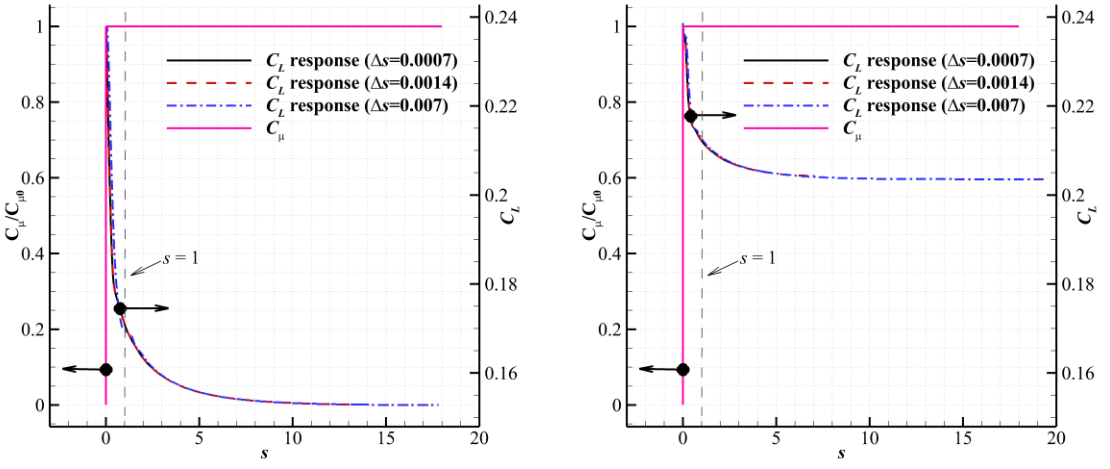

(a) CC

(b) normal microjet blowing

Figure 4.24 Influence of the time steps (M_∞= 0.3, α= 3°, C_μ= 1.28×10^{-3})

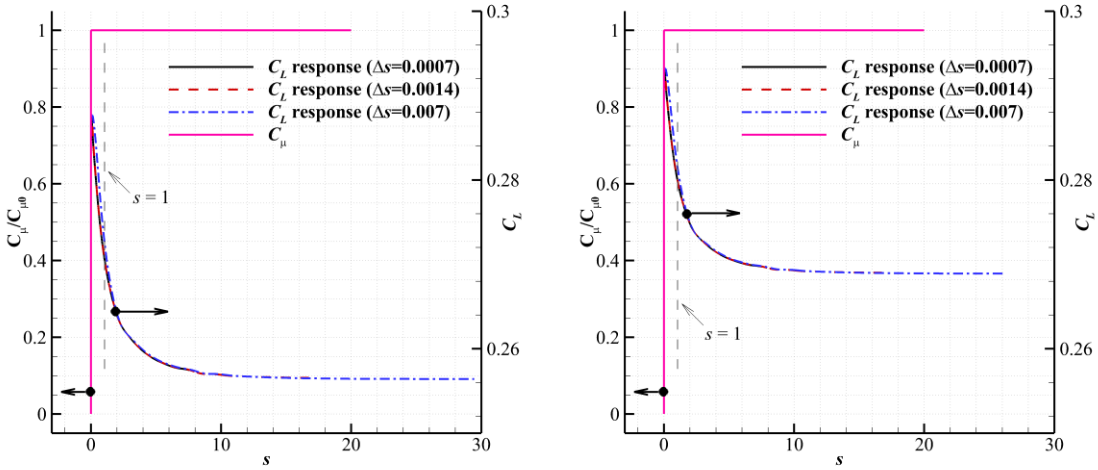

(a) CC (b) normal microjet blowing

Figure 4.25 Influence of the time steps (M_∞= 0.7, α= 3°, C_μ= 2.9×10^{-4})

4.3.2 Periodic actuation

To understand the behaviour of the lift responses under dynamic actuation of CC and normal microjet blowing, the periodic actuation with the following expression in Eq. (4-1) is studied under M_∞= 0.3 and 0.7, α= 3° on the BAH wing.

$$C_\mu = C_{\mu 0} \cdot |\sin(2\pi f \cdot s)| \tag{4-1}$$

The reduced frequency is $k = \frac{\pi f \bar{c}}{U_\infty}$. For a typical gust length which is $12.5\bar{c}$ defined by EASA CS-25 [2], the reduced frequency is about 0.25. Here, three different reduced frequencies, $k = 0.125, 0.25, 0.5$ are used to carry out the evaluations of the influences from actuation frequencies. The maximum momentum coefficient $C_{\mu 0}$ is 1.28×10^{-3} and 2.9×10^{-4} for M_∞= 0.3 and M_∞= 0.7, respectively.

The results reflected in the hysteresis loops of the lift changes as a function of the blowing momentum coefficients are shown in Figure 4.26 and Figure 4.27. All loops are clockwise. From the results, the following information can be noticed:

- In general, the results show similar load control effects in terms of lift responses under dynamic actuations for CC and normal microjet blowing. The hysteresis loops as a whole start and end with negative slopes indicating effective increasing load control ability with the increasing blowing momentum coefficients.

- At M_∞= 0.3, for both CC and normal microjet blowing, the magnitudes of the slopes decrease slightly with the increasing reduced frequency. This indicates the reduction of load control effects with increasing frequency of unsteady CC and normal microjet blowing.

- At M_∞= 0.7, the slops are also negative for these three different reduced frequencies and the magnitudes of the slops also decrease with the increase in reduced frequency. The difference to M_∞= 0.3 is the more apparent decreased amplitude and increased phase lag with the increase in reduced frequency. This characteristic indicates more significant decreasing load control effects of these two approaches with the increase in the actuation frequency under transonic incoming flow relative to the subsonic speed.
- For CC, the hysteresis loops start with a small positive slope. This is because the momentum coefficient starts from zero, thus the CC-jet flow velocity also starts from zero. Initially, when the momentum coefficient is too small, the CC-jet flow velocity is too small to attach to the Coanda surface.

- As the typical gust frequency defined by EASA CS-25 is k = 0.25, the reduced frequency range (from 0.125 to 0.5) tested here demonstrates that both CC and normal microjet blowing are capable for load control with the dynamic actuations. It is expected that both approaches are capable for gust load alleviation of gusts with these frequency range, which will be demonstrated in the following chapter.

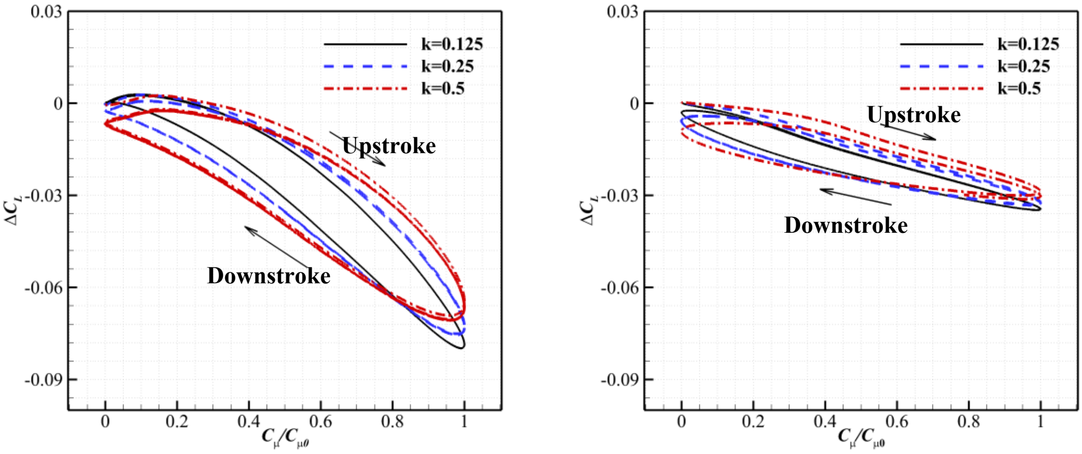

(a) CC

(b) normal microjet blowing

Figure 4.26 Lift response with dynamic actuation of CC (M_∞= 0.3, α= 3°, $C_{\mu 0}$= 1.28×10^{-3})

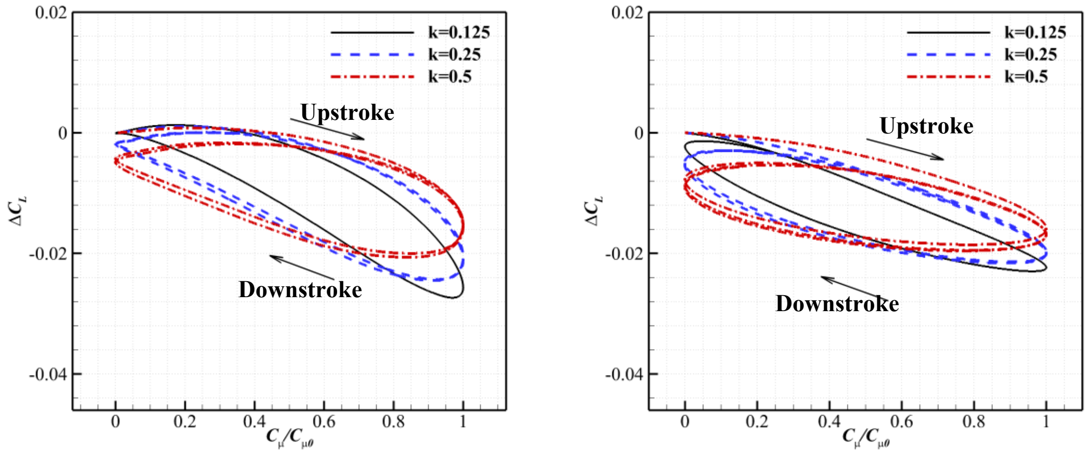

(a) CC

(b) normal microjet blowing

Figure 4.27 Lift response with dynamic actuation of CC (M_∞= 0.7, α= 3°, $C_{\mu 0}$= 2.9×10^{-4})

Figure 4.28 presents the time-dependent changes in normalized lift coefficient as a function of the normalised non-dimensional time s/T (where, T is the time of one period of actuation) at M_∞= 0.3 and M_∞= 0.7 under k= 0.25. The lift coefficient changes of ΔC_L are normalized by the respective maximum changes in lift coefficient due to CC and normal microjet blowing. s/T = 0.5 and 1.0 correspond to the time where the blowing momentum coefficient is at its maximum value and minimum value respectively. As shown in the results, the peaks in (ΔC_L/ $\Delta C_{L\,max}$) due to CC and normal microjet blowing occur at the same time for both M_∞= 0.3 and M_∞= 0.7. The valleys in (ΔC_L/ $\Delta C_{L\,max}$) due to CC and normal microjet blowing occur also at the similar time. At M_∞= 0.3, the peaks in (ΔC_L/ $\Delta C_{L\,max}$) do not occur at s/T= 0.5 when the blowing momentum coefficient peaks but shift afterwards with $\Delta s/T$= 0.035. This indicates CC and normal microjet blowing have a close time delay in load control. At M_∞= 0.7, the peaks in (ΔC_L/ $\Delta C_{L\,max}$) shift afterwards further with $\Delta s/T$= 0.1, indicating the increased time delay with the increase in incoming flow velocity.

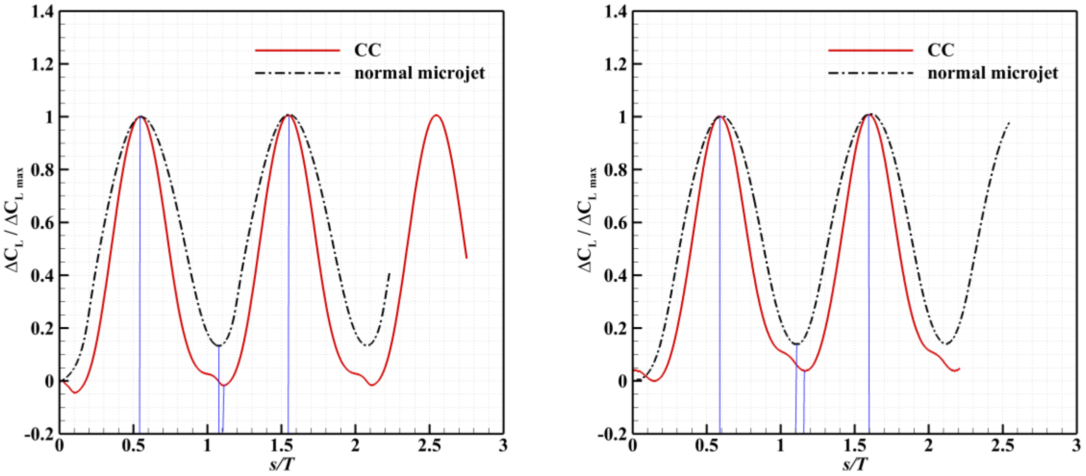

(a) M_∞= 0.3 (b) M_∞= 0.7

Figure 4.28 Periodic blowing actuation time variant lift response under k= 0.25

4.4 Summary

This chapter compared the load control effects between CC and normal microjet blowing. Firstly, the results with constant blowing momentum coefficients showed the difference in flow control mechanisms and in load control capabilities between CC and normal microjet blowing, while the unsteady actuations demonstrated the dynamic load control characteristics. These results can be summarised as follows:

- For CC deployed under the lower wing surface, it uses the entrainment by the high-speed jet flow following the Coanda surface to accelerate the external flow streamlines under the lower surface. Therefore, if the external flow velocity is low, for example, the freestream flow is subsonic, the capability of CC entrainment will be strong. However, if the incoming flow is transonic, the entrainment capability will be limited as the external flow velocity is already high relative to the high-speed jet flow. Consequently, the load control capability will be limited. That is why CC has a much stronger load control capability under subsonic incoming flow than that of transonic speeds.

- For normal microjet blowing placed on the aerofoil or wing upper surface, the high-speed jet flow presents itself as a blockage for the flow ahead the jet slot, thus decelerates the flow and increases the pressure coefficients on the upper surface. If the external flow velocity is high, the blockage effects will significantly decelerate the external flow ahead the blowing location, thus has a stronger load control capability under transonic range compared to that at subsonic speed. Behind the microjets, the pressure recovers rapidly due to the strong separation region formed behind the jet slot. Therefore, it is more effective when jet slots are placed around the trailing edge for the normal microjet blowing.

- Due to the early occurrence of 'C_μ-stall' at transonic range, the load control capability of CC declines with the increase in blowing momentum coefficient above 'C_μ -stall'. Normal microjet blowing has better endurance in terms of the range of usable momentum coefficient. Therefore, it can achieve higher lift reduction using a larger blowing momentum coefficient compared to CC under transonic range.

- Despite of the difference in load control mechanisms and load control effects under different incoming flows for CC and normal microjet blowing, their load control outcomes are similar. That is to increase the pressure on the wing or aerofoil upper surface and decrease the pressure on the lower surface.

- For CC and normal microjet deployed only on a part of the span around the wing tip, apart from significant load control effects being noticed around the jet deployment region, load reduction has also been obtained on the span region where there is no jet deployment towards the wing root.

- In general, the responses of CC and normal microjet blowing under transient and dynamic actuation are similar with two main characteristics: the first is that more than 50% of the total change in load control can be obtained within s= 1, indicating the fast response characteristic; the second is that with the increase in actuation frequency, the load control effects decrease.

- The results of periodic actuation also demonstrated that both CC and normal microjet blowing are capable for load control under dynamic actuations with the reduced frequency ranging from 0.125 to 0.5 tested in this study with practical importance, as the typical gust reduced frequency is 0.25.

Chapter 5

Aerofoil and BAH wing gust load alleviation

In this chapter, the feasibility and effects of gust load alleviation by means of CC and normal microjet blowing are investigated, firstly on the 2-D NACA0012 aerofoil and then on the BAH wing. Comprehensive studies of gust load alleviation effects by CC are firstly conducted via steady blowing, unsteady blowing, and designed adaptive blowing on the 2-D NACA0012 aerofoil for subsonic and transonic incoming flows. The insights into the feasibility and effects of gust load alleviation by CC are obtained. This is followed by tests and comparisons of gust load alleviation effects by normal microjet blowing.

5.1 Aerofoil gust load alleviation

5.1.1 Case studies at M_∞= 0.3 by circulation control

5.1.1.1 Gust load alleviation effects of circulation control under a step change in the angle of attack

Initially, gust load alleviation effects are tested by a step change in the angle of attack $\Delta\alpha = 4.6°$ at the cruise state of M_∞= 0.3, α= 1°, Re_c= 1.0×10^6. Three different momentum coefficients which are switched on instantaneously at s= 0 are applied to the test and the gust load alleviation characteristics are compared to the gust response of the baseline model without CC as shown in Figure 5.1 (a). It is clear that CC has significant effects on gust load alleviation. With the increase of momentum coefficients, the gust load is further controlled. To be specific, the amplitudes of the lift coefficients are reduced by 25%, 54% and 78% compared to the baseline model after s= 10 with C_μ= 0.0015, 0.0028 and 0.004 respectively. Interestingly, with C_μ= 0.004, the lift coefficient is in the similar value with that of the steady state after s= 1 when the non-circulatory lift decay. That is to say, with a certain amount of momentum coefficient, CC can completely counteract the gust load. Figure 5.1 (b) shows the time history of the reduction in lift coefficient relative to the baseline model. The numbers in percentage in Figure 5.1 (b) mean the ratio of lift coefficient reduction at the current non-dimensional time s to that of the total lift coefficient reduction at $s\to\infty$, that is $\frac{(\Delta C_L)_s}{(\Delta C_L)_{s\to\infty}}$. From the results, we can see that more than 50% of the total change in lift coefficient can be obtained within the non-dimensional time $s = \frac{U_\infty t}{c} = 1$. This result is consistent with the previous findings on the unsteady actuations in Section 4.3. As the freestream speed is U_∞= 102 m/s, the non-dimensional time s= 1 refers to the real time t= 0.0098 s and frequency f= 102 Hz. Compared to current gust load alleviation techniques using conventional flaps which exhibit a response frequency of approximately 6 Hz proposed by Al-Battal *et al.* [3], gust load alleviation by means of CC has a faster frequency response characteristic.

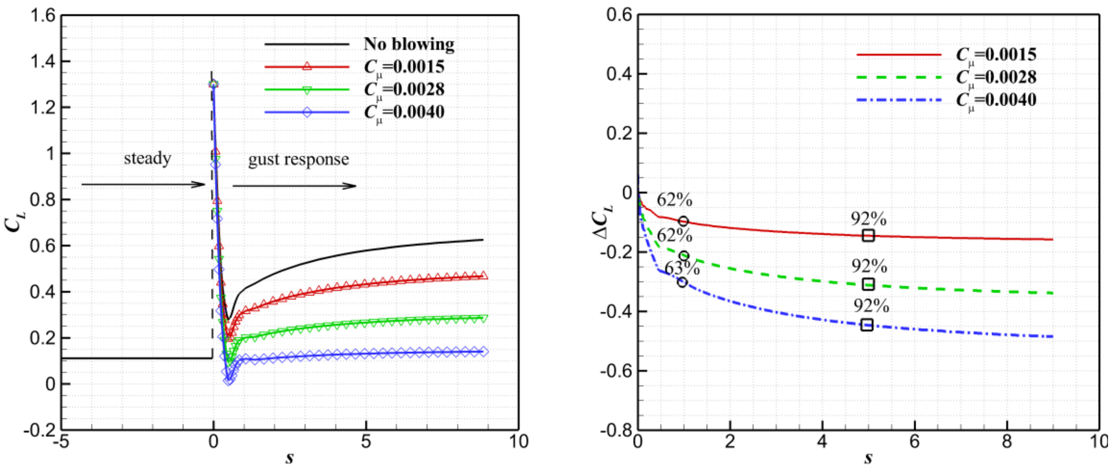

(a) total lift coefficient responses

(b) relative lift coefficient reduction to the baseline model

Figure 5.1 Gust alleviation characteristic to a step change in angle of attack

The streamlines of the baseline model and the model with C_μ= 0.004 at s= 5 are shown in Figure 5.2 and Figure 5.3. A significant difference of the streamlines exists in the rear region of the aerofoil for these two models. The streamlines from the upper and lower surfaces of the baseline model are almost symmetric about the aerofoil centreline at the trailing edge. However, due to the high-speed jet flow, streamlines are entrained upwards obviously at the trailing edge of the model with CC, resulting in the streamlines from the upper surface being deflected upwards. With the increase in the momentum coefficient, the streamlines around the lower trailing-edge surface are entrained more upwards as shown in Figure 5.4, causing an increase in flow velocity near the lower surface, but a decrease near the upper surface. This difference in flow velocity near the aerofoil surface makes a significant change in pressure coefficients on the aerofoil as shown in Figure 5.5. In general, with the increase in momentum coefficients, the pressure coefficients on the upper surface increase, but decrease on the lower surface, resulting in a total lift reduction. This is consistent to the load control mechanism of CC under steady incoming flows demonstrated in Section 4.1.

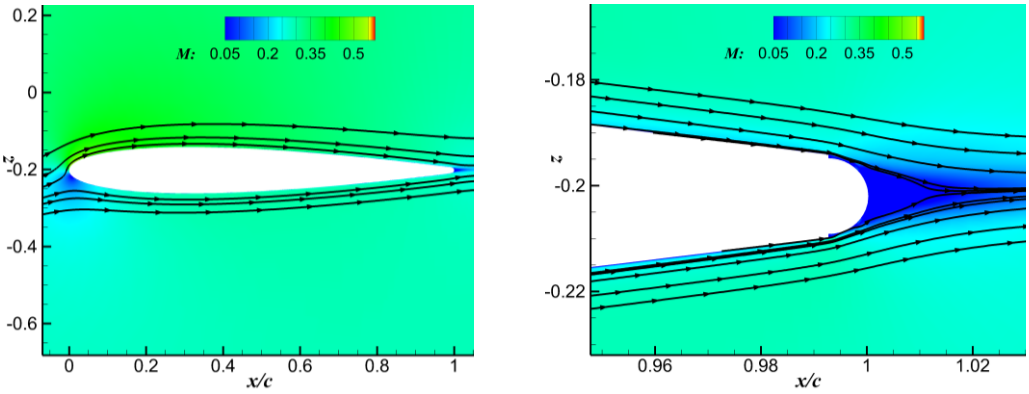

Figure 5.2 Streamlines of the baseline model at s =5

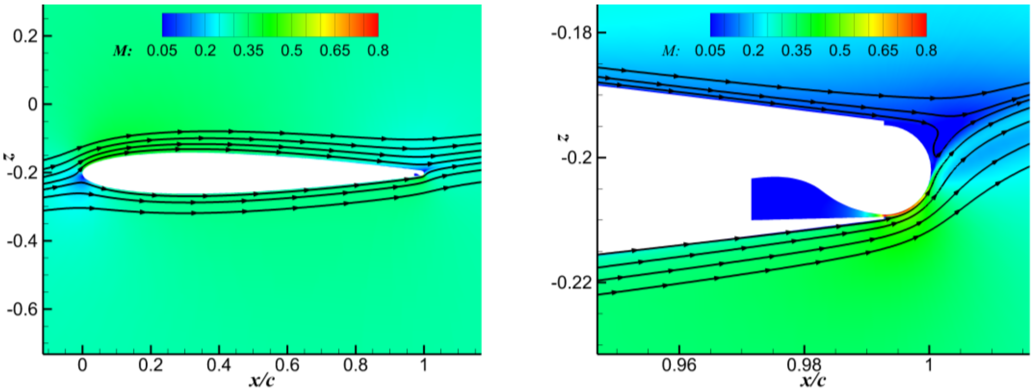

Figure 5.3 Streamlines of the model with C_μ=0.004 at s =5

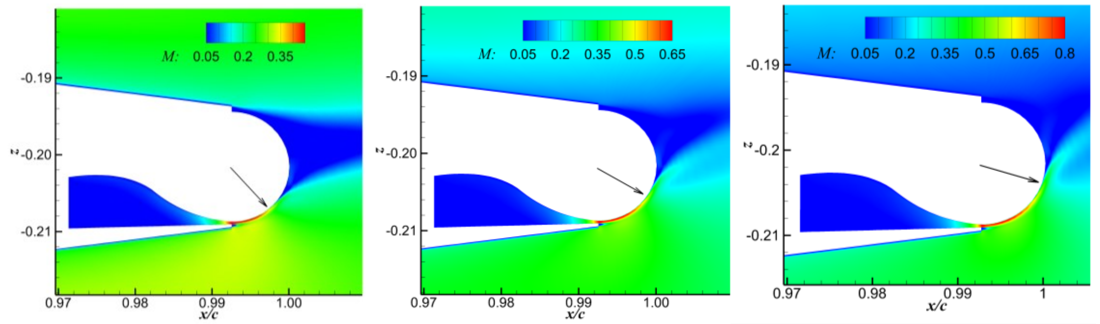

(a) C_μ= 0.0015 (b) C_μ= 0.0028 (c) C_μ= 0.004

Figure 5.4 The entrainment characteristic with the increase in momentum coefficient

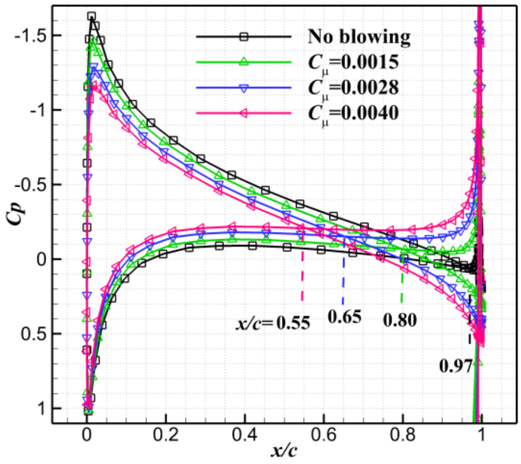

Figure 5.5 Pressure coefficients due to changes in momentum coefficients (*s*=5)

5.1.1.2 Gust load alleviation effects of CC under one-minus-cosine gusts

Gust load alleviation effects are tested with the one-minus-cosine gust with the gust velocity of $w_0/U_\infty = 0.067$ and the gust wavelength of 5*c*. The gust profile in the non-dimensional time domain can be expressed in equation (5-1) and is shown in Figure 5.6. At *s*= 0, the gust hits the aerofoil leading edge and travels past the aerofoil with the freestream Mach number 0.3. Therefore, it takes *s*= 6 for the gust to pass through the aerofoil. The angle of attack is kept to *α*= 1°.

$$\begin{cases} w_g = 0 & s < 0 \\ w_g = \frac{1}{2} w_0 \left(1 - cos\frac{2\pi s}{5}\right) & 0 \le s \le 5 \\ w_g = 0 & s > 5 \end{cases} \tag{5-1}$$

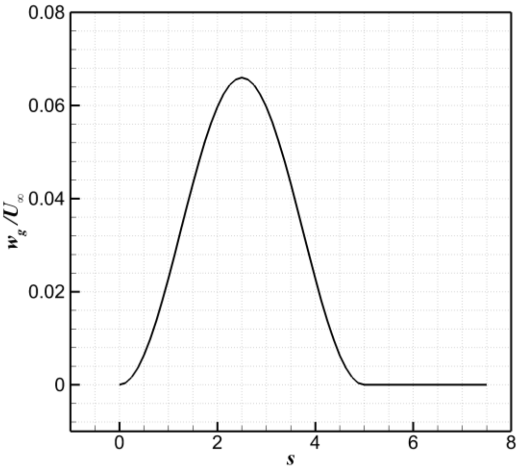

Figure 5.6 The one-minus-cosine gust profile

- **CC with constant blowing momentum coefficient**

Firstly, the control strategy with the CC jet on at *s*= 0 and jet off at *s*= 6 with a constant momentum coefficient C_μ= 0.0028 is applied to the test. The gust response is compared to that of the baseline model without CC as shown in Figure 5.7 (a). The CC jet is turned on at *s*= 0 (point a), from when the lift coefficient saw a sharp decrease to point b (*s*≈ 1) due to the rapid response characteristic mentioned previously. From Figure 5.7 (b) which shows the alleviation magnitude of the lift coefficient, similar gust load alleviation characteristic to the previous result in Figure 5.1 (b) can be observed. That is more than 50% of the total change in lift coefficient can be obtained within the non-dimensional time *s*= 1. After the jet is turned off at point c, the lift coefficient increases sharply and generally returns to the value in the steady state. Compared to the baseline model, the CC model does reduce the peak gust load significantly. However, the magnitude of the lift coefficient still has a large fluctuation under the gust perturbation indicating that it is improper to use a constant blowing momentum coefficient to alleviate a discrete gust perturbation. A straightforward idea is to use an unsteady blowing with the jet blowing momentum coefficient changing proportionally to the variation of the gust velocity.

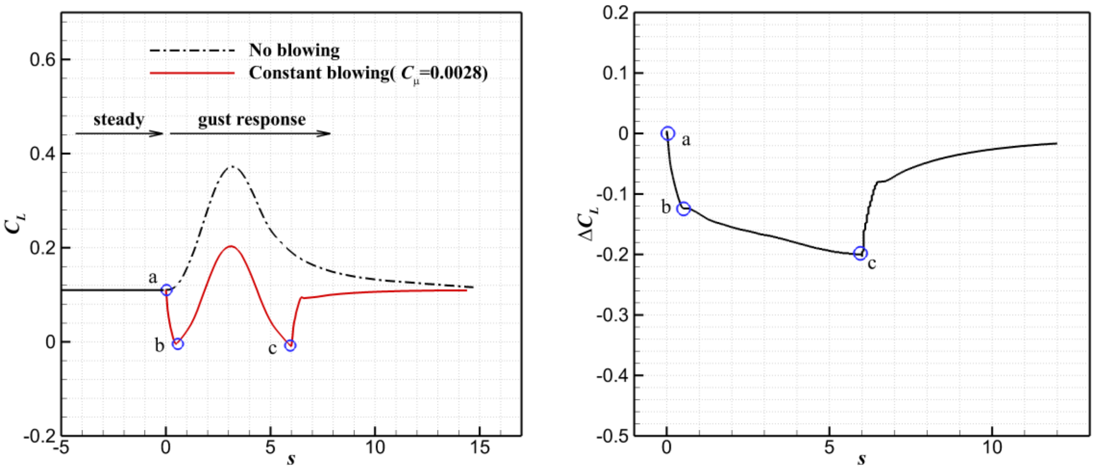

(a) total lift coefficient responses
(b) relative lift coefficient reduction to the baseline model

Figure 5.7 Gust alleviation characteristic to one-minus-cosine gust with constant blowing

- **CC with unsteady blowing momentum coefficient**

To this end, the momentum coefficient with a ‘one-minus-cosine’ profile which is the same as that of the gust is employed for the test, which can be expressed as

$$\begin{cases} C_\mu = 0 & s < 0 \\ C_\mu = \frac{1}{2} C_{\mu 0} \left(1 - cos \frac{2\pi s}{6}\right) & 0 \le s \le 6 \\ C_\mu = 0 & s > 6 \end{cases} \tag{5-2}$$

where, $C_{\mu 0}$ is the magnitude of the peak momentum coefficient. Two different cases with the peak momentum coefficients of $C_{\mu 0}$ =0.0028 and 0.004, respectively are applied. The freestream condition is the same as the former case study. The gust response in terms of lift coefficients is shown in Figure 5.8 together with the response of the baseline model without blowing. As shown in the result, compared to the baseline model, these two unsteady blowing reduce the peak lift coefficients caused by the gust penetration by approximately 54% and 85% respectively. For the characteristic of the ‘time-lag’ in response, the high deployed momentum coefficients around and after *s*= 3 (see the momentum coefficient profile in Figure 5.8 (b)) will influence the lift response afterwards making the lift coefficients even lower than the steady state at non-dimensional time between *s*= 4 and *s*= 5.5 (where the gust velocity diminishes generally) for the jet with $C_{\mu 0}$ = 0.0040. However, compared to the steady blowing case shown in Figure 5.7, the fluctuation of the lift coefficients using unsteady blowing is much smaller under the same gust perturbation, indicating a better control effect. Thus, a further question may be asked about whether CC has the capability to control the gust load timely with adaptive characteristics?

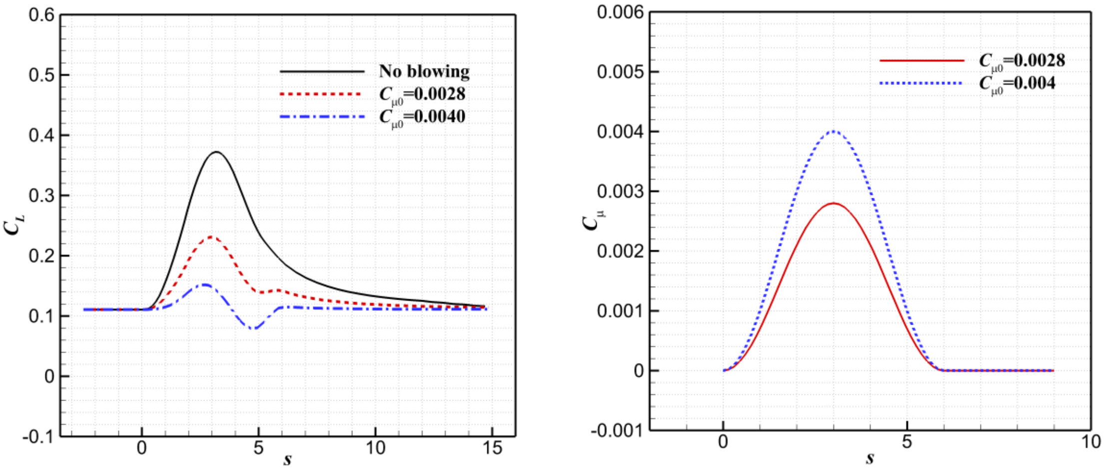

(a) Lift response (b) C_μ profile

Figure 5.8 The response of lift coefficients with unsteady CC jet blowing under gust condition

- **CC with designed adaptive blowing momentum coefficient**

From the results shown in Figure 5.8, it can be seen that even though the profile of the gust load alleviation value in terms of lift coefficients is not completely the same as that of the deployed momentum coefficients in the time domain, the gust load alleviation value is indeed proportional to the momentum coefficient with a small ‘time-lag’ effect. For this reason, CC jet is proposed to have the capability to control the gust load timely with adaptive characteristics. To test this, based on the data for $C_{\mu0} = 0.0040$ shown in Figure 5.8, the relationship of the lift coefficient reduction caused by CC jet named $\Delta C_L(CC)$ and *s* relative to $C_\mu(s)$ can be interpolated, which can be expressed as

$$C_\mu(s) = f\left(s, \Delta C_L(CC)\right) \tag{5-3}$$

where, f is the fitting function based on the data of $\Delta C_L(CC)$, s and $C_\mu(s)$. A quadratic polynomial function is used here. Based on this function, from the gust response value of the baseline model, the increment of the lift coefficient due to the gust, named as $\Delta C_L(gust)$ can be obtained. Therefore, to compensate $\Delta C_L(gust)$ with the control of unsteady CC jet, the required value of the momentum coefficient can be predicted by the expression of the following equation as

$$C_\mu(s) = f\big(s, -\Delta C_L(gust)\big) \tag{5-4}$$

The profile of the predicted momentum coefficients marked as 'Adaptive' is shown in Figure 5.9. For the comparison, the momentum coefficients with the same peak value but has a 'one-minus-cosine' profile are also shown in the figure. As expected, the values of the momentum coefficients after *s*= 3 decrease and the point of the peak value shifts forwards a little.

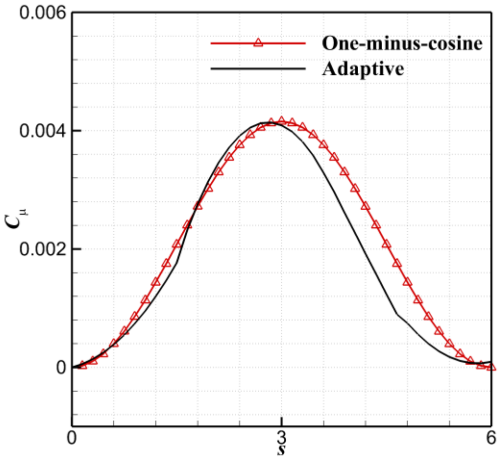

Figure 5.9 The profile of the predicted momentum coefficient

The predicted momentum coefficients are applied in the following test case and the results are shown in Figure 5.10 marked as 'Adaptive blowing'. From the results, it is clear that dynamically adapting the momentum coefficient effectively counteracts the gust load and a near constant lift coefficient is obtained under gust perturbations.

It is true that the adaptive blowing of this case study is obtained under a certain gust perturbation and freestream condition. The function obtained in Eq. (5-4) is not appropriate for all gust perturbations. In practice, a database of the ability of CC for various momentum coefficients according to different gust velocities and freestream conditions should be set for an open-loop or closed-loop control. This case study indicates the capability of CC for adaptive gust load controls due to the combined CC properties including the strong ability for lift reduction, the fast response characteristic and the small 'time-lag' in response.

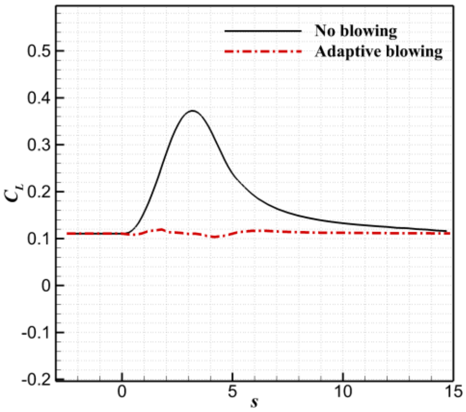

Figure 5.10 The gust response of the adaptive blowing

5.1.2 Case studies at M_∞= 0.5 by circulation control

At M_∞= 0.5, gust load alleviation effects are tested under two blowing conditions. One is the unsteady blowing with the one-minus-cosine profile, where the peak momentum coefficient is $C_{\mu 0} = 0.0024$. The response of this unsteady blowing is then used to design an adaptive blowing through the same method described previously for the test of adaptive control. The gust is the one-minus-cosine gust with the velocity $w_0/U_\infty = 0.04$ and the wavelength of 9c corresponding to s= 10 for the gust to pass through the aerofoil. The freestream condition is M_∞= 0.5, α= 1°, Re_c= 1.67×10^6. Figure 5.11 shows the lift responses under these two blowing conditions and the case without blowing. Similar to the results at M_∞= 0.3, the unsteady blowing is able to alleviate the gust load dramatically and a near constant lift coefficient is also obtained under the designed adaptive blowing.

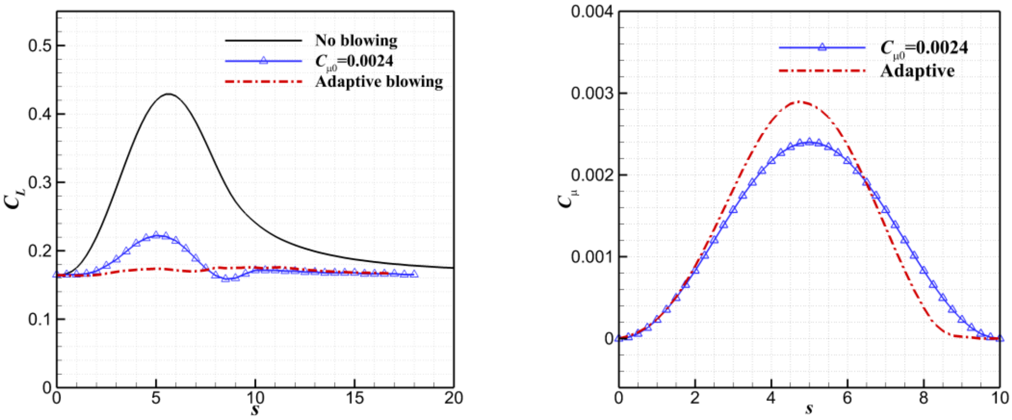

(a) Lift response (b) C_μ profile

Figure 5.11 The gust response at M_∞=0.5

5.1.3 Case studies at M_∞= 0.7 by circulation control

To test CC for gust load alleviation at transonic speeds, the one-minus-cosine gust with gust velocity of w_0/U_∞= 0.033 and wavelength of 20c, corresponding to s= 21 for the gust to pass through the aerofoil is applied for the freestream flow condition of M_∞= 0.7, α= 3°, Re_c= 5.0×10^6. From the lift reduction due to CC on the 2-D NACA0012 aerofoil at M_∞= 0.7, α= 3° shown in Figure 4.4 (a) under steady condition, it is known that the 'C_μ-stall' point is at around C_μ= 1.32×10^{-3}. This project focuses on the evaluation of CC properties before 'C_μ-stall'. The unsteady blowing with the 'one-minus-cosine' shape of momentum coefficients having two peak values of $C_{\mu 0}$= 5.05×10^{-4} and $C_{\mu 0}$= 1.20×10^{-3}, respectively are used for the tests.

The lift coefficient responses are shown in Figure 5.12. For both blowing cases, the gust loads are alleviated. Figure 5.13 shows the Mach number contours of the models at the initial time (s= 0) and at the time when gust load peaks (s=11). It is demonstrated clearly that the shock wave becomes stronger under the peak gust load compared to the initial time. Figure 5.14 compares the pressure coefficients between the baseline model and the model with $C_{\mu 0}$= 1.20×10^{-3} under the peak gust load at s=11. CC has little influence on the shock strength but moves the shock a little forward to the leading edge. This is consistent with the Mach number contours shown in Figure 5.13 (b) and (c). As shown in the results, CC with $C_{\mu 0}$= 1.20×10^{-3} reduced about 50% of the peak gust load, which is about ΔC_L= -0.11. From Figure 4.4 (a), it is known that CC with $C_{\mu 0}$= 1.20×10^{-3} can achieve the lift reduction of about ΔC_L= -0.23 under steady condition of M_∞= 0.7, α= 3°. This value is much higher than that obtained under the peak gust load, due to the increase of the external flow velocity under the peak gust condition compared to the steady state at the initial time.

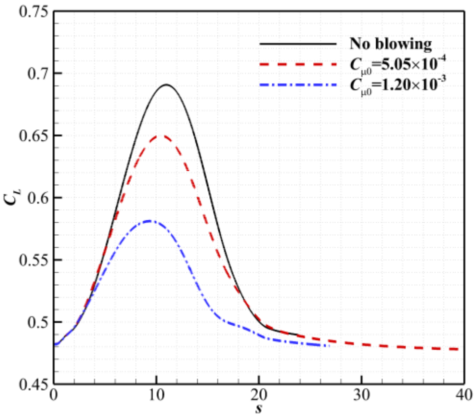

Figure 5.12 The gust responses at M_∞= 0.7

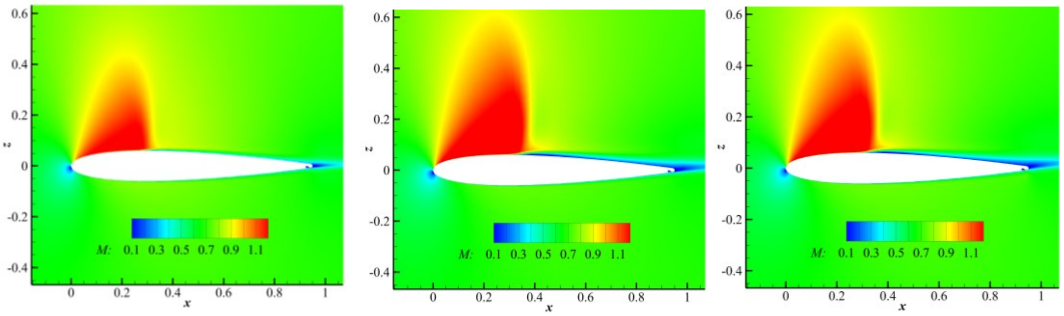

(a) s= 0 (b) s= 11 (No blowing) (c) s=11 ($C_{\mu 0}$= 1.20×10^{-3})

Figure 5.13 The Mach number contours at the initial time and the peak gust load

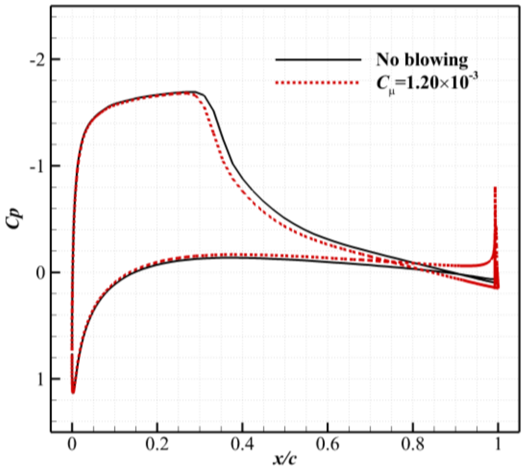

Figure 5.14 The pressure coefficient for models with and without CC at peak gust load (s= 11)

5.1.4 Comparison of circulation control and normal microjet blowing for gust load alleviation

According to the comparison of the load control effects between CC and normal microjet blowing on the 2-D NACA0012 aerofoil at M_∞= 0.7, α= 3° shown in Figure 4.5 (b) that normal microjet blowing can achieve higher lift reduction compared to CC under steady condition. It is expected to have a stronger gust load alleviation than CC under gust conditions. To test this, the same one-minus-cosine gust as that used in the previous CC case study at M_∞= 0.7 is applied here.

Firstly, the unsteady normal microjet blowing with the one-minus-cosine profile having the same peak value of $C_{\mu 0}$= 1.20×10^{-3} is tested and the results are shown in

Figure 5.15. As shown in the results, the lift-coefficient evolutions of the baseline CC and normal microjet models are similar. Under the same $C_{\mu0}= 1.20\times10^{-3}$, CC achieved a stronger gust load alleviation effect, which is consistent to the load control effects demonstrated under steady conditions shown in Figure 4.5 (b).

It has been demonstrated through the comparison of the load control capability under transonic steady condition shown in Figure 4.5 (b) that normal microjet blowing has better endurance in terms of the range of usable momentum coefficient than CC. Two higher peak momentum coefficients of $C_{\mu0}= 1.75\times10^{-3}$ and $C_{\mu0}= 4.87\times10^{-3}$ are then tested here.

Figure 5.16 shows the gust load alleviations effects. It is clear that the peak gust load is better controlled with the increase in the blowing momentum coefficient. The response of this unsteady blowing with $C_{\mu0}= 4.87\times10^{-3}$ is used to design an adaptive blowing through the same method described previously for the test of adaptive control by normal microjet blowing at $M_\infty= 0.7$. The lift responses and the blowing momentum coefficient profiles are shown in Figure 5.17. A near constant lift response under gust condition is obtained by normal microjet blowing. This case study indicates that normal microjet blowing is also capable for adaptive gust load control. Figure 5.18 and Figure 5.19 compares the Mach number contours and surface pressure distributions among the baseline model, the model with $C_{\mu0}= 1.75\times10^{-3}$ and the model with the adaptive blowing under the peak gust load. Compared to the baseline model, the shock strength is weakened and pushed forwards with the microjet blowing.

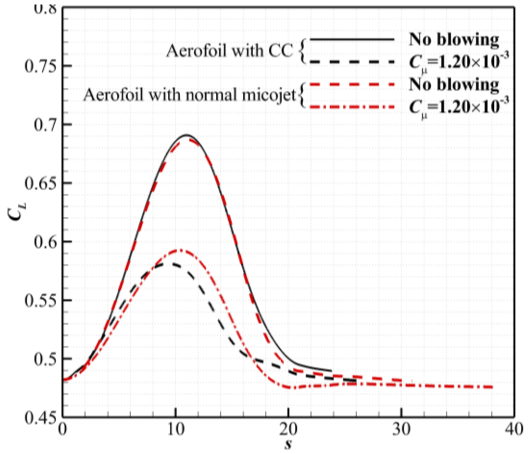

Figure 5.15 The gust load alleviation by CC and normal microjet blowing at $M_\infty= 0.7$

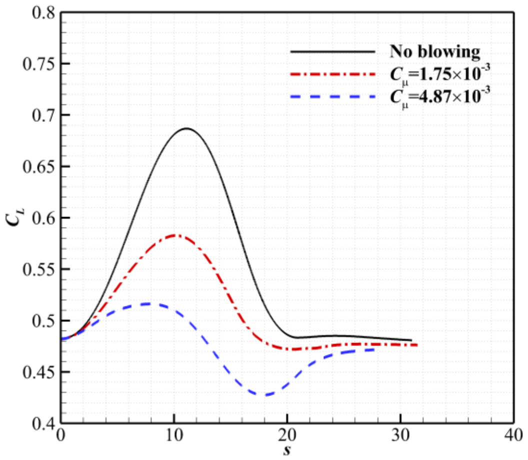

Figure 5.16 The gust load alleviation by normal microjet blowing at M_∞= 0.7

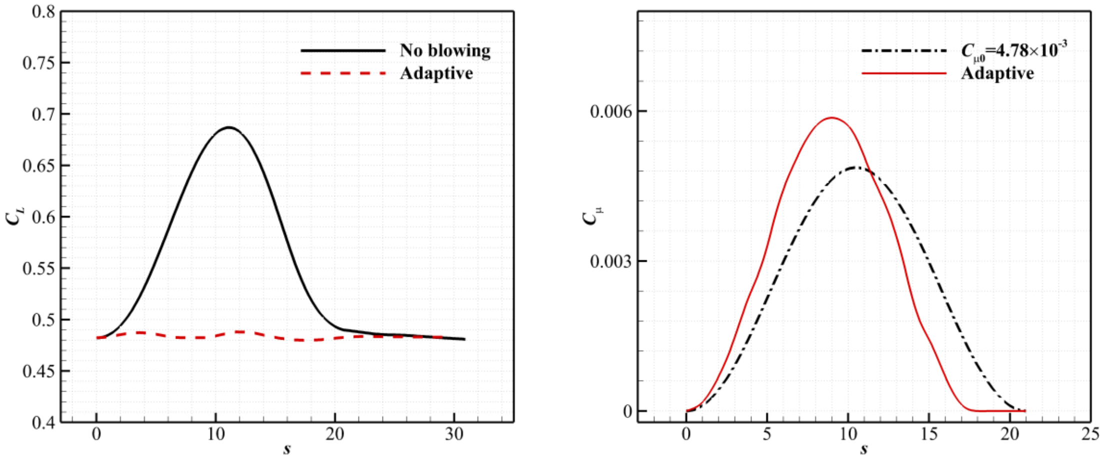

(a) Lift response (b) C_μ profile

Figure 5.17 The gust response using adaptive microjet blowing at M_∞= 0.7

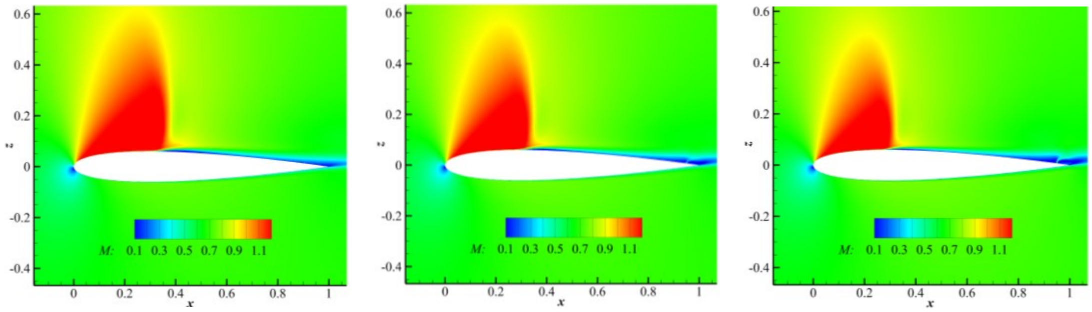

(a) No blowing (b) $C_{\mu0}$= 1.75×10^{-3} (c) Adaptive

Figure 5.18 The Mach number contours at the peak gust load (*s*= 11) for normal microjet blowing

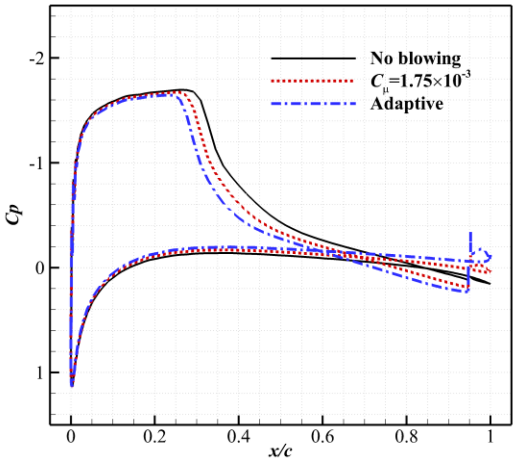

Figure 5.19 The pressure coefficient for models with and without CC at peak gust load (*s*= 11)

5.2 BAH wing gust load alleviation

5.2.1 Case studies at M_∞= 0.3

According to the typical gust models described in Section 2.4 by EASA CS-25 [2] for the certification specifications of large commercial aircraft, the gust wavelength is taken as 12.5c_{ref} (c_{ref} is the mean aerodynamic chord length), which is 51.6 m for the BAH wing. For M_∞= 0.3, considering the BAH wing flies at sea level, the gust velocity is set to be 6.74 m/s with F_g= 0.5 corresponding to a gust-induced angle of attack variation of about 3.8º. At *s*= 0, the gust hits the leading edge of the root wing section and travels past the wing with the freestream Mach number 0.3. The angle of attack of the BAH wing is kept to α= 3º.

Figure 5.20 shows the responses of lift and root bending moment coefficients to the gust. After the gust hits the root-chord leading edge at *s*=0, the lift and root bending moment coefficients increase as the gust proceeds. The lift and root bending moment coefficients peak at around *s*= 6.7. To be specific, the peak gust load caused a maximum increase of lift and root bending moment coefficients to around C_L= 0.5 and C_{mx}= 0.22, respectively. These peak values are more than twice of the initial values which are C_L= 0.238 and C_{mx}= 0.102 at *s*= 0. Three specific points in time are labelled from *s*= 0 to *s*= 6.7, and the corresponding evolutions of the spanwise loading are shown in Figure 5.21. As shown in the results, significant load increases have been observed along the whole span with the increase in the gust load.

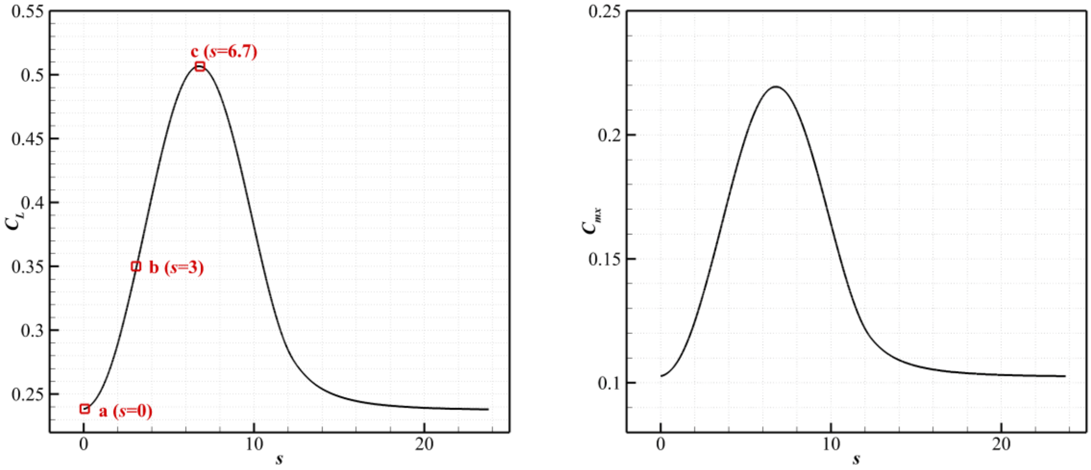

(a) lift response (b) root bending moment

Figure 5.20 Responses of lift and root bending moment coefficients to the gust

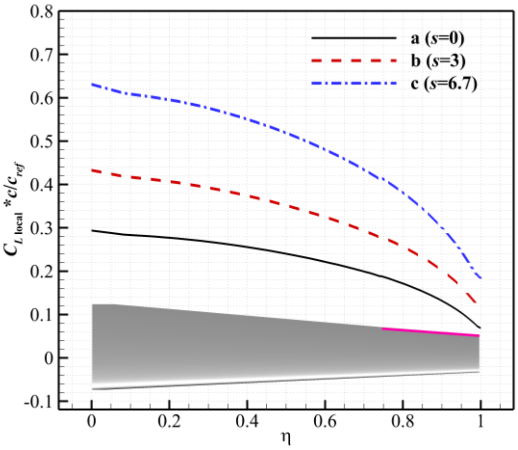

Figure 5.21 Evolution of the spanwise loading to the gust

According to the load control effects of the BAH wing due to CC under steady state at M_∞= 0.3 shown in Figure 4.19, the 'C_μ-stall' occurs at around C_μ= 1.9×10^{-3}. Two different cases with the peak momentum coefficients of $C_{\mu0}$= 1.28×10^{-3} and $C_{\mu0}$= 1.76×10^{-3} are applied for the gust load alleviation tests.

The gust responses in terms of lift and root bending moment coefficients are shown in Figure 5.22 together with the response of the baseline model. As shown in the results, these two unsteady CC achieved significant alleviation of the gust loads. To be specific, compared to the baseline model, CC with $C_{\mu0}$= 1.76×10^{-3} reduced the peak lift coefficient caused by the gust by approximately 44%, with the alleviation of lift coefficient increment from 0.268 to 0.117. For the root bending moment, the peak value is reduced by 71%. It can be seen that CC achieved more relative reduction in root bending moment (71%) than that in lift (44%). It is because CC is deployed around the wingtip where the variation of the load will have a significant influence on the root bending moment due to the large moment arm. This can be noticed from the comparisons of the spanwise load distributions between these three models at the initial time *s*=0 and *s*=6.7 when the gust load peaks shown in Figure 5.23. A significant load reduction can be observed around the wing-tip region for the CC models compared with the baseline one. The load control effect is so significant that for the CC models with $C_{\mu0}$= 1.28×10^{-3} and 1.76×10^{-3}, the load around the wing-tip area under the peak gust load at *s*= 6.7 is alleviated to be even lower than that at the initial time. Therefore, assuming CC is deployed along the whole span, the gust load in terms of lift increments can be completely alleviated.

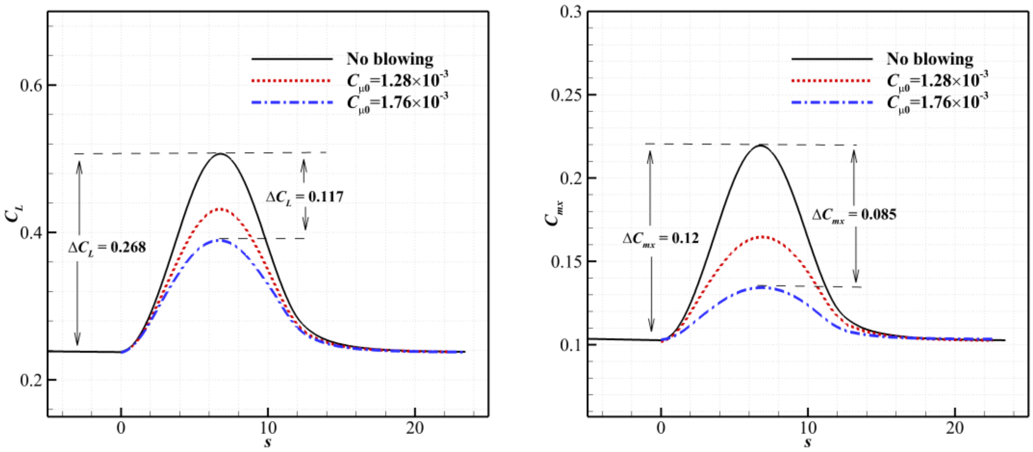

(a) lift coefficient (b) root bending moment coefficient

Figure 5.22 Load control effects with an unsteady jet blowing under gust condition

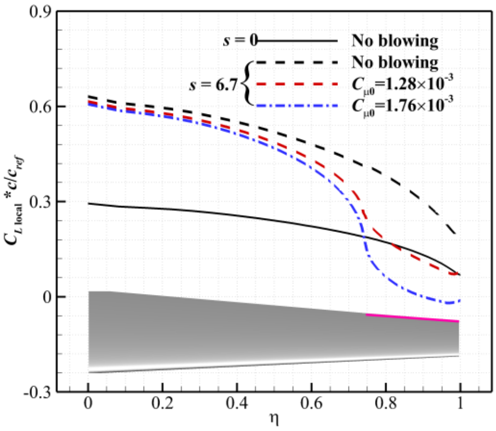

Figure 5.23 Comparisons of the spanwise load distributions

The response of the BAH wing with normal microjet blowing is tested under the same gust load and the same peak momentum coefficients of $C_{\mu 0}$= 1.76×10^{-3} as the previous test case with CC. The evolution of the lift and root bending moment coefficients are shown in Figure 5.24. For the baseline model with normal microjet, the responses of the lift and root bending moment coefficients are consistent with the baseline BAH wing with CC. It is clear that CC has a much stronger gust load alleviation effects than that of the normal microjet blowing under the same $C_{\mu 0}$ at M_∞= 0.3. It is consistent to the load control capabilities of these two approaches demonstrated under steady conditions shown in Figure 4.19.

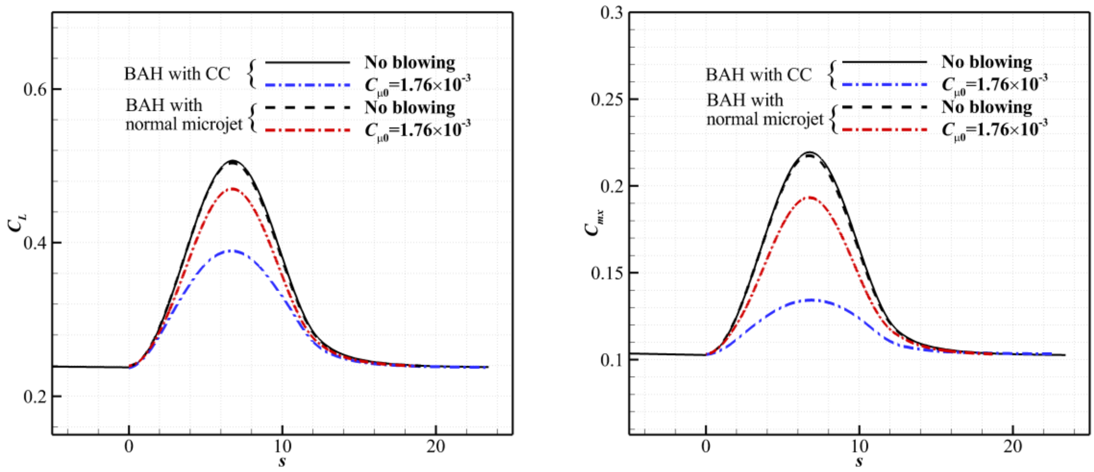

(a) lift coefficient (b) root bending moment coefficient

Figure 5.24 Comparison of gust load alleviation effects between CC and normal microjet

5.2.2 Case studies at M_∞= 0.7

In this case study, the 'one-minus-cosine' gust wavelength is set to be 12.5$\bar{c}$ with an estimated gust velocity of 5.85 m/s. The BAH wing is kept to α= 3°. The 'C_μ-stall' point is around 3.0×10^{-4} at the steady state of M_∞ = 0.7, α= 3° for CC as shown in Figure 4.19 (b). The same peak momentum coefficient of $C_{\mu 0}$ = 2.5×10^{-4} for CC and normal microjet blowing is chosen for the tests of gust load alleviation.

The gust responses in terms of lift and root bending moment coefficients under these two blowing conditions and the condition without blowing are shown in Figure 5.25. As shown in the results, CC and normal microjet achieved similar gust load alleviation effects. An alleviation of the peak of 20% due to CC and normal microjet blowing can be noticed on lift, and about 32% on the root bending moment.

For CC with $C_{\mu0}$= 2.5×10^{-4}, it is near its utmost capability for lift reduction as demonstrated in the steady state of M_∞ = 0.7 as shown in Figure 4.19 (b). However, normal microjet blowing has better endurance in terms of the range of usable momentum coefficient than CC as shown in Figure 4.19 (b). Higher peak momentum coefficients of $C_{\mu0}$= 2.3×10^{-3} is tested for normal microjet blowing. Figure 5.26 shows the gust load alleviation effects. Figure 5.27 presents the spanwise load distributions for the BAH wing with CC and normal microjet blowing controls. It is clear that the peak gust load and the span loading is better controlled with the increase in normal microjet blowing momentum coefficient. An alleviation of the peak of 72% due to normal microjet has been obtained on the root bending moment, indicating its strong load control capability under transonic range.

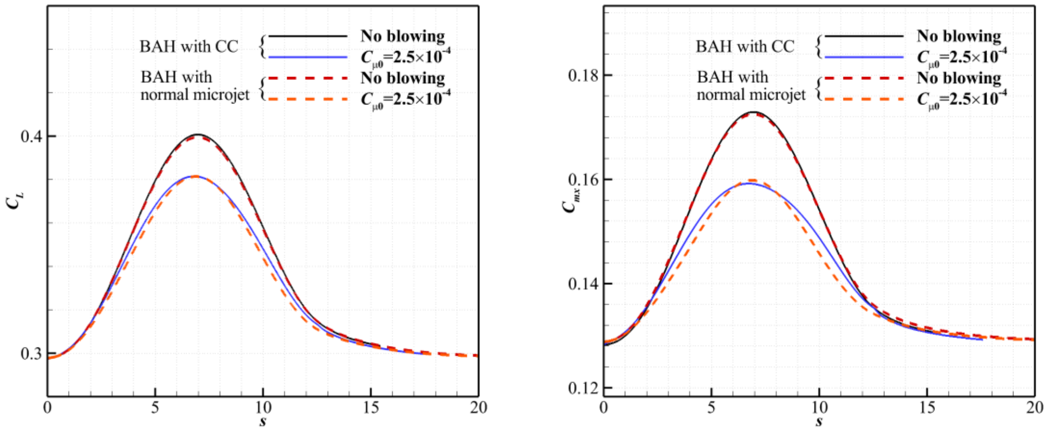

(a) lift coefficient (b) root bending moment coefficient

Figure 5.25 Comparison of load control effects by CC and normal microjet

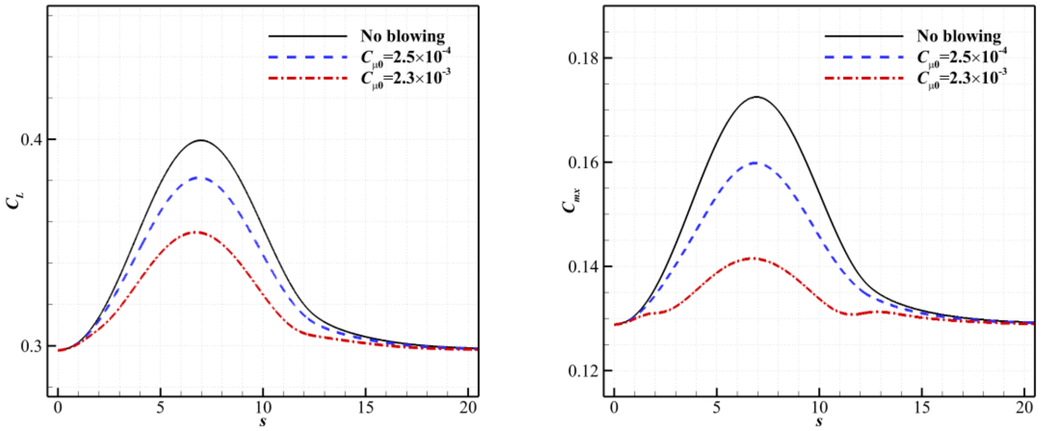

(a) lift coefficient (b) root bending moment coefficient

Figure 5.26 Load control effects by normal microjet blowing for the BAH wing

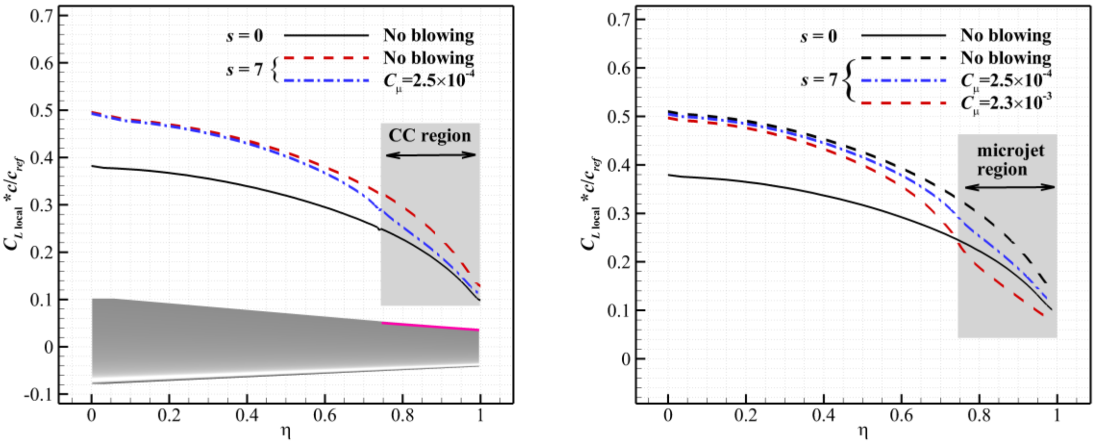

(a) CC

(b) Normal microjet

Figure 5.27 Spanwise load distributions for BAH wing with normal microjet blowing

5.3 Summary

This chapter evaluated the feasibility and effects of CC and normal microjet blowing for gust load alleviation based on the 2-D NACA0012 and 3-D BAH wing for subsonic and transonic speeds.

The case studies concluded that both CC and normal microjet blowing are capable for gust load alleviations. The gust load alleviation capability of CC and normal microjet blowing is relevant to their load control capability under steady conditions which are demonstrated in Chapter 4. That is CC has a much stronger gust load alleviation capability at subsonic speed. Normal microjet blowing has better endurance in terms of the range of usable momentum coefficients at transonic speed. Therefore, it can achieve a stronger gust load alleviation with a higher blowing momentum coefficient than CC at transonic speed.

As both methods have the fast frequency response characteristic, more than 50% of the total change in load responses caused by these two load control methods can be achieved within the non-dimensional time *s*= 1. This characteristic allows timely adaptive load control to counteract the gust disturbances. The results of unsteady CC and normal microjet blowing verified that by dynamically adapting the momentum coefficients, the gust loads can be eliminated, resulting in a near constant load response under gust conditions as tested on the 2-D aerofoil. For the 3-D BAH wing with CC and normal microjet deployed around the wing-tip region, apart from the alleviation of the lift coefficient, significant root bending moment relief under the gust load by these two methods have been obtained.

Chapter 6

Blended-wing-body model setup and the influence of spanwise load distributions on the performance

The final aim of this study is to evaluate the feasibility of gust load alleviation by circulation control and normal microjet blowing on a blended-wing-body (BWB) model and to show the potential of wing structure weight reduction due to gust load controls. Before conducting this evaluation, in this chapter, a BWB geometry is generated and optimised together with the setup of its structural model. The correlation between the wing structure weight reduction and the spanwise loading relief is built up based on the available references. The influence of spanwise load distributions on the BWB aerodynamic and overall performance is evaluated in this chapter.

6.1 Initial blended-wing-body geometry and optimisation

6.1.1 Initial blended-wing-body geometry

BWB configurations, also known as the hybrid-wing-body (HWB) configurations, have been studied for the past few decades. Some results including the geometric design parameters and aerodynamic characteristics are available in the literature. BWB research models include the Boeing first and 2nd-generation BWB models [36] for the BWB design study, the BWB model for the EU MOB project [50], SAX-40 model [161] investigated by researchers at Cambridge and MIT for the feasibility of low noise and fuel efficiency, as well as the N2-A/B/EXTE HWB designs [51, 162] by Boeing to meet the ERA program's N+2 targets. These configurations have been served as the basis for various kinds of studies. Typically, based on the second-generation of Boeing BWB design, Lyu *et al*, [163] built a similar planform shape for aerodynamic design optimization studies. To simplify the model, the nacelle and the winglet were not included. In this study, a similar BWB planform is chosen for the initial BWB design with a scale factor of 0.6 from Boeing-2nd generation BWB model for a medium size.

The geometry is created from the lofting of an aerofoil profile stack to conform to the prescribed planform shape. Three aerofoil cross-sections as shown in Figure 6.1 and the quadratic interpolation of adjacent aerofoil sections are used to define the aerofoil profile at each spanwise location. The modified NASA SC(2)-0414 aerofoil with a reduced maximum camber from 1.5% to 0.5%, NASA SC(2)-0412 and SC(2)-0410 are used at the centre plane, mid-span section, and the wingtip, respectively.

As shown in Figure 6.1, the BWB centre body is between 35% semi-span and the root centre line. The outer 65% of the BWB is defined as the wing similar to the definition in Ref. [36]. The spanwise loading is for the whole wing-body span as treated in the studies on BWB in Ref. [53, 163, 164]. For the wing root bending moment, the load is on the wing with reference to the wing-body junction. The geometry parameters of the designed BWB model is shown in Table 6.1.

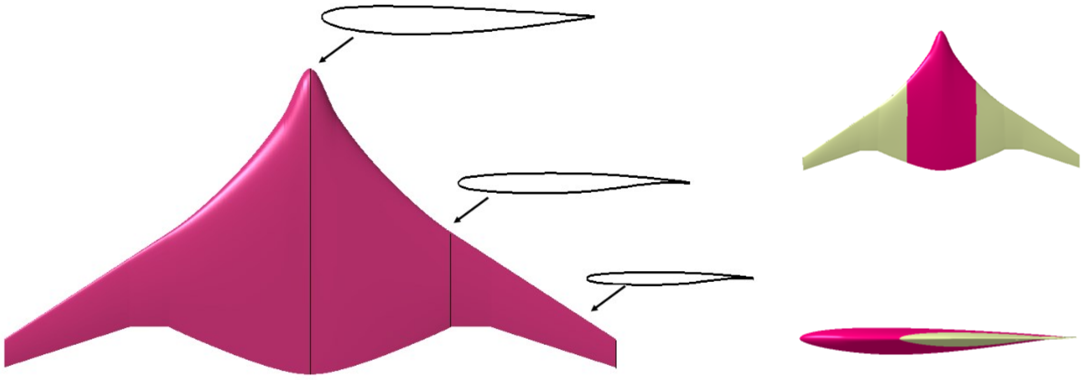

Figure 6.1 Aerofoil sections, planform shape of the initial BWB model

Table 6.1 Geometry parameters of the BWB model

Parameter	Value
Span	53.6m
Length of the centre body	26.9m
Reference centre point of weight	16.14m
Mean aerodynamic centre	15.27m
Aspect ratio	5.1
Outer wing Leading-edge swept angle	33°
Outer wing rear swept angle	0°, 18°
Area	563 m^2

6.1.2 Assessment of aerodynamic performance of the initial model

- **Grid convergence study**

Based on the cruise condition of the second-generation BWB model [36], the cruise lift coefficient of the present study is constrained to 0.23 at a cruise Mach number of 0.8 and a cruise altitude of 11 km. The Reynolds number is 7.9×10^7 based on the mean aerodynamic chord length.

Half model is used in the study by applying symmetry boundary condition for the centre plane. Figure 6.2 shows the BWB mesh on the model surface and the symmetry plane. The spacing on the first layer uses a $y^+\approx 0.4$ with an average growth ratio of 1.15 matched out to the far field located at a distance of about 25 times the span length. The mesh shown in Figure 6.2 has 2.53 million cells. For the grid convergence study to determine the grid resolution accuracy, several grid resolutions with a coarse or a refined spacing are generated, and computational analysis is performed on each of them to obtain the aerodynamic coefficients at $M_\infty= 0.8$, $\alpha= 2.5°$, as shown in Table 6.2. The first three grids have the same number of points in the *j* direction. Approximately doubled number of points in the *i* direction is used to generate the second one and then doubled number of points in the *k* direction for the third one, with a total grid size of 0.77 and 1.26 million respectively. The fourth grid doubles the number of points in *j* direction from the third one. The last three grids double again the number of points in *j*, *k*, *i* directions, respectively from the fourth grid. The results show that the number of points in *k* direction has a significant influence on both the lift and drag coefficients if not enough points were assigned in this direction. Lift coefficient converges earlier to the grid size than that of the drag coefficient. The grid with 2.53 million points is within 2 drag counts of that for the grid with 17.7 million points. Therefore, the fourth grid resolution is chosen for the study because it allows a reasonable computational time while providing enough accuracy.

Table 6.2 Grid sensitivity analysis M=0.8, α=2.5°

Grid No.	Grid size ($\times 10^6$)	y^+_{max}	C_L	$C_{D,\,total}$	$C_{D,pressure}$	$C_{D,friction}$
1	0.33	3	0.19835	0.01696	0.00765	0.00930
2	0.77	3	0.21482	0.01511	0.00711	0.00800
3	1.26	3	0.22260	0.01243	0.00679	0.00564
4	2.53	1.0	0.23059	0.01085	0.00598	0.00487
5	5.51	0.4	0.23265	0.01076	0.00595	0.00481
6	8.65	0.4	0.23291	0.01069	0.00584	0.00483
7	17.7	0.4	0.23311	0.01065	0.00583	0.00482

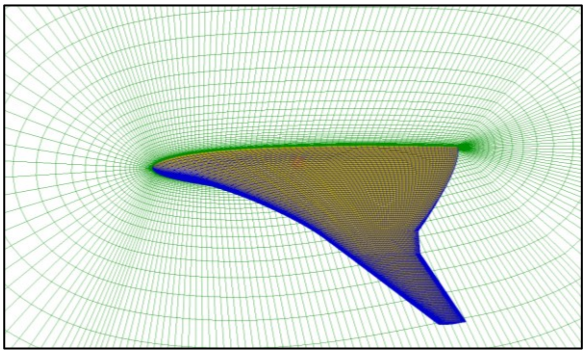

Figure 6.2 BWB grid showing the surface and the centre plane

■ Aerodynamic performance of the initial BWB model

A series of computations at different angles of attack for M_∞=0.8 were carried out to get a general insight of the aerodynamic performance of the initial BWB model as shown in Figure 6.3. The results show a good aerodynamic performance in terms of lift-to-drag ratio (K), as an approximate K= 21.3 was obtained at the cruise point with C_L= 0.23. Figure 6.3 (d) shows the decomposition of the total drag to pressure drag and skin-friction drag. The friction drag is relatively insensitive to the increase of lift coefficient, although a slight decrease can be observed, which is consistent with the result in Ref. [53]. At the cruise point, the total drag is composed by 59% pressure drag and 41% skin drag. This is slightly different from the skin-friction drag of a typical conventional transport aircraft which accounts for a nearly 50% of the total drag [165]. Qin [53] believed that this difference is due to the lower surface-area-to-volume ratio for the BWB design.

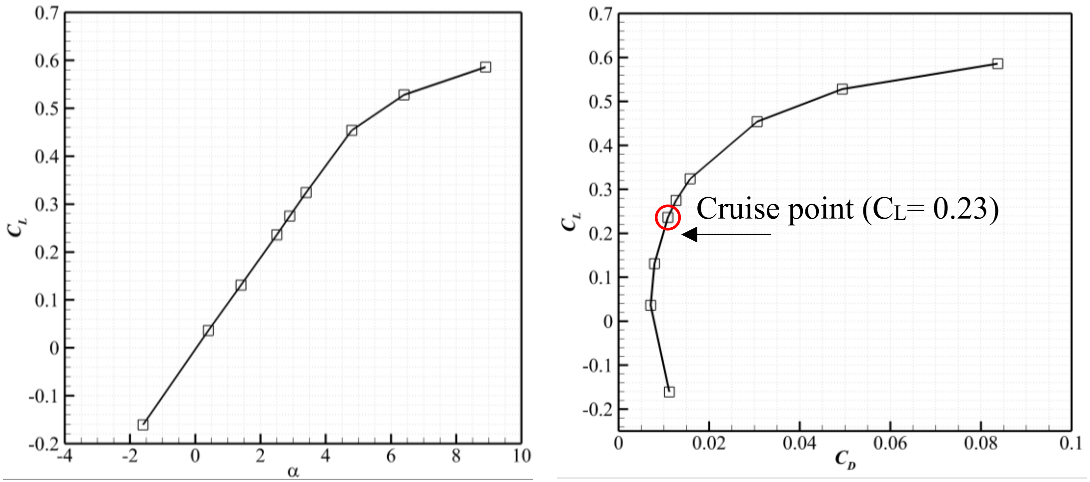

(a) $C_L \sim \alpha$ (b) $C_L \sim C_D$

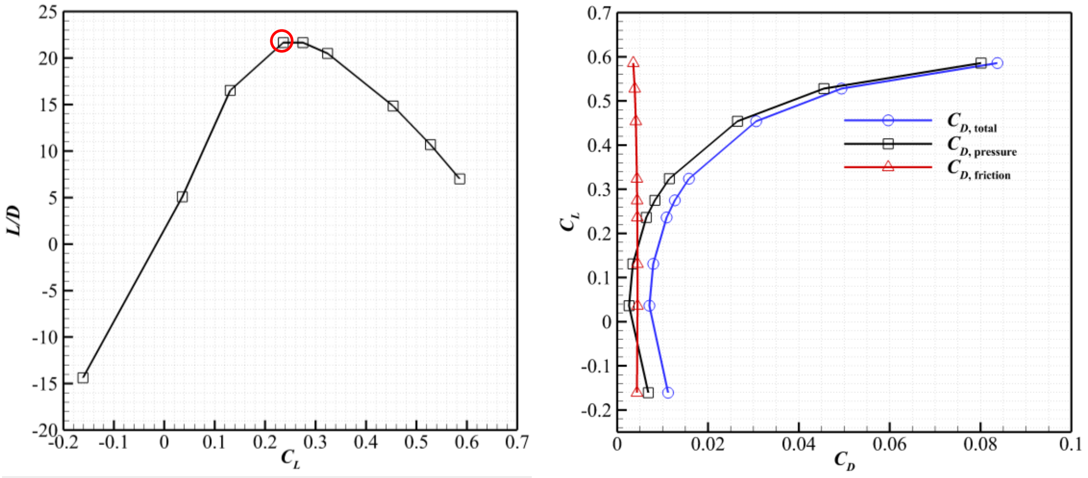

(c) $L/D \sim C_L$ (d) $C_L \sim C_{Dtotal}, C_{Dp}, C_{Dv}$

Figure 6.3 Aerodynamic performance of the initial BWB model at M_∞= 0.8

Distributions of the spanwise loading and spanwise local lift coefficient at the cruise condition are shown in Figure 6.4. As for comparison, the theoretical elliptic distribution for the cruise total lift coefficient C_L=0.23 is also shown in the results. In the figure, $\eta = y/b$ refers to the spanwise location in the percentage of the semi-span length. The results show a near-elliptic design for the outer wing. The centrebody ($\eta < 0.35$) has an apparent lower loading compared to the elliptic one. On the contrary, the outer wing ($0.65 < \eta < 1.0$) is highly loaded where the chord is much shorter than the inner wing ($0.35 < \eta < 0.65$) and the centre body. At this design condition, the local lift coefficient peaks at about 85% of the span with a local C_L= 0.52, while the local lift coefficient for the centre body is only about 0.12. The shock wave which can be seen from the pressure distribution shown in Figure 6.5, is the result of the high loading on the outer wing. The shock is smeared into a compression wave on the centerbody where the local lift coefficient is much lower.

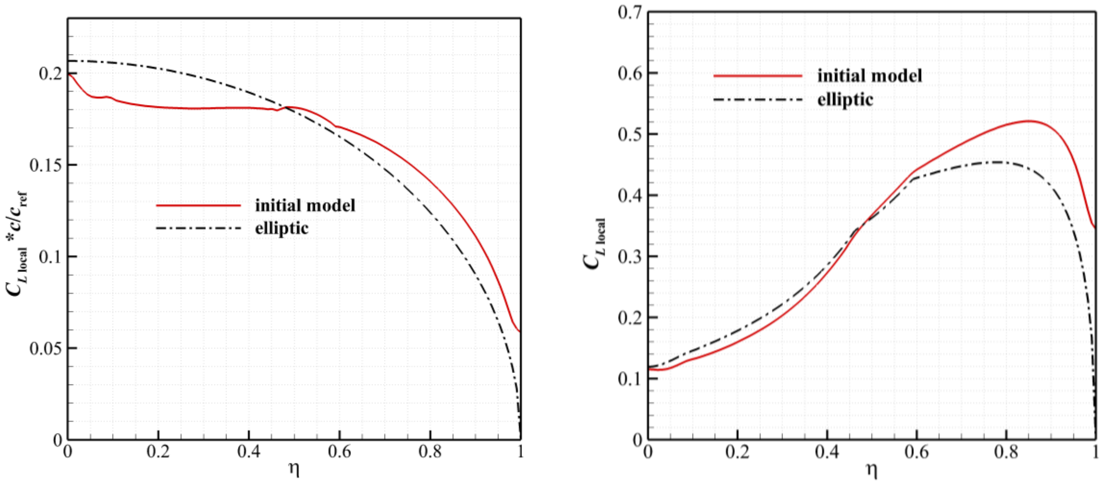

(a) $C_{L\ local}$ $*c/c_{ref}$ ~ η (b) $C_{L\ local}$ ~ η

Figure 6.4 Spanwise loading and spanwise local lift coefficient at cruise condition

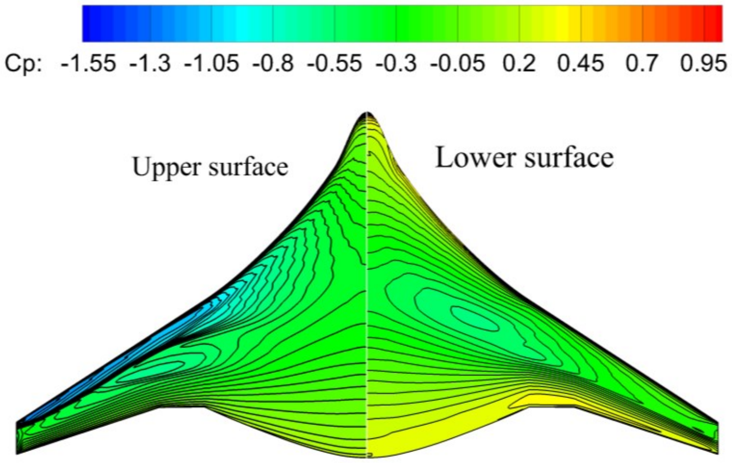

Figure 6.5 the pressure distribution on the initial model at cruise condition

6.1.3 Optimisation of aerofoil sections

As the general NASA aerofoils are used to generate the BWB model, an optimisation work is carried out at the cruise condition to check whether there is any improvement of the aerofoil geometries for a better aerodynamic performance.

- **Geometric parametrisation and mesh deformation**

An in-house code of surface parametrisation using the Bézier-Bernstein method is employed to represent the shape to be modified during the optimisation process. For a two-dimensional aerofoil, deformations in the vertical coordinates z can be expressed as the sum of the original shape with the perturbation from the Bézier-Bernstein parametrization as

$$z = z_{initial} + \delta z \tag{6-1}$$

$$\delta z = \sum_{k=0}^{N} B_{k,N}(u) P_{zk} \tag{6-2}$$

where, $B_{k,N}(u)$ is the Bernstein polynomial and P_{zk} is the control point. More details about this method can be found in Ref. [166].

For the three-dimensional wings, the wing is divided into a series of master sections connected by a cubic spline. Each section is free to deform according to the two-dimensional parameterization by Bézier-Bernstein method. An additional design variable controlling the change of the angle of attack for each master section defines the spanwise twist of the wing. After the wing surface is deformed, the volume grid is propagated smoothly from the wing surface to the farfield. For example, the grid coordinates of x is changed according to the following method and the deformations of coordinates y and z are done in the same way.

$$x_j^{new} = x_j^{original} + [1 - arc(j)]\left(x_{surface}^{new} - x_{surface}^{original}\right) \tag{6-3}$$

where,

$$arc(j) = \frac{\sum_{l=2}^{j} L_l}{\sum_{l=2}^{jn} L_l} \tag{6-4}$$

$$L_l = \sqrt{(x_l - x_{l-1})^2 + (y_l - y_{l-1})^2 + (z_l - z_{l-1})^2} \tag{6-5}$$

l= 1 represents the surface points and the point at the farfield boundary is l= jn.

■ Optimisation algorithm

An in-house Genetic Algorithm (GA) code is used for the optimisation. GA tries to mimic the evolutionary process based on Darwin's natural selection mechanism, where a population of random individuals are generated within the boundaries of the design variable values. Each individual is then evaluated against a fitness function, and only the individuals that meet the designed selection criteria, can be selected for the process of mating and mutation to generate a new generation of individuals. An iterative procedure of the selection, mating and mutation will be performed until successive generations have progressively improved towards the design objective. In this code, selection is done by Stochastic Universal Sampling [167] method which is a variant of Roulette Wheel Selection, but has the advantage to reduce the risk of premature convergence. Mating is done by a mating operator between two individuals randomly selected from the mating pool, and the distance between the newly generated individuals is measured to set their probabilities for mutation. Gaussian mutation is then followed to mutate the new individuals.

■ Optimization results

An optimization platform was set up coupling with RANS solver (CFL3D), optimization code (GA) and the mesh deformation module mentioned above to carry out the optimization. Four master sections as shown in Figure 6.6 are used to impose the Bézier-Bernstein parametrisation and geometrical constraints. The design variables are 16 control points for Bézier-Bernstein parametrisation and one twist angle for each section, thus results in the together 68 design variables. The optimisation problem is to minimise drag at the cruise lift condition while maintaining the internal volume of the aircraft obtained by the requirements that each master section should maintain its original area. This can be described as:

$$\begin{aligned}&\text{Minimize } C_D\\&\text{Subject to: } C_L \geq 0.23\\&\qquad\qquad V_i \geq V_{0i}, i = 1, \dots, 4\end{aligned} \tag{6-6}$$

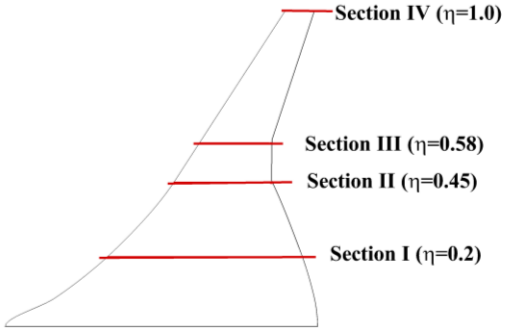

Figure 6.6 Location of the master sections for the optimization

The aerodynamic coefficients of the optimised BWB compared to the initial one is given in Table 6.3. The results confirm the improvement in aerodynamic performance gained by the optimization. The drag was reduced by 9 drag counts with the efficiency increasing from 21.29 to 23.21. Figure 6.7 compares the pressure coefficient distributions on the upper surface of the initial and optimised BWBs. The shock wave on the outer wing of the initial model is weakened through the optimization. As shown in Figure 6.8 of the comparison of the pressure coefficient at the station η= 0.9, the shock wave on the initial model has been eliminated. The comparison of the spanwise loading and spanwise local lift coefficient shown in Figure 6.9 indicates that the loading is shifted from outer wing to the centrebody after optimization, and the loading on the outer wing is near the elliptic one. The optimized model is set as the baseline model for the following studies.

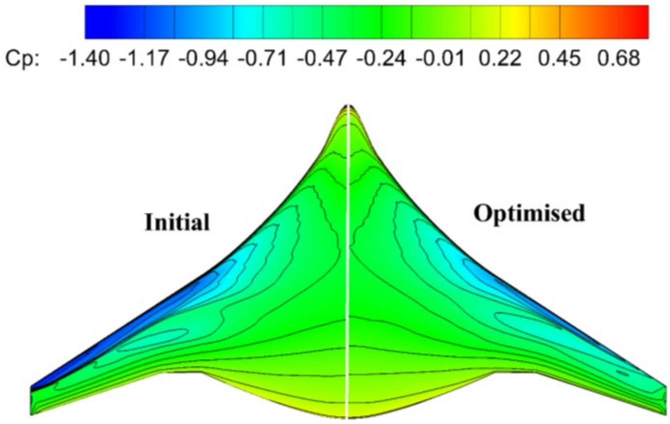

Figure 6.7 Comparison of the pressure coefficient distributions before and after optimized

Table 6.3 Results of the optimisation

Geometry	C_L	C_D	K
Initial	0.231	0.01085	21.29
Optimised	0.231	0.00995	23.21

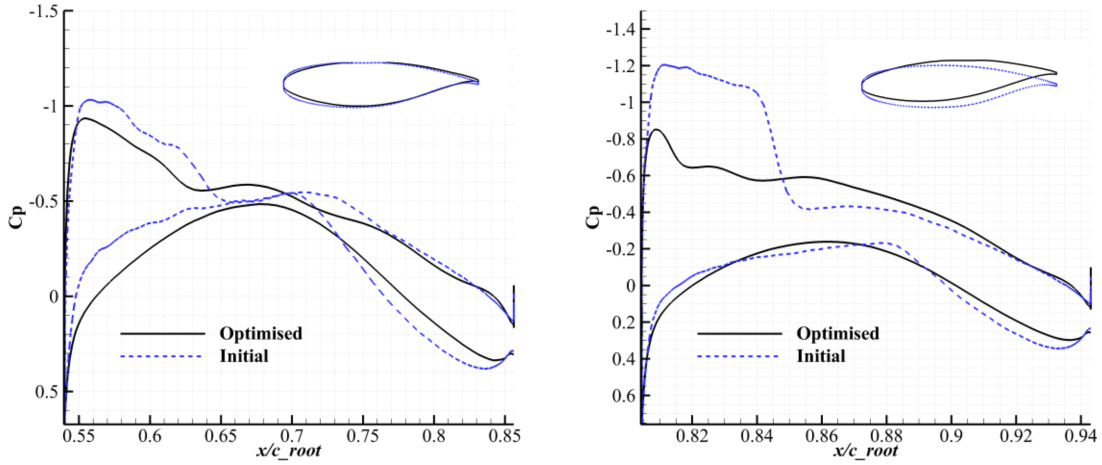

(a) η= 0.45 (b) η= 0.9

Figure 6.8 Comparison of the pressure coefficients on typical sections

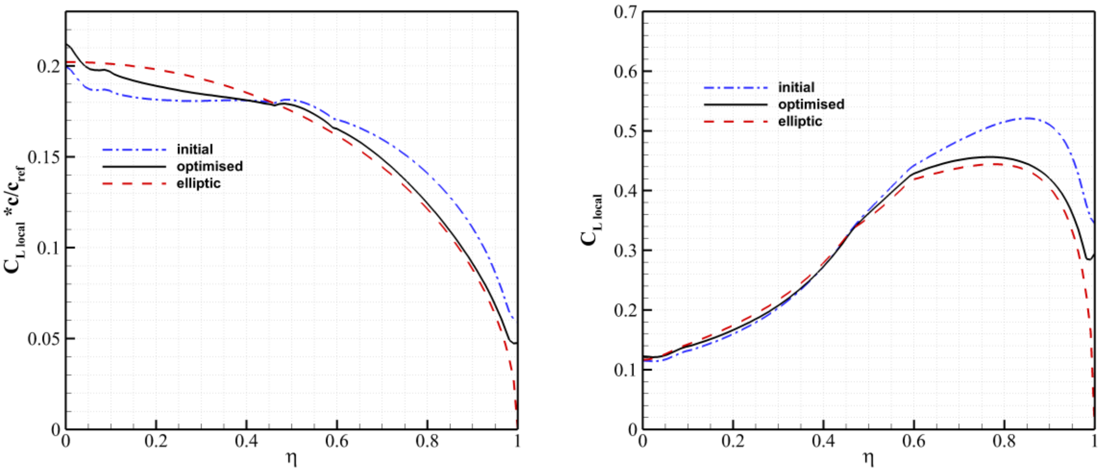

(a) $C_{L\ local}*c/c_{ref}\sim\eta$ (b) $C_{L\ local}\sim\eta$

Figure 6.9 Comparison of spanwise loading and spanwise local lift coefficient

6.2 Structural model design

As indicated by Liebeck [36], the structure of the BWB wings is similar to that of the conventional transport aircraft. However, for the BWB fuselage design, it was a high-risk task due to the significantly larger pressurization loads acting on the BWB fuselage structure compared to the conventional cylindrical fuselage as pointed out by Kukhopadhyay *et al*. [168]. This study does not aim at designing a structural model in detail but providing a structural model especially on the section of the outer wing, which can exhibit reasonable bending and torsion under aerodynamic loading. Therefore, in the structural design, the traditional wing box can be used to represent its structural characteristics. A finite-element model of the BWB model was built using the typical layout composing of ribs, spars, and skins for the eigenvalue analysis to obtain the parameters needed for the aeroelastic analysis. Non-structural masses are included in the finite element model as mass points to match the design take-off weight. Some of the design parameters from the Boeing BWB model in Ref. [36] are taken as reference data for the structural model design. A synopsis of the BWB configuration parameters used in this study is shown in Table 6.4. The thrust-specific fuel consumption (TSFC) is estimated based on the available data from Liebeck [36]. As estimated by Liebeck on the 2nd-generation Boeing BWB model, the wing structure weight is about 14.5% of the maximum take-off weight (W_{MTOW}) obtained from the figure showing the comparison of structural weight fractions between a BWB and a conventional configuration in Ref. [36]. This value is 13% in the study by Takahashi [44] on the B-777 class commercial transport. Since the values used in those two studies are similar, in this study, a value of 13% of W_{MTOW} is adopted for the wing structural weight fraction.

For the centre body part, ribs and spars are used to construct the frame. The sketch of the structural layout is shown in Figure 6.11. The structural properties of the model are shown in Table 6.5. The natural frequencies of the first five structural modes range from 1.83 Hz to 14.05 Hz. The first five structural modes and natural frequencies are shown in Figure 6.11.The analysis of this structural model under 2.5*g* load shows an approximately 3 m in vertical displacement at the wing-tip region and the strength analysis indicates that the structure meets the strength requirement. This structural model is then used for the following study.

Table 6.4 Parameters of the BWB model in this study

Parameter	Value
Design W_{MTOW}	140,000 kg
Cruise altitude	11 km
Maximum range	5000 km
Specific fuel consumption	0.459 lb/hr/lb
Wing structural weight fraction	～13% (of W_{MTOW})
Design load factor	2.5 *g*

Table 6.5 Properties of the BWB finite element model

Parameter	Value
Skin thickness (centre body/wing)	5, 3 mm
Rib thickness (centre body/wing)	50, 20mm
Spar thickness (centre body/wing)	30, 30mm
Young's modulus	72GPa
Poisson's ratio	0.33
Density	2810 Kg/m^3

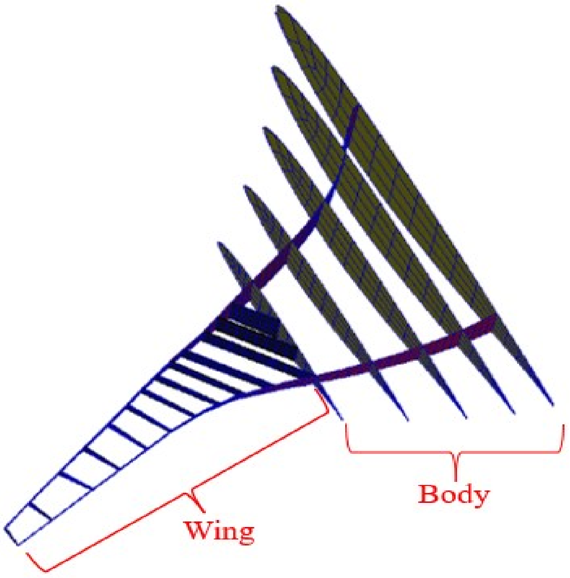

Figure 6.10 Structural layout of the ribs and spars

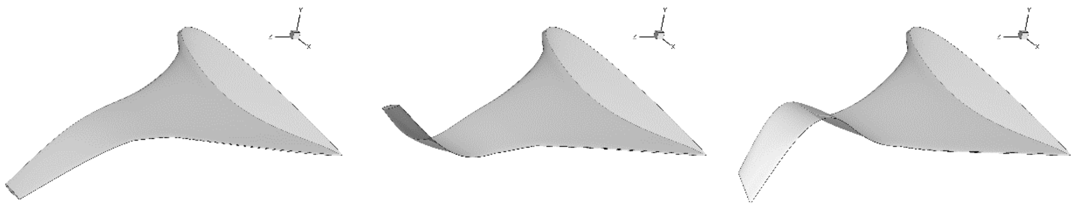

(a) Mode1, f_1= 1.83 Hz (b) Mode2, f_2= 5.87 Hz (c) Mode3, f_3= 10.72 Hz

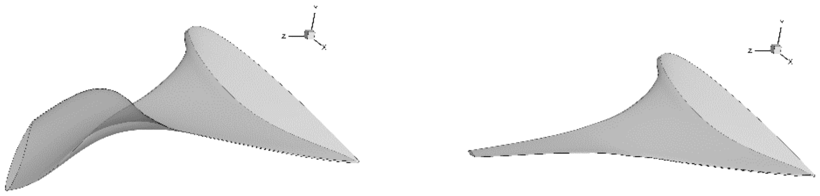

(d) Mode4, f_4= 13.59 Hz (e) Mode5, f_5= 14.05 Hz

Figure 6.11 First five modes and natural frequencies for the BWB structural model

6.3 Correlation between structural weight and root bending moment

Through the literature review in Chapter 2, it has been demonstrated that the traditional elliptic load distribution for the minimum induced drag does not guarantee the optimal overall performance if the wing structural weight is considered. Takahashi [44] and Iglesias *et al.* [42] have conducted the trade-off studies of spanwise loading on aerodynamic efficiency and wing structural weight. Qin *et al.* [53] first investigated the effects of spanwise lift distribution on aerodynamic efficiency for a BWB configuration without the consideration of structural weight. It is worth to explore how the spanwise load distributions will influence the BWB performance when wing structure weight is taken into the consideration because the BWB configuration has its own unique characteristics. Unlike the conventional traditional civil transports, for a BWB model, the wing-body is highly integrated and the spanwise load distribution is along the whole wing-body span, but for the wing root bending moment, only the load on the wing accounts for it.

Based on the work done by Qin *et al.* [53] and the correlation between wing structure weight reduction and spanwise load relief demonstrated by Takahashi [44], the influence of spanwise load distributions on the performance of a BWB configuration by taking both the aerodynamic characteristics and the structure weight into consideration under transonic speed is evaluated here.

Overall mission performance in terms of Breguet's Equation [169] is:

$$R = \frac{V}{TSFC}\left(\frac{L}{D}\right) \cdot \log_e\left(\frac{W_i}{W_f}\right) \tag{6-7}$$

where, V is the cruise speed, $TSFC$ is the thrust-specific fuel consumption, $\frac{L}{D}$ is the aerodynamic efficiency, W_i is the weight in the beginning of mission and W_f is the weight in the end of mission.

The fuel consumption will be

$$W_{fuel} = W_i - W_f = W_{MTOW}\left[1 - e^{\frac{R \cdot TSFC}{V \cdot \left(\frac{L}{D}\right)}}\right] \tag{6-8}$$

where, $W_{MTOW} = W_i$ is the maximum allowable weight at take-off.

In terms of incremental weights, referenced to the $\left(\frac{L}{D}\right)_{ref}$ as the baseline design, then for other designs, the increment of fuel consumption is

$$\Delta W_{fuel} = W_{MTOW}\left[e^{\frac{R \cdot TSFC}{V \cdot \left(\frac{L}{D}\right)}} - e^{\frac{R \cdot TSFC}{V \cdot \left(\frac{L}{D}\right)_{ref}}}\right] \tag{6-9}$$

From Eq. (6-9), in subsonic range, if the elliptic spanwise load design is the baseline design, any new designs deviating from the elliptic design will increase the fuel consumption for a certain cruise mission, as the elliptic design has the maximum lift-to-drag ratio.

For the basic operation weight W_{BOW} reduction

$$\Delta W_{BOW} = -W_{MTOW} \cdot k_1 \cdot rmbr \tag{6-10}$$

where, k_1 is the wing weight fraction proportional to wing root bending moment relief.

Combining Eq. (6-9) with Eq. (6-10), the net weight saving can be obtained as the percentage to the take-off weight as:

$$\text{Net (\%)} = \frac{\Delta W_{fuel} + \Delta W_{BOW}}{W_{MTOW}} = \left(e^{\frac{R \cdot TSFC}{V \cdot \left(\frac{L}{D}\right)_{ref}}} - e^{\frac{R \cdot TSFC}{V \cdot \left(\frac{L}{D}\right)_{new}}}\right) - k_1 \cdot rmbr \tag{6-11}$$

From Eq. (6-11), whether to design an elliptically loaded wing or to tailor the wing for bending moment relief for better overall performance is actually transferred to whether the fuel consumption increment is less than the structural weight saving.

6.4 Influence of spanwise loading on the performance

Based on the baseline model and its structural model, inverse twist designs for specified spanwise loading are performed under static aeroelasticity. Five models with typical spanwise loading are generated. The wing root bending moment relief factors of these models are then evaluated under critical gust load case, followed by the assessment of the influence of the spanwise load distributions on aerodynamic efficiency and system performance.

6.4.1 Inverse twist design for specified spanwise loading

- **Calculation of target span loading**

Given the cruise lift coefficient C_L= 0.23 as the target lift coefficient, for particular spanwise load distribution, the lift coefficient distribution can be calculated by the following equations. The circulation Γ associated with the target spanwise loading is

$$\Gamma(\eta) = \frac{1}{2} C_{L\,local}(\eta) \cdot c(\eta) \cdot U_\infty \tag{6-12}$$

where, $C_{L\,local}(\eta)$ is the spanwise sectional lift coefficient, $c(\eta)$ is the chord distribution and U_∞ is the freestream flow velocity.

for the elliptic circulation distribution,

$$\Gamma_e(\eta) = \Gamma_{0,e}\sqrt{1-\eta^2} \tag{6-13}$$

for the triangular case,

$$\Gamma_t(\eta) = \Gamma_{0,t}(1-\eta) \tag{6-14}$$

for the averaged distribution of the upper two cases

$$\Gamma_a = \frac{\Gamma_e + \Gamma_t}{2} \tag{6-15}$$

First, calculate the total circulation based on the lift coefficient distribution or the total lift coefficient C_L

$$\Gamma_0 = \frac{1}{2} V_\infty \cdot \int_0^1 C_{L\,local}(\eta) \cdot c(\eta)\, d\eta = \frac{1}{2} \cdot V_\infty \cdot \frac{C_L \cdot s}{b} \tag{6-16}$$

then, we can get

$$\Gamma_{0,e} = \frac{4}{\pi}\Gamma_0 \tag{6-17}$$

$$\Gamma_{0,t} = 2\Gamma_0 \tag{6-18}$$

where, $\frac{4}{\pi}$ and 2 are the integral value of $\sqrt{1-\eta^2}$ and $(1-\eta)$ respectively. The lift distribution for the elliptic and triangular loading will be

$$C_{L,e}(\eta) = \frac{2\cdot\Gamma_{0,e}\sqrt{1-\eta^2}}{c(\eta)} = 2\cdot\frac{\frac{4}{\pi}\Gamma_0\sqrt{1-\eta^2}}{c(\eta)U_\infty} \tag{6-19}$$

$$C_{L,t}(\eta) = \frac{2\cdot\Gamma_{0,t}(1-\eta)}{c(\eta)} = 2\cdot\frac{2\Gamma_0(1-\eta)}{c(\eta)U_\infty} \tag{6-20}$$

Here, considering the elliptic and triangular loading as the two extreme distributions, the design with other load distributions can be defined as

$$C_L(\eta) = \xi C_{L,e}(\eta) + (1-\xi)C_{L,t}(\eta) \tag{6-21}$$

where $0 \le \xi \le 1$, which is the weighting coefficient between elliptic and triangular distributions. This means that $\xi = 1$ represents an elliptic design, $\xi = 0$ for a triangular design, and $\xi = 0.5$ for an averaged elliptic-triangular design.

For the cruise condition with $C_L = 0.23$, the design with the target elliptic, triangular and averaged spanwise load and lift coefficient distributions can be calculated as shown in Figure 6.12.

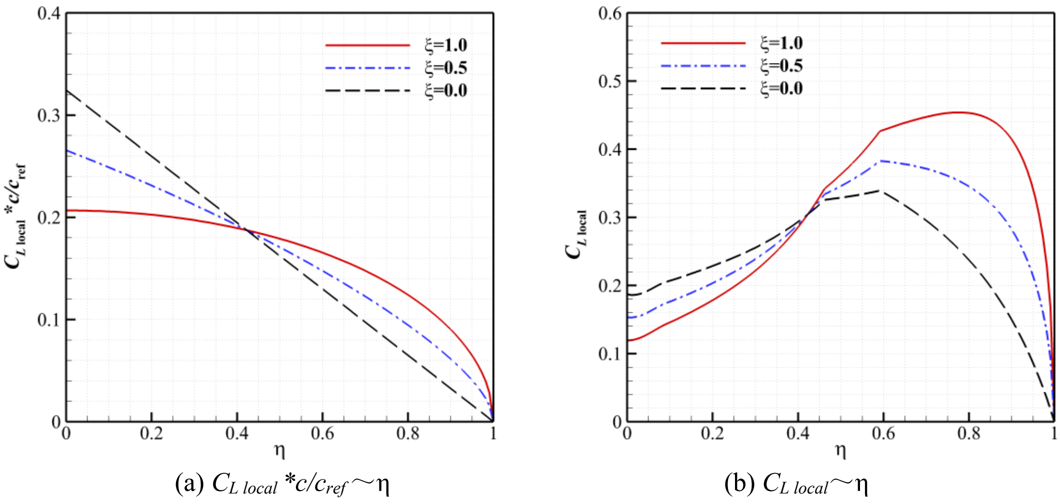

(a) $C_{L\ local}*c/c_{ref}\sim\eta$ (b) $C_{L\ local}\sim\eta$

Figure 6.12 Spanwise loading and spanwise local lift coefficient for three target cases

- **Results of the inverse twist designs**

The inverse twist design for specified spanwise loading is considered as an optimization problem described as follows:

Objective function: minimize $\sum_{i=1}^{n} \left| C_{L\,local}(i) - C_{L\,local_{target}}(i) \right|$

where, $C_{L\,local_{target}}$ is the sectional lift coefficient of the target design, *n* is the spanwise section number or the number of the spanwise grid points.

Design variables: Twelve sectional twist angles shown in Figure 6.13 are used as the design variables. The twist rotation centre is fixed at the leading edge of each section.

The process of the inverse designs is described in the flow chart in Figure 6.14. For the inverse design, the twelve sectional twist angles as shown in Figure 6.13 are optimized to minimize the objective function, resulting in the spanwise loading approaching to the objective target loading. The optimization approach is the genetic algorithm used previously. The population number is set to 48 for these 12 variables and the maximum generation number is set to 100. For mesh deformation, surface mesh is first deformed with new twist angles. The volume grid is then propagated from the wing surface to the far-field using the methods described in Section 6.1. The fluid-structure interaction is performed by URANS solutions considering the static aeroelasticity.

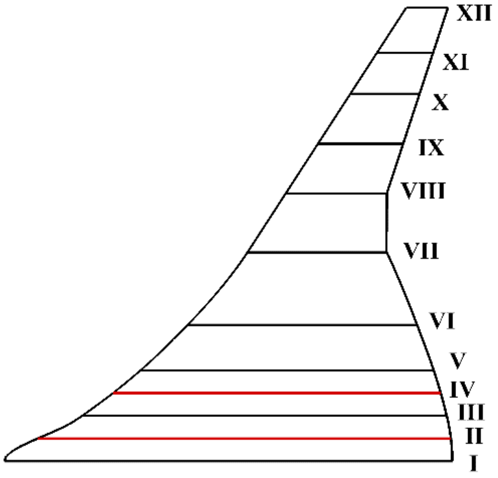

Figure 6.13 Sectional twist design variables

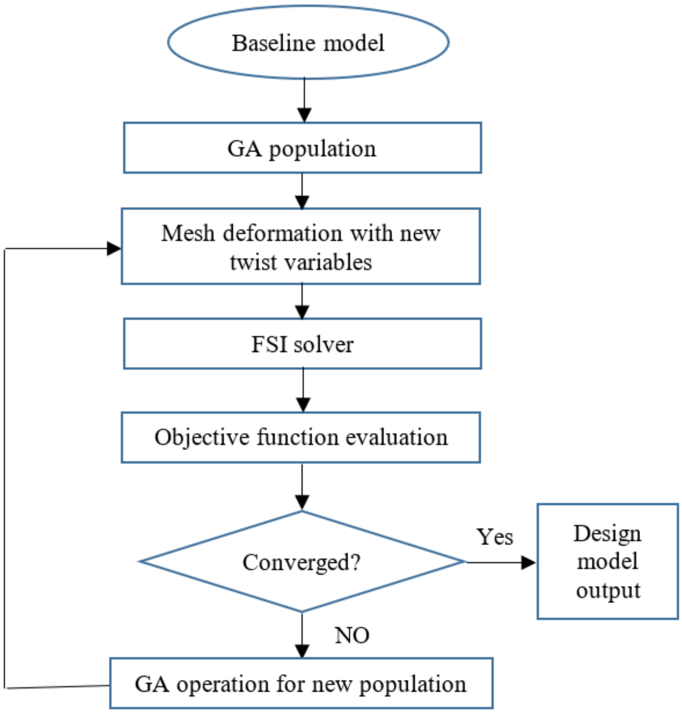

Figure 6.14 Flow chart of the inverse design

The results of the inverse twist designs are presented in Figure 6.15. Five models with ξ= 0.0, 0.25, 0.5, 0.75, 1.0 are designed. In the figure, the target data are also shown for comparison. The comparison shows a good agreement between the designed results and the target ones, which indicates that the inverse twist designs are effective and the intended spanwise loading distributions are reasonably achieved.

Among these five designs, the elliptic design and the triangular design are two extreme designs. For the elliptic design, the local lift coefficient peaks at about 75% of the span with a local C_L= 0.44, whereas the triangular design has a much lower loading on the outer wing, as the peak value of the local lift coefficient is only 0.34 at about 60% of the span. It is clear that the triangular design shifts the lift gradually from the outer wing to the centre part, as the local lift coefficient on the centre section reaches to 0.19 compared to only 0.115 for the elliptic design. Due to the higher loading on the outer wing, the wing-tip deformation of the elliptic design is also higher than other designs as shown in Figure 6.16. Figure 6.17 compares the pressure coefficient distributions for the ξ= 0.0, 0.5, 1.0 designs. The shift of the load from the outer wing to the centre body for the triangular and averaged designs compared to the elliptic design is clearly shown.

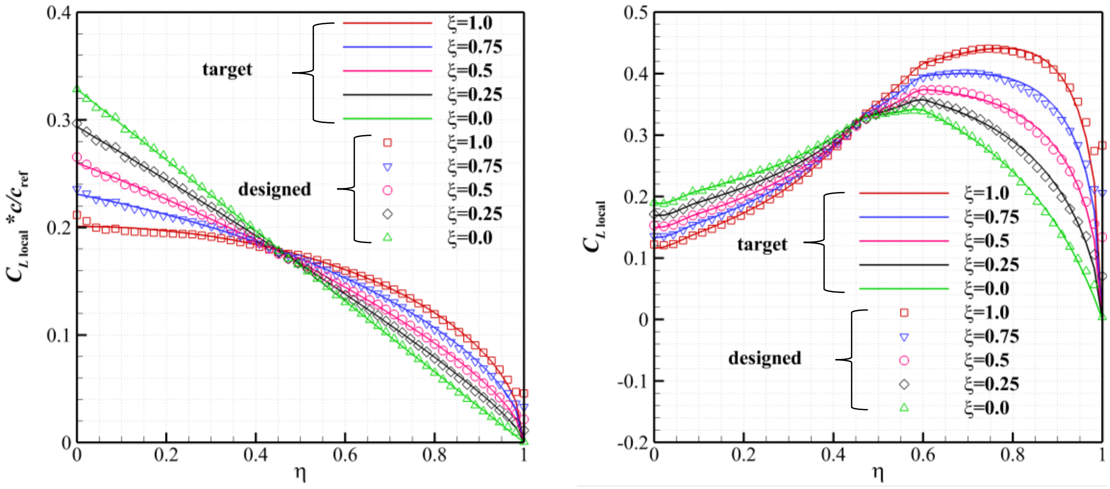

(a) Spanwise loading (b) Spanwise local lift coefficient

Figure 6.15 Comparison between the designed results and the target data

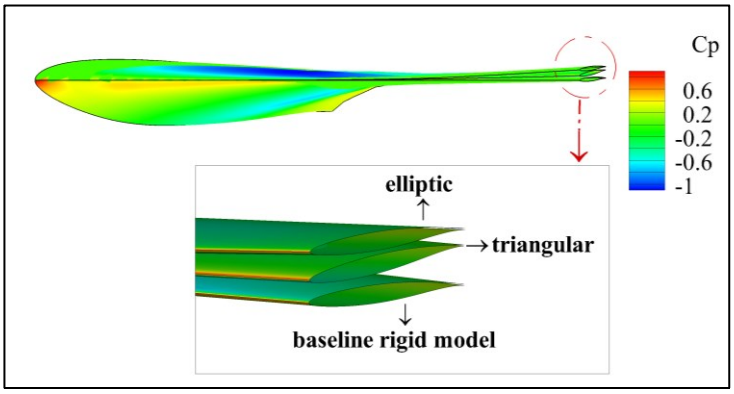

Figure 6.16 Comparison of the wing-tip deformation

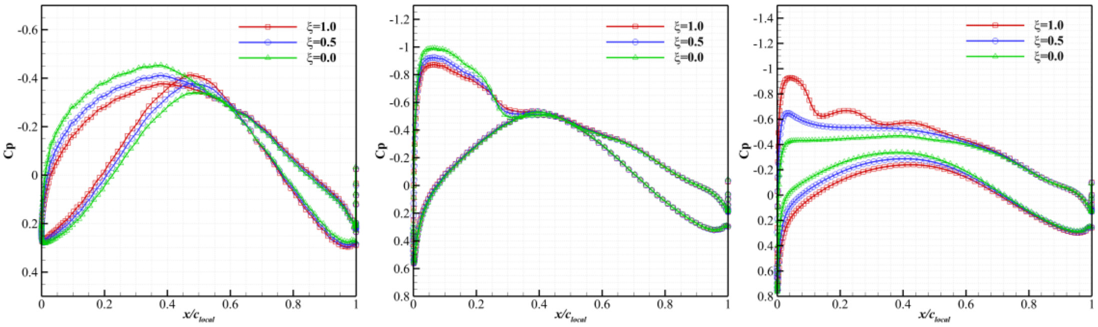

(a) η= 0.05 (b) η= 0.40 (c) η= 0.80

Figure 6.17 Comparison of chordwise distribution of pressure coefficient at different spanwise sections

6.4.2 Comparison of the aerodynamic performance among these designs

Table 6.6 shows the drag coefficients and lift-to-drag ratios for these new designs at the design lift coefficient C_L= 0.23 and the cruise speed M_∞= 0.8. The results show that, among these five designs, the design with the minimum total drag is the one with elliptic distribution, and thus, the highest aerodynamic efficiency with C_L/C_D= 23.25. This is consistent with the transonic aerodynamic design optimization study on the similar BWB configuration by Lyu *et al.* [163] using a discrete adjoint method, where the optimized design has a near elliptic lift distribution. On the other hand, the triangular distribution has the maximum total drag, with 18 counts more than the elliptic design, and the lift-to-drag ratio is reduced to 19.67. However, it is noticeable that the drag and aerodynamic efficiency of the designs with ξ= 0.5, 0.75 is quite close to the elliptic design, with only 4.6 and 1.6 drag counts penalty respectively. As expected, the variation of the skin friction drag with the difference of spanwise loading is rather small.

As compared with the elliptic design, the other four designs have a much smaller wing root bending moment as shown in Table 6.6. For example, the wing root bending moment is reduced to 0.0492 for the triangular design relative to C_{mx} =0.0757 for the elliptic design. That results in about 35% for the wing root bending moment relief factor. That is the main difference between a BWB model and a traditional transport aircraft. For the traditional transport aircraft, the subject of both the spanwise load distribution and the wing root bending moment is the wing. The wing root bending moment relief from an elliptic design to a triangular design cannot reach such a high value. As indicated by Takahashi [44], this value is about 15%. For the comparison, considering the BWB model as the traditional wing that the root bending moment is measured through the whole span from the tip to the centre section, the root bending moment relief from the elliptic design to the triangular one is only 15.8%, which is close to the result obtained by Takahashi.

Table 6.6 Comparison of drag coefficients and aerodynamic efficiency at cruise condition

Distribution	$C_{D,\,total}$	$C_{D,pressure}$	$C_{D,friction}$	C_L/C_D	C_{mx}
ξ=1.0	0.00989	0.00542	0.00447	23.25	0.0757
ξ=0.75	0.01005	0.00556	0.00449	22.89	0.0671
ξ=0.5	0.01036	0.00585	0.00450	22.21	0.0613
ξ=0.25	0.01103	0.00649	0.00454	20.85	0.0551
ξ=0.0	0.01170	0.00711	0.00459	19.67	0.0492

6.4.3 Evaluation of the *rmbr* under critical ultimate load condition

As compared with the elliptic design, the other four designs have a smaller wing root bending moment and benefit from the structural point of view. Therefore, if the benefits from the structural weight overweigh the penalty in the aerodynamic efficiency, then the elliptic distribution will be not the one with the best overall aircraft performance.

As the aircraft structure weight is determined by the critical load not the cruise condition, the wing root bending moment of these designed models should be compared under critical load conditions to determine the wing root bending moment relief factor $rmbr$. The one-minus-cosine gust with the peak gust value producing a near ultimate $2.5g$ load factor is used for the simulation. To meet this critical load, the one-minus-cosine gust velocity is about w_{g0}/U_{∞}= 0.12 with the gust wavelength of 12.5c_{ref}.

For the calculation, the aircraft is initially assumed at cruise flight and then encounters the gust perturbations. Figure 6.18 shows the comparison of the time evolution of the lift coefficient of the models with elliptic, triangular and averaged spanwise load distributions. As these models are designed under the same cruise lift coefficient, the lift coefficients of the three models shown in Figure 6.18 started from the same value at the initial time. With the time evolution, the gust value increases, and the differences of the lift coefficients among different models start to appear. The elliptic distribution has the smallest lift coefficient at s= 8.6 where the gust peaks, while the triangular one has the largest value. From the comparison of the model deformations between the elliptic design and the triangular design shown in Figure 6.19, we can see that the elliptic design has a much larger model deformation than that of the triangular one under the same gust condition due to the higher loading on the outer wing. To be specific, the wing-tip displacement of the elliptic one reaches to 2.9 m, whereas the triangular one is only 1.8 m at s= 8.6 as shown in Figure 6.20. In the meantime, the increment of the twist angle due to the elasticity from s=0 to s= 8.6 along the span is also larger than that of the triangular one as shown in Figure 6.20 (b). At s= 8.6, the nose-down twist angle increment is 2.4° for the elliptic model, while this value is only 1.6 ° for the triangular design.

The reduction of the lift coefficient under the same gust load of the elliptic design compared to other models does not change the fact that it has the largest wing root bending moment as shown Figure 6.22. However, the time evolution of the wing root bending moment relief factor of the triangular design relative to the elliptic design

($rmbr_{triangular} = 1 - \frac{(wing\ root\ bending\ moment)_{triangular}}{(wing\ root\ bending\ moment)_{elliptic}}$) does show a reduction under the critical load at s=8.6 which is 30%, while this value is 35% at the initial cruise condition as shown in Figure 6.22 (b). That is because under the same gust condition, the elliptic design has a larger deformation on the outer wing compared to the triangular design. This deformation in return will cause a more load alleviation on the outer wing, resulting in the reduction of the wing root bending moment.

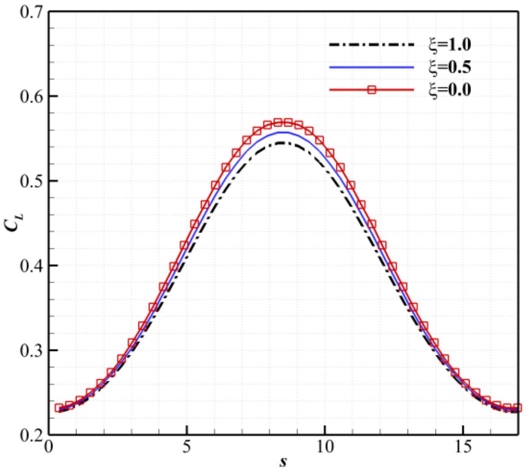

Figure 6.18 Time evolution of the lift coefficient

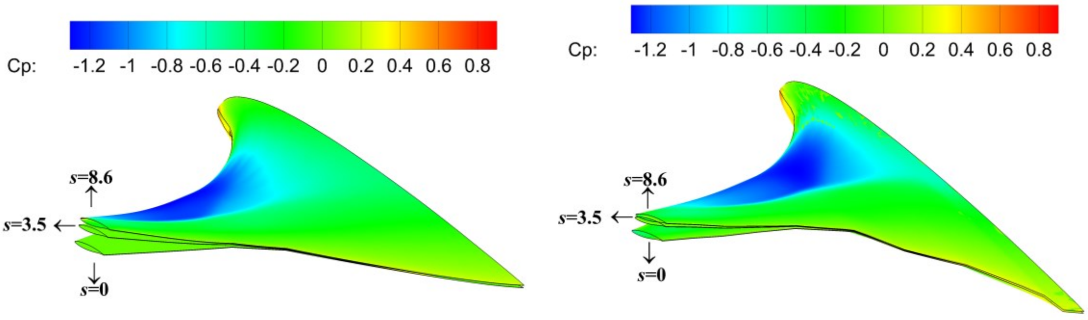

(a) elliptic design (b) triangular design

Figure 6.19 The model deformation at different times

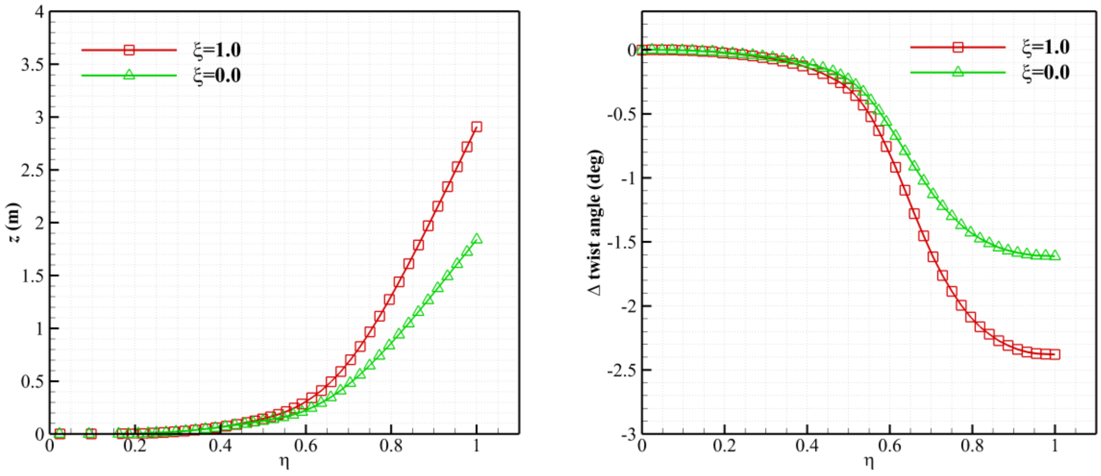

(a) wing-tip displacement (b) Δ twist angle (twist angle $_{s=8.6}$ - twist angle $_{s=0}$)

Figure 6.20 Comparison of the wing-tip displacement and twist angle changes

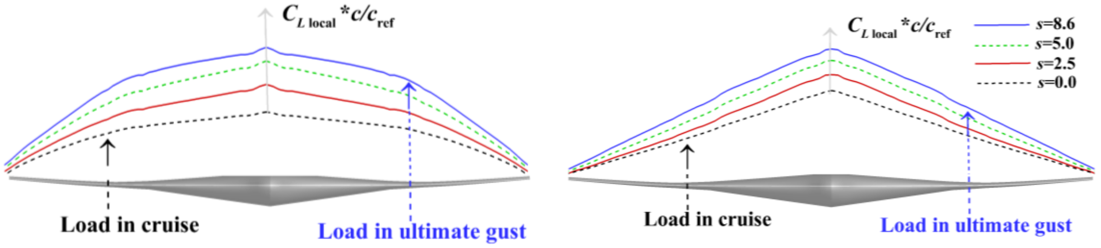

(a) Elliptic design (b) Triangular design

Figure 6.21 Time evolution of the spanwise load distribution

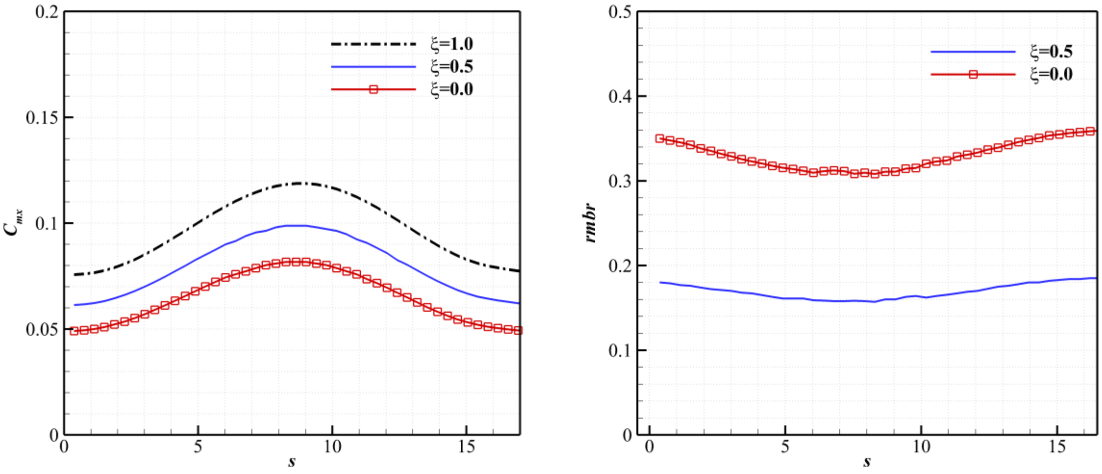

(a) wing root bending moment coefficient (b) wing root bending moment relief factor

Figure 6.22 Time evolution of the wing root bending moment coefficient and the relief factor

6.4.4 Results of the trade-off study

Based on Eq. (6-11) and the parameters listed in Table 6.4, the structural weight reduction and fuel increase can be calculated for the new designs relative to the elliptic one. The net weight saving is the sum of the structural weight saving and the fuel consumption increase. For the proportional correlation between wing structural weight and the wing root bending moment relief, two different values: 50% argued by Takahashi [44] and 100% believed by Iglesias and Mason [42], are both tested in this study. Since the wing structure is of 13% W_{MTOW}, the effects of wing root bending moment relief upon structural weights will result in 6.5% W_{MTOW} and 13% W_{MTOW} proportional to the wing root bending moment according to the arguments of Takahashi and Iglesias, respectively.

The effect of wing root bending moment relief on the cruise lift-to-drag ratio is shown in Figure 6.23. The result gives that tailoring the spanwise load distribution to favour a reduced wing root bending moment (decrease in the value of ξ) results in a decrease in lift-to-drag ratio, thus an increase of fuel consumption. The result of the wing root bending moment relief factor in Figure 6.23 (b) indicates a significant gain in *rmbr* with the spanwise load shifting from the elliptic to the triangular ones.

If 6.5% of the overall aircraft weight were governed by the wing root bending moment, the reduction of the structure weight will compensate the increased fuel weight for *rmbr* less than about 0.2 as shown in Figure 6.24 (a). As for the net weight saving, the averaged elliptic-triangular design has the best performance, as about 0.37% of the W_{MTOW} weight saving is obtained.

However, if 13% of the overall airframe weight were governed by wing root bending moments, a structurally tailored design would have a more significant system performance benefit as shown in Figure 6.24 (b). A 16.7% reduced wing root bending moment design would lead to a net saving of 1.3% W_{MTOW}. However, a further reduction in wing root bending moment will have no further improvement on net weight saving despite of its favourable influence on structural weight saving. That is because the fuel consumption weight presents a parabolic increase with the wing root bending moment relief, while the structural weight saving appears a linear trend. Therefore, a near plateau of net saving appears under the value of *rmbr* between 16.7% and 31%.

For the same initial take-off weight, the fuel consumption weight is taken as 30% W_{MTOW} for the elliptic design. If the weight saving from structure is used for carrying extra fuel to maintain W_{MTOW}, the cruise range for different designs can be compared to the elliptic design as shown in Figure 6.25. For the case that 6.5% of the overall aircraft weight governed by the wing root bending moment, no significant increase in range is obtained for tailoring the loading from elliptic to triangular designs. However, 3.1% increase in range is achieved for the design with $\xi = 0.5$ if 13% of the overall aircraft weight were governed by wing root bending moments.

From the results of this BWB model, it is clear that moderately tailoring the model for a reduced bending moment is beneficial for the net weight saving. This is different from the conclusion of the studies on the traditional civil transports. As mentioned before, Takahashi [44] indicated that the design for a reduced wing root bending moment would impair the mission performance. The reason is mainly due to the lower wing root bending moment relief factor that the traditional civil transports can achieve from shifting the load from wing tip to wing root compared to BWB models. For the BWB model, the wing-body is highly integrated and the spanwise load distribution is along the whole wing-body configuration, but for the wing root bending moment relief factor, only the load on the wing is taken into consideration. For the traditional civil transports, only the wing is studied on both the spanwise load and wing root bending moment. Therefore, the wing root bending moment relief factor of the BWB model will be higher than that of the traditional civil transports for a specified load distribution relative to the elliptic design. For example, the triangular design of a BWB model in this study has a wing root bending moment relief factor of 35% under cruise condition, while it is only about 15% in the study of Takahashi.

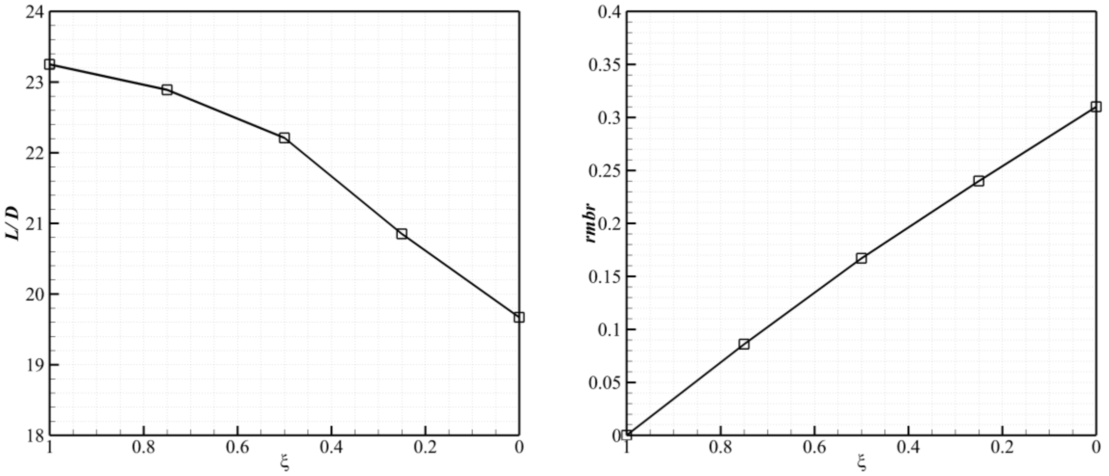

(a) *L/D* (b) *rmbr*

Figure 6.23 Effects of wing root bending moment relief on cruise lift-to-drag ratio

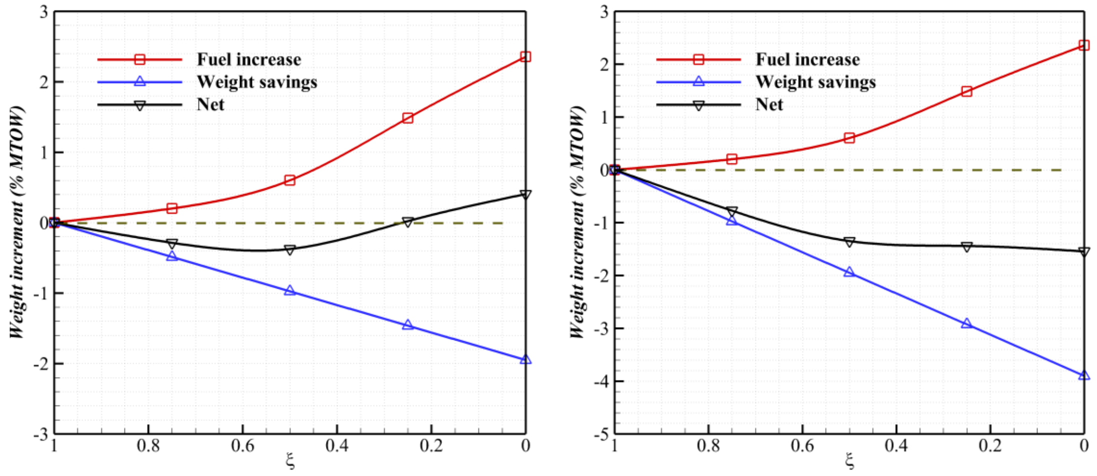

(a) 6.5% W_{MTOW} proportional to *rmbr* (b) 13% W_{MTOW} proportional to *rmbr*

Figure 6.24 Effects of wing root bending moment relief on weight saving

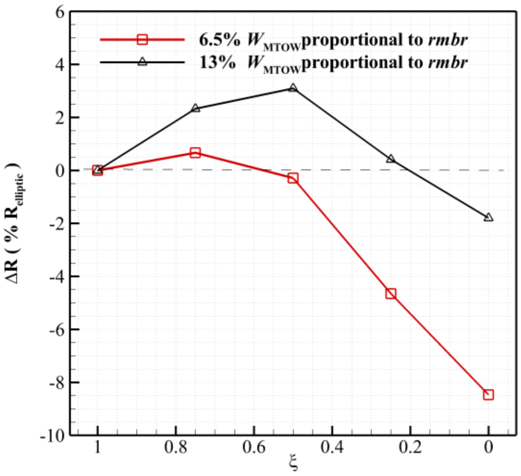

Figure 6.25 Comparison of the range for different designs

6.5 Summary

A BWB model reference to Boeing 2nd-generation BWB planform was generated and optimised at a transonic cruise condition together with the setup of its structural model. Based on the studies by Qin *et al*. [53] and Takahashi [44], the trade-offs between aerodynamic efficiency and wing structure weight governed by wing root bending moment was investigated. Typical models with tailored spanwise loading have been designed at the design transonic cruise lift condition using high-fidelity URANS solutions coupling inverse optimization code considering the static elasticity. The aerodynamic efficiencies were compared, followed by the evaluation of the wing root bending moment among these models. Some findings are summarized here.

In terms of aerodynamic efficiency, the elliptic design shows the best performance under the design transonic cruise condition, which has the lowest total drag. For the triangular design, the increase in total drag of up to 18 counts compared to elliptic design comes from the increase in the pressure drag.

A slight shifting of the span load from the outer wing to the centre body can achieve a significant reduction in wing root bending moment relief with a small penalty in aerodynamic efficiency, due to the integrated wing-body characteristics. 19% of wing root bending moment relief is obtained for the averaged elliptic-triangular design relative to the elliptic design, while the loss in aerodynamic efficiency is only 4.4% with the drag increase of 4.6 counts.

Given that 50% and 100% of the wing structure weight is governed by the root bending moment, net weight savings between 0.37% and 1.3% of W_{MTOW} have been achieved for the averaged elliptic-triangular design relative to the elliptic design. Even though these results are obtained under the given cruise range, propulsive efficiency and wing weight, these results provide a useful insight into the impact of spanwise load distribution on aerodynamic efficiency and wing structure weight saving for the BWB model.

Chapter 7

Blended-wing-body gust load alleviation

In this chapter, the assessment of the gust load alleviation effects by CC and normal microjet blowing is extended on the BWB model designed in Chapter 6. The understanding of the capability of gust load alleviation by these two fluidic actuators on this kind of layout can provide useful insights into the potential application. The baseline BWB model used in Chapter 6 is firstly modified to include the Coanda devices and normal microjet slots on different spanwise locations. The load control effects of these different located CC and microjets are then evaluated and compared at subsonic and transonic speeds. Gust load alleviation effects of these two approaches are then tested under typical discrete gusts defined by EASA CS-25 [2]. Finally, for a demonstration case, the BWB wing structure weight reduction is estimated due to the alleviation of the $2.5g$ critical gust load at cruise condition by CC and normal microjet blowing.

7.1 Blended-wing-body with circulation control

7.1.1 Setup of the blended-wing-body model with trailing-edge Coanda device

In order to include the trailing-edge Coanda device on the SACCON model, Hoholis [15] truncated the wings' trailing edge at the location where the thickness is adequate. Then, a new semi-circular trailing edge was added as the Coanda surface. As the supercritical aerofoils used widely in the modern commercial aircraft wings tend to have a small thickness ratio, especially near the trailing edge. Modification by truncating the trailing edge will inevitably reduce the area of the wing, resulting in the problem for providing enough lift force at the original flying conditions. On the numerical study of CC on a supercritical aerofoil, Forster [153] modified the aerofoil through enlarging the trailing-edge thickness symmetrically along the camber line. This method was demonstrated having negligible influence on the aerofoil aerodynamic characteristics. Here, a similar modification is applied to the baseline BWB model. Along the camber line, the rear 30% wing aerofoil sections are thickened symmetrically. Geometry parameters of the Coanda surface used for the BWB model are the same as those used in the previous studies. To be specific, the trailing-edge Coanda surface is semi-circular with the radius of 0.5%c_{local}, and the height of the slot exit is 1:20 to the radius. Based on the designed radius, the required increment of the thickness on each wing aerofoil section along the span can be calculated for the Coanda surface design. The comparisons of the baseline aerofoil sections against the modified ones at the spanwise section of η=0 and η= 0.5 are shown in Figure 7.1. For the section of η=0, the trailing edge thickness was changed from 0.35%$c_{\eta=0}$ to 1.23%$c_{\eta=0}$.

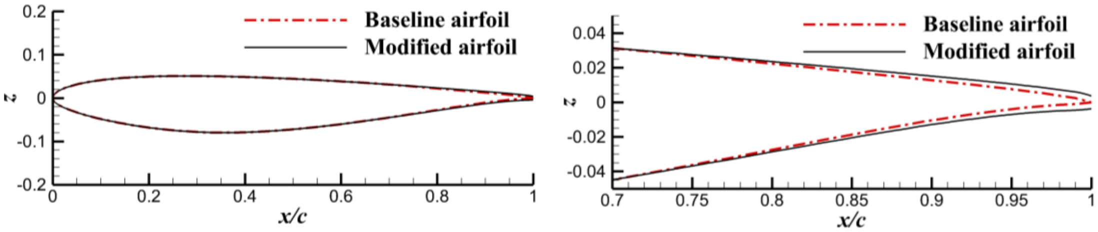

(a) η= 0

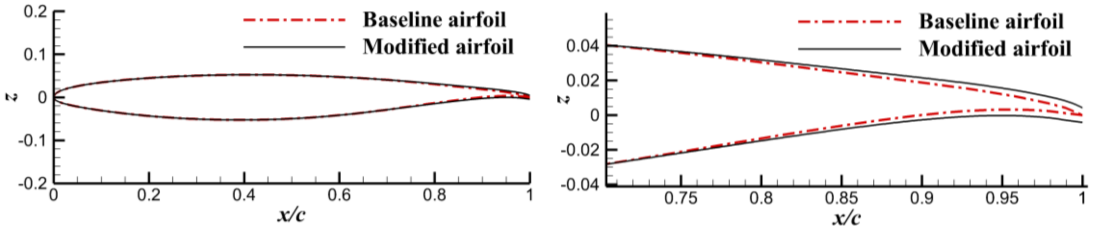

(b) η= 0.5

Figure 7.1 Comparison of the aerofoil section between the baseline and the modified ones

In order to test the efficiency of CC deployed on different spanwise locations, three slots on the centre body, inner and outer wings, respectively with equal spanwise length (l_{cc}=0.3b, 30% of the half span) are studied as shown in Figure 7.2.

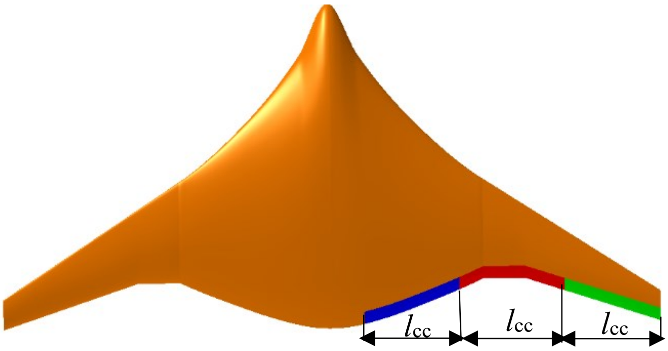

Figure 7.2 The locations of CC on the BWB model

7.1.2 Grid convergence of the model with circulation control

Based on the grid convergence results of the baseline model described in Chapter 6, a further refinement to include additional cells on the Coanda surface is conducted to generate the baseline grid for the BWB model with Coanda surface. Figure 7.3 shows the sketch of the baseline grid with the total cells of about 7×10^6 in the half span domain. From this, a coarser and a finer grid are generated with a refinement factor of about 1.5 in each direction. Table 7.1 gives the effects of grid resolutions on the aerodynamic coefficients at M_∞= 0.8, α= 2.5° under a blowing momentum coefficient of C_μ= 1.78×10^{-4}. The estimation of aerodynamic coefficients with an 'infinite' grid is performed using the Richardson extrapolation by $C_{continuum} = C_{23.6m} + \frac{(C_{23.6m} - C_{7.0m})}{(r^2-1)}$, where r= 1.5. The lift coefficient of the medium grid is within 1.7% of the continuum estimate, and it is less than 3% for the drag and root bending moment coefficients. The medium grid was chosen for the following studies.

Table 7.1 Effect of half-span grid resolution on aerodynamic

Grid size	2.1×10^6	7.0×10^6	23.6×10^6	Continuum
C_L	0.1307	0.1315	0.1328	0.1338
C_D	0.01085	0.01073	0.01064	0.01056
C_{mx}	0.0602	0.0611	0.0621	0.0629

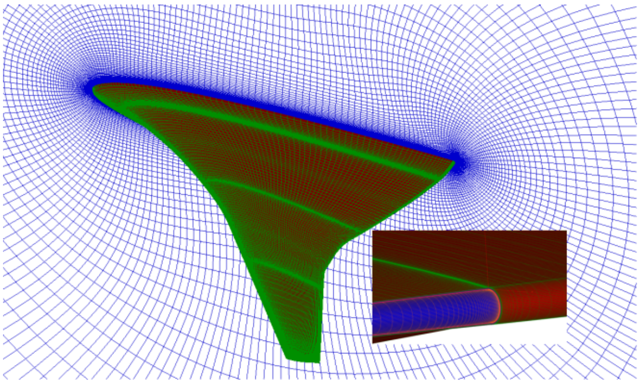

Figure 7.3 Grid detail on the trailing edge near the centrebody

7.1.3 Evaluation of the influence of including the Coanda device on the blended-wing-body performance

To understand how the modifications to the baseline BWB model influence the aerodynamic behaviour, the aerodynamics of the models before and after the including of the CC devices are compared at $M_\infty = 0.8$ under a series of angles of attack as shown in Figure 7.4. The results indicate that the influence of the Coanda surfaces and the thickened trailing edges is small, especially on the lift characteristic. At small angles of attack, a slight increase in drag by 4 counts relative to the baseline model is observed. This drag penalty results in approximately 3.8% reduction in the aerodynamic efficiency under the cruise condition. The influence on drag coefficients declines with increasing angles of attack.

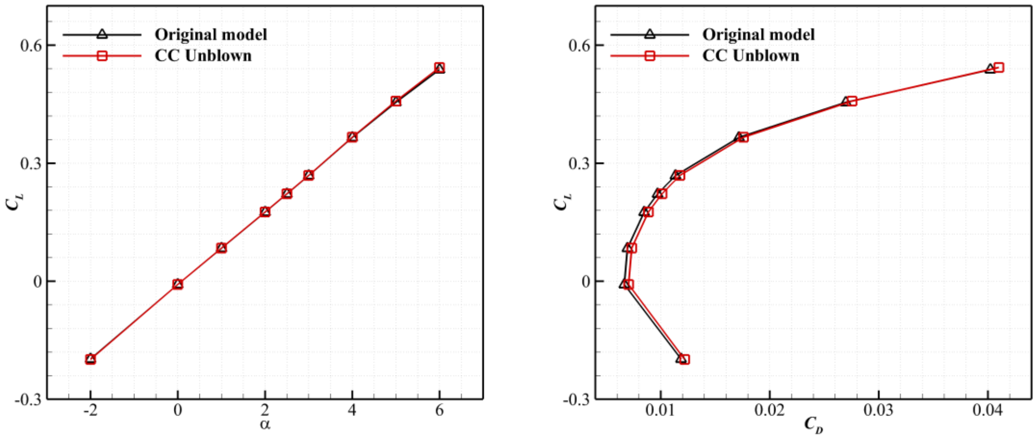

(a) $C_L \sim \alpha$ (b) $C_L \sim C_D$

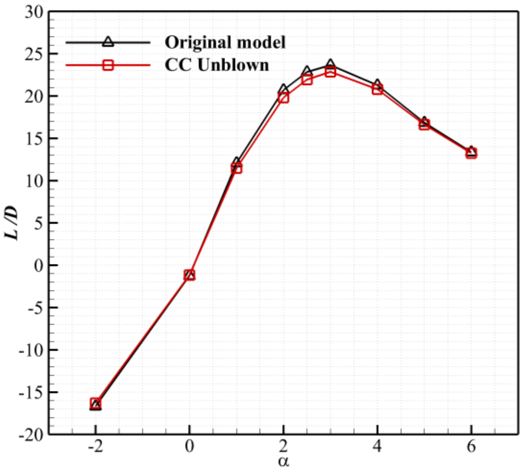

(c) $L/D \sim \alpha$

Figure 7.4 Comparisons of the aerodynamic performance between models before and after the including of CC devices at $M_\infty = 0.8$

7.1.4 Load control performance of circulation control under steady conditions

To get an understanding of the load control performance of CC deployed on the three different locations, the load control effects in terms of lift and root bending moment at a range of momentum coefficients are compared under subsonic and transonic steady conditions.

- **Transonic speed case at $M_\infty = 0.8$**

Figure 7.5 presents the comparisons of load control effects in terms of lift coefficient reduction at cruise condition. As expected, the outer wing located CC has the lowest maximum lift reduction compared to another two located CC, which is due to the smaller chord length and wing area on the outer wing sections. The maximum ability of outer-wing CC in terms of lift coefficient reduction is only -0.016, while it is -0.041 and -0.063 for the models with CC on the inner wing and centre body, respectively.

Through adjusting the blowing momentum coefficient to obtain the same lift coefficient reduction of $\Delta C_L = -0.016$ for the three located CC models, the distribution of spanwise local lift coefficient can be compared as shown in Figure 7.6. This comparison indicates that under the same total lift reduction, the local lift coefficient reduction is more significant for the outer-wing CC model than the other two models. The reduction in root bending moment coefficient is compared under the same $\Delta C_L = -$

0.016 for the three located CC models as shown in Table 7.2. The outer-wing CC generates the most reduction of -0.0101 in root bending moment coefficient, while this value is only -0.0024 and -0.0067 for the centre-body CC and inner-wing CC, respectively. Before the 'C_μ-stall' region, the outer-wing CC can generate more root bending moment reduction under the same integrated lift reduction due to the longer moment arm. The utmost abilities of these three located CC for lift and root bending moment coefficients reductions are shown in Table 7.3. The centre-body CC generates the most lift coefficient reduction of -0.063 which is four times of the value from the outer-wing CC, but the maximum root bending moment reduction by these two CC is similar. The inner-wing CC has a stronger capability for root bending moment relief as a maximum value of -0.0152 has been obtained.

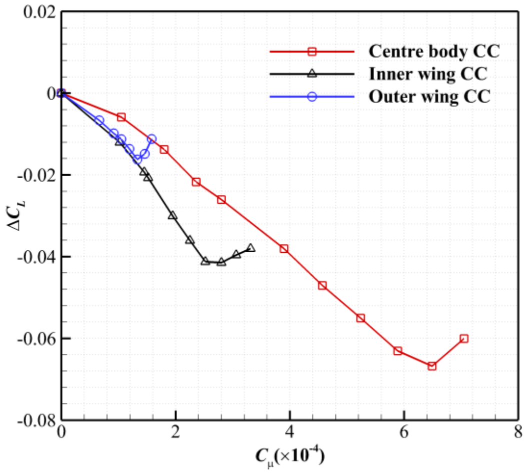

Figure 7.5 Comparisons of lift reduction from different located CC

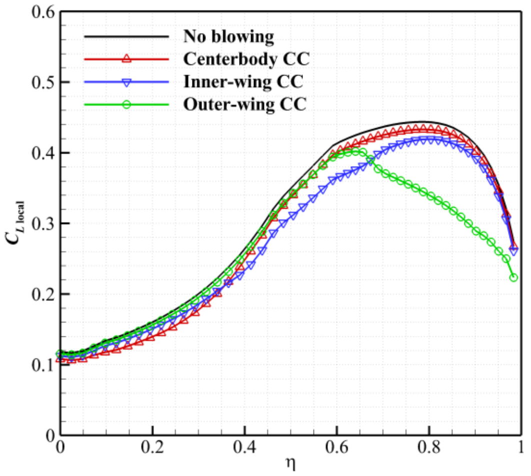

Figure 7.6 Comparisons of the spanwise local lift coefficients under the same ΔC_L= -0.016 for the three located CC models

Table 7.2 Root bending moment coefficient under the ΔC_L= -0.016

Model	C_{mx}	ΔC_{mx}
Unblown	0.0779	---
Centre body CC	0.0755	-0.0024
Inner wing CC	0.0712	-0.0067
Outer wing CC	0.0678	-0.0101

Table 7.3 The utmost ability of CC for root bending moment and lift coefficient reduction

Model	C_L	ΔC_L	C_{mx}	ΔC_{mx}
Unblown	0.222	---	0.0779	---
Centre body CC	0.159	-0.063	0.0684	-0.0095
Inner wing CC	0.181	-0.041	0.0627	-0.0152
Outer wing CC	0.205	-0.016	0.0678	-0.0101

The influence of the three located CC on spanwise local lift coefficients under different momentum coefficients is presented in Figure 7.7. For each located CC, a significant reduction of local lift coefficient can be noticed around the CC working region. However, a significant difference is the influenced region by CC when it works at different spanwise locations. When CC works on the centre body and inner wing, it influences almost all the semi-span region. However, outer-wing CC performs little influence on the load along the spanwise locations towards the centre body. Figure 7.8 shows the streamlines on η= 0.3 for the centre body CC working at C_μ= 5.89×10^{-4}. From Figure 7.8, it can be noticed that the high-speed CC jet flow stay attached on the circular Coanda surface. This high-speed jet flow entrains external flow near the lower wing surface to follow the jet with a faster speed, while the ‘bend-up’ flow will hinder and decelerate the flow around the upper surface. Consequently, the pressure on the upper wing trailing-edge increases, while the pressure on the lower side decreases, resulting in lift reduction as shown in Figure 7.9 for the surface pressure differences between CC models (NPR= 2.4) and the baseline model.

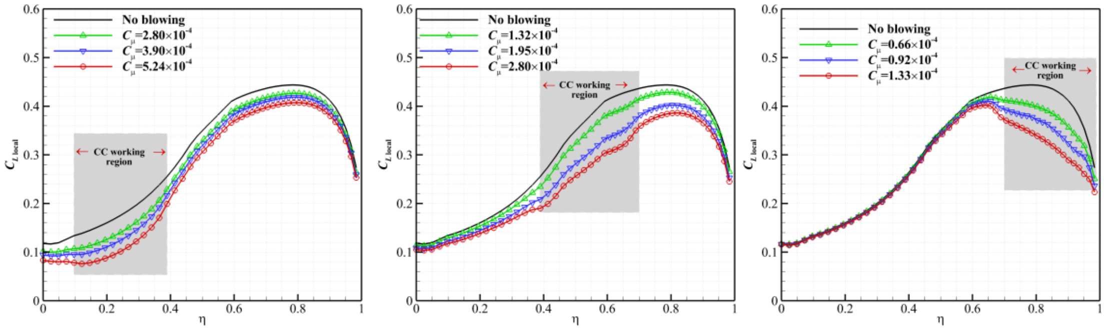

(a) Centre body CC (b) Inner-wing CC (c) Outer-wing CC

Figure 7.7 The influence on spanwise local lift coefficient of the three located CC under different momentum coefficients

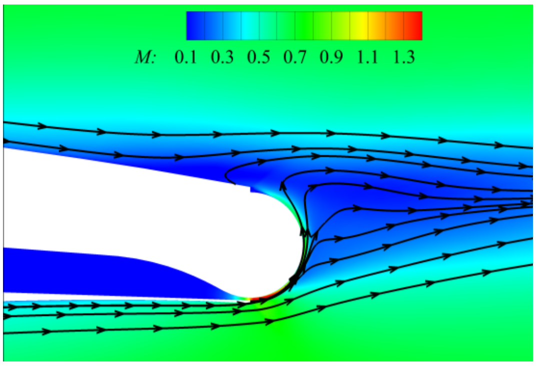

Figure 7.8 Streamline on η=0.3 for the center-body CC working at C_μ= 5.89×10^{-4}

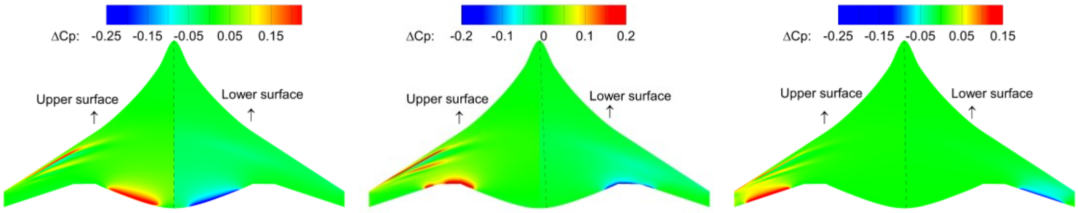

(a) Centre-body CC (b) Inner-wing CC (c) Outer-wing CC

Figure 7.9 Pressure differences ($\Delta Cp = Cp_{\text{CC model}} - Cp_{\text{baseline model}}$)

It has been demonstrated from the 2-D case studies that at transonic speed, the CC capability is reduced compared to subsonic range. Therefore, for the 3-D BWB model, if the CC is only deployed on finite spanwise location, the load control capability will be further reduced compared to the 2-D cases. It is expected that the three-located CC should work together to obtain a significant load control effect. The efficiency of the three located CC working together is tested under NPR= 2.4. The total reduction in root bending moment and lift coefficients is given in Table 7.4. The maximum reduction of -0.125 in lift coefficient and -0.036 in root bending moment coefficient is obtained. This value is close to the maximum lift coefficient reduction of the 2-D aerofoil under M_∞=0.8 demonstrated in the previous CC validation study. Therefore, it is predictable that the maximum lift alleviation under gust conditions for the three located CC working together is about -0.125 at the cruise condition. The comparisons of the spanwise local lift coefficients between the three-located CC working together and the unblown model are given in Figure 7.10. Significant reduction in local lift coefficients along the entire span has been obtained.

Table 7.4 Three located CC working together for lift coefficient and root bending moment coefficient reduction

Model	C_L	ΔC_L	C_{mx}	ΔC_{mx}
Unblown	0.222	---	0.0779	---
CC working together	0.097	-0.125	0.0419	-0.036

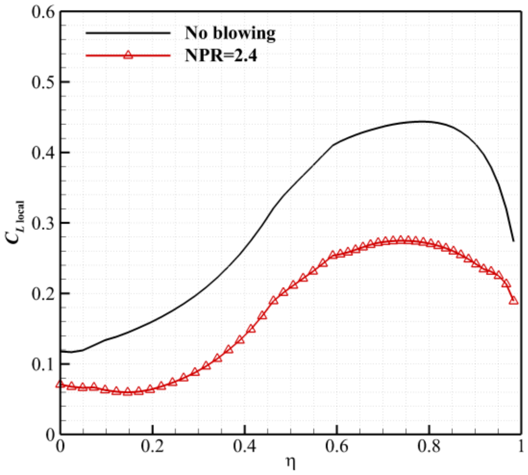

Figure 7.10 The influence on spanwise local lift coefficients of the three located CC working together

To conclude, CC has the capability to decrease the lift and root bending moment no matter where it is located along the span. However, due to the early occurrence of 'C_μ-stall' at transonic speed, the capability of CC for load control is limited especially when CC is only working on finite local span region. Therefore, to get a significant load control effect at M_∞= 0.8, CC should be deployed as long as possible along the span. It is obvious that the longer CC is deployed, the larger the amount of the mass flow is needed for the CC working system under a certain NPR. To get a quantitative understanding of the required mass flow value, it is calculated and is given in Table 7.5 based on Eq.(3-28). As shown in the result, the mass flow rate is 6.99 kg/s under NPR= 2.4. As pointed out in [14] that the supply of mass flow for the CC plenum is probably the bleed air from the jet engine of the aircraft. Here, as to obtain a quantitative knowledge of whether the CC mass flow rate is small or large, the data of the engine used for A310-200 which has a similar maximum take-off weight as the BWB model studied here is shown in Table 7.6. For this engine, the mass flow rate is 651 kg/s at M_∞= 0.8 and H=11 km. This comparison shows that the maximum mass flow rate required by CC at M_∞= 0.8 is less than 1.1% of the engine's value.

Table 7.5 Mass flow rate for three located CC working together under NPR=2.4

M	H(km)	U_{jet}(m/s)	C_μ	$\dot{m}$(kg/s)
0.8	11	354.6	8.68×10^{-4}	6.99

Table 7.6 Mass flow rate for CF6-80A2 from [170]

Airplane	Engine	W_{MTOW}(kg)	H (km)	M	$\dot{m}$ (kg/s)
A310-200	CF6-80A2	142,000	11	0.8	651

- **Subsonic speed case at M_∞= 0.3**

For subsonic range, the lift reduction effects by the three located CC working together are tested at M_∞= 0.3, Re= 10.6×10^7 based on the mean aerodynamic chord. The results are compared with the data at M_∞= 0.8, as shown in Figure 7.11. For M_∞= 0.3, the simulation is conducted under C_L=0.403 corresponding to the angle of attack of 6° for the estimation to support the same aircraft weight as that under the cruise condition.

As can be seen from the results that CC has a much stronger control ability at M_∞= 0.3 than M_∞= 0.8, which is the same as the results demonstrated previously on the 2-D aerofoil and the BAH wing. The maximum lift coefficient reduction is up to -0.44 at M_∞= 0.3 compared to the value of only -0.125 at M_∞= 0.8. Figure 7.12 shows the comparisons of spanwise local lift coefficients between CC model with C_μ= 1.28×10^{-3} and the baseline model at M_∞= 0.3. The spanwise local lift coefficients decrease significantly under CC. For instance, at η= 0.6, the local lift coefficient for the baseline model is 0.68, while this value is only 0.36 for the CC model with C_μ= 1.28×10^{-3}.

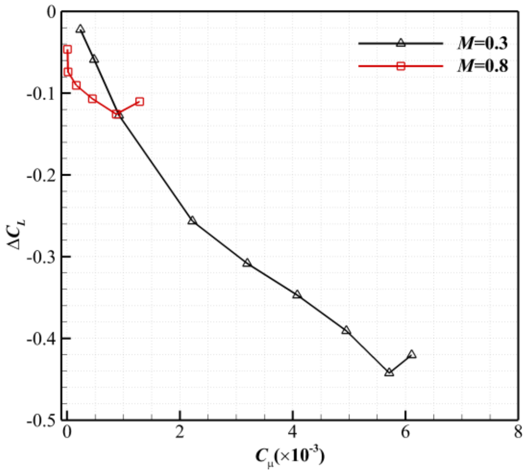

Figure 7.11 Comparisons of lift reductions between M_∞= 0.3 and M_∞= 0.8

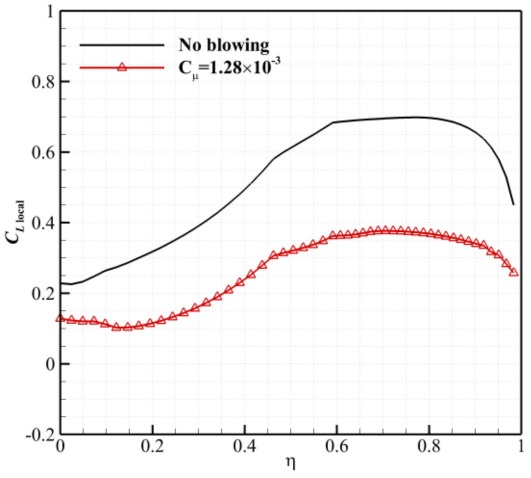

Figure 7.12 Comparisons of local spanwise lift coefficients at M_∞= 0.3

7.1.5 Blended-wing-body gust load alleviation by circulation control

7.1.5.1 M_∞= 0.3

- **Gust responses of the baseline model**

According to EASA CS-25 described in section 2.4, for this BWB model, F_g is around 0.7 with the assumption of R_1= 0.74, R_2= 0.60 and Z_{m0}= 14000 by reference to the performance definition of the Boeing 2nd-generation BWB model in Ref. [36]. Therefore, the peak gust velocity w_{g0} is about 12 m/s. To meet this reference gust velocity, the one-minus-cosine gust with the gust velocity w_{g0}/U_∞=0.12 and the gust wavelength of 12.5c_{ref} is used for the gust load alleviation study under M_∞= 0.3, α= 6°.

Figure 7.13 gives the time evolution of the lift coefficients under the gust. In general, it is in accordance with the lift-response trend under one-minus-cosine gusts. However, it is noticeable that the lift coefficient has a plateau and even a slight decrease from the non-dimensional time *s*= 6.5 to 7, when the gust velocity still increases in this period. It is because of the high value of the peak gust velocity that makes the lift stall during this period. Figure 7.14 displays the time evolution of the upper surface streamlines and pressure distributions from *s*= 0 to *s*= 7.5. At the initial time *s*= 0, the upper surface flow is all attached. As time goes to 5, the attached flow still maintains with a significant rise of the leading-edge suction as shown in the blue region, due to the increase in gust velocity. Flow separation appears on outer wing region when the time goes to 6.2. As the gust velocity continues to increase to the peak value at *s*=7.5, the flow on the outer wing completely separates (see Figure 7.13 (d)). Assuming the local angle of attack is defined by the sum of the cruise angle of attack and the angle induced by the gust as

$$\alpha_{\text{local}} = \alpha_{\text{cruise}} + tan^{-1}\left(\frac{w_{\text{g}}}{U_\infty}\right) \tag{7-1}$$

The local angle of attack reaches to about 12.8° when gust velocity peaks with the sum of α_{cruise} = 6° and angle induced by gust of $tan^{-1}(0.12)$= 6.8°. That gives the explanation of the slight decrease of the lift response in Figure 7.13 and the flow separation near the outer wing upper surface in Figure 7.14.

From the time evolution of the spanwise load distributions and spanwise local lift coefficient distributions shown in Figure 7.15, a dramatic change in spanwise loading due to gust can be observed. At the initial time, the spanwise load distribution is near elliptic. As time goes to 5, a near constant increase of local lift coefficient along the whole span can be noticed in Figure 7.15 (b). Due to the smaller local chord length, the increase in load on the outer wing is less than that on the centre body and inner wing. The elliptic spanwise loading from the initial time transformed to a near triangular one at *s*= 5. As the gust velocity reaches its maximum value at *s*= 7.5, the local lift coefficient on the centre body and inner wing still increase compared to the previous time. However, the load on the outer wing does not follow the increase. The load around the wing tip even decreases to around the initial value, due to the significant flow separation mentioned above.

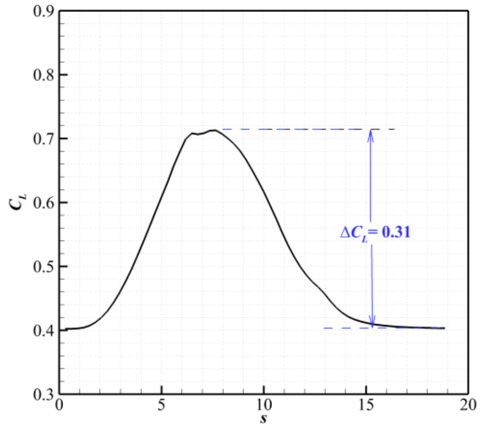

Figure 7.13 Lift coefficient response of the baseline model under gust condition M_∞= 0.3

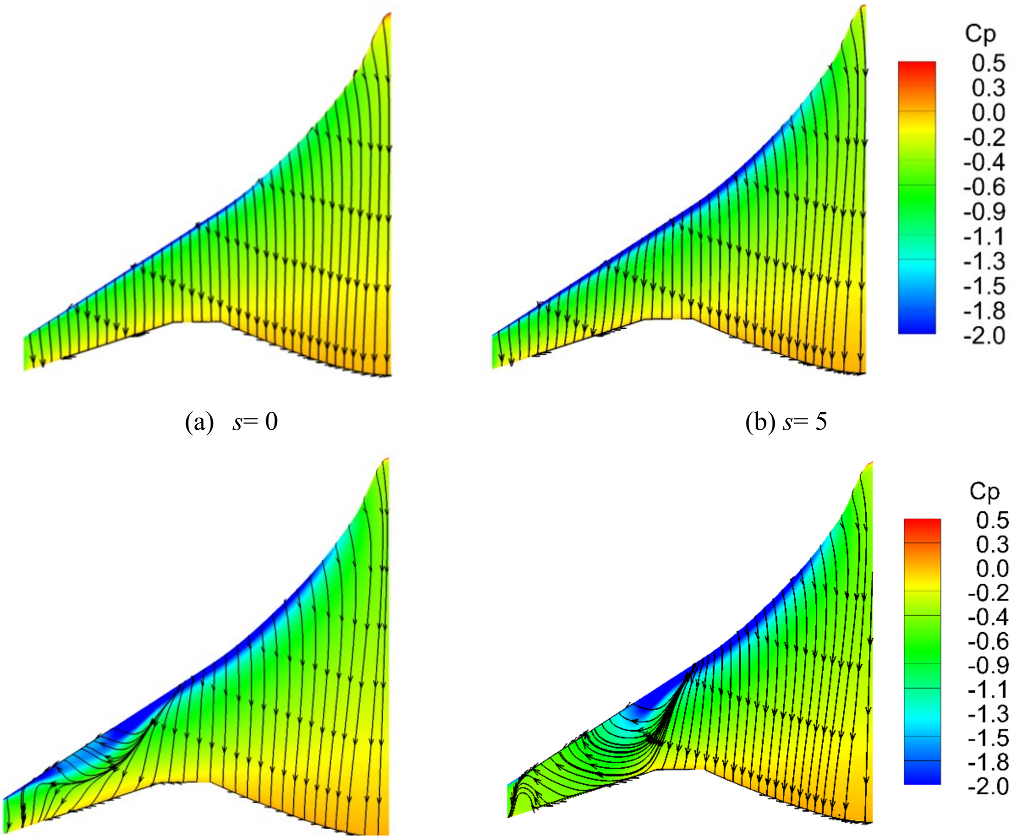

(a) *s*= 0

(b) *s*= 5

(c) *s*= 6.2

(d) *s*= 7.5

Figure 7.14 Evolution of the upper surface streamlines and pressure distributions of the baseline model at M_∞= 0.3, α= 6°

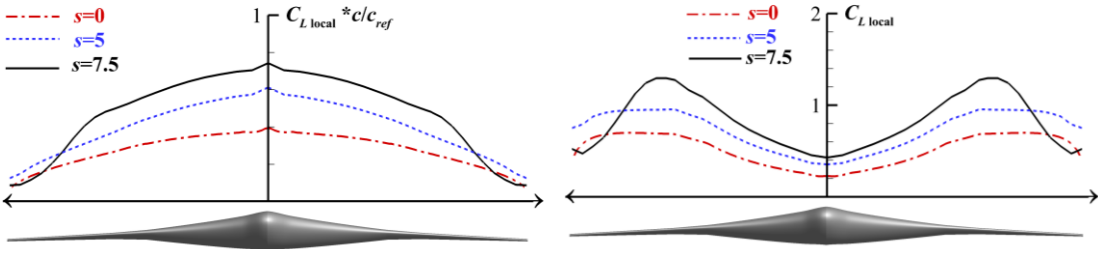

(a) spanwise load (b) spanwise local lift coefficient

Figure 7.15 Evolution of the spanwise loading and local lift coefficients at M_∞= 0.3, α= 6°

- **Gust load alleviation effects of CC with one-minus-cosine momentum coefficient**

The momentum coefficient with one-minus-cosine profile is chosen for the test of the gust load alleviation effect by CC on this BWB model at M_∞= 0.3, α= 6°. Based on the knowledge of the load control capability by CC shown in Figure 7.11 and the gust load responses shown in Figure 7.13, a medium peak value of $C_{\mu 0}$= 0.0021 is used for the one-minus-cosine momentum coefficient.

The results of gust load alleviation are shown in Figure 7.16, where significant gust load alleviation effects can be noticed with the peak gust load in terms of lift coefficient reduction of -0.21. This is close to the value of -0.26 obtained under the steady condition shown in Figure 7.11. Noticeably, there is a different lift response of the CC model from *s*= 0 to *s*= 3 compared to the baseline model, where a decrease in the response of lift coefficient is witnessed. This is because, at *s*= 3, the transient momentum coefficient is about 0.0014 which can make a lift coefficient reduction of about -0.17 from the knowledge obtained from the steady state given in Figure 7.11. However, the lift coefficient increase due to gust at *s*= 3 is only 0.05, resulting in the decrease in the overall lift coefficient during this period. Figure 7.17 displays comparisons of upper surface streamlines and pressure distributions between the baseline model and CC model at *s*= 7.5 when the gust velocity peaks. Compared to the baseline model, a separation line appears near CC model trailing edges due to the high-speed CC jet flow which entrains the low-speed flow around the rear upper surface backward as shown in Figure 7.18. Consequently, the pressure coefficients on the upper trailing edge surface are much higher than those on the baseline model as presented in Figure 7.17(a), resulting in gust load alleviation. For the spanwise loading, a significant reduction can be noticed on the centre body and inner wing from Figure 7.19, compared to the baseline model at s= 7.5. As the large flow separation remains on the outer wing of the CC model, the load around this area is not changed much by CC.

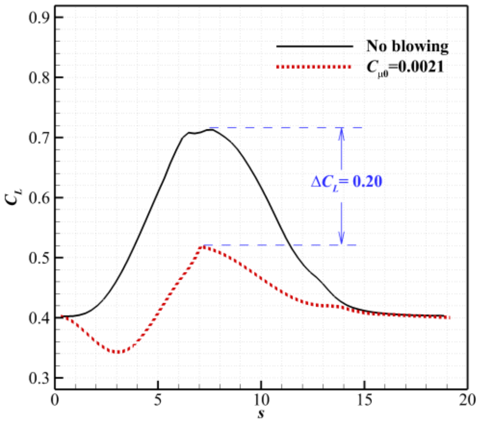

Figure 7.16 Gust load alleviation by CC with $C_{\mu 0}$= 0.0021

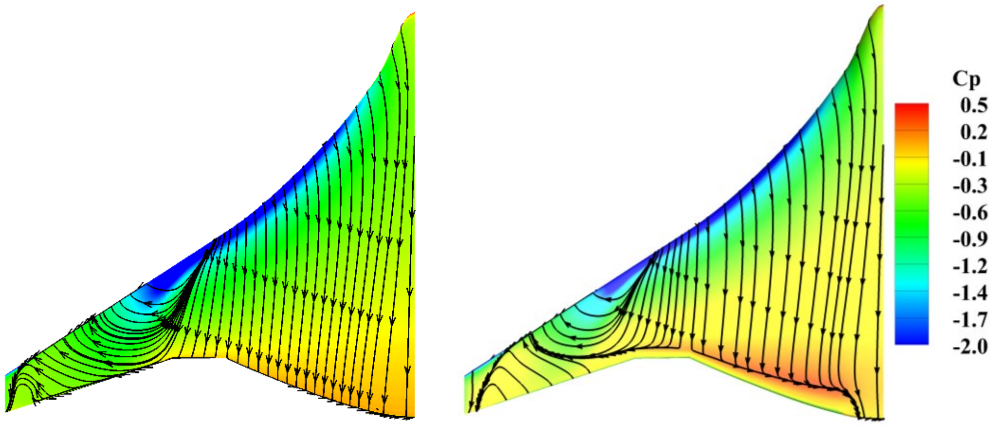

(a) No blowing

(b) $C_{\mu 0}$= 0.0021

Figure 7.17 Comparisons of the upper surface streamlines at s= 7.5

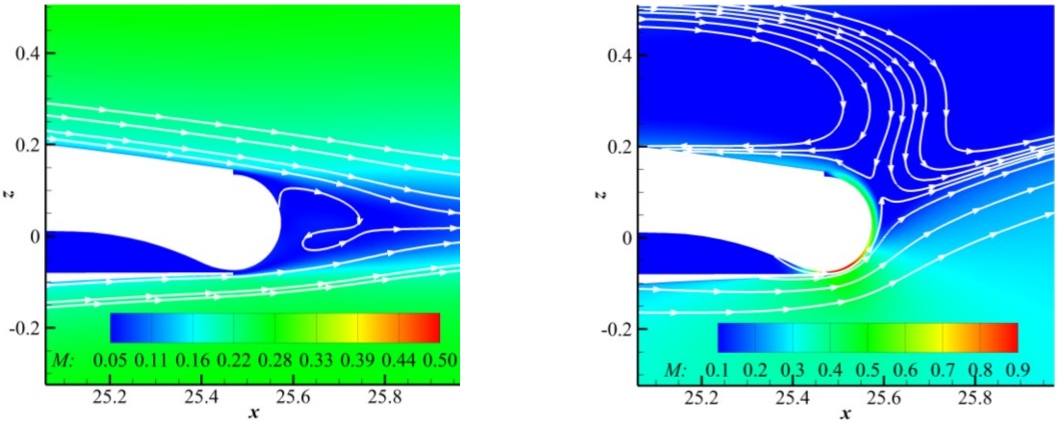

(a) No blowing

(b) $C_{\mu 0}$= 0.0021

Figure 7.18 Comparisons of the streamlines around the trailing edge of η= 0.2 at s= 7.5

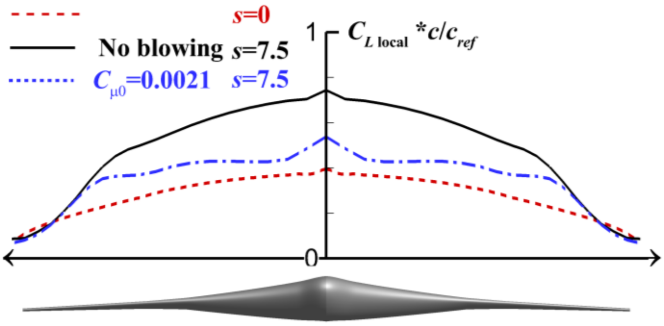

Figure 7.19 Comparison of the spanwise load between the baseline model and the CC model

- **Gust Load alleviation effects by adaptive CC**

It has been demonstrated in Chapter 5 that CC has a fast frequency response characteristic which allows timely adaptive control to counteract the gust disturbances.

Based on the results of the gust load alleviation shown in Figure 7.16, an adaptive profile of momentum coefficients is designed and compared with the previous one-minus-cosine profile as shown in Figure 7.20. It can be noticed that the design momentum coefficients reduced significantly before s= 3 compared with the previous one-minus-cosine profile. Also shown is the increase in the peak momentum coefficient, because it had been demonstrated that the peak momentum coefficient used in the previous case study was not high enough to counteract the peak gust load.

The adaptive blowing is then tested, and the time evolutions of the lift and root bending moment coefficients are shown in Figure 7.21. The gust load is better controlled by the adaptive blowing and near constant lift and root bending moment coefficients are obtained under the gust condition. The maximum gust-induced lift coefficient increment of ΔC_L= 0.31 is almost completely counteracted by CC. A significant reduction of the spanwise load distributions of the adaptive CC model compared with the baseline model at s= 7.5 when the gust load peaks is demonstrated in Figure 7.22. Also shown is the similar spanwise load distributions between the adaptive CC model at s=7.5 and the baseline model at s= 0, indicating a good gust control effect by CC.

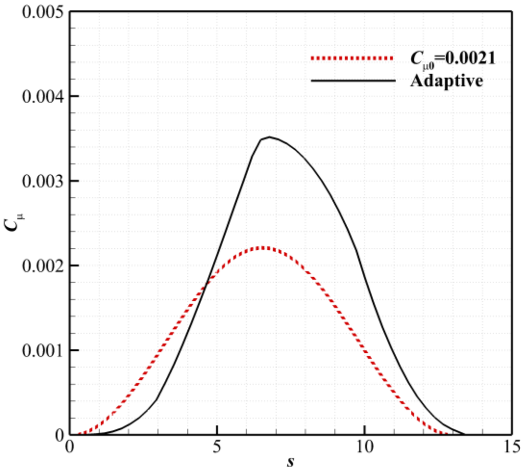

Figure 7.20 Adaptive momentum coefficient profile

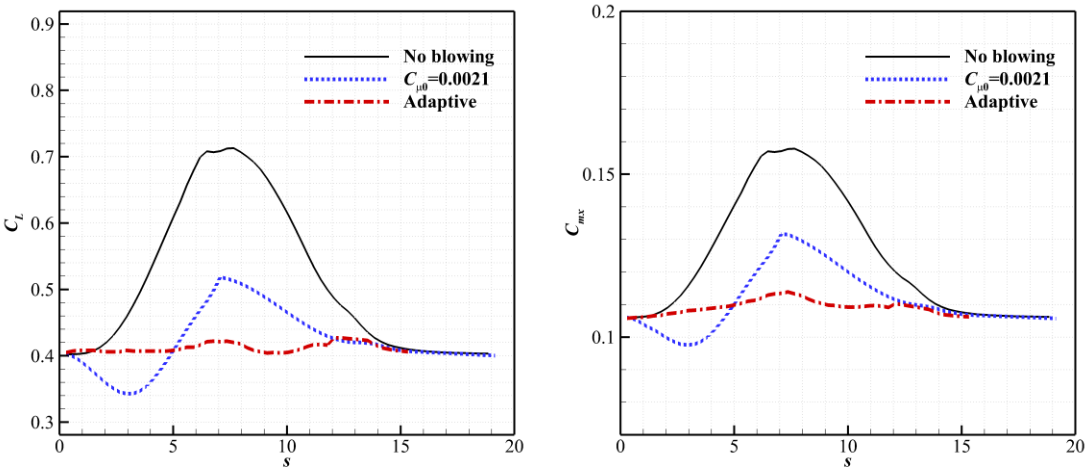

(a) lift response (b) root bending moment

Figure 7.21 Lift coefficient reduction by the adaptive CC at M_∞= 0.3

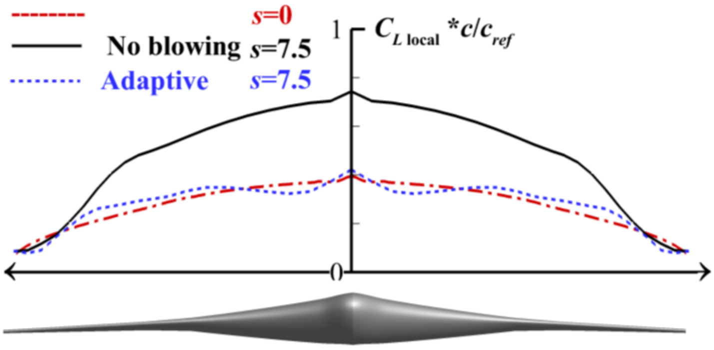

Figure 7.22 Comparisons of the spanwise loading between the baseline model and adaptive CC model at M_∞= 0.3

7.1.5.2 M_∞= 0.8

For the cruise condition at 11 km, the estimated reference gust velocity is about 6.5 m/s. To meet this reference gust condition, the one-minus-cosine gust with the gust velocity of w_{g0}/U_∞= 0.027 and the wavelength of 12.5c_{ref} is used for the following gust load alleviation studies under M_∞= 0.8, α= 2.5°.

- **Gust responses of the baseline model**

Firstly, the lift coefficient response of the unblown model is analysed, as presented in Figure 7.23. The gust load peaks at s=8.5 with a maximum gust load of about 0.13 in terms of lift coefficient increment. Due to the gust load, strong shock wave is introduced to the inner and outer wings' upper surfaces at s= 8.5 compared to the initial time s= 0 as presented in Figure 7.24. The sectional pressure distributions shown in Figure 7.25 further confirm the significant changes on surface pressures under the gust encountering. The spanwise load distributions are compared between s=8.5 and the initial time in Figure 7.26. As shown in Figure 7.26 (a), even though the increase of load on outer wing is less than that on centre body and inner wing because of the smaller wing area, more significant increase in local lift coefficient has been obtained on the outer wing. This explains why shock wave formed firstly on the wing sections.

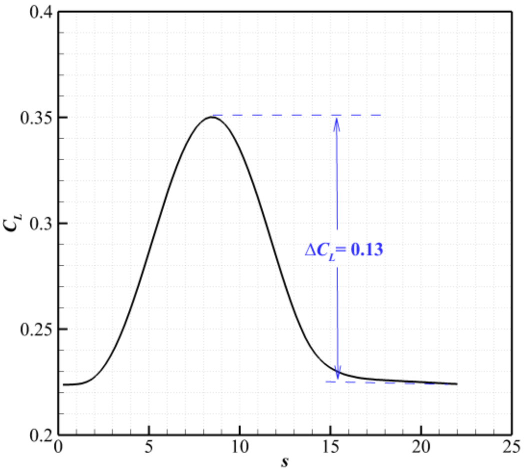

Figure 7.23 Lift coefficient response of the baseline model under gust condition at M_∞= 0.8

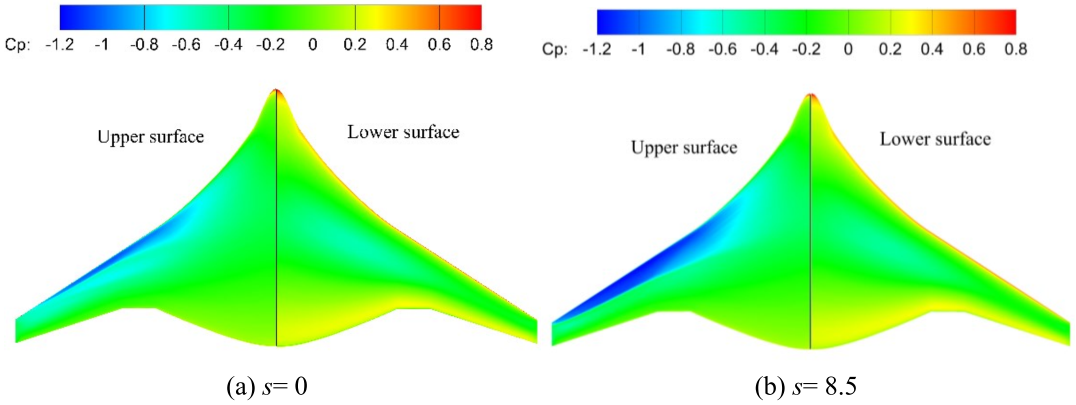

(a) s= 0 (b) s= 8.5

Figure 7.24 The pressure-distribution comparisons

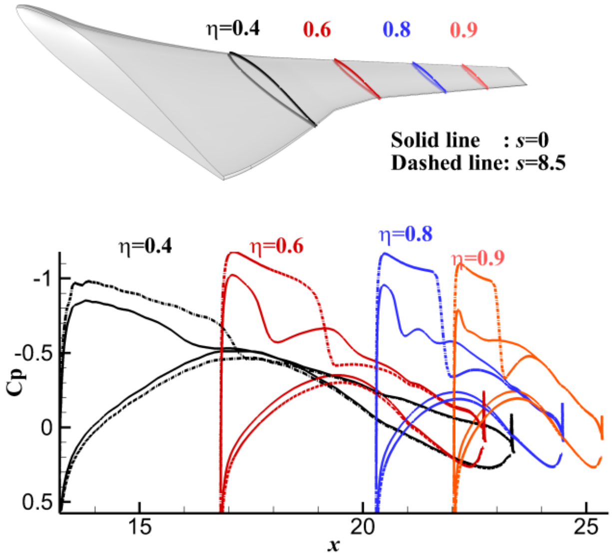

Figure 7.25 Comparisons of pressure distributions on typical sections

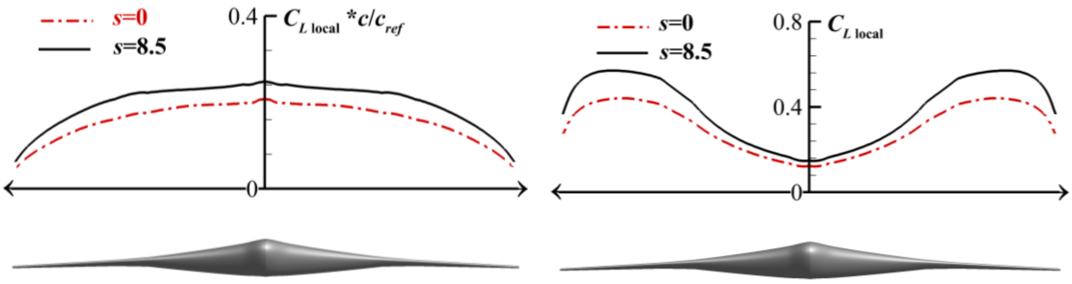

(a) Load distribution (b) Local lift coefficient

Figure 7.26 Comparisons of spanwise loading and local lift coefficient between s=0 and s=8.5

- **Gust Load alleviation effects of CC**

According to the results of lift coefficient reduction due to CC at steady flow condition shown in Figure 7.11, the 'C_μ-stall' momentum coefficient is around 1.3×10^{-3} at M_∞= 0.8. Firstly, the one-minus-cosine momentum coefficient with the peak value of $C_{\mu0}$= 0.65×10^{-3} is chosen to test the gust load alleviation effects. After the lift response is obtained, the results are used to design the adaptive momentum coefficients for the adaptive control study.

The results of these two cases are shown in Figure 7.27. The peak gust load is reduced by 0.07 in terms of lift coefficient for the $C_{\mu0}$= 0.65×10^{-3} model, which is above 50% of the peak load caused by the gust. The adaptive blowing achieved about 87% and 85% of the peak gust load alleviation in terms of the lift and root bending moment coefficient increments, respectively.

As expected, the spanwise loading under the gust is well controlled by the adaptive blowing as shown in Figure 7.28. At s= 8.5 when the gust load peaks, the spanwise loading with the adaptive CC is close to the initial load distributions indicating a good control effect.

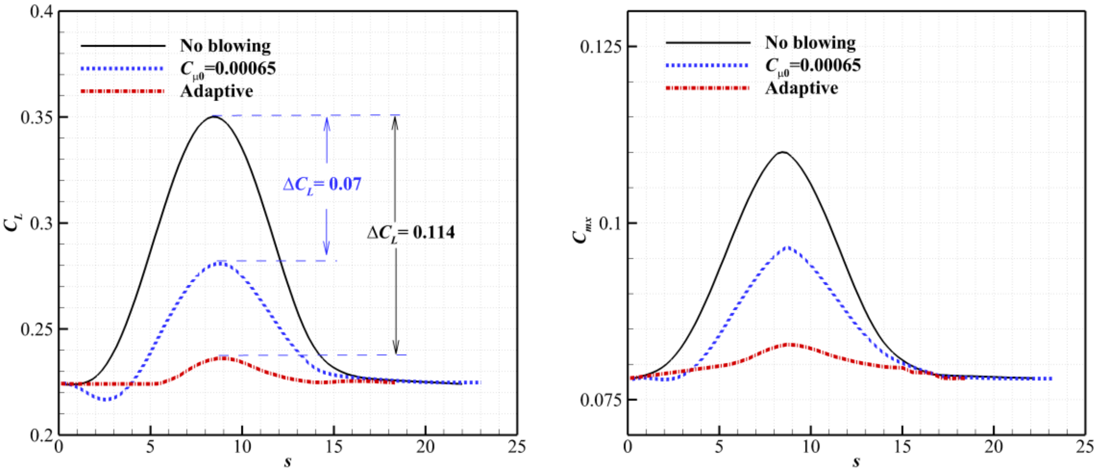

(a) Lift coefficients (b) Root bending moments

Figure 7.27 Responses of the lift and root bending moment coefficients at M_∞= 0.8

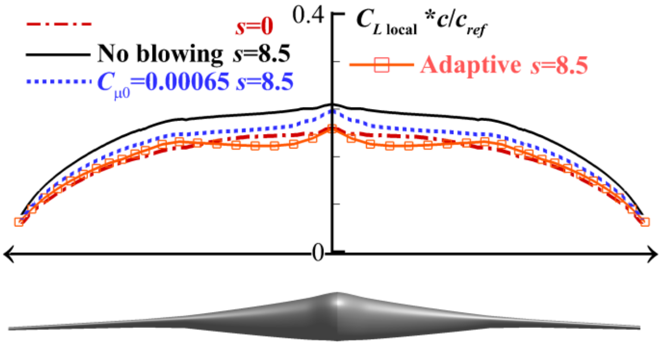

Figure 7.28 Comparison of the spanwise load distributions between the no blowing model and the CC models

To conclude, under subsonic speeds, CC has been demonstrated having strong load control capabilities. The fast response characteristic and the complete suppression of the reference gust load defined by EASA CS-25 on the BWB model indicates that CC has a promising potential as actuators for flight control applications under subsonic range. Due to the occurrence of 'C_μ-stall' at small momentum coefficient at transonic speed, it is unable to completely suppress the reference gust load as demonstrated in this case study.

As has been demonstrated that normal microjet blowing has an opposite load control behaviour compared to CC. Normal microjet blowing performs much better under transonic incoming flow than that at subsonic speed. The following sections will demonstrate the gust load alleviation effects by normal microjet blowing on this BWB model under transonic speed.

7.2 Blended-wing-body with microjet slot

7.2.1 Numerical model setup of the blended-wing-body with microjet slot

To keep consistent with the way of the CC deployment on the span, three microjet slots on the outer wing, inner wing and centre body with equal spanwise width, are included on the BWB model. The slots are located on 95% of the local chord length from the local leading edge. The slot width is 0.5% of the local chord length, as shown in Figure 7.29.

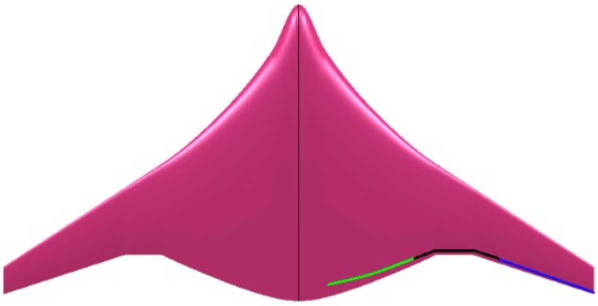

Figure 7.29 The sketch of the deployment of the microjet slots

7.2.2 Grid convergence study

Figure 7.30 shows the half-span grid used for simulation of microjet blowing on the BWB model. The baseline grid has approximately 6.25×10^6 cells. From this, a coarser and a finer grid were generated for a grid refinement study with a refinement factor of about 1.5 in each direction. Table 7.7 gives the effects of grid resolutions on aerodynamic coefficients at $M_\infty= 0.8$, $\alpha= 2.5°$ with the three slots blowing simultaneously under the blowing momentum coefficient $C_\mu= 1.72\times10^{-3}$. A Richardson extrapolation was performed to estimate the aerodynamic coefficients with an 'infinite' grid by $C_{\mathrm{cont}} = C_{21.1\mathrm{m}} + (C_{21.1\mathrm{m}} - C_{6.2\mathrm{m}})/(r^2 - 1)$, where r=1.5. The lift coefficient of the grid with 6.2×10^6 cells is within 1.1% of the continuum estimate, and it is less than 1.7% for the drag and root bending moment coefficients. The results indicate that the medium grid has reasonably accurate results while provides computational cost efficiency.

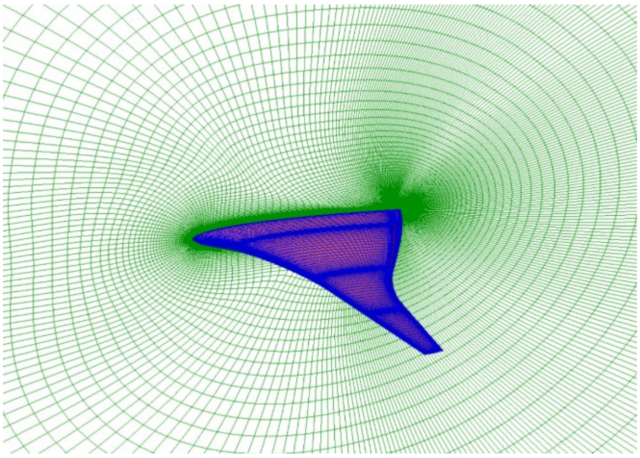

Figure 7.30 Half span grid of the BWB with normal microjet slot

Table 7.7 Effect of half-span grid resolution on aerodynamic coefficients at M_∞= 0.8, α= 2.5°, C_μ= 1.72×10^{-3}

Grid size	1.8×10^6	6.2×10^6	21.1×10^6	Continuum
C_L	0.1045	0.0984	0.0978	0.0973
C_D	0.0804	0.0750	0.0743	0.0738
C_{mx}	0.0456	0.0430	0.0427	0.0425

7.2.3 Load control performance under steady conditions

To get an understanding of the load control performance of normal microjet blowing on the BWB model, the lift coefficient reduction ($\Delta C_L = C_{L,\text{ with microjet blowing}} - C_{L,\text{ baseline}}$) at a range of momentum coefficients are evaluated at M_∞= 0.8, α= 2.5°. The comparisons of lift reduction are presented in Figure 7.31. The maximum jet velocity through the slot is set to M_{jet}= 1.4. Because with a further increase in the jet velocity, a slight oscillation in the lift coefficient started to appear during the simulation.

The results show that the slot placed on the centre body has the highest capability in terms of lift reduction under the same microjet slot-exit velocity. However, it is more efficient for the slot placed on the inner wing, as it can generate more lift reduction under the same momentum coefficient compared to the slots placed on the centre body and outer wing.

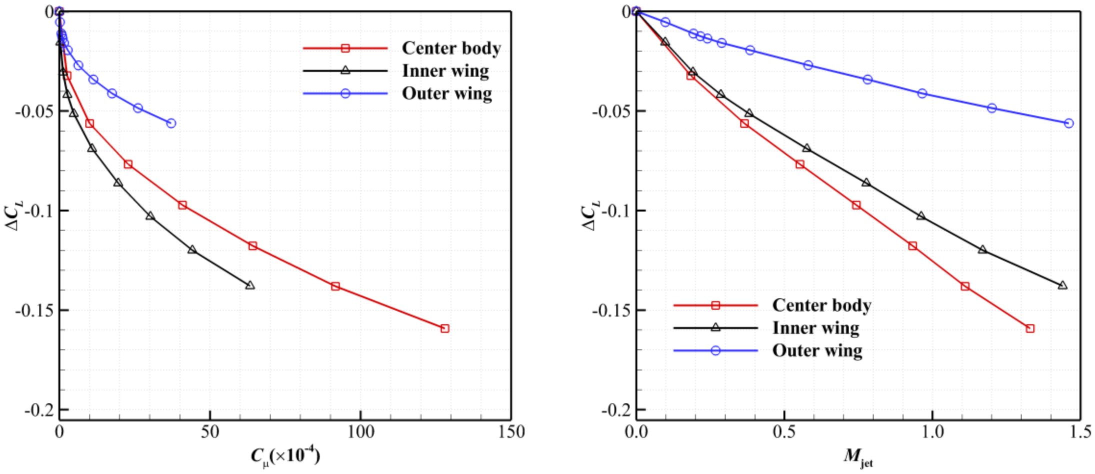

(a) $\Delta C_L \sim C_\mu$ (b) $\Delta C_L \sim M_{\text{jet}}$

Figure 7.31 Comparisons of lift reduction with different located of microjet slot

Figure 7.32 shows the comparison of load control capability in terms of lift reduction between normal microjet blowing and CC at cruise condition. It is consistent with the previous results of the 2-D aerofoil and BAH wing that normal microjet blowing has a much stronger endurance for load control than CC. Also shown in the inserts in Figure 7.32 is that normal microjet can generate more lift reduction than that of CC under the same momentum coefficient, which indicates its higher efficiency at transonic range. Figure 7.33 gives the Mach number contours on the slice along η= 0.93 and the surface pressure coefficient distributions under M_{jet}= 1.2. The differences of the surface pressure coefficients due to the three located microjets blowing separately with M_{jet}= 1.2 relative to the baseline model are presented in Figure 7.34. Noticeably, the microjet blowing leads to a significant pressure increase on the upper surface ahead the microjet slot and a decrease of the pressure on the lower surface, resulting in lift reduction. Figure 7.35 demonstrates the influence of microjet blowing on spanwise local lift coefficients under different microjet velocities. For each located normal microjet slot blowing, a significant reduction of local lift coefficient can be noticed around the microjet working region. Like the results with the control of CC, when microjet works on the centre body and inner wing, it influences almost all the semi-span region. However, when microjet is deployed on the outer wing, the influence of the load on the centre body is relatively small. As shown in Figure 7.35 (c) for the microjet slot working on outer wing, the maximum local lift coefficient for the baseline model is around 0.44 at η= 0.77. It is reduced to 0.32 and 0.24 when microjet is blowing with M_{jet}= 0.4 and 0.8, respectively, indicating a significant load control effect.

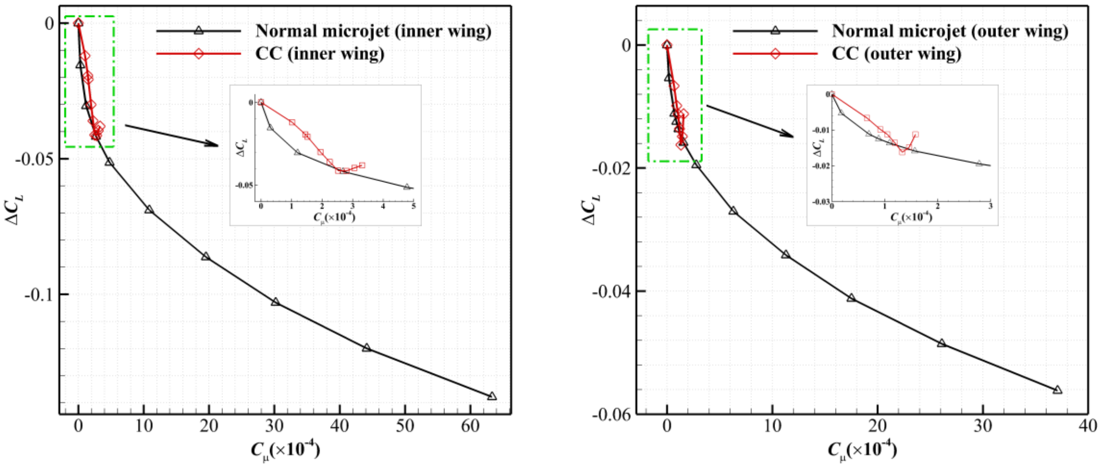

(a) inner wing (b) outer wing

Figure 7.32 Comparison of load control capability between normal microjet and CC

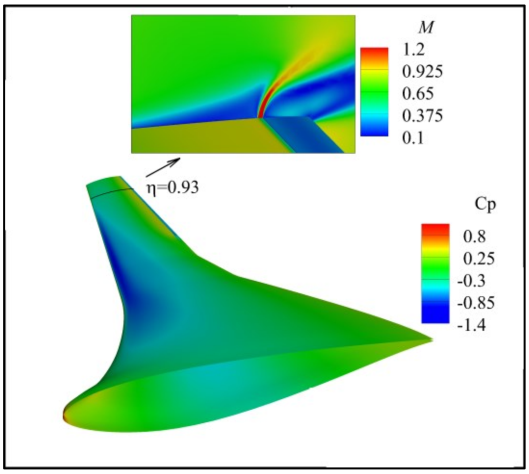

Figure 7.33 The Mach number contours on the slice of η= 0.93 and the surface pressure coefficient distributions under M_{jet}= 1.2

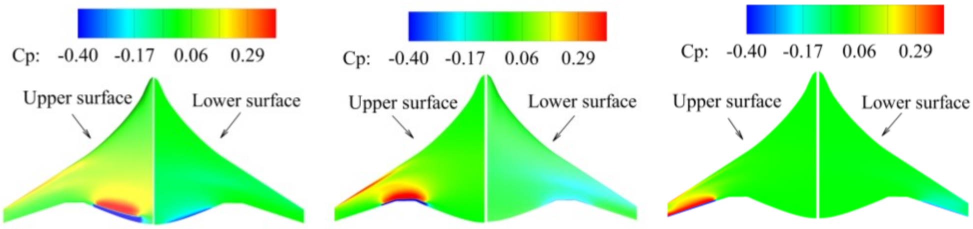

(a) Centrebody (b) Inner wing (c) Outer wing

Figure 7.34 Pressure difference between the model with microjet blowing with M_{jet}= 1.2 and the baseline model

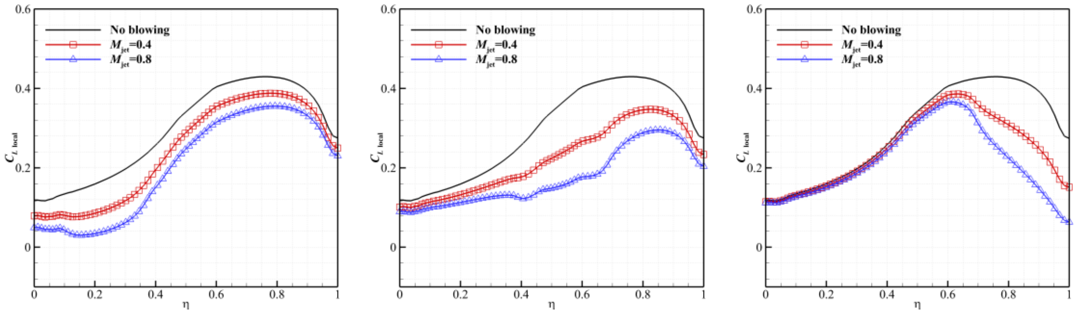

(a) Centre body (b) Inner wing (c) Outer wing

Figure 7.35 The influence on spanwise local lift coefficient of the three slots under different microjet blowing velocity

7.2.4 Gust load alleviation by microjet blowing on the BWB model

It has been demonstrated that even though the CC is deployed through almost the whole span, it is unable to alleviate completely the reference gust load at M_∞= 0.8. Since normal microjet has a stronger load control capability at transonic range, it is not necessarily to deploy microjet slot along the whole span of the BWB model. To test the gust load alleviation effects of normal microjet blowing, only the slots placed on the outer and inner wings are actuated in the following test cases.

7.2.4.1 Baseline model gust responses

The gust is the same 'one-minus-cosine' gust as the one used in the previous gust load alleviation study under M_∞= 0.8, α= 2.5°, which is:

$$\begin{cases} \text{gust velocity:} & \dfrac{w_{\text{g0}}}{U_\infty} = 0.027 \\ \text{gust wavelength:} & 12.5c_{ref} \end{cases}$$

The time evolution of the lift coefficient of the baseline model is given in Figure 7.36. The results are similar to the responses of the baseline model with CC device shown in Figure 7.23. The evolutions of spanwise loading and local lift coefficients from the initial non-dimensional time to s=8.6 when the gust load peaks are shown in Figure 7.37. With the increase in gust load, the whole spanwise loading increases. Also shown is the significant increase in local lift coefficients on outer wing around η= 0.78. At s= 0, the local lift coefficient at η= 0.78 is about 0.46, while it increases to 0.66 when gust load peaks.

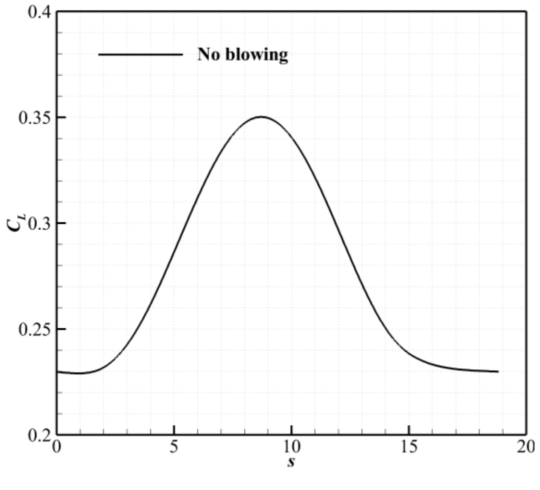

Figure 7.36 Lift coefficient responses

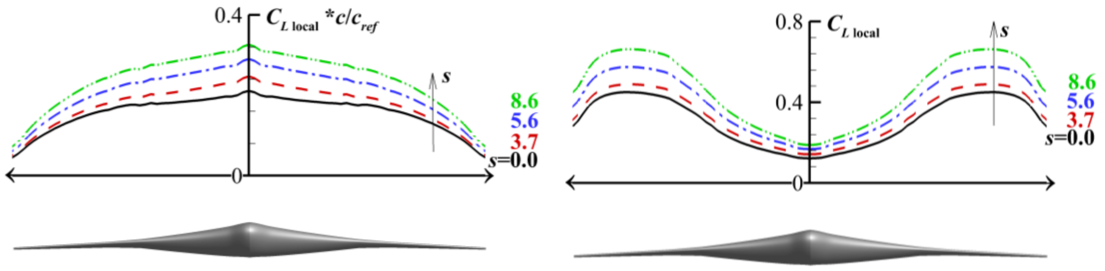

(a) Load distribution (b) Local lift coefficient

Figure 7.37 Evolutions of the spanwise loadings and local lift coefficients from *s*= 0 to *s*= 8.6

7.2.4.2 Gust load alleviation effects by normal microjet blowing with one-minus-cosine momentum coefficient

Based on the results of the lift reduction capability by normal microjet blowing presented in Figure 7.31 and the gust load responses shown in Figure 7.36, two one-minus-cosine momentum coefficient profiles with the peak values of $C_{\mu 0}$= 0.00075 and 0.00182, respectively, are used for the test as shown in Figure 7.38.

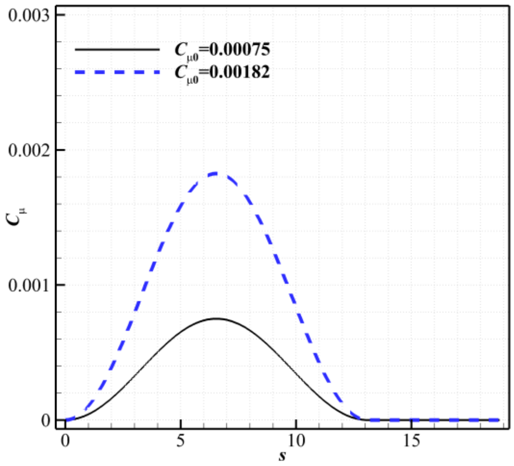

Figure 7.38 One-minus-cosine momentum coefficient profile

Significant gust load alleviation effects have been obtained as shown in Figure 7.39 for the time evolutions of the lift and bending moment coefficients. Peak gust loads in terms of no matter lift or root bending moment are nearly completely suppressed by the microjet with $C_{\mu 0}$= 0.00182. The evolutions of the spanwise loading and local lift coefficients from *s*=0.0 to *s*= 8.6 for these two test cases are shown in Figure 7.40 and Figure 7.41. Unlike the baseline model that the whole spanwise load is increased with the increase in gust load, the spanwise load around the inner and outer wing is effectively controlled due to the microjet blowing there. Also shown is that the spanwise load distributions which are near elliptic at the initial time deviate to a near triangular one at s= 8.5 due to the significant gust load alleviation around the inner and outer wing region.

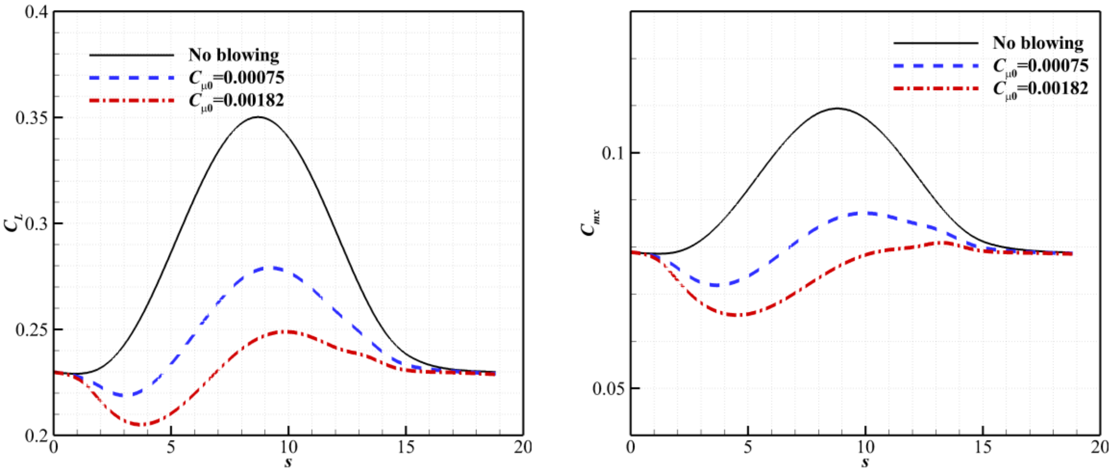

(a) Lift coefficients (b) Root bending moment coefficients

Figure 7.39 Responses of lift and root bending moment coefficients

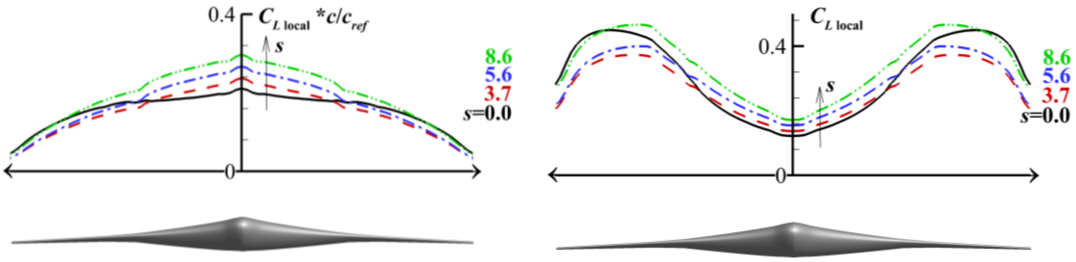

(a) Load distributions (b) Local lift coefficients

Figure 7.40 Evolution of the spanwise loadings and local lift coefficients ($C_{\mu 0}$= 0.00075)

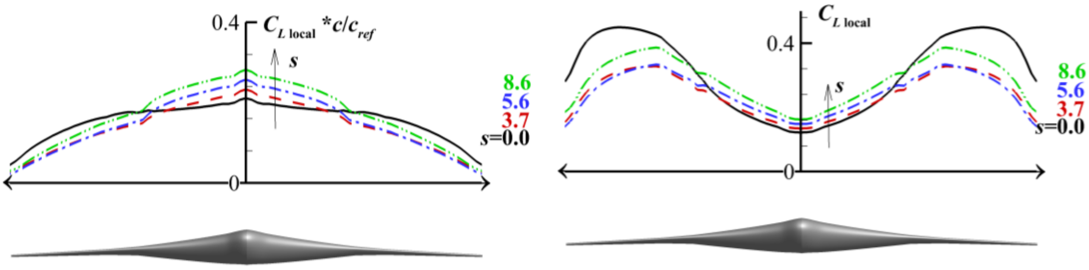

(a) Load distribution (b) Local lift coefficients

Figure 7.41 Evolutions of the spanwise loadings and local lift coefficients ($C_{\mu 0}$= 0.00182)

7.2.4.3 Gust load alleviation effects by normal microjet blowing with adaptive momentum coefficient

According to the lift coefficient reduction shown in Figure 7.39, an adaptive profile of momentum coefficients is designed and compared to the previous one-minus-cosine profiles as given in Figure 7.42. Noticeably, the peak value of the adaptive momentum coefficient increases to 0.00204 and shifts a little afterwards from s= 6.5 to s= 7.5. Also shown is that the value before s= 6.5 is smaller than the one with $C_{\mu 0}$= 0.00182 as it has been demonstrated from Figure 7.39 (a) that it is too large before s= 6.5.

The gust load is better controlled by the adaptive blowing and a near constant lift coefficient is obtained under the gust condition as shown in Figure 7.43. The evolutions of the spanwise loading and local lift coefficients from s=0.0 to s= 8.6 are shown in Figure 7.44. As expected, the spanwise loads around the inner and outer wing where the microjet slots are actuated are significantly alleviated by the microjet blowing. On the contrary, the load on the centre body increases with the increase in gust load from s= 0 to s= 8.6. Figure 7.45 and Figure 7.46 show the comparisons of pressure coefficients on upper surface and two wing sections between the no-blowing model and the model with adaptive blowing at s= 8.6. From the results, shock wave can be noticed on inner and outer wing regions under the peak gust load for the no-blowing model. With microjet blowing, the shock wave is pushed towards the wing leading edges and the strength is significantly weakened relative to the baseline model.

The maximum mass flow rate for the adaptive blowing is calculated and shown in Table 7.8. The maximum mass flow rate is 16.9 kg/s which is about 2.6% of the reference mass flow rate from the engine used for A310-200 shown in Table 7.6.

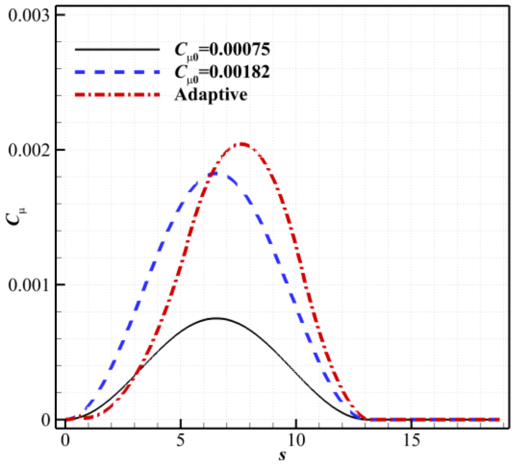

Figure 7.42 One-minus-cosine momentum coefficient profile

Table 7.8 Maximum mass flow rate for the adaptive normal microjet blowing

M	H(km)	U_{jet}(m/s)	C_μ	$\dot{m}$(kg/s)
0.8	11	354.6	2.1×10^{-3}	16.9

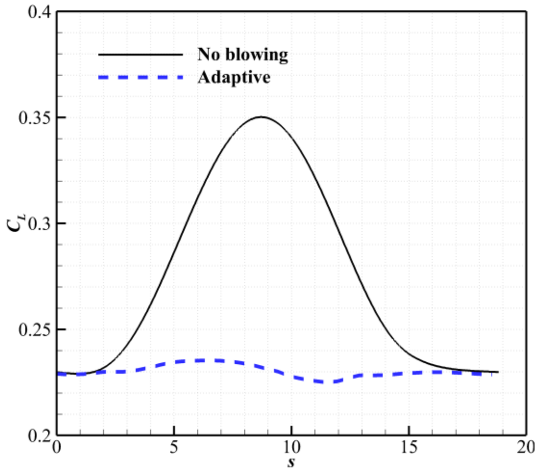

Figure 7.43 Lift coefficient responses with the adaptive blowing

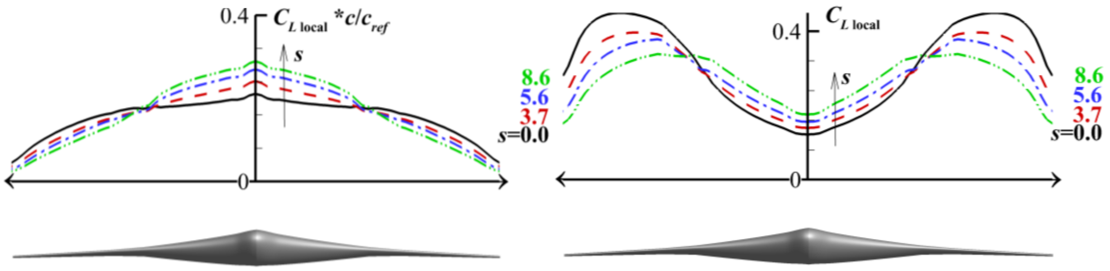

(a) Load distributions

(b) Local lift coefficients

Figure 7.44 Evolutions of the spanwise loading and local lift coefficients (adaptive blowing)

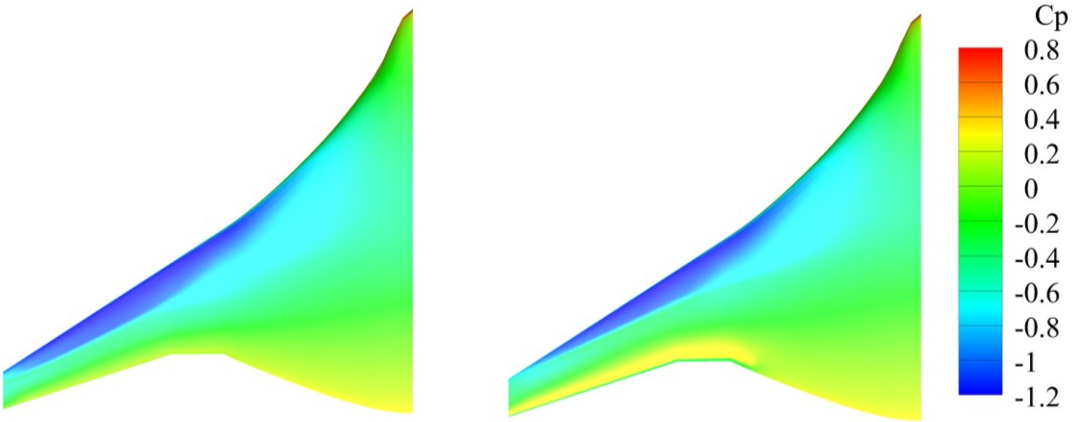

(a) No blowing (b) Adaptive blowing

Figure 7.45 Comparisons of the upper surface pressure coefficients at *s*= 8.6

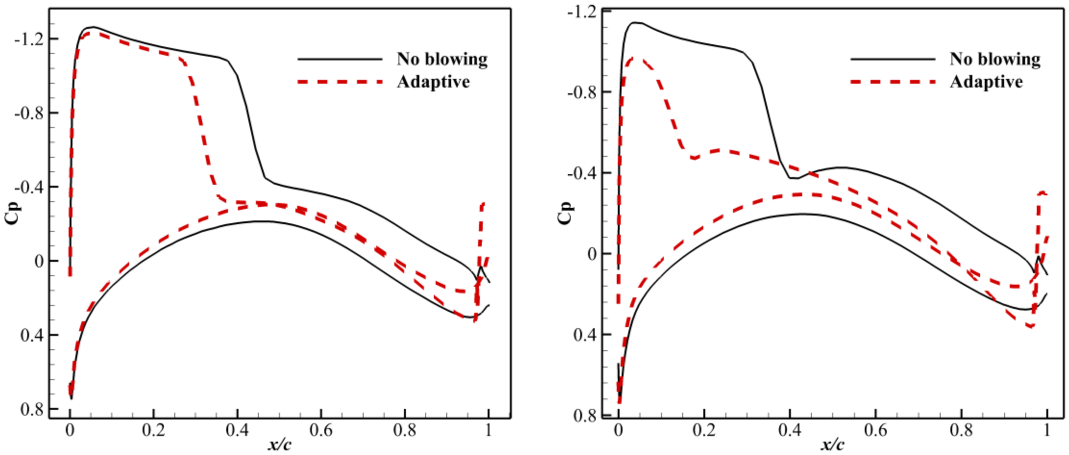

(a) η= 0.49 (b) η= 0.93

Figure 7.46 Comparisons of the pressure coefficients on typical sections at *s*= 8.6

7.3 Aeroelastic gust load alleviation by normal microjet blowing on the blended-wing-body model

Based on the BWB model with normal microjet slot, the effects of aeroelasticity on the gust response are demonstrated in this section. The BWB structural model is the same as the one used in Chapter 6.

7.3.1 Static aeroelastic results

The BWB model is initially assumed flying at cruise condition and then encounters the gusts. The results from a static fluid-structure interaction (FSI) are used to initialize the simulations for the gust responses. For the rigid model, the incoming flow condition is M_∞= 0.8, α= 2.5° to obtain the cruise lift coefficient of C_L= 0.23. Due to the aeroelastic deformation, the lift coefficient is smaller compared to the rigid model under the same incoming flow. In order to initialize from the same cruise lift condition, the incoming flow condition is set to M_∞= 0.8, α= 2.7° for the elastic model.

The pressure distribution and model deformations resulting from the static FSI are shown in Figure 7.47, also shown is the rigid model for the comparison. To get a quantitative insight into the model deformation, the spanwise vertical deformation and twist angle increment relative to the rigid model is given in Figure 7.48. The wing-tip deformation under static aeroelasticity is about 0.7m, and a nose-down twist angle increment is about 1.6º. As a result, the load and local lift coefficient around the outer wing region is reduced compared to the rigid model under the same cruise lift coefficient as shown in Figure 7.49.

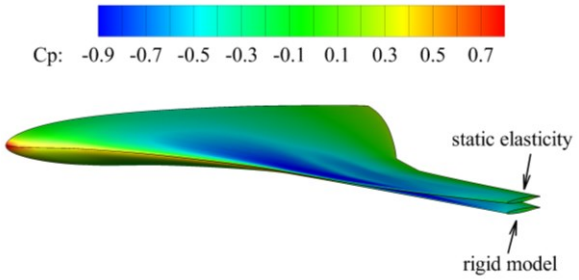

Figure 7.47 Model deformation and pressure distributions under static aeroelasticity

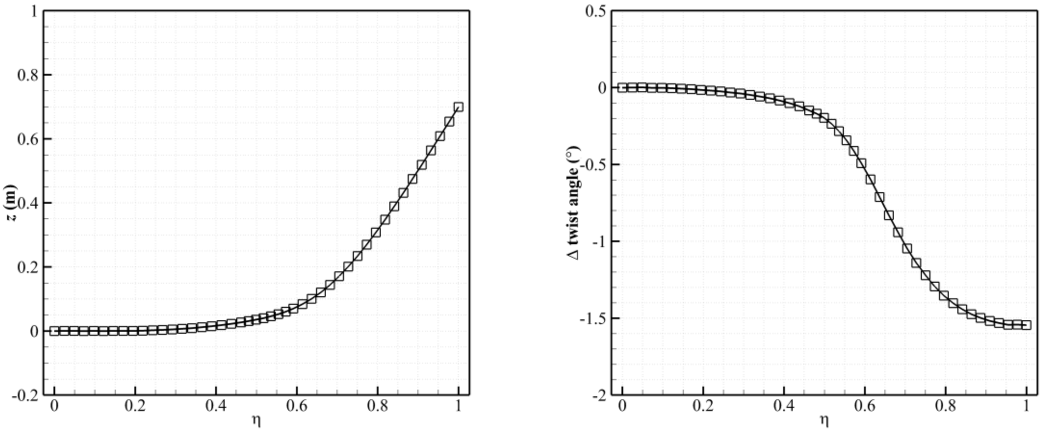

(a) Deformation (b) Twist angle

Figure 7.48 Spanwise deformations and twist angle increments under the static aeroelasticity relative to the baseline rigid model

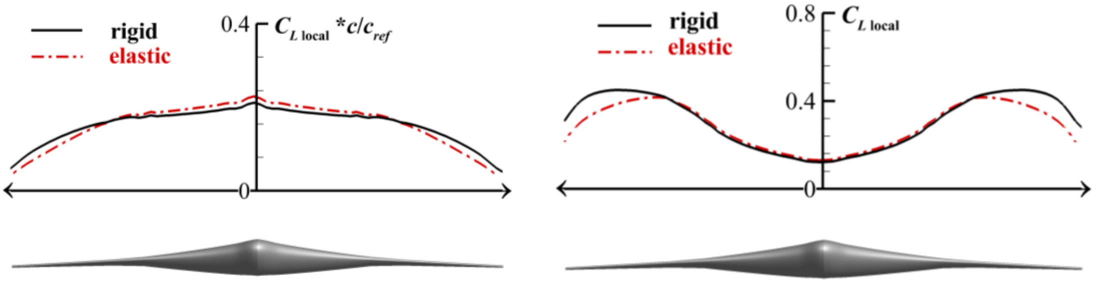

(a) Load distribution (b) Local lift coefficient

Figure 7.49 Comparison of the spanwise loading and local lift coefficients between the rigid and elastic models under the same cruise lift coefficient of C_L= 0.23

7.3.2 Aeroelastic gust response of the baseline model

The gust response considering aeroelasticity for the baseline model is firstly evaluated under the same 'one-minus-cosine' gust as the one used in the previous case study. The responses of lift and root bending moment coefficients are shown in Figure 7.50. Figure 7.51 shows the time evolutions of the vertical displacement and acceleration measured at the wing-tip section. The maximum wing-tip displacement relative to the initial time is about 0.56 m and the peak acceleration is about 25 m/s^2. After passing the gust, structural deformations oscillate and decay generally to revert to the original equilibrium state.

Figure 7.52 presents the time evolutions of the pressure distribution and model deformations, where an increase in vertical deformation especially around the outer-wing region can be noticed from s= 0.0 to 8.6 when the gust load peaks. Under the peak gust load, the wing-tip vertical displacement is about 1.25 m as shown in Figure 7.53 and the twist angle increment reaches to -2.4°. Also shown is that the deformation around the centre body is relatively small, which is understandable as the structure has a larger strength on this region. This also explains why the oscillation is not apparent in the lift coefficient response shown in Figure 7.50(a). That is because of that the lift generated on the outer wing is smaller than that of the inner wing and centre body and the oscillation in the structural deformation during the gust encountering process is mainly on the outer wing part. Therefore, the oscillation in the lift response coming from the outer wing is not noticeable. However, as the outer wing part has a larger contribution to the root bending moment, the oscillation in root bending moments is noticeable as shown in Figure 7.50(b).

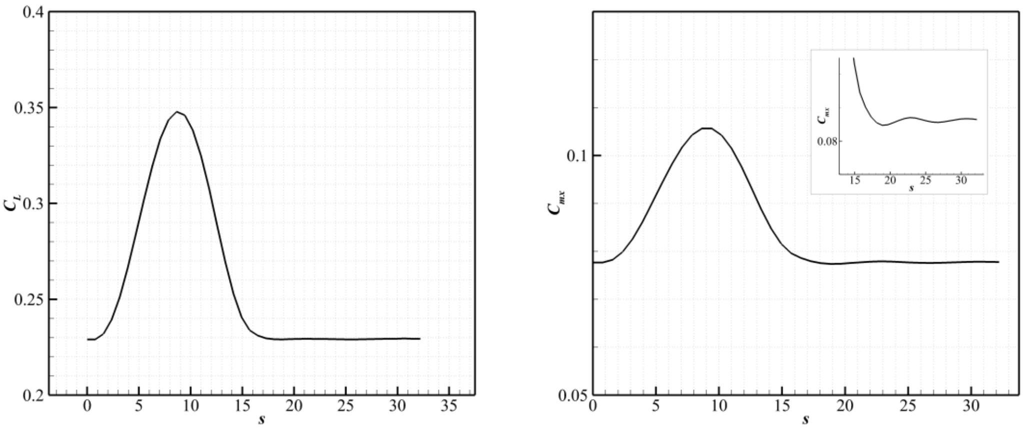

(a) Lift coefficients (b) Root bending moment coefficients

Figure 7.50 Lift and root bending moment coefficient responses

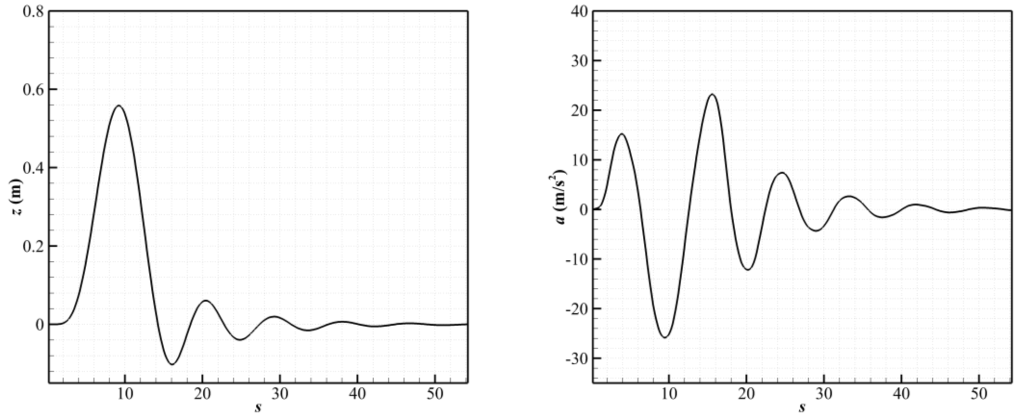

(a) Vertical displacement (b) Acceleration

Figure 7.51 Time evolutions of the vertical displacement (relative to the model under static aeroelasticity) and acceleration of the leading edge along the wing-tip section

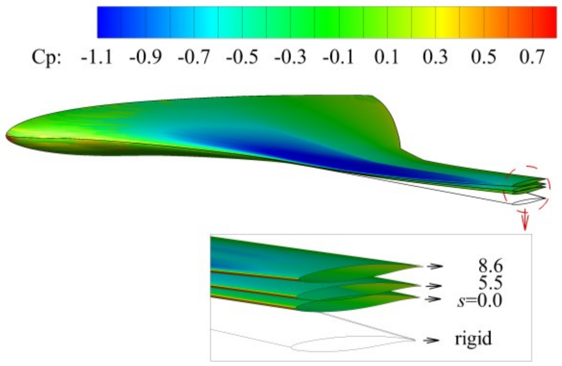

Figure 7.52 Evolution of pressure distribution and wing deformations under the gust. Inset shows the detail around the wing-tip region

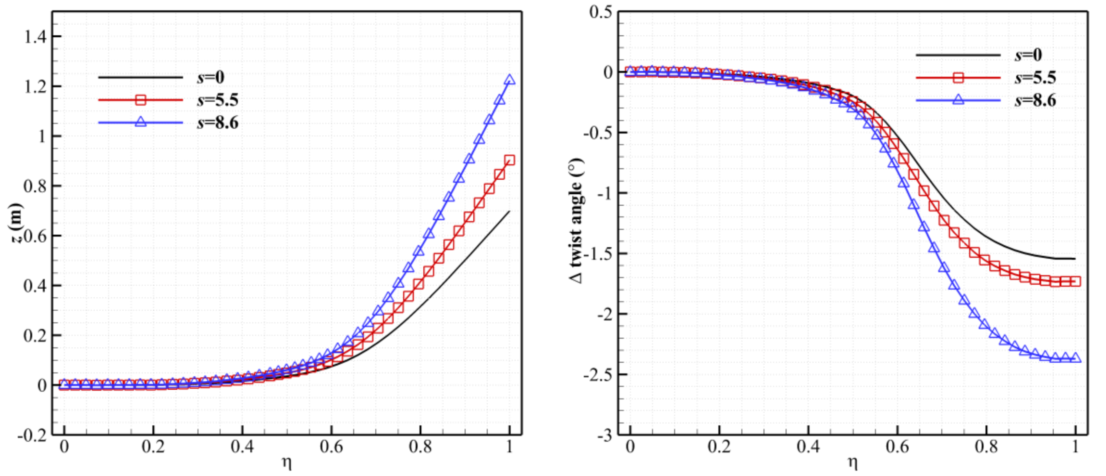

(a) Deformation (b) Twist angle

Figure 7.53 Evolution of the spanwise deformation and the changes of spanwise twist angles under the gust condition relative to the baseline rigid model

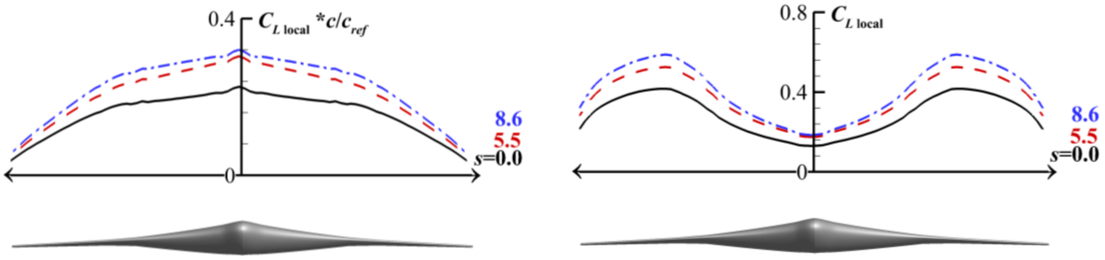

(a) Load distributions (b) Local lift coefficients

Figure 7.54 Evolutions of the spanwise loading and local lift coefficients under the gust condition

7.3.3 Aeroelastic gust load alleviation by normal microjet blowing

The momentum coefficient with one-minus-cosine profile of $C_{\mu 0}$= 0.00075 is chosen for the test of the gust load alleviation effect. The responses of lift and root bending moment coefficients are shown in Figure 7.55. As expected, significant alleviation in lift and root bending moment coefficients has been obtained.

Figure 7.56 represents the time evolutions of the vertical displacement and acceleration at the wing-tip section. An alleviation of more than 70% of the peak vertical displacement due to the microjet blowing can be noticed. The value is reduced from 0.56 m of the baseline model to 0.15 m for the model with microjet blowing.

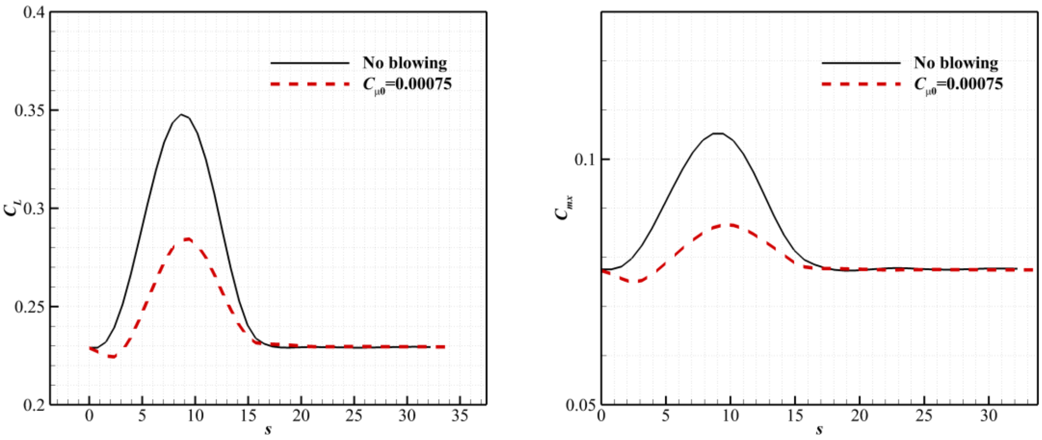

(a) Lift coefficients (b) Root bending moment coefficients

Figure 7.55 Lift coefficient responses

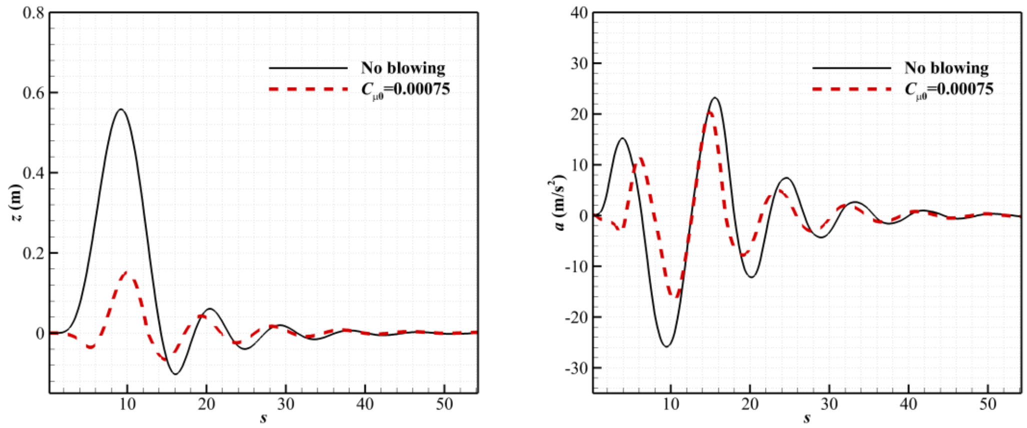

(a) Vertical displacement (b) Acceleration

Figure 7.56 Comparisons of the time evolutions of the vertical displacement and the acceleration of the wing-tip section

7.3.4 Aeroelastic gust load alleviation by normal microjet blowing with adaptive momentum coefficient

Based on the results of gust load alleviation in terms of lift coefficients shown in Figure 7.55, an adaptive profile of momentum coefficients is designed (the peak momentum coefficient is about 0.00197 with a jet Mach number of 0.72) and the gust load alleviation effects are tested as shown in Figure 7.57. As expected, a near constant lift coefficient is obtained under the gust condition. What interesting is the response of the vertical displacement at the wing-tip section as shown in Figure 7.58. For the baseline model, the initial vertical displacement is upwards, but it is downwards for the model with microjet blowing. That is because the load on the outer wing area is significantly alleviated by the blowing to counteract the gust load. When the gust load peaks at *s*= 8.6, the loads on the outer wing region are even lower compared to the initial time *s*= 0 as shown in Figure 7.59. Consequently, the wing-tip deformation of the model with the adaptive blowing under the peak gust load is even smaller than that at the initial time as shown in Figure 7.60. Also shown in Figure 7.59 is that spanwise loading shifts from the elliptic one from the initial time to a triangular-like one at *s*= 8.6 due to the load alleviation on the wing sections due to the significant load controls.

The results from the gust responses of the rigid and elastic models indicate that the gust load of the elastic model is smaller than that of the rigid model under the same incoming flow condition due to the load alleviation from the elastic deformation. However, in general, the gust response and gust load alleviation process of the elastic and the rigid models are similar.

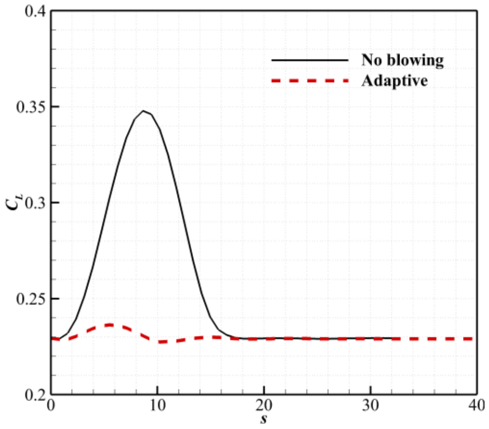

Figure 7.57 Lift coefficient responses under adaptive blowing

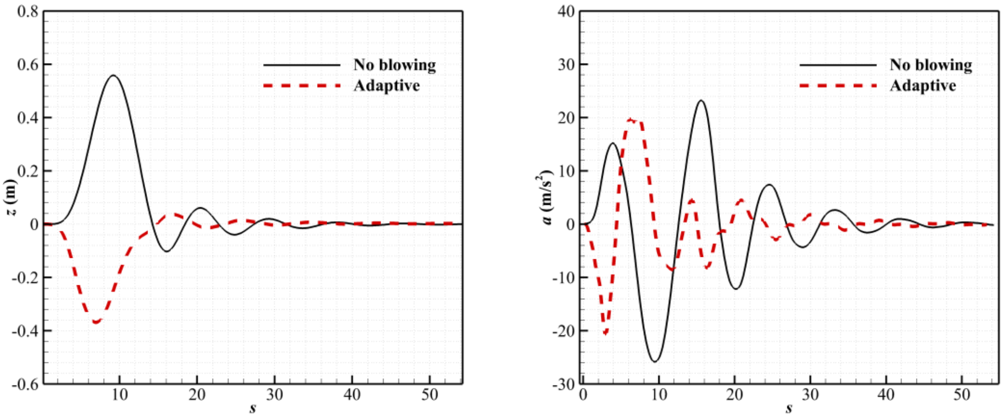

(a) Vertical displacement (b) Acceleration

Figure 7.58 Time evolutions of the wing-tip vertical displacements and accelerations

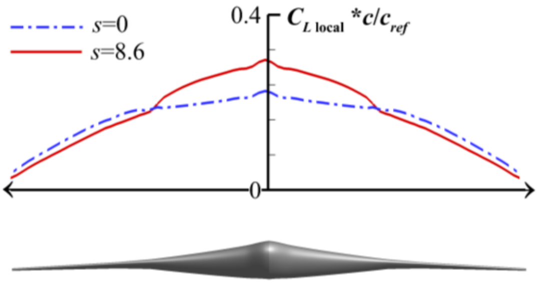

Figure 7.59 Comparison of the spanwise load distributions between the initial time and the *s*= 8.6 when gust load peaks

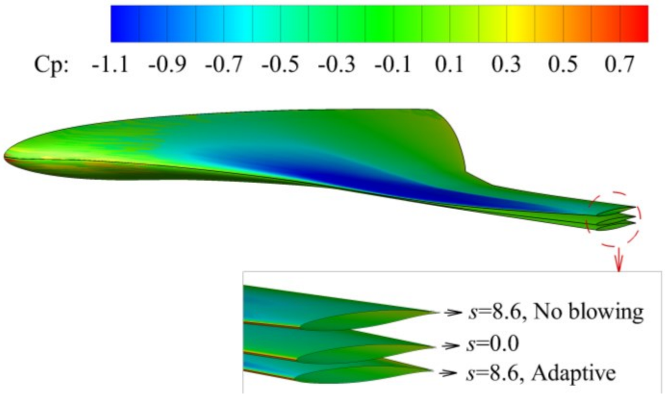

Figure 7.60 Comparisons of the pressure distributions and wing deformations between the baseline model and the adaptive blowing model under the peak gust. Inset shows the detail around the wing-tip region

7.4 Wing structure weight reduction due to circulation control and normal microjet blowing

As demonstrated in Chapter 6, the wing structure weight determined by critical load can be reduced due to the wing root bending moment relief. Assuming gust load is the critical load, it has been demonstrated in the previous case studies that both CC and normal microjet blowing are capable for gust load alleviation on the BWB model. Therefore, the deployment of either CC or normal microjet blowing is theoretically beneficial for the wing structure weight reduction.

For a test case, assuming the BWB critical ultimate 2.5*g* load is defined by a one-minus-cosine gust at the cruise condition. Under this critical gust condition, the wing root bending moment relief factor can be calculated due to gust load alleviation by CC and normal microjet blowing. The amount of wing structure weight reduction then can be estimated based on the methods described in Chapter 6.

To meet this critical load, the one-minus-cosine gust velocity is approximately w_{g0}/U_{∞}= 0.12 and the gust wavelength is set to be 12.5c_{ref}. The BWB models with CC and normal microjet blowing are the same as those used in the previous gust response studies. CC jets on centre body, inner wing and outer wing are actuated for the BWB model with CC. Blowing slots only on the inner and outer wing are actuated for the BWB model with normal microjet. Based on the load control effects of CC and normal microjet blowing shown in Figure 7.11 and Figure 7.31, the momentum coefficients of 1.2×10^{-3} and 2.5×10^{-3} for these two approaches, respectively are used for this test case.

The responses of lift and root bending moment coefficients are shown in Figure 7.61. Both CC and normal microjet blowing can significantly alleviate the peak root bending moment caused by the gust. The estimation of the wing structural weight saving, and the net weight saving based on the Eq. (6-10) and Eq. (6-11) are listed in Table 7.9. As estimated for this case, with the employment of CC and normal microjet blowing, the wing structure weight can lead to a 17% and 26% reduction, respectively, if the correction between wing structural weight reduction and root bending moment relief is 100% as assumed by Iglesias *et al.* [42]. This value will be 8.5% and 13% based on the argument by Takahashi [44]. For the net weight saving, a 4% loss in the aerodynamic efficiency due to the including of CC and normal microjet slots is used for the calculation. As shown in the results, a net weight saving from 0.57% to 1.67%W_{MTOW} can be achieved for the CC model, and this value is from 1.15% to 2.84%W_{MTOW} for the microjet model.

It is just a test case with the theoretical assumption of the correlation between wing structural weight and the root bending moment relief. It is true that wing structural weight design should consider many other factors under the entire flight envelope. Nevertheless, since both CC and normal microjet blowing can alleviate the gust load for subsonic and transonic speeds with fast frequency, they are beneficial for load control and thus structural weight reduction.

Table 7.9 Wing structural weight saving due to load control

Correlation between wing structural weight and *rmbr*	Model	*rmbr*	Wing structural weight saving	Net weight saving (% W_{MTOW})
50% (Takahashi [44])	CC	0.17	8.5%	0.57%
	Microjet	0.26	13%	1.15%
100% Iglesias *et al.* [42]	CC	0.17	17%	1.67%
	Microjet	0.26	26%	2.84%

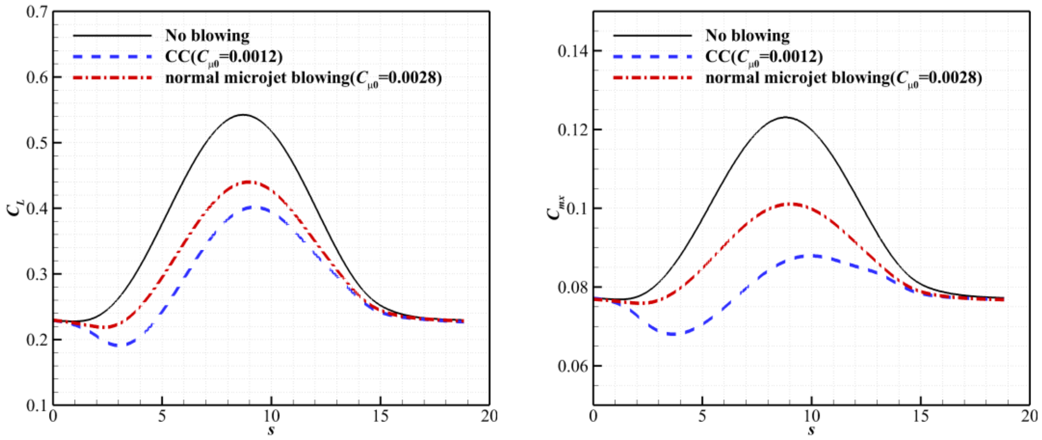

(a) Lift coefficients (b) Root bending moment coefficients

Figure 7.61 Lift and root bending moment coefficient responses

7.5 Summary

Firstly, in this chapter, the capabilities of CC for load control and gust load alleviation on the BWB model have been demonstrated. The results can be summarised as follows:

- Modifications to include the Coanda surfaces in the baseline BWB model are shown to have little influence on the aerodynamic performance under the cruise condition. The thickened trailing edge to install the CC device produces a slight increase in drag by 4 drag counts.

- For the designed CC located from centre body to outer wing working together, the utmost load control capability in terms of lift coefficient reduction under steady conditions is up to -0.44 and -0.125 for M_∞= 0.3 and 0.8, respectively.

Significant local lift coefficient reduction along the whole span by CC is obtained, indicating its promising load control capability.

- Under the reference gust velocity defined by EASA CS-25, the gust load in terms of lift and root bending moment augmentations can be completely counteracted by CC under $M_\infty = 0.3$, resulting in a near constant lift and root bending moment under the gust condition. About 87% and 85% of the peak lift and root bending moment caused by the gust can be suppressed by CC at transonic cruise condition. These results indicate a promising potential for application of CC for load control and gust load alleviation on BWB models.

- The mass flow required by the CC system under cruise condition is proved to be small which is less than 1.1% of the value from the engine of CF5-80A2 equipped on the A310-200 aircraft which has the similar maximum take-off weight with the BWB model studied here.

This chapter then explores the capability of normal microjet blowing for load control and gust load alleviation on the BWB model under cruise condition. The results can be concluded below.

- Under the reference gust velocity defined by EASA CS-25, the gust load in terms of lift and root bending moment augmentations can be completely suppressed by normal microjet blowing at $M_\infty = 0.8$, even though only the microjets on the outer wing and inner wing are actuated. It indicates an attractive prospect of using normal microjet blowing for load control and gust load alleviation at transonic speed.

- Based on the BWB model with normal microjet slot, the effects of aeroelasticity on the gust response are demonstrated. With the microjet blowing on, the results show that significant alleviation of the vertical displacement and acceleration on the wing-tip section of the elastic BWB model has been achieved.

- In general, the gust response and gust load alleviation process of the elastic and the rigid models are similar. The elastic model has a slightly smaller peak gust load than that of the rigid model under the same incoming gust flow condition due to the load alleviation from the elastic deformation.

Overall, this chapter demonstrates the strong gust load alleviation effects of CC on subsonic speed and normal microjet blowing on transonic range on the BWB model. Presumably, a manoeuvring system consists both CC and normal microjets and it can be switched between these two fluidic actuators according to the incoming flow velocity. This system will have strong load control capabilities at both subsonic and transonic speeds.

Chapter 8

Conclusions

8.1 Summary of work

The fundamental aim of this study is to increase understandings of load control capabilities of fluidic actuators including circulation control using Coanda effect and normal microjet blowing, and to evaluate their performance in gust load alleviation for subsonic and transonic flows.

The state of the art of researches on gust load prediction methods, load control and gust load alleviation approaches have been reviewed. An assessment into the use of Field Velocity Methods for gust response simulations through URANS solutions was conducted. Based on the CFL3D code, the numerical tool was set up and validated for gust response simulations for both the rigid and elastic models. Following the validation of CC via jet blowing over trailing-edge Coanda surface and normal microjet blowing, the load control capabilities, load control mechanisms and dynamic actuation responses of these two approaches were compared under steady subsonic and transonic flow conditions with constant, transient and periodic blowing momentum coefficients. The feasibility and effects of gust load alleviation by means of CC and normal microjet blowing were then firstly studied on the 2-D NACA0012 aerofoil and the 3-D BAH wing. The BWB model was generated and optimised together with the setup of its structural model, and the influence of spanwise load distributions on BWB performance was evaluated. Finally, load control and gust load alleviation effects on the BWB model were demonstrated.

The detailed conclusions have been summarized at the end of each chapter.

Through this study, the major findings and the recommendations for future researches are made as follows.

8.2 Major findings

- URANS solutions via FVM are capable and efficient to simulate arbitrary gust encounters and overcome the numerical dissipation from gust disturbances compared to the method by introducing gust perturbations into the far-field boundary of the flow domain.

- From the validation cases of the CC and normal microjet blowing described in Chapter 3, the results suggest that RANS-based CFD can give reasonably reliable results validated by the reference experimental data. For both the subsonic and transonic test cases, the CFD can capture the trends in lift augmentation with increased C_μ and the 'C_μ-stall' phenomenon.

- The results of the influence of normal microjet-slot location showed that it is more effective to place the slot at the trailing edge due to the rapid pressure recovery behind the microjet slot. For the influence of jet-slot width ranging from 0.2%c to 1.0%c, the lift reduction increases and then becomes stable with the increase in jet-slot width under the same blowing momentum coefficient.

- The results of load control effects on the aerofoils, BAH wing and the BWB model indicate that CC has a much stronger load control capability under subsonic range compared to the transonic flow. The load control capability starts to decrease when the momentum coefficient reaches to some extent, which is known as 'C_μ-stall' for both the subsonic and transonic conditions. However, normal microjet blowing has better endurance of usable momentum coefficient under transonic range. Therefore, it can achieve stronger load control effects.

- The flow control mechanisms using Coanda jet and normal microjet are different. For CC deployed under the lower wing surface, it uses the entrainment by the high-speed jet flow following the Coanda surface to accelerate the external flow under the lower surface. Therefore, if the external flow velocity is low, for example, the freestream is subsonic, the entrainment capability of CC will be strong. On the other hand, if the incoming flow is transonic, the entrainment capability will be limited as the external flow velocity is close to the jet flow velocity. Therefore, the load control capability will be limited. That is why CC has a much stronger load control capability under subsonic incoming flow. For the normal microjet blowing, the high-speed jet flow presents itself as a blockage to the flow ahead the jet slot, thus decelerates the flow and increases the pressure coefficients when blowing through the upper surface. If external flow velocity is high, the blockage effect will significantly decelerate the external flow ahead the blowing slot, thus has a strong load control capability under transonic range compared to CC.

- Despite of the difference in load control mechanisms and load control effects under different incoming flows of CC and normal microjet blowing, their load control outcomes are similar. That is to increase the pressure on the wing or aerofoil upper surface and reduce the pressure on the lower surface. For CC and normal microjet on a 3-D wing, deploying the slots only on a partial span region, load control effects have been achieved through the entire span. For the BWB model studied here, it is more efficient to deploy the fluidic actuators on the inner wing as stronger load control achievement can be obtained under the same momentum coefficient compared to that on the centre body and outer wing.

- In general, the dynamic responses of CC and normal microjet blowing under transient and unsteady actuation are similar. Both approaches have fast frequency responses and their load control capabilities will decrease with the increase in jet blowing frequency. Under the same jet blowing frequency and the same incoming flow condition, the 'time-lag' in lift responses by these two methods are close.

- For both CC and normal microjet blowing, they have the capability to suppress the gust load disturbances. The results show that these control methods have a fast frequency response characteristic. More than 50% of the total change in lift coefficient can be achieved within the non-dimensional time $s = 1$. This characteristic allows timely adaptive control to counteract the gust disturbances.

- Under the reference gust velocity defined by EASA CS-25, the gust load in terms of lift augmentation can be completely counteracted by CC under $M_\infty = 0.3$, resulting in a near constant load response under the gust condition. About 87% of the gust load can be suppressed by CC at transonic cruise condition. Since normal microjet blowing has a much stronger load control capability under transonic speeds, the reference gust load can be completely suppressed by normal microjet blowing at $M_\infty = 0.8$, even though only the microjets on the outer wing and inner wing are actuated. It indicates an attractive prospect of using normal microjet blowing for load control and gust load alleviation at transonic speed.

- By comparison to the mass flow rate of a reference engine which is supposed as the supplement of the mass flow for these two fluidic actuators, the required mass flow rate for both actuators are proved to be small to counteract the reference gust load on the BWB model.

- With the aeroelasticity being considered, the gust load is slightly smaller than rigid model under the same incoming flow and gust condition due to the load alleviation from elastic deformation. In general, the gust response is similar to that of the rigid model. For the elastic model, apart from the gust load alleviation, the suppression of the elastic displacement and acceleration due to the load control has also been observed.

8.3 Recommendations for future work

- The 'C_μ-stall' and the oscillation of the jet flow when the momentum coefficient reaches a certain value are recommended for more detailed investigations. This may require wind tunnel tests or higher fidelity models such as LES for the understanding of the interactions of jet flow and external flow.

- Comparisons of load control and gust load alleviation effects between the traditional flaps and the fluidic actuators are recommended for investigations. The response characteristics of these approaches under unsteady actuation are also worth being studied.

- The design of control laws for closed-loop controls in the gust load alleviation process with the consideration of trimming approaches to maintain the longitudinal stability are recommended for a future study.

- A design study is recommended to carry out the coupling of CC and normal microjet blowing together into a single system. According to the incoming flow speed, the flow control method can be switched freely between these two approaches.

Publications

Yonghong Li and Ning Qin, "*Airfoil Gust Load Alleviation by Circulation Control*". Aerospace Science and Technology, Vol. 98, March 2020, Article No. 105622. Available online 11 December 2019. doi.org/10.1016/j.ast.2019.105622

Yonghong Li and Ning Qin, "*Influence of Spanwise Load Distribution on Blended-Wing–Body Performance at Transonic Speed*". Journal of Aircraft. Published online: 2 April 2020. doi.org/10.2514/1.C035696

References

1. Guo, S., J. Los, and Y. Liu, *Gust Alleviation of a Large Aircraft with a Passive Twist Wingtip.* Aerospace, 2015. **2**(2): p. 135-154.
2. *EUROPEAN AVIATION SAFETY AGENCY - Certification Specifications for Large Aeroplanes CS-25.*
3. Al-Battal, N., D. Cleaver, and I. Gursul, *Lift reduction by counter flowing wall jets.* Aerospace Science and Technology, 2018. **78**: p. 682-695.
4. Al-Battal, N., D. Cleaver, and I. Gursul, *Aerodynamic Load Control through Blowing*, in *54th AIAA Aerospace Sciences Meeting, AIAA 2016-1820*. 2016.
5. Alam, M., M. Hromcik, and T. Hanis, *Active gust load alleviation system for flexible aircraft: Mixed feedforward/feedback approach.* Aerospace Science and Technology, 2015. **41**: p. 122-133.
6. Liu, J., W. Zhang, X. Liu, Q. He, and Y. Qin, *Gust response stabilization for rigid aircraft with multi-control-effectors based on a novel integrated control scheme.* Aerospace Science and Technology, 2018. **79**: p. 625-635.
7. Liu, X., Q. Sun, and J.E. Cooper, *LQG based model predictive control for gust load alleviation.* Aerospace Science and Technology, 2017. **71**: p. 499-509.
8. Liu, X. and Q. Sun, *Improved LQG Method for Active Gust Load Alleviation.* Journal of Aerospace Engineering, 2017. **30**(4).
9. Frost, S., B. Taylor, and M. Bodson, *Investigation of Optimal Control Allocation for Gust Load Alleviation in Flight Control*, in *AIAA Atmospheric Flight Mechanics Conference, AIAA 2012-4858*. 2012.
10. Paterson, E., W. Baker, R. Kunz, and L. Peltier, *RANS and detached-eddy simulation of the NCCR airfoil*. Vol. 0. 2004. 112-122.
11. Anonymous, *BAE Systems success in flapless flight.* Aircraft Engineering and Aerospace Technology, 2006. **78**(2).

12. Crowther, W., P. Wilde, K. Gill, and S.M. Michie, *Towards Integrated design of fluidic flight controls for a flapless aircraft.* Aeronautical Journal, 2009. **113**(1149): p. 699-713.
13. John, P., *The flapless air vehicle integrated industrial research (FLAVIIR) programme in aeronautical engineering.* Proceedings of the Institution of Mechanical Engineers. Part G: Journal of Aerospace Engineering, 2010. **224**(4): p. 355-363.
14. Cook, M.V., A. Buonanno, and S.D. Erbslöh, *A circulation control actuator for flapless flight control.* Aeronautical Journal, 2008. **112**(1134): p. 483-489.
15. Hoholis, G., R. Steijl, and K. Badcock, *Circulation Control as a Roll Effector for Unmanned Combat Aerial Vehicles.* Journal of Aircraft, 2016. **53**(6): p. 1875-1889.
16. Wilde, P.I.A., W.J. Crowther, and C.D. Harley, *Application of circulation control for three-axis control of a tailless flight vehicle.* Proceedings of the Institution of Mechanical Engineers, Part G: Journal of Aerospace Engineering, 2010. **224**(4): p. 373-386.
17. de Vries, H., C. Boeije, I. Cleine, E. van Emden, G. Zwart, H. Stobbe, A. Hirschberg, and H. Hoeijmakers, *Fluidic Load Control for Wind Turbine Blades.* 47th AIAA Aerospace Sciences Meeting including The New Horizons Forum and Aerospace Exposition, AIAA 2009-684, 2009.
18. Psaraftis, H., *Green Transportation Logistics: The Quest for Win-Win Solutions*. International Series in Operations Research & Management Science ed. Vol. 226. 2015: Springer.
19. Salam, I.R. and C. Bil, *Multi-disciplinary analysis and optimisation methodology for conceptual design of a box-wing aircraft.* Aeronaut. J., 2016. **120**(1230): p. 1315-1333.
20. Chakraborty, I., T. Nam, J.R. Gross, D.N. Mavris, J.A. Schetz, and R.K. Kapania, *Comparative Assessment of Strut-Braced and Truss-Braced Wing Configurations Using Multidisciplinary Design Optimization.* Journal of Aircraft, 2015. **52**(6): p. 2009-2020.
21. Colliss, S.P., H. Babinsky, K. Nöbler, and T. Lutz, *Vortical structures on three-dimensional shock control bumps.* Journal of Aircraft, 2016. **53**(4): p. 2338-2350.
22. K. Bruce, P.J. and H. Babinsky, *Experimental Study into the Flow Physics of Three-Dimensional Shock Control Bumps.* Journal of Aircraft, 2012. **49**(5): p. 1222-1233.

23. König, B., M. Pätzold, T. Lutz, E. Krämer, H. Rosemann, K. Richter, and H. Uhlemann, *Numerical and Experimental Validation of Three-Dimensional Shock Control Bumps.* Journal of Aircraft, 2009. **46**(2): p. 675-682.
24. Ogawa, H., H. Babinsky, M. Pätzold, and T. Lutz, *Shock-Wave/Boundary-Layer Interaction Control Using Three-Dimensional Bumps for Transonic Wings.* AIAA Journal, 2008. **46**(6): p. 1442-1452.
25. Messing, R. and M.J. Kloker, *Investigation of suction for laminar flow control of three-dimensional boundary layers.* J. Fluid Mech., 2010. **658**: p. 117-147.
26. Chernoray, V.G., A.V. Dovgal, V.V. Kozlov, and L. Lfdahl, *Experiments on secondary instability of streamwise vortices in a swept-wing boundary layer.* J. Fluid Mech., 2005. **534**: p. 295-325.
27. Krishnan, K.S.G., O. Bertram, and O. Seibel, *Review of hybrid laminar flow control systems.* Progress in Aerospace Sciences, 2017. **93**: p. 24-52.
28. Brion, V., J. Dandois, and l. Jacquin, *Laminar buffet and flow control.* 2017, Proceedings of the 7th European Conference for Aeronautics and Space Sciences. Milano, Italy, 3-6 july 2017.
29. Ashill, P.R., J.L. Fulker, and K.C. Hackett, *A review of recent developments in flow control.* Aeronautical Journal, 2005. **109**(1095): p. 205-232.
30. Joslin, R.D., *Overview of Laminar Flow Control - NASA/TP-1998-208705.* 1998, Sponsoring Organization: NASA Langley Research Center.
31. *HYBRID LAMINAR FLOW CONTROL STUDY FINAL TECHNICAL REPORT.* NASA-CR-165930. 1982.
32. Murai, Y., *Frictional drag reduction by bubble injection.* Experiments in Fluids, 2014. **55**(7): p. 1-28.
33. Fuaad, P.A., M.F. Baig, and B.A. Khan, *Turbulent drag reduction using active control of buoyancy forces.* International Journal of Heat and Fluid Flow, 2016. **61**: p. 585-598.
34. Ahmad, H., M.F. Baig, and P.A. Fuaad, *Numerical investigation of turbulent-drag reduction induced by active control of streamwise travelling waves of wall-normal velocity.* European Journal of Mechanics / B Fluids, 2015. **49**: p. 250-263.
35. Wang, Y.-S., W.-X. Huang, and C.-X. Xu, *Active control for drag reduction in turbulent channel flow: the opposition control schemes revisited.* Fluid Dynamics Research, 2016. **48**(5): p. 055501.
36. Liebeck, R.H., *Design of the Blended Wing Body Subsonic Transport.* Journal of Aircraft, 2004. **41**(1): p. 10-25.

37. Graham, W.R., C.A. Hall, and M. Vera Morales, *The potential of future aircraft technology for noise and pollutant emissions reduction.* Transport Policy, 2014.
38. Lebofsky, S., E. Ting, N. Nguyen, and K. Trinh, *Optimization for Load Alleviation of Truss-Braced Wing Aircraft With Variable Camber Continuous Trailing Edge Flap*, in *33rd AIAA Applied Aerodynamics Conference*. 2015.
39. P. O. Jemitola, J.P.F., *Box wing aircraft conceptual design*, in *28th International Congress of the Aeronautical Sciences*. 2012.
40. Guo, Y. and R.H. Thomas, *System Noise Assessment of Hybrid Wing–Body Aircraft with Open-Rotor Propulsion.* Journal of Aircraft, 2015. **52**(6): p. 1767-1779.
41. Jones, R.T., *The spanwise distribution of lift for minimum induced drag of wings having a given lift and a given bending moment*. NACA-TN-2249, 1950.
42. Mason, W. and S. Iglesias. *Optimum spanloads incorporating wing structural weight*. in *1st AIAA, Aircraft, Technology Integration, and Operations Forum*. 2001.
43. Jansen, P.W., R.E. Perez, and J.R. R. A. Martins, *Aerostructural Optimization of Nonplanar Lifting Surfaces.* Journal of Aircraft, 2010. **47**(5): p. 1490-1503.
44. Takahashi, T.T., *Optimum Transverse Span Loading for Subsonic Transport Category Aircraft.* Journal of Aircraft, 2012. **49**(1): p. 262-274.
45. Carter, M., D. Vicroy, and D. Patel. *Blended-Wing-Body Transonic Aerodynamics: Summary of Ground Tests and Sample Results (Invited)*. in *47th AIAA Aerospace Sciences Meeting including The New Horizons Forum and Aerospace Exposition*. 2009.
46. Potsdam, M., M. Page, R. Liebeck, M. Potsdam, M. Page, and R. Liebeck. *Blended Wing Body analysis and design*. in *15th Applied Aerodynamics Conference*. 1997.
47. Cho, S., C. Bil, and J. Bayandor. *Structural Design and Analysis of a BWB Military Cargo Transport Fuselage*. in *46th AIAA Aerospace Sciences Meeting and Exhibit*. 2012.
48. Goraj, Z., *Design and Optimisation of Fuel Tanks for BWB Configurations.* Archive of Mechanical Engineering, 2016. **63**(4): p. 605-617.
49. Wong, W., A. Le Moigne, and N. Qin, *Parallel adjoint-based optimisation of a blended wing body aircraft with shock control bumps.* Aeronaut. J., 2007. **111**(1117): p. 165-174.

50. Qin, N., A. Vavalle, A. Le Moigne, M. Laban, K. Hackett, and P. Weinerfelt, *Aerodynamic considerations of blended wing body aircraft.* Progress in Aerospace Sciences, 2004. **40**(6): p. 321-343.
51. Bahr, C.J., T.F. Brooks, W.M. Humphreys, T.B. Spalt, and D.J. Stead. *Acoustic Data Processing and Transient Signal Analysis for the Hybrid Wing Body 14-by 22-Foot Subsonic Wind Tunnel Test*. in *20th AIAA/CEAS Aeroacoustics Conference*. 2014.
52. Rocha, J., A. Suleman, and F. Lau, *Prediction of turbulent boundary layer induced noise in the cabin of a BWB aircraft.* Shock and Vibration, 2012. **19**(4): p. 693-705.
53. Qin, N., A. Vavalle, and A.L. Moigne, *Spanwise Lift Distribution for Blended Wing Body Aircraft.* Journal of Aircraft, 2005. **42**(2): p. 356-365.
54. Huvelin, F., S. Dequand, A. Lepage, and C. Liauzun, *On the validation and use of high-fidelity numerical simulations for gust response analysis.* AerospaceLab Journal, ONERA, 2019: p. 1-16.
55. Wright, J.R., *Introduction to aircraft aeroelasticity and dynamic loads*. Second edition. ed, ed. J.E. Cooper. 2015: Chichester, West Sussex, United Kingdom : Wiley, 2015.
56. Vartio, E., A. Shimko, C. Tilmann, and P. Flick, *Structural Modal Control and Gust Load Alleviation for a SensorCraft Concept*, in *46th AIAA/ASME/ASCE/AHS/ASC Structures, Structural Dynamics and Materials Conference*. 2005.
57. Silva, W., E. Vartio, A. Shimko, R. Kvaternik, K. Eure, and R. Scott, *Development of Aeroservoelastic Analytical Models and Gust Load Alleviation Control Laws of a SensorCraft Wind-Tunnel Model Using Measured Data*, in *47th AIAA/ASME/ASCE/AHS/ASC Structures, Structural Dynamics, and Materials Conference*. 2006.
58. Vartio, E., E. shaw, and T. Vetter, *Gust Load Alleviation Flight Control System Design for a SensorCraft Vehicle*, in *26th AIAA Applied Aerodynamics Conference*. 2008.
59. Castelluccio, M.A., D.A. Coulson, J. Heeg, and R.C. Scott, *Aeroservoelastic Wind-Tunnel Tests of a Free-Flying, Joined-Wing SensorCraft Model for Gust Load Alleviation*, in *52nd AIAA/ASME/ASCE/AHS/ASC Structures, Structural Dynamics and Materials Conference*. 2011.

60. Mangalam, S., A. Mangalam, and P. Flick, *Unsteady Aerodynamic Observable for Gust Load Alleviation and Flutter Suppression*, in *26th AIAA Applied Aerodynamics Conference*. 2008.

61. Moulin, B., E. Ritz, P.C. Chen, D. Lee, and Z., *CFD-Based Control for Flutter Suppression, Gust Load Alleviation, and Ride Quality Enhancement for the S4T Model*, in *51st AIAA/ASME/ASCE/AHS/ASC Structures, Structural Dynamics, and Materials Conference*. 2010.

62. Shao, K., Z. Wu, C. Yang, L. Chen, and B. Lv, *Design of an Adaptive Gust Response Alleviation Control System: Simulations and Experiments.* Journal of Aircraft, 2010. **47**(3): p. 1022-1029.

63. Bi, Y., C. Xie, C. An, and C. Yang, *Gust load alleviation wind tunnel tests of a large-aspect-ratio flexible wing with piezoelectric control.* Chinese Journal of Aeronautics, 2017. **30**(1): p. 292-309.

64. Neumann, J. and H. Mai, *Gust response: Simulation of an aeroelastic experiment by a fluid-structure interaction method.* J. Fluids Struct., 2013. **38**: p. 290-302.

65. Neumann, J. and H. Mai, *Gust response: Simulation of an aeroelastic experiment by a fluid-structure interaction method.* Journal of Fluids and Structures, 2013. **38**: p. 290-302.

66. *AEROGUST project (funded by the European Commission under grant agreement number 636053). https://www.aerogust.eu. Accessed: 2017-05-26.*

67. Bisplinghoff, R.L., *Aeroelasticity*, ed. H. Ashley and R.L. Halfman. 1996, New York : London: New York : Dover, London : Constable, 1996.

68. Xu, X., X. Zhu, Z. Zhou, and R. Fan, *Application of Active Flow Control Technique for Gust Load Alleviation.* Chinese Journal of Aeronautics, 2011. **24**(4): p. 410-416.

69. Parameswaran, V. and J.D. Baeder, *Indicial Aerodynamics in Compressible Flow-Direct Computational Fluid Dynamic Calculations.* Journal of Aircraft, 1997. **34**(1): p. 131-133.

70. Singh, R. and J.D. Baeder, *Direct Calculation of Three-Dimensional Indicial Lift Response Using Computational Fluid Dynamics.* Journal of Aircraft, 1997. **34**(4): p. 465-471.

71. Raveh, D.E. and A. Zaide, *Numerical Simulation and Reduced-Order Modeling of Airfoil Gust Response.* AIAA Journal, 2006. **44**(8): p. 1826-1834.

72. Jones, R.T., *The unsteady lift of a wing of finite aspect ratio*. 1940, NACA-TR-681.

73. Jones, R.T., *The Unsteady Lift of a Finite Wing*. 1939, NACA-TN-682.
74. Leishman, J.G., *Validation of approximate indicial aerodynamic functions for two-dimensional subsonic flow.* Journal of Aircraft, 1988. **25**(10): p. 914-922.
75. Lomax, H., M.A. Heaslet, and L. Sluder, *The Indicial Lift and Pitching Moment for a Sinking or Pitching Two-Dimensional Wing Flying at Subsonic or Supersonic Speeds*, A. National and D.C. Space Administration Washington, Editors. 1951.
76. Marzocca, P., G. Chiocchia, and L. Librescu, *Unsteady aerodynamics in various flight speed regimes for flutter/dynamic response analyses*, in *18th Applied Aerodynamics Conference*. 2000.
77. Mazelsky, B. and J.A. Drischler, *Numerical Determination of Indicial Lift and Moment Functions for a Two-Dimensional Sinking and Pitching Airfoil at Mach Numbers 0.5 and 0.6*, A. National and D.C. Space Administration Washington, Editors. 1952.
78. Lomax, H., *"Indicial Aerodynamics," AGARD Manual of Aeroelasticity, Part II, Chapter 6*. 1960.
79. Ghoreyshi, M., A. Jirásek, and R.M. Cummings, *Computational Investigation into the Use of Response Functions for Aerodynamic-Load Modeling.* AIAA Journal, 2012. **50**(6): p. 1314-1327.
80. Zhou, Q., G. Chen, A. Da Ronch, and Y. Li, *Reduced order unsteady aerodynamic model of a rigid aerofoil in gust encounters.* Aerospace Science and Technology, 2017. **63**: p. 203-213.
81. Raveh, D.E., *Gust-Response Analysis of Free Elastic Aircraft in the Transonic Flight Regime.* Journal of Aircraft, 2011. **48**(4): p. 1204-1211.
82. Raveh, D.E., *CFD-Based Models of Aerodynamic Gust Response.* Journal of Aircraft, 2007. **44**(3): p. 888-897.
83. Wang, Z., Z. Zhang, P.-C. Chen, and D. Sarhaddi, *A Compact CFD-Based Reduced Order Modeling for Gust Analysis.* 52nd AIAA/ASME/ASCE/AHS/ASC Structures, Structural Dynamics and Materials Conference, Structures, Structural Dynamics, and Materials and Co-located Conferences, AIAA 2011-2041, 2011.
84. Bartels, R.E., *Development, Verification and Use of Gust Modeling in the NASA Computational Fluid Dynamics Code FUN3D - NASA/TM-2012-217771*. 2012, Sponsoring Organization: NASA Langley Research Center.

85. Levy, Y., *Numerical Simulation of Dynamically Deforming Aircraft Configurations Using Overset Grids.* Journal of Aircraft, 2001. **38**(2): p. 349-354.
86. Rigaldo, A. and D. Borglund, *Aerodynamics Gust Response Prediction*. 2011, Master's Thesis, Royal Institute of Technology.
87. Timme, S., B. K. J, and A. Da Ronch, *Linear reduced order modelling for gust response analysis using the DLR-TAU code*. 2013.
88. Wales, C., D. Jones, and A. Gaitonde, *Prescribed Velocity Method for Simulation of Aerofoil Gust Responses.* Journal of Aircraft, 2015. **52**(1): p. 64-76.
89. Sucipto, T., M. Berci, and J. Krier, *Gust response of a flexible typical section via high- and (tuned) low-fidelity simulations.* Computers & Structures, 2013. **122**: p. 202-216.
90. Palacios, R., J. Murua, and R. Cook, *Structural and Aerodynamic Models in Nonlinear Flight Dynamics of Very Flexible Aircraft.* AIAA Journal, 2010. **48**(11): p. 2648-2659.
91. Castellani, M., J. Cooper, and Y. Lemmens, *Flight Loads Prediction of High Aspect Ratio Wing Aircraft Using Multibody Dynamics.* International Journal of Aerospace Engineering, 2016. **2016**(2016).
92. Yang, G. and S. Obayashi, *Numerical Analyses of Discrete Gust Response for an Aircraft.* Journal of Aircraft, 2004. **41**(6): p. 1353-1359.
93. Chen, G., Q. Zhou, A.D. Ronch, and Y. Li, *Computational-Fluid-Dynamics-Based Aeroservoelastic Analysis for Gust Load Alleviation.* Journal of Aircraft, 2018: p. 1-10.
94. Zhou, Q., G. Chen, Y. Li, and A. Da Ronch, *Transonic Aeroelastic Moving Gust Responses and Alleviation based on CFD.* AIAA Modeling and Simulation Technologies Conference, AIAA AVIATION Forum, AIAA 2016-3837, 2016.
95. Frederick, M., E.C. Kerrigan, and J.M.R. Graham, *Gust alleviation using rapidly deployed trailing-edge flaps.* Journal of Wind Engineering & Industrial Aerodynamics, 2010. **98**(12): p. 712-723.
96. Ng, B., R. Palacios, E.C. Kerrigan, J. Graham, and H. Hesse, *Aerodynamic load control in horizontal axis wind turbines with combined aeroelastic tailoring and trailing-edge flaps.* Wind Energy, 2016. **19**(2): p. 243-263.
97. Johnston, J.F., *Accelerated Development and Flight Evaluation of Active Controls Concepts for Subsonic Transport Aircraft. Volume 1: Load*

Alleviation/Extended Span Development and Flight Tests. 1979(NASA-CR-159097).

98. Disney, T.E., *C-5A Active Load Alleviation System.* Journal of Spacecraft and Rockets, 1977. **14**(2): p. 81-86.

99. Al-Battal, N., *Flow control for loads control.* 2019, Ph.D. thesis. University of Bath.

100. Payne, B.W., *Designing a Load Alleviation System for a Modern Civil Aircraft.* 1986(15th Congress of the International Council of the Aeronautical Sciences, ICAS-86-5.2.3).

101. Guo, S., Z.W. Jing, H. Li, W.T. Lei, and Y.Y. He, *Gust response and body freedom flutter of a flying-wing aircraft with a passive gust alleviation device.* Aerospace Science and Technology, 2017. **70**: p. 277-285.

102. Castrichini, A., V.H. Siddaramaiah, D.E. Calderon, J.E. Cooper, T. Wilson, and Y. Lemmens, *Preliminary investigation of use of flexible folding wing tips for static and dynamic load alleviation.* Aeronautical Journal, 2017. **121**(1235): p. 73-94.

103. Castrichini, A., J.E. Cooper, T. Wilson, A. Carrella, and Y. Lemmens, *Nonlinear Negative Stiffness Wingtip Spring Device for Gust Loads Alleviation.* Journal of Aircraft, 2017. **54**(2): p. 627-641.

104. Castrichini, A., V. Siddaramaiah, D. Calderon, J. Cooper, T. Wilson, and Y. Lemmens, *Nonlinear Folding Wing Tips for Gust Loads Alleviation.* Journal of Aircraft, 2016. **53**(5): p. 1391-1399.

105. Chan, D.T.J., Gregory S.; Milholen, William E., II; Goodliff, Scott L., *Transonic Drag Reduction Through Trailing-Edge Blowing on the FAST-MAC Circulation Control Model.* 35th AIAA Applied Aerodynamics Conference, AIAA AVIATION Forum, AIAA 2017-3246, 2017.

106. *Assessment of Fluidic Control Effectors using Computational Fluid Dynamics.* Ph.D. thesis, University of Liverpool, 2016.

107. Parekh, D.E., A.B. Cain, and C.N. Vaporean, *Characterization of Receptivity in Jet Flow Control*, M.O. McDonnell Douglas Corp St Louis, Editor. 1997.

108. Lin, J.C., M.Y. Andino, M.G. Alexander, E.A. Whalen, M.A. Spoor, J.T. Tran, and I.J. Wygnanski, *An Overview of Active Flow Control Enhanced Vertical Tail Technology Development*, in *54th AIAA Aerospace Sciences Meeting, AIAA 2016-0056*. 2016.

109. Englar, R., M. Smith, S. Kelley, and I.R. Rover, *Development of circulation control technology for application to advanced subsonic transport aircraft*, in *31st Aerospace Sciences Meeting, AIAA-93-0644*. 1993.

110. Shmilovich, A. and Y. Yadlin, *Flow Control Techniques for Transport Aircraft.* AIAA Journal, 2011. **49**(3): p. 489-502.

111. Planchenault, P., *Modifications of Wingtip Vortices Using Pulsed and Steady Jets*, S.V. Shkarayev, I. Wygnanski, and Y. Zohar, Editors. 2017, ProQuest Dissertations Publishing.

112. Cui, W., H. Zhu, C. Xia, and Z. Yang, *Comparison of Steady Blowing and Synthetic Jets for Aerodynamic Drag Reduction of a Simplified Vehicle.* Procedia Engineering, 2015. **126**(C): p. 388-392.

113. Chabert, T., J. Dandois, É. Garnier, and L. Jacquin, *Experimental detection of flow separation over a plain flap by wall shear stress analysis with and without steady blowing.* Comptes rendus - Mécanique, 2014. **342**(6-7).

114. Yousefi, K., R. Saleh, and P. Zahedi, *Numerical study of blowing and suction slot geometry optimization on NACA 0012 airfoil.* Journal of Mechanical Science and Technology, 2014. **28**(4): p. 1297-1310.

115. Luedke, J., P. Graziosi, K. Kirtley, and C. Cerretelli, *Characterization of Steady Blowing for Flow Control in a Hump Diffuser.* AIAA Journal, 2005. **43**(8): p. 1644-1652.

116. Chen, C., R. Seele, and I. Wygnanski, *Flow Control on a Thick Airfoil Using Suction Compared to Blowing.* AIAA Journal, 2013. **51**(6): p. 1462-1472.

117. Greenblatt, D. and I.J. Wygnanski, *The control of flow separation by periodic excitation.* Progress in Aerospace Sciences, 2000. **36**(7): p. 487-545.

118. Wygnanski, I., *The Variables Affecting the Control of Separation by Periodic Excitation*, in *2nd AIAA Flow Control Conference, AIAA 2004-2505*. 2004.

119. Araya, G., S. Leonardi, and L. Castillo, *Steady and time-periodic blowing/suction perturbations in a turbulent channel flow.* Physica D: Nonlinear Phenomena, 2011. **240**(1): p. 59-77.

120. Gebhardt, A. and J. Kirz, *Numerical investigation of slot variations on the efficiency of tangential blowing at a vertical tailplane with infinite span.* An Official Journal of the Council of European Aerospace Societies, 2018. **9**(1): p. 195-206.

121. Rao, P., T. Strganac, and O. Rediniotis, *Control of aeroelastic response via synthetic jet actuators*, in *41st Structures, Structural Dynamics, and Materials Conference and Exhibit*. 2000.

122. De Breuker, R., M. Abdalla, P. Marzocca, and Z. Gürdal, *Flutter suppression using synthetic jet actuators: The typical section*. 2006. 402-409.

123. De Breuker, R., M. Abdalla, and P. Marzocca, *Aeroelastic Control and Load Alleviation using Optimally Distributed Synthetic Jet Actuators*, in *48th AIAA/ASME/ASCE/AHS/ASC Structures, Structural Dynamics, and Materials Conference*. 2007.

124. Blaylock, M., R. Chow, and C.P. van Dam, *Comparison of Microjets with Microtabs for Active Aerodynamic Load Control*, in *5th Flow Control Conference, AIAA 2010-4409*. 2010.

125. Blaylock, M., R. Chow, A. Cooperman, and C.P. Dam, *Comparison of pneumatic jets and tabs for Active Aerodynamic Load Control.* Wind Energy, 2014. **17**(9): p. 1365-1384.

126. Heathcote, D., N. Al-Battal, I. Gursul, and D. Cleaver, *Control of Wing Loads by Means of Blowing and Mini-Tabs*, in *European Drag Reduction and Flow Control Meeting – EDRFCM 2015, 2015, Cambridge, UK*. 2015.

127. Al-Battal, N.H., D.J. Cleaver, and I. Gursul, *Unsteady actuation of counter-flowing wall jets for gust load attenuation.* Aerospace Science and Technology, 2019. **89**: p. 175-191.

128. Mueller-Vahl, H., C. Nayeri, C.O. Paschereit, and D. Greenblatt, *Control of Unsteady Aerodynamic Loads Using Adaptive Blowing*, in *32nd AIAA Applied Aerodynamics Conference*. 2014.

129. Alexander, M.G., S.G. Anders, S.K. Johnson, J.P. Florance, and D.F. Keller, *Trailing Edge Blowing on a Two-Dimensional Six-Percent Thick Elliptical Circulation Control Airfoil Up to Transonic Conditions - NASA/TM-2005-213545*. 2005, Sponsoring Organization: NASA Langley Research Center.

130. Ahuja, K., L. Sankar, R.J. Englar, S. Munro, and Y. Liu, *Application of Circulation Control Technology to Airframe Noise Reduction*, ed. G.I.o.T. Annual Performance Report. Vol. 5928. 2000. 1-2146.

131. Nichols, J.H. and R.J. Englar, *Advanced circulation control wing system for navy stol aircraft.* Journal of Aircraft, 1981. **18**(12): p. 1044-1050.

132. Englar, R., M. Smith, and S. Kelley, *Application of circulation control to advanced subsonic transport aircraft. I - Airfoil development. II - Transport application.* Journal of Aircraft (0021-8669), 1994. **31**(5): p. 1160-1177.

133. Min, B.-Y., W. Lee, R. Englar, and L.N. Sankar, *Numerical Investigation of Circulation Control Airfoils.* Journal of Aircraft, 2009. **46**(4): p. 1403-1410.

134. Rumsey, C.L. and T. Nishino, *Numerical study comparing RANS and LES approaches on a circulation control airfoil.* International Journal of Heat and Fluid Flow, 2011. **32**(5): p. 847-864.

135. Swanson, R.C. and C.L. Rumsey, *Computation of circulation control airfoil flows.* Computers & Fluids, 2009. **38**(10): p. 1925-1942.

136. Forster, M. and R. Steijl, *Design study of Coanda devices for transonic circulation control.* The Aeronautical Journal, 2017. **121**(1243): p. 1368-1391.

137. Krist, S.L., C.L. Rumsey, and R.T. Biedron, *CFL3D User's Manual (Version 5.0) - NASA/TM-1998-208444*. 1998, Sponsoring Organization: NASA Langley Research Center.

138. Rumsey, C.L. and J.L. Thomas, *Application of FUN3D and CFL3D to the Third Workshop on CFD Uncertainty Analysis - NASA/TM-2008-215537*. 2008, Sponsoring Organization: NASA Langley Research Center.

139. Sclafani, A.J., M.A. Dehaan, J.C. Vassberg, C.L. Rumsey, and T.H. Pulliam, *Drag Prediction for the Common Research Model Using CFL3D and OVERFLOW.* Journal of Aircraft, 2014. **51**(4): p. 1101-1117.

140. Park, M.A., K.R. Laflin, M.S. Chaffin, N. Powell, and D.W. Levy, *CFL3D, FUN3D, and NSU3D Contributions to the Fifth Drag Prediction Workshop.* Journal of Aircraft, 2014. **51**(4): p. 1268-1283.

141. Rumsey, C.L., *CFL3D Contribution to the AIAA Supersonic Shock Boundary Layer Interaction Workshop - NASA/TM-2010-216858*. 2010, Sponsoring Organization: NASA Langley Research Center.

142. Rumsey, C.L. and R.T. Biedron, *Computation of Flow Over a Drag Prediction Workshop Wing/Body Transport Configuration Using CFL3D - NASA/TM-2001-211262*. 2001, Sponsoring Organization: NASA Langley Research Center.

143. Richardson, P.F., *Hypersonic CFD applications at NASA Langley using CFL3D and CFL3DE*, in *NASA, Ames Research Center, NASA Computational Fluid Dynamics Conference*. 1989.

144. Cunningham, H.J., J.T. Batina, and R.M. Bennett, *Modern wing flutter analysis by computational fluid dynamics methods.* Journal of Aircraft, 1988. **25**(10): p. 962-968.

145. Robinson, B.A., H.T.Y. Yang, and J.T. Batina, *Aeroelastic analysis of wings using the Euler equations with a deforming mesh.* Journal of Aircraft, 1991. **28**(11): p. 781-788.

146. Edwards, J.W., R.M. Bennett, W. Whitlow, and D.A. Seidel, *Time-marching transonic flutter solutions including angle-of-attack effects.* Journal of Aircraft, 1983. **20**(11): p. 899-906.
147. Qin, N., R. Howell, N. Durrani, K. Hamada, and T. Smith, *Unsteady Flow Simulation and Dynamic Stall Behaviour of Vertical Axis Wind Turbine Blades.* Wind Engineering, 2011. **35**(4): p. 511-527.
148. Theodorsen, T., *General Theory of Aerodynamic Instability and the Mechanism of Flutter*, NACA-TR-496, Editor. 1949.
149. Bisplinghoff, R.L., G. Isakson, and T.F. Obrien, *Gust Loads on Rigid Airplanes with Pitching Neglected.* Journal of the Aeronautical Sciences, 1951. **18**(1): p. 33-42.
150. Howcroft, C., D. Calderon, L. Lambert, M. Castellani, J.E. Cooper, M.H. Lowenberg, and S. Neild, *Aeroelastic Modelling of Highly Flexible Wings*, in *15th Dynamics Specialists Conference*. 2016.
151. Rodden WP, H.R., Bellinger ED, *Aeroelastic additions to NASTRAN.*, in *Technical Report Contractor Report 3094, NASA; 1979.*
152. Corporation, M.S., *MSC.Nastran Aeroelastic Analysis User's Guide. Printed in U.S.A*. 2002.
153. Forster, M. and R. Steijl, *Numerical Simulation of Transonic Circulation Control.* 53rd AIAA Aerospace Sciences Meeting, AIAA 2015-1709, 2015.
154. Anders, S.G. and J. Cruz, *Assessment of an Unstructured-Grid Method for Predicting Aerodynamic Performance of Jet Flaps*, in *24th AIAA Applied Aerodynamics Conference, Fluid Dynamics and Co-located Conferences, AIAA 2006-3868*. 2006.
155. Cook, M.V., A. Buonanno, and S.D. Erbslöh, *A circulation control actuator for flapless flight control.* The Aeronautical Journal, 2016. **112**(1134): p. 483-489.
156. Wetzel, D.A., J. Griffin, and L.N. Cattafesta Iii, *Experiments on an elliptic circulation control aerofoil.* Journal of Fluid Mechanics, 2013. **730**: p. 99-144.
157. Cruz, J. and S. Anders, *Assessment of an Unstructured-Grid Method for Predicting Aerodynamic Performance of Jet Flaps*, in *24th AIAA Applied Aerodynamics Conference, Fluid Dynamics and Co-located Conferences, AIAA 2006-3868*. 2006.
158. Rumsey, C., *Successes and Challenges for Flow Control Simulations (Invited).* International Journal of Flow Control, 2008: p. 1-27.

159. Leopold, D., A. Krothapalli, and D. Tavella, *Some observations on the aerodynamics of an airfoil with a jet exhausting from the lower surface*, in *21st Aerospace Sciences Meeting*. 1983.

160. Eggert, C.A.a., *CFD study of NACA 0018 airfoil with flow control*. 2017: Hampton, Virginia : National Aeronautics and Space Administration, Langley Research Center, NASA/TM-2017-219602, 2017.

161. Hileman, J.I., Z.S. Spakovszky, M. Drela, M.A. Sargeant, and A. Jones, *Airframe Design for Silent Fuel-Efficient Aircraft.* Journal of Aircraft, 2010. **47**(3): p. 956-969.

162. Gatlin, G., D. Vicroy, and M. Carter, *Experimental Investigation of the Low-Speed Aerodynamic Characteristics of a 5.8-Percent Scale Hybrid Wing Body Configuration*, in *30th AIAA Applied Aerodynamics Conference*. 2012.

163. Lyu, Z. and J.R.R.A. Martins, *Aerodynamic Design Optimization Studies of a Blended-Wing-Body Aircraft.* Journal of Aircraft, 2014. **51**(5): p. 1604-1617.

164. Dehpanah, P. and A. Nejat, *The aerodynamic design evaluation of a blended-wing-body configuration.* Aerospace Science and Technology, 2015. **43**: p. 96-110.

165. Marec, J.-P., *Drag Reduction: a Major Task for Research*. 2001, Berlin, Heidelberg: Springer Berlin Heidelberg. 17-27.

166. Moigne, A.L., *A discrete Navier-Stokes adjoint method for aerodynamic optimisation of Blended Wing-Body configurations*, in *Ph.D. thesis, Cranfield University*. 2002.

167. Blickle, T. and L. Thiele, *A Comparison of Selection Schemes Used in Evolutionary Algorithms.* Evolutionary Computation, 1996. **4**(4): p. 361-394.

168. Mukhopadhyay, V. and M.R. Sorokach. *Composite Structure Modeling and Analysis of Advanced Aircraft Fuselage Concepts*. in *AIAA Modeling and Simulation Technologies Conference*. 2015.

169. Anderson, J.D., *Introduction to flight*. Eighth edition. New York : McGraw-Hill Education, 2016.

170. L.Jenkinson, P.S., D. Rhodes. *"Civil jet aircraft design: Data B: Engine Data File," https://booksite.elsevier.com/9780340741528/appendices/data-b/table-3/default.htm, 2001, Accessed: March 2019.*; Available from: https://booksite.elsevier.com/9780340741528/appendices/data-b/table-3/default.htm.